Toward Accelerated Qualification of ATF Claddings: An In-Situ Burst Testing Framework and Insights into Zr Alloy LOCA Behavior

A Dissertation Presented for the

Doctor of Philosophy

Degree

The University of Tennessee, Knoxville

Samuel Bernat Walker Bell

December 2023

Copyright © by Samuel Bernat Walker Bell, 2023
All Rights Reserved.

To my first of many professors, Graham and Julie Bell

Disclaimer

This dissertation comprises research sponsored by an agency of the United States Government. Neither the United States Government nor any agency thereof, nor any of their employees, makes any warranty, express or implied, or assumes any legal liability or responsibility for the accuracy, completeness, or usefulness of any information, apparatus, product, or process disclosed, or represents that its use would not infringe privately owned rights. Reference herein to any specific commercial product, process, or service by trade name, trademark, manufacturer, or otherwise, does not necessarily constitute or imply its endorsement, recommendation, or favoring by the United States Government or any agency thereof. The views and opinions of authors expressed herein do not necessarily state or reflect those of the United States Government or any agency thereof.

Acknowledgements

This dissertation and my journey through graduate school would not have been possible with the mentorship, guidance, and opportunity given to me by my advisor, Dr. Steven Zinkle. I am deeply grateful to Dr. Zinkle for the support over the years to pursue this dream, for always being understanding, patient, and quick to offer your expertise. Thank you to Dr. Kenneth Kane and Dr. Mackenzie Ridley for their open-door policy, tolerating my endless questions, and providing the freedom to grow and navigate my way in the lab. I would also like to express my gratitude to Dr. Nathan Capps, who without his support and guidance this dissertation would not have been realized. Thank you to Dr. Brian Wirth and Dr. Eric Lass for their guidance with this research, mentorship, and willingness to be a part of this process.

I owe a lot to many at Oak Ridge National Laboratory, especially the staff in the Corrosion Science and Technology Group. Their influence on my graduate experience, whether through insightful discussions or informal chats, was instrumental in shaping my understanding of the world of research. Special gratitude is extended to Dr. Bruce Pint and Dr. Sebastien Dryepondt for letting me be a part of this group. Brandon Johnston, your support was instrumental in completing much of the work in this dissertation. Thank you for your friendship, and best wishes for your future with Lexi. I also wish to express my gratitude to Adam Willoughby for all the help over the years. A great deal of gratitude is owed to Dr. Caleb Massey and Dr. Tim Gräning for always showing a willingness to help when I needed it, engage in discussions, and provide mentorship.

To my friends gained during this graduate experience—Jeff, Josh, Ian, Jack, Dylan, Katy, Clayton, and Marissa—your friendship was invaluable. To my friends back home in California, of which there are too many to list, thank you for always being there and keeping me sane, even if it was from across the country.

Finally, I owe a profound debt of gratitude to my family. To my parents, for their unwavering support, and the many enjoyed Sunday dinners. To Graham and Dally, for always being the big brother and sister I needed. Karen and Mike Simonson, thank you for all the support, and for being a great part of mine and my family's lives. To my lovely girlfriend Katelyn, I truly appreciate everything you have done to keep me going all these years, moving across the country for this, and always keeping me smiling. I look forward to the future we have together. To Chelle,

thank you for all your kindness and help towards Katelyn and I—we appreciate it more than words can express.

The work presented in this dissertation was supported by Advanced Fuels Campaign from the Office of Nuclear Energy in the U.S. Department of Energy.

Abstract

This dissertation introduces a robust burst testing framework with *in-situ* measurement capabilities, for the purpose of accelerating the characterization and qualification of cladding materials under accident conditions, specifically design-basis loss-of-coolant accidents (LOCAs) in nuclear reactors. The framework combines digital image correlation and infrared thermography to generate high-fidelity thermomechanical data, providing insight into deformation mechanisms such as creep and plasticity during LOCA conditions. The framework was initially developed to evaluate accident-tolerant fuel (ATF) claddings, including Cr-coated Zr and FeCrAl alloys. However, testing of historic Zr claddings was conducted to demonstrate the framework's versatility as well as address existing modeling gaps and expound on the deformation mechanisms of Zr during LOCAs.

In the first four chapters of this dissertation, historical use of burst testing is detailed, recent *ex-situ* testing of FeCrAl and Cr-coated alloys are presented, and the benefits of an *in-situ* framework for ATF systems are high-lighted. Subsequent chapters focus on Zr as a demonstration of the in-situ framework, where current modeling gaps are identified, the prevailing reliance on steady-state creep in LOCA models is challenged, and possible anisotropy effects are explored.

The steady-state creep assumption for Zr LOCA behavior was investigated with *in-situ* thermomechanical data, and a novel transition in deformation behavior during transiently heated burst testing was found. The onset of this behavior was compared to plasticity models which indicated the majority of ballooning deformation is likely related to plastic instability. Accelerated creep testing methods were also demonstrated on Zr alloys where creep parameters were recovered and compared to literature models.

Preliminary application of the validated framework to Cr coated Zr systems is presented to demonstrate the experimental resolution gained from implementing *in-situ* techniques. A change in deformation behavior related to ballooning was also identified during initial testing of Cr coated Zr. The characteristics of this ballooning process mirrored those of the uncoated reference, but were shifted by roughly 80 °C. This temperature shift corresponded with the observed difference in burst temperature between the coated and uncoated samples from *ex-situ* testing. This correlation suggested the coating delays ballooning rather than alter the deformation process.

Table of Contents

Chapter 1: Introduction to Fuel Claddings, Accident Scenarios, and Conventional Characterization Methods 1

Chapter Foreword 1

Section 1.1: Fuel Claddings and Background on Conventional Zr Materials 1

1.1.1: Fuel claddings as structural components in nuclear systems 1

1.1.2: Material and microstructural characteristics of Zr alloys used for claddings 3

Section 1.2: Loss-of-Coolant Accidents and Burst Testing Efforts 7

1.2.1: Design Basis LOCAs 7

1.2.2: Historic burst testing and conventional ex-situ parameters 11

1.2.3: The Severe Accident Test Station and standard simulated LOCA burst testing 16

1.2.4: Reflection on standard burst testing and recent SATS improvements 19

Chapter 2: Accident Tolerant Fuel Claddings and Previous Burst Testing Efforts 21

Chapter Foreword 21

Section 2.1: Motivation for ATF Claddings and Candidate Systems 21

2.1.1: Fukushima nuclear disaster as a driver for ATF materials 21

2.1.2: General goals of Accident Tolerant Fuel systems 22

2.1.3: Candidate systems for ATF claddings 25

Section 2.2: The State of ATF LOCA Burst Testing 26

2.2.1: Previous ex-situ burst testing of FeCrAl Claddings 26

2.2.2: Previous ex-situ burst testing of Cr coated claddings 28

2.2.3: Potential mechanisms for Cr coating influence on Zr 31

Chapter 3: Ex-situ Burst Testing of Cr-coated Zirconium alloys 34

Chapter Foreword 34

Section 3.1: METHODS AND MATERIALS 35

3.1.1: Cr coated systems and deposition parameters 35

3.1.2: As-received coating characterization 37

Section 3.2: EXPERIMENTAL RESULTS 37

3.2.1: Conventional burst strength characterization 37

3.2.2: Ballooning and deformation 42

3.2.3: Opening geometry analysis 49

3.2.4: Oxidation analysis of regions opposite from burst 53

3.2.5: Oxidation analysis of regions of high strain 61
Section 3.3: DISCUSSION 67
3.3.1: Effect of thin coatings on burst strength 67
3.3.2: Lack of reduction in diametric strain from thin Cr coatings 68
3.3.3: Effect of Cr coating on rupture geometry 70
3.3.4: A critique of generalized statements about improved burst behavior from as-received testing 71
3.3.5: Cr coating integrity near and away from the burst region 72
3.3.6: Reaction product formation in regions of complete mitigation 73
3.3.7: Insights to be gained from in-situ strain data 74
Section 3.5: CONCLUSIONS 74
Chapter 4: Ex-situ Burst testing of Down-selected C26M FeCrAl 76
Chapter foreword 76
Section 4.1: INTRODUCTION 77
Section 4.2: METHODS AND MATERIALS 78
Section 4.3: EXPERIMENTAL RESULTS 81
4.3.1: Burst behavior and tensile strength 81
4.3.2: Microstructure characterization 86
4.3.3: Ex-situ Cladding deformation 89
4.3.4: Burst opening characterization 93
Section 4.4: DISCUSSION 97
4.4.1: Conventional burst characterization 97
4.4.2: Proposed mechanisms of rupture formation, dynamics, and relation to tensile properties 97
4.4.3: Impacts of thermal gradients, microstructure, and irradiation 99
4.4.4: Proposed benefits from an in-situ burst framework for modeling campaigns 101
Section 4.5: CONCLUSIONS 105
Chapter 5: LOCA Modeling Gaps in Zr alloys and High Burn-up Concerns 106
Chapter Foreword 106
Section 5.1: High burnup extension and Zr LOCA behavior 106
Section 5.2: Historic and Contemporary Zr LOCA Models 108
5.2.1: Erbacher model and anisotropy considerations 108
5.2.2: The Donaldson Model 113

5.2.3: The Kaddour Model 113
5.2.4: Failure criteria for LOCA models 115
5.2.5: Comparison of high temperature creep models and a critique of general models for Zircaloys 117
Section 5.3: BISON Modeling of Zircaloys 119
5.3.1: Preliminary comparison of BISON predictions to literature data 119
5.3.2: Handling of anisotropy in BISON models 119
5.3.3: Summary of BISON modeling of Zircaloys 121
Section 5.4: Role of time independent plasticity in LOCA behavior 122
5.4.1: Instability criterion 122
5.4.2: Loss of uniformity, variability in necking, and short falls of analytical methods 124
5.4.3: Potential application to LOCA modeling 126
5.4.4: Finite element inverse and virtual field method 127
Chapter 6: *In-situ* Experimental Techniques and Augmentations to SATS 130
Chapter Foreword 130
Section 6.1: Background on In-situ Techniques 130
6.1.1: Fundamentals of digital image correlation 130
6.1.2: Fundamentals of infrared thermography 134
Section 6.2: 2D DIC integration and experimental details 138
6.2.1: Physical integration of 2D DIC and IRT into the SATS 138
6.2.2: Cladding train augmentations and 2D DIC patterning 143
Section 6.3: 3D DIC transient and step loaded isothermal creep testing details 149
6.3.1: 3-dimensional DIC configuration for SATS testing 149
6.3.2: 3D DIC transient testing methods and augmentations 152
6.3.3: 3D DIC isothermal creep testing 155
Chapter 7: Transient Testing of Zircaloy-4 with 2-dimensional DIC 158
Chapter Foreword 158
Section 7.1: INTRODUCTION 158
Section: 7.2: EXPERIMENTAL METHODS 161
Section 7.3: RESULTS 172
7.3.1: In-situ Strain Comparison 172
7.3.2: Comparison of BISON modeling to 2D DIC results 179
7.3.3: IR thermography and Limitations 182

7.3.4: Strain Rates at Failure 187
7.3.5: Ex-situ Strain Comparison 189
7.3.6: Strain Rate and Arrhenius Temperature Dependence 194
7.3.7: Comparison of transition points against plasticity models 200
7.3.8: SEM and Oxide Analysis 201
Section 7.4: DISCUSSION 204
7.4.1: Arrhenius Temperature dependence and steady state creep assumption 204
7.4.2: Strain-time behavior and loading considerations 207
Section 7.5: CONCLUSIONS 208
Chapter 8: Accelerated Creep Testing of Zircaloy-4 using *In-situ* Techniques 210
Chapter Foreword 210
Section 8.1: INTRODUCTION 210
Section 8.2: EXPERIMENTAL METHODS 211
Section 8.3: RESULTS 217
8.3.1: Strain-curves from lower temperature testing (550 and 600 °C) 217
8.3.2: Strain rate – stress dependence of the lower temperature regime 217
8.3.3: Comparison of low temperature testing to model predictions 219
8.3.4: Higher temperature testing and the effects of hold time before pressurization 224
8.3.5: Strain-rate and stress dependency for 650 and 700 °C testing 224
8.3.6: Preliminary considerations of a shift in creep behavior at low stresses 231
8.3.7: Comparison of high temperature testing to literature models 233
8.3.8: Model fitting across all tested temperatures 233
8.3.9: Axial Strain Measurements, and future testing 237
Section 8.4: DISCUSSION 239
8.4.1: Recovered creep parameters and comparisons to literature models 239
8.4.2: Validation of methods and uncertainties in drawing effective comparisons 240
8.4.3: Effective isotropy due to activation of deformation mechanisms 241
8.4.4: Implications for LOCA models and future work 241
Section 8.5: CONCLUSIONS 242
Chapter 9: Preliminary Application of Framework to ATF claddings 244
Section 9.1: INTRODUCTION 244
Section 9.2: EXPERIMENTAL METHODS 245

Section 9.3: RESULTS..... 248
9.3.1: Transient testing of bare and Cr coated Zry-4 using 3D DIC..... 248
9.3.2: Step-loaded isothermal testing of Cr coated Zry-4 254
9.3.3: Transient testing of C26M FeCrAl 257
9.3.4: Consideration of error in stereo-DIC and future strategies to mitigate error 264
Section 9.4: DISCUSSION AND CONCLUSIONS 265
Chapter 10: Conclusions 268
References:..... 273
Vita:..... 290

List of Tables

Table 1. Representative fuel and cladding design parameters of PWR and BWR designs 2

Table 2. Alloy composition ranges for reactor grade Zr alloys according U.S. regulations in weight percent. 4

Table 3. Sample geometry and coating thickness for Cr coated and bare samples. 36

Table 4. Burst criteria for all bare and Cr coated Zr testing presented in this chapter 41

Table 5. Chemical composition in weight % of FeCrAl alloys. 79

Table 6. Pre-transient geometry for C26M and T35Y2 claddings..... 79

Table 7. Burst temperature and hoop stress data for all three materials. Burst hoop stress was calculated using burst pressure. 83

Table 8. Tensile data from C26M from tube geometry testing: yield strength (YS), elongation at yield (YE), ultimate tensile strength (UTS), uniform elongation (UE), and total elongation (TE). Commas separate values from different tests at the same temperature. 84

Table 9. BISON model parameters for LOCA strain calculations for the α, α +β, and β phases [125]. 109

Table 10. Hill parameters for a range of metallurgical conditions of α-phase Zry-4 modeled by Suman [126]. 111

Table 11. Parameters from the Donaldson model for Zry-4 in the α phase..... 114

Table 12. Parameters generated from Kaddour et al. for Zry-4 in the α phase..... 116

Table 13. Ingot chemistry for SRA Zry-4 in weight percent. 162

Table 14. Test matrix, loading conditions, and burst data for all tests presented in this work. *Sample was repressurized at 300 °C to 14.8 MPa. 167

Table 15. Activation energies and transition parameters for two segment linear fits..... 198

Table 16 Low temperature Zry-4 test conditions..... 215

Table 17. High temperature Zry-4 test conditions. 216

Table 18. Parameters of fit from the data in this chapter including all tests at 550, 600, 650, and 700 °C. These parameters are only applicable to the hoop direction for this specific Zry-4 material. 235

Table 19. Material condition and geometry of the ATF and reference claddings. 246

Table 20. Activation energies determined from each segment in the strain-rate temperature dependence curves. 255

List of Figures

Figure 1. Phase diagram for Zr with respect to oxygen concentration. 5

Figure 2. SEM images and EBSD maps of RXA and CWSR/SRA Zircaloy-4.. 8

Figure 3. Response of Zircaloy-4 cladding during a double-ended guillotine break LOCA..... 10

Figure 4. Example temperature and pressure history for a transient burst test with constant gas inventory. 12

Figure 5. Historic data of burst temperature and engineering hoop stress for Zr claddings subjected to heating rates from 0-28 C/s and plots of maximum circumferential strain and temperature. 13

Figure 6. Image of a Zircaloy cladding post-burst test and light-optical micrographs of sections at and away from the center of the balloon region..... 15

Figure 7. A schematic and image of the SATS furnace from Massey et al.. 18

Figure 8. Burst hoop stress and temperature of Zircaloy-4 and 2nd generation FeCrAl compared to a historic correlation. 20

Figure 9. Illustration detailing goals beyond improvement in oxidation and deformation behavior..... 23

Figure 10. Plot of parabolic rate constants in high temperature steam of ATF cladding concepts (silica, alumina, and chromia formers) 24

Figure 11. Plots of burst temperature vs hoop stress and burst temperature vs burst pressure for Zry-2, Zry-4, 1st generation FeCrAl T35Y2 and B154Y, and 304 SS. 27

Figure 12. Plot of hoop stress and cladding surface temperature vs time for burst testing simulating cyclic dry out transients. 29

Figure 13. Surface roughness of the SRA Zry-4 before polishing and after polishing. Coating-cladding interface for Cr#1 and Cr#2. 38

Figure 14. SEM micrograph of a cross-section from the base of a Cr-coated Zirlo cladding prior to testing. 39

Figure 15. Burst temperature and hoop stress of all systems presented in this chapter. 40

Figure 16. Optical macrographs of burst Zirlo and Cr-coated Zirlo at initial pressures of 1 MPa, 3.4 MPa, and 5.9 MPa. 43

Figure 17. Post-burst diametrical strain measurements along cladding axial distance for Zirlo and Cr-coated Zirlo at initial pressures of ~1 MPa and ~3.4 MPa.. 45

Figure 18. Optical scans of claddings that failed at ~9.5 MPa burst pressure.. 46

Figure 19. Maximum diametric strain as a function of burst temperature and burst pressure. 47

Figure 20. Higher magnification optical images of the burst regions for claddings that had ~3.4 and ~5.9 MPa initial pressures 50

Figure 21. Burst opening area and burst opening length versus hoop stress for Cr-coated and bare Zirlo..... 51

Figure 22. Burst opening area as a function burst temperature and burst pressure. 52

Figure 23. Cross-sectional optical macrograph taken from the burst region of Zirlo (1 MPa initial pressure) and higher magnification micrograph of region opposite burst opening. 54

Figure 24. BSE micrograph of the Cr-Zirlo interface taken in a region opposite burst (1 MPa initial pressure) and EDS line scan across the reaction layers.. 55

Figure 25. Thickness data of reaction layers found in lower strain regions opposite burst. 56

Figure 26. EDS maps of the region away from burst for the Cr#1 sample initially pressurized to 5.52 MPa. 58

Figure 27. EDS mapping for the region away from burst of the Cr#1 sample initially pressurized to 8.27 MPa. 59

Figure 28. EDS mapping of the region away from burst for the Cr#2 sample initially pressurized to 5.52 MPa 60

Figure 29. Optical macrograph of the burst tip of a Cr-coated Zirlo sample (1 MPa initial pressure) showing the tapering of zirconia formation away from the burst region and OD oxide thickness and wall-strain versus fractional distance along the cross-section.. 62

Figure 30. BSE micrograph of the oxide scales that form in the burst tip vicinity and higher magnification BSE micrograph representative of regions where the Cr-coating was partially consumed. 64

Figure 31. Higher magnification micrograph of a region of intermediate wall-strain, illustrating the areas of localized corrosion..... 65

Figure 32. EDS mapping of the region near the burst vicinity for the Cr#2 sample initially pressurized to 5.52 MPa..... 66

Figure 33. Solid works rendering of the extensometer, an illustration of the tube specimen, and the dimension specifications of tube specimen used for tensile testing in this study.. 80

Figure 34. Burst temperature and burst engineering hoop stress curves for all test claddings..... 82

Figure 35. Ultimate tensile strength and yield strength vs temperature data for C26M and T35Y2.. 85

Figure 36. EBSD map of a C26M cladding cross-section.. 87

Figure 37. EBSD map of T35Y2 cross-section from the end of the full-length tube, where temperature was much colder than the burst region. 88

Figure 38. Ballooning profiles with circumferential strain vs. distance along the axial direction of burst claddings. 90

Figure 39. Optical macrographs of C26M and Zry-2 cross-sections from samples that burst at ~60 MPa hoop stress.. 91

Figure 40. Curves illustrating wall-thinning for samples around ~60MPa burst hoop stress..... 92

Figure 41. BSE micrographs of the burst tips for the ~60 MPa burst hoop stress samples..... 94

Figure 42. Burst area and length vs hoop stress for all claddings tested. 95

Figure 43. Images of C26M claddings that burst at 80, 100, and 110 MPa hoop stress illustrating the development of the opening and transition in burst area ~100 MPa. 96

Figure 44. Thermal gradients during burst testing of C26M for a burst hoop stress of 100 MPa, and 38 MPa 100

Figure 45. Plastic portions of the uniaxial tensile testing at 700 and 800 °C where samples were held for 10 min at temperature prior to starting the test (solid lines) and updated curves at 700 and 800 °C curves where the tensile test was initiated once reaching temperature (dashed lines). 103

Figure 46. Burst criteria predictions using the tensile data for C26M..... 104

Figure 47. Comparison of the models in the ZryCreepLOCAUpdate module in BISON at 650 °C and 700 °C.. 118

Figure 48. Difference of measured strain from predicted strain by BISON for a range of temperatures in the α phase..... 120

Figure 49. Illustration from showing a typical 2D DIC setup andimage of reference grid and subset displacement in subsequent image.. 132

Figure 50. A simple ray diagram illustrating how out-of-plane motion produces strain bias.. .. 133

Figure 51. Spectral energy density for a given wavelength at LOCA relevant temperatures. ... 135

Figure 52. Illustration showing transmission, reflection, and emission of IR that occur when interacting with a material.. 137

Figure 53. Illustrations of the standard SATS furnace and DIC furnace. 139

Figure 54. A top-down illustration of the integration of DIC and thermography to SATS testing.. 141

Figure 55. Optical image of the mirror showing the perspective of the IR camera. 142

Figure 56. Burst hoop stress versus burst temperature for 10.16 cm and 30 cm segments of Zry-4..... 144

Figure 57. SEM micrograph after a test from the side of the cladding opposite burst and profilometry results from the structured light scan. 145

Figure 58. Thermal image of a unoxidized Zry-4 segment in the DIC furnace..... 147

Figure 59. Optical images from the DIC camera of cladding segments ~8 s before burst and just after burst began.. 148

Figure 60. Image of the SiC Hexoloy “C” shell employed to block filament reflections. 150

Figure 61. Thermal image from a test run with the C shell implemented.. 151

Figure 62. 3D surface generated from a test near the final stages of ballooning and hoop strain measurements projected on the image from the same stage in ballooning. 153

Figure 63. Graphical illustration of the 3D DIC setup with two cameras at a stereo angle of ~20 ° and photograph of the camera setup and lighting. 154

Figure 64. Example of a typical strain and pressure history from a SATS step-loaded isothermal creep test.. 157

Figure 65. Band contrast and IPF maps of the SRA Zry-4.. 163

Figure 66. Grain size distribution for the tested SRA Zry-4..... 164

Figure 67. Band contrast map overlaid with KAM..... 165

Figure 68. Pole figures for three {0001}, {10-10} and {11-20} orientations.. 166

Figure 69. Schematic of the furnace and optical setup and example image of a laser-engraved specimen. 168

Figure 70. Example temperature and pressure histories for open and closed valve tests. 170

Figure 71. Image of a cladding specimen before ballooning and right before burst showing the region of analysis 171

Figure 72. Hoop and axial strain-time curves for the closed valve and open valve tests.. 173

Figure 73. Illustrations of the relative orientations between the rupture opening and camera perspective for specimens that burst “in-view” and “out-of-view” of the camera. 174

Figure 74. Strain and pressure against time for the 6.2 MPa closed valve and 8.2 MPa open valve tests. 176

Figure 75. Hoop strain – temperature curves for the open valve tests to demonstrate the difference between the time and temperature domains. 178

Figure 76. BISON predicted hoop strain compared to DIC measurements for the 6.2 MPa and 15 MPa open valve tests, respectively. 180

Figure 77. BISON comparisons to DIC data generated from KAERI experiments at 8 MPa internal pressure. 181

Figure 78. Axial temperature profiles generated from IR images right before burst for all tests in the 2D DIC data set. 183

Figure 79. SEM micrograph of the oxide scale formed after testing in air. 185

Figure 80. IR images and axial profoles at 475 °C and right before burst 186

Figure 81. Final hoop and effective strain rates against burst pressure and T_{Sample} reading at burst for tests that burst out-of-view of the camera. 188

Figure 82. Burst temperature versus pressure data for all tests.. 190

Figure 83. Optical images of the 6.2 MPa closed and 8.2 MPa open valve tests and diametric engineering strain versus normalized distance along the axial direction for all tests. 192

Figure 84. Diametric strain profiles along the axial direction alongside numerical derivatives of those profiles to demonstrate symmetry of the peaks. 193

Figure 85. Natural logarithm of strain rate against inverse temperature for the tests that burst out-of-view of the DIC camera. 195

Figure 86. Arrhenius style plots for the tests that burst in-view of the camera.. 196

Figure 87. Comparison of PNNL YS models with 0% and 50% CW compared to hoop effective stress at the transition point..... 202

Figure 88. SEM micrograph of the backside of a cladding after testing and higher magnification micrograph showing the structure of a side of a laser engraving. 203

Figure 89. Image of the DIC and furnace during testing and top-down schematic of the furnace and DIC system.. 213

Figure 90. Cladding strain with Zry-4 specimen and 304 SS extension pieces and image from one of the cameras illustrating thermocouple placement. 214

Figure 91. Strain curves and pressure histories for the 550 °C and 600 °C accelerated creep testing.. 218

Figure 92. Strain rate and stress trends for the 550 °C and 600 °C testing.. 220

Figure 93. Strain rate data compared to model predictions using anisotropic and isotropic factors. 222

Figure 94. Hoop strain profiles and corresponding pressure steps for (a) 650 °C and (b) 700 °C tests. 225

Figure 95. Log-log plot of strain rate and stress for all tests at 650 °C and 700 °C.. 226

Figure 96. Thermocouple setup for temperature gradient determination. 229

Figure 97. Temperature readings from and absolute difference between the centerline thermocouple and control thermocouple 12 mm above.. 230

Figure 98. Piece-wise fits of the hoop strain rate and stress data. 232

Figure 99. Comparative log-log plot of stress and strain rate between experimental results and Kaddour model..... 234

Figure 100. Compensated hoop strain rate versus hoop stress and predictions using model parameters against experimental data. 236

Figure 101. Hoop and axial strain profiles for two of the tests that show a transition from negative axial strain rates to positive values.. 238

Figure 102. Hoop strain map of a preliminary sample showing the centerline thermocouple placement. 247

Figure 103. Burst temperature and pressure for the bare and Cr#2 coated DIC tests..... 249

Figure 104. Line profiles of hoop strain collected along the axial direction using the strain map. 250

Figure 105. Hoop strain and hoop strain rate data with respect to temperature. 252

Figure 106. Semi-log plot of hoop strain rate and inverse temperature to highlight Arrhenius temperature dependence..... 253

Figure 107. Strain and strain rate data from the accelerated creep test of Cr#2 at 600 °C compared to bare Zry-4..... 256

Figure 108. Hoop strain map from frame just before rupture. TC location at cladding centerline and 12 mm above are presented..... 258

Figure 109. Thermocouple readings at burst and burst hoop stress for centerline and 12 mm above positions compared to previous ex-situ data. 259

Figure 110. Hoop strain data from the 3 points illustrated in the previous figure and centerline thermocouple reading during the test..... 261

Figure 111. Hoop strain, axial strain, and temperature reading through the test for P_2..... 262

Figure 112. Arrhenius plot of raw and smoothed strain rate data for P_2. 263

Chapter 1: Introduction to Fuel Claddings, Accident Scenarios, and Conventional Characterization Methods

Chapter Foreword

This section gives a brief background of Zr claddings, light-water reactor accident conditions and historic attempts to assess fuel cladding behavior during such conditions. Specifically, an overview of loss-of-coolant accidents and design basis criteria is covered. General burst testing, particularly that used to develop conventional safety criteria, is discussed. Contemporary testing at ORNL is detailed and the basis for improving current burst testing is set.

Section 1.1: Fuel Claddings and Background on Conventional Zr Materials

1.1.1: Fuel claddings as structural components in nuclear systems

In light-water reactors (LWRs), fuel takes the form of cylindrical UO_2 pellets stacked within Zr alloy cladding. This thin-walled tubing serves to structurally stabilize the fuel, maintain a coolable geometry, and contain the fuel during operation and long-term storage. Claddings serve a critical role as a barrier during operation by separating radioactive material, including fission products, from the rest of the reactor coolant system. Cladding and fuel system dimensions vary with reactor design. Table 1 presents representative fuel design parameters for pressurized water reactors (PWRs) and boiling water reactors (BWRs) [1]. Fuel assemblies, consisting of arrays of fuel claddings, form the complete reactor configuration in a grid pattern. PWRs typically have fuel assemblies in 14x14 to 17x17 arrays, while BWRs utilize 7x7 to 10x10 arrays [1]. The total number of assemblies and claddings in a reactor depends on the design, with PWRs containing roughly 150-200 assemblies and BWRs having 400-800. Consequently, a LWR contains around 40,000-60,000 clad fuel pins, meaning claddings constitute a significant portion of the structural material in LWRs. It is important to note that not all pins in an assembly contain nuclear fuel, as some PWR assembly spaces house instrumentation or control rod guide tubes [2].

Zr-based claddings have been the standard cladding choice for 70 years, primarily due to their favorable neutronics [3–5]. Zr alloys are known for their low thermal neutron absorption cross-section, allowing for a greater number of neutrons to participate in the fission chain reaction and subsequently more efficient utilization of the fuel. Additionally, Zr alloys demonstrate adequate hydrothermal corrosion behavior [6,7], making Zr alloys a suitable choice for use in

Table 1. Representative fuel and cladding design parameters of PWR and BWR designs [1].

Parameter	PWR		BWR	
	15 x 15	17 x 17	7 x 7	8 x 8
Rod diameter (mm)	10.7	9.5	14.3	12.5
Fuel height (m)	3.66	3.66	3.66	3.66
Clad thickness (mm)	0.61	0.58	0.81	0.86
Pellet-clad diametrical gap (mm)	0.19	0.17	0.28	0.23

reactors. However, claddings must also protect against the release of radioactive material during off-normal or accident events. Under such conditions, Zr claddings can rapidly oxidize and balloon in high-temperature steam environments, potentially compromising their structural role and the overall safety of the reactor. Understanding cladding behavior in both design-basis accidents (DBAs), such as a loss-of-coolant accident (LOCA), and severe accidents is critical for defining safety and operational criteria.

1.1.2: Material and microstructural characteristics of Zr alloys used for claddings

Zirconium alloys, from historic variations like Zircaloy-2 and -4 to modern Nb alloys such as M5 or Zirlo, have found extensive application in LWRs. These Zr alloys, predominantly used for cladding, contain over 97% Zr by weight, with minor alloying elements contributing to strengthening, corrosion resistance, and dimensional stability. Table 2 details the nominal composition ranges associated with reactor grade Zircaloys and Zr-2.5Nb. It should be noted that impurity limits also exist for reactor grade Zr alloys but are not presented.

Three phase regions are critical to consider for accident conditions: the low-temperature hexagonally close-packed (hcp) α-phase, the high-temperature body-centered cubic (bcc) β-phase, and an intermediate mixed α + β phase. Zr alloy phase stability is strongly composition-dependent. Elements such as O and Sn known to stabilize the α-phase, while Fe, Cr, and Ni stabilize the β-phase [8]. Consequently, the exact boundaries between these phase regions can vary between manufacturers.

The Zr phase diagram in Figure 1 illustrates the effect of oxygen concentration, relevant to steam and hydrothermal environments. The phase boundaries of Zircaloy-4 (Zry-4) utilized in this dissertation are based on the work of Miquet et al. [9]. For Zry-4, the α phase exists below 808 °C, the mixed α +β phase from 808 °C to 1008 °C, and the β phase above 1008 °C. Due to high burnup concerns addressed later, the majority of the work in this dissertation with Zircaloys focuses on the α-phases. Given this, the crystallographic characteristics and preferential deformation modes of the α phase is detailed.

α-Zr, belonging to the $P6_3$ /mmc space group, has ‘a’ and ‘c’ lengths of 3.232 and 5.147 Å, respectively, resulting in a less than idea c/a ratio of 1.593. At all temperatures, Zr slips easiest, Zr slips easiest along the prismatic plane (10-10) in the direction of <11-20> , with <a> type

Table 2. Alloy composition ranges for reactor grade Zr alloys according U.S. regulations in weight percent.

Alloy	Fe	Sn	Cr	Ni	Nb	Zr
Zircaloy-2 (R60802)	0.07-0.2	1.20-1.70	0.05-0.15	0.03-0.08	---	bal.
Zircaloy-4 (R60804)	0.18-0.24	1.20-1.70	0.07-0.13	---	---	bal.
Zr-2.5Nb (R60904)	---	---	---	---	2.40-2.80	bal.

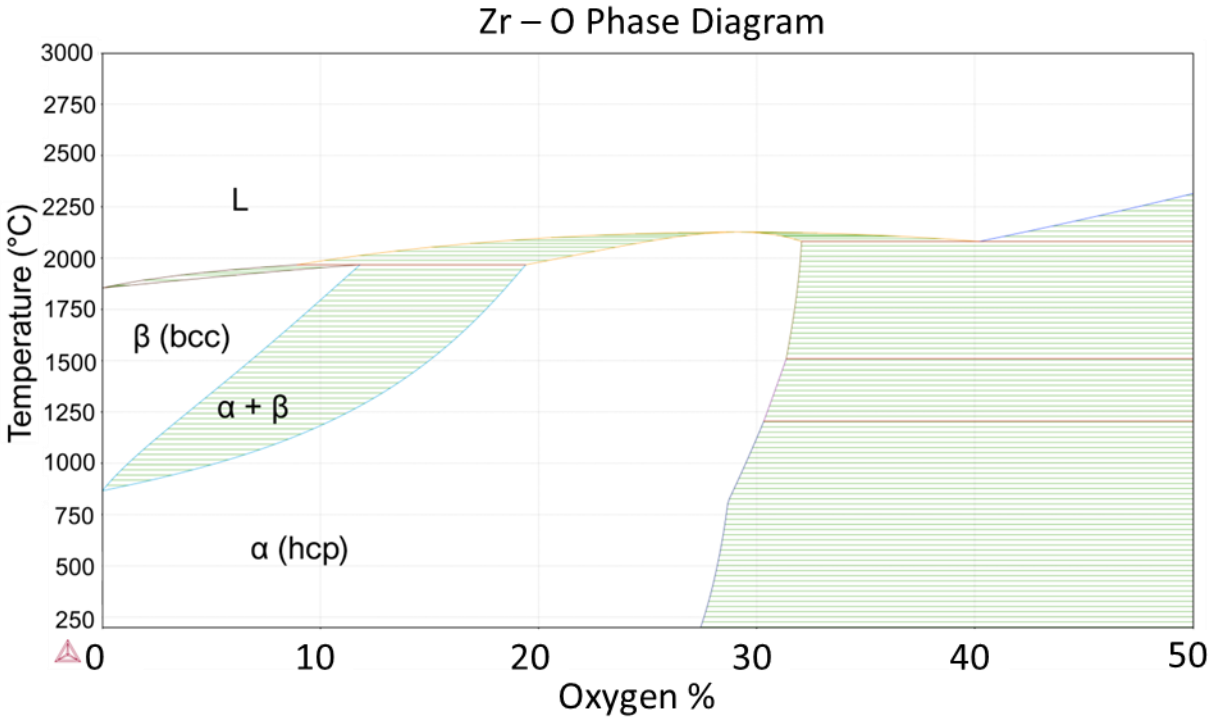

Figure 1. Phase diagram for Zr with respect to oxygen concentration. Courtesy of Rishi Pillai.

dislocations [10]. Oxygen and other solute atoms play a significant role in the glide of <a> type dislocations along the prismatic plane, as solute O has been shown to pin mobile dislocations in pure Zr, thus controlling the rate of their mobility [10]. Oxygen concentration is, however, a critical component of reactor grade Zr alloy strength, as less than 1000 ppm concentrations leads to substandard strength performance [8].

At lower temperatures (< 577 °C), the next easiest deformation mechanism for Zircaloy-4 is twinning [11,12] . Two twins are prominent based on loading conditions [13]: (1) the {10-12} tensile twin common amongst hcp alloys with less-than-ideal c/a ratios and (2) the {11-22} compressive twin. Above 577 °C, prismatic and basal slip were observed to be dominant by Akhtar and Teghtsoonian in single crystal investigations [11], with twinning absent. The pyramidal plane is hard to promote slip along compared to the prismatic or basal planes. However, cross-slip from the prismatic system to the basal or pyramidal systems have been posited to play an important role at higher temperatures for <a> type dislocations [10], possibly relevant for LOCA conditions. Consequently, the deformation of α-Zr is complex due to low symmetry and each slip system having individual dependencies on temperature, strain, loading, and strain rate [12].

The low symmetry of the hcp α-phase structure facilitates an inherent anisotropy in Zr claddings from processing, with preferential alignment of the basal plane parallel to the drawing direction during cold rolling [14]. The basal pole figures are typically distributed ~30 ° on either side of the radial direction [15]. This texturing has implications for irradiation growth during operation [16,17] and balloon behavior in accident conditions [18,19]. The choice of heat treatment after forming can have significant effects on the cladding performance and naturally microstructure. After cold-rolling, Zircaloy claddings are typically subjected to one of the following two heat treatments [20]:

(1) recrystallized anneal (RXA), often called “annealed” or “fully recrystallized” where the Zircaloy is heat treated at high temperatures (~620 – 790 °C) where new strain-free grains nucleate and grow, replacing the deformed grains. This process relieves stresses and improves ductility at the expense of a reduction in strength.

(2) stress-relief anneal (SRA) or often called “cold-worked stress relieved” (CWSR), where an annealing process (~400°C) after cold-rolling helps to relieve the internal

stresses. This microstructure is characterized by much smaller, elongated, and less equiaxed grains compared to RXA.

Figure 2 presents scanning electron microscopy (SEM) micrographs and corresponding electron backscatter diffraction (EBSD) maps for a RXA and CWSR/SRA material from Lan et al. [21]. Note the significantly larger, more equiaxed grains characteristic of the RXA process.

RXA and SRA materials are subject to variation themselves, as exact heat treatments are often proprietary. These annealing processes are most pertinent to the work in this dissertation, representing the ends of the spectrum for material condition. It should be noted that other metallurgical processes exist such as partially recrystallized annealing or β quenching that are beyond the scope of this dissertation.

Section 1.2: Loss-of-Coolant Accidents and Burst Testing Efforts

1.2.1: Design Basis LOCAs

LOCAs are postulated DBA conditions where the coolant supply in an LWR is suddenly lost, such as from a break in one of the coolant system components. Due to the sudden loss of coolant and subsequent effects of decay heat, temperatures increase rapidly. This, combined with the loss of coolant pressure and internal loading from helium and fission gas products can lead to Zr cladding ballooning and rupture. Furthermore, residual water coolant is vaporized, causing rapid oxidation of the Zr claddings [22]. This reaction generates hydrogen gas and is highly exothermic, further exacerbating the severity of an accident [5]. In summary, a LOCA scenario can subject fuel claddings to rapid thermal transients, dynamic internal loading, and high-temperature steam environments. Effective response by safety systems is critical to prevent significant core damage during a LOCA, guarding against radioactive material release.

Emergency core coolant systems (ECCS) are vital for mitigating LOCA severity by reintroducing coolant flow and maintaining core integrity. As such, definitions of design-basis LOCAs (DB-LOCAs) assume that ECCS can respond in a timely manner. ECCS varies with LWR design, but generally follows the “defense-in-depth” strategy of the many nuclear regulatory agencies and advisory groups [23,24].

This dissertation focuses on DB-LOCAs, defined by the expected response of ECCS. According to U.S. Nuclear Regulatory Commission (NRC) regulation 10.CFR§50.46, ECCS

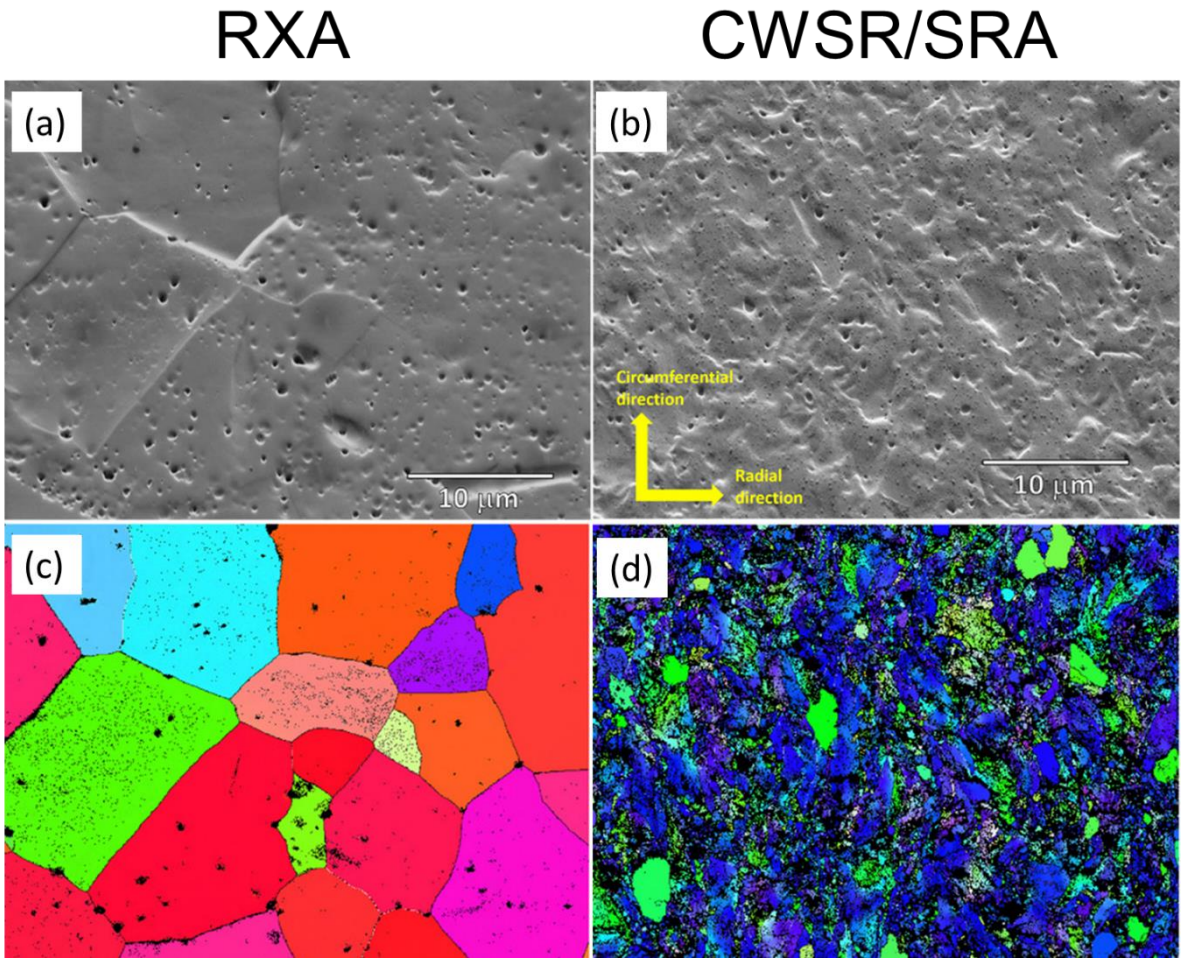

Figure 2. SEM images and EBSD maps of (a,c) RXA and (b,d) CWSR/SRA Zircaloy-4. These figures were taken from Lan et al. [21] and modified for this dissertation. Images were reproduced with permission from Wiley.

should reestablish coolant flow, meeting two design basis criteria: (1) peak cladding temperature shall not exceed 1204 °C, and (2) equivalent cladding reacted due to oxidation cannot surpass 17%. These criteria were developed for incumbent Zr alloys based on the criterion that fuel rods maintain ductility after the reflood phase [25]. The LOCA severity and definition can vary depending on the failed system component, with conservative safety limits established for severe cases like large-break LOCAs (LB-LOCAs) from double leg guillotine breaks. Consequently, experimental efforts typically involve characterizing cladding behavior under simulated LB-LOCA conditions.

DB-LOCA have been historically divided into four distinct phases [22]: (1) the blowdown phase marked by rapid depressurization and temperature increase as coolant leaks through the break, (2) the refill phase where coolant reintroduction is started via injection systems and coolant fills the lower plenum, (3) the reflood phase as water fills up beyond the lower plenum and into the reactor core, and (4) the post-accident phase where the coolant levels are restored and the core stabilized for long-term management. Note the boundary between the refill and reflood phase is not discrete, as they encompass parts of the same process of reintroducing coolant to the reactor system. Figure 3 provides a generic description of the thermomechanical setting expected for Zry-4 cladding during a double-guillotine break LOCA from Erbacher et al. [26].

During the blowdown phase (1), the claddings are rapidly heated, and coolant is flashed to steam due to loss of pressure. This phase is where much of the cladding deformation is expected to occur. The refill phase (2) is critical in terms of stability due to large fluctuations in pressure and fluid flow from interactions between the low temperature injected water and residual coolant that has been mostly turned into steam. During the reflood phase (3), temperatures begin to level off due to adequate reintroduction of coolant to the core. Eventually, sufficient cooling is introduced to stabilize the reactor core and the post-accident phase (4) begins. In general, a LOCA transient can be described by rapid heating from operation temperatures followed by a subsequent stabilization of temperature and finally a quench. Depending on internal pressure and temperature conditions, the claddings could balloon and burst during the temperature ramp.

Over the last 50 years, significant effort has been dedicated to characterizing the balloon and burst behavior of claddings under simulated LOCA transients. These characterization methods have provided a valuable basis for evaluating cladding LOCA behavior. An overview of these conventional methods, and ways to improve the throughput, quantity, and quality of data is the

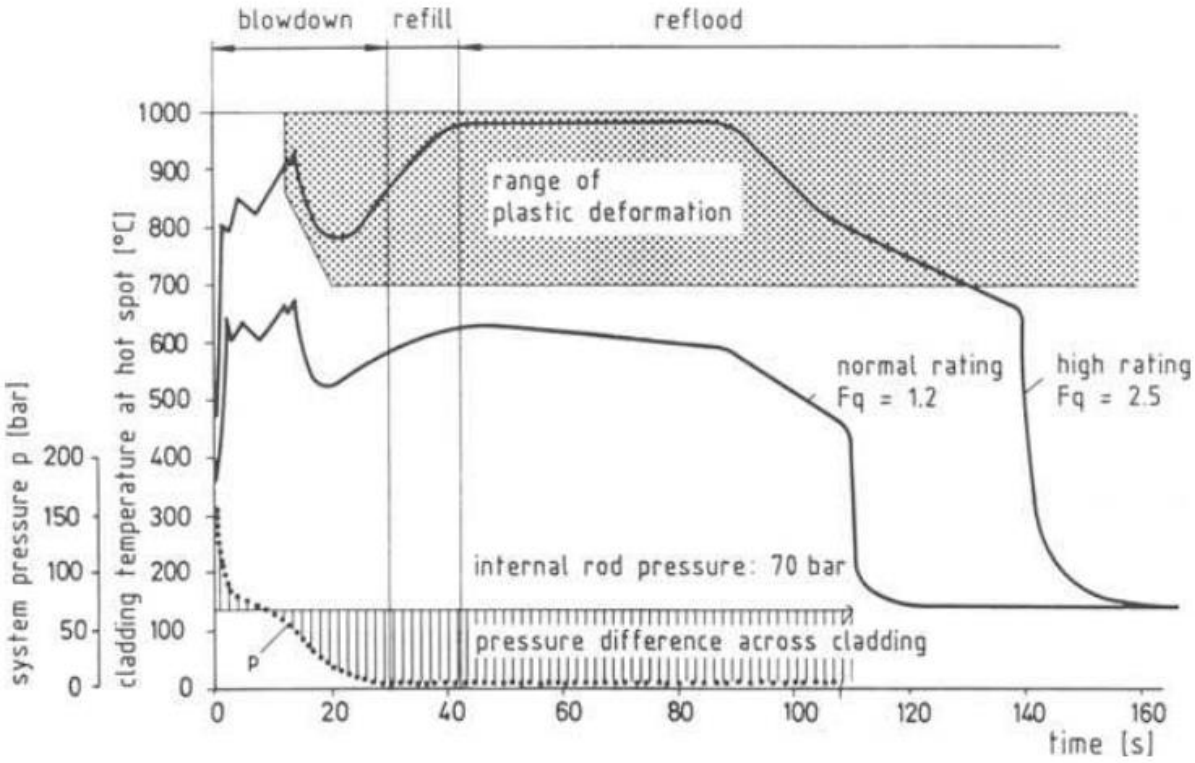

Figure 3. Response of Zircaloy-4 cladding during a double-ended guillotine break LOCA [26]. Reproduced with permission of ASTM International.

the focus of this dissertation.

1.2.2: Historic burst testing and conventional ex-situ parameters

The nuclear community has long used "burst testing" to evaluate fuel cladding performance in LOCA conditions. There are two main types of burst testing: (1) transient heating, where pressurized claddings are heated at a specific rate, and (2) traditional isothermal creep, constant loading burst testing. Transient testing can be further divided into (a) isobaric testing, where cladding samples are connected to a fixed pressure reservoir, and (b) constant gas inventory testing, where the amount of gas in the rod is fixed, and pressure changes with temperature. The former testing separates the effects of varying pressure on analysis while the latter is more prototypic of pressure conditions during an accident transient. An example of the pressure and temperature histories for a transient burst test with constant gas inventory are shown in Figure 4. While steam environments have the most fidelity to accident conditions, testing under vacuum or in argon environments is useful for determining separate effects. Until recently, burst testing focused primarily on Zr alloys due to the prominence of the material system as claddings.

In the 1970s, Chapman [27,28] conducted extensive single-rod and multi-rod bundle testing of Zircaloy claddings at Oak Ridge National Laboratory (ORNL). This research led to the establishment of empirical relations between burst engineering hoop stress and burst temperature, depending on ramp rate, shown in Figure 5. Powers and Meyers [29,30] built on Chapman's work and developed the empirical correlation in Eq. 1,

$$T_R = 3960 - \frac{20.4\sigma_{eng}}{1+H} - \frac{8{,}510{,}000\sigma_{eng}}{100(1+H)+2790\sigma_{eng}} \quad (1)$$

where T_R is the rupture temperature (°C), σ_{eng} is the engineering hoop stress, and H is defined as the test heating rate divided by 28.

Although numerous investigations were conducted in the same timeframe across multiple institutions [18,31,32], the Chapman correlation serves as a prime example of cladding behavior in accident conditions and conventional characterization. Widely used in current burst testing analysis and adopted by the U.S. NRC, the Chapman correlation for Zircaloys offers a consistent experimental baseline with exceptional fidelity. The four often-considered *ex-situ* burst parameters are: (1) burst temperature, (2) burst pressure, (3) engineering burst hoop stress, and (4) post-test

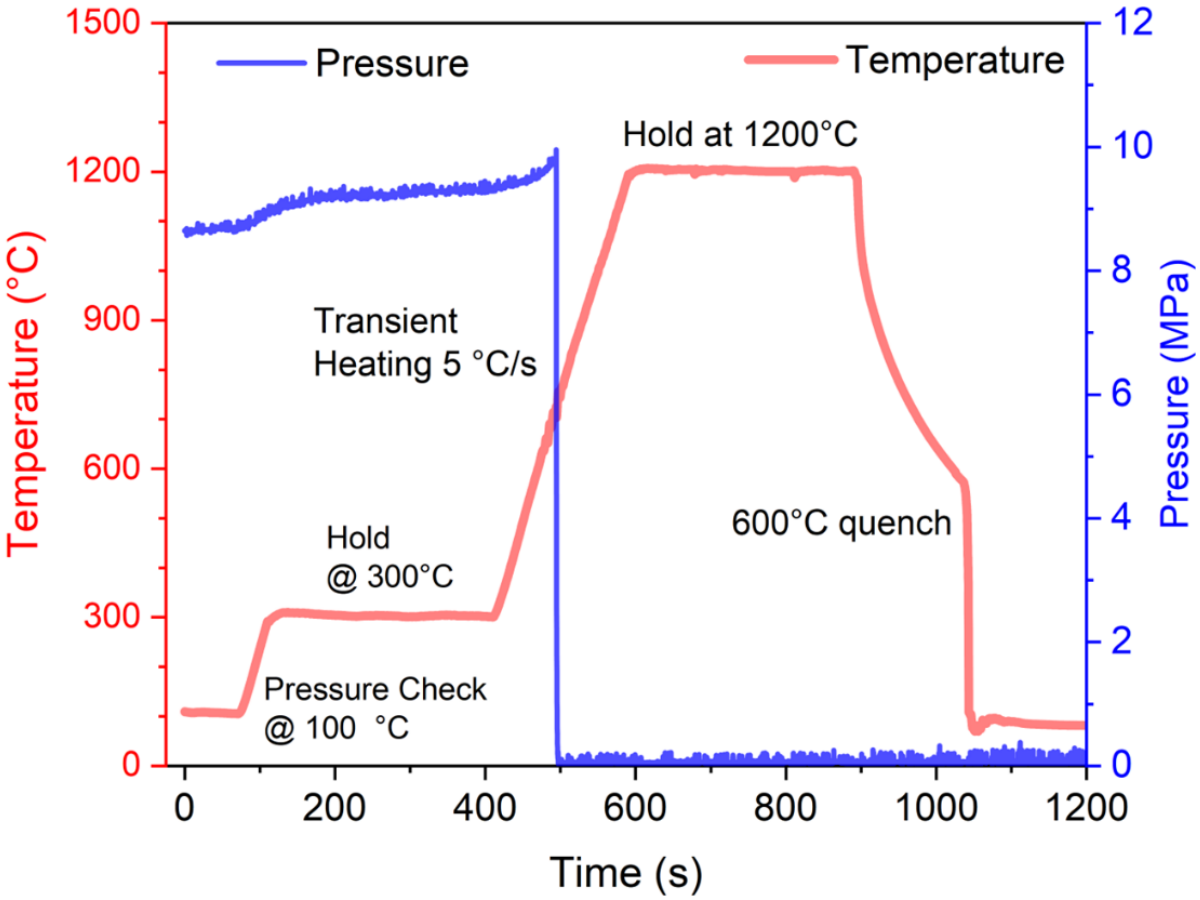

Figure 4. Example temperature and pressure history for a transient burst test with constant gas inventory.

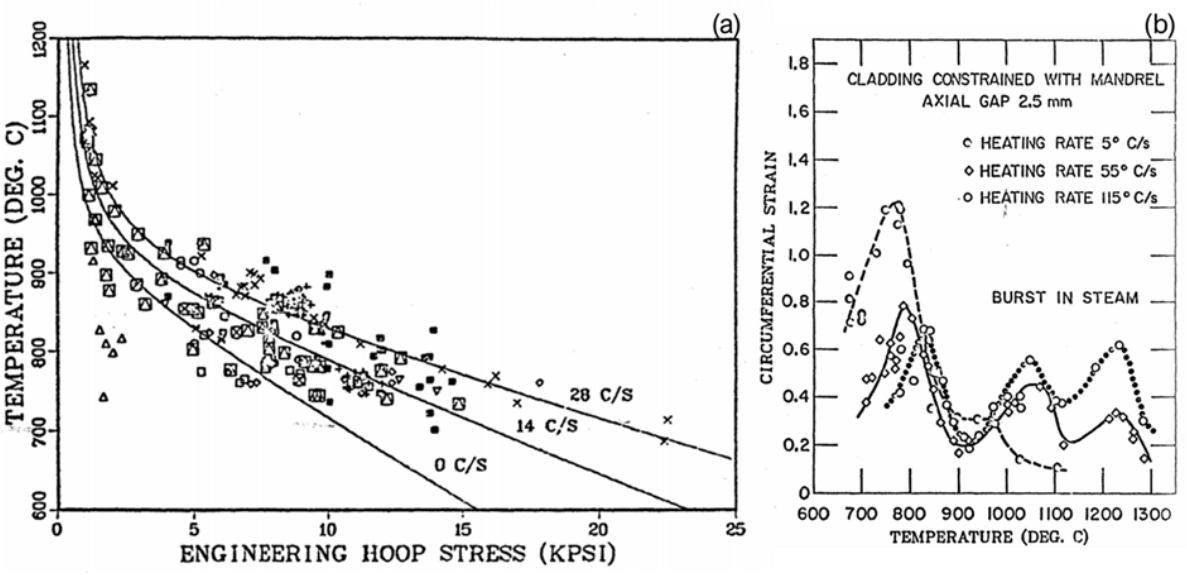

Figure 5. (a) shows a from Powers and Meyers [30] of burst temperature and engineering hoop stress for Zr claddings subjected to heating rates from 0-28 C/s from testing conducted by Chapman [27]. (b) presents a figure also from Powers and Meyers that plots maximum circumferential strain and temperature, illustrating the three super plastic regions found associated with the three phases. This figure was taken from U.S. NRC NUREG 0630, available in the public domain.

maximum diametric/circumferential strain of the balloon region. Burst temperature refers to the cladding temperature at failure, while burst pressure and engineering burst hoop stress represent the internal pressure and engineering hoop stress at failure, respectively. Higher internal pressures or hoop stresses result in lower burst temperatures for a given heating rate, as presented in Figure 5(a). Figure 5(b) presents diametric strain as a function of burst temperature and heating rating and will be discussed shortly. Engineering burst hoop stress is usually considered as it normalizes for cladding geometry, but in certain cases, burst pressure may be more relevant as it indicates the maximum load a cladding concept can withstand. This consideration is particularly important for new cladding materials, where cladding thickness can be considerably thinner due to neutronic considerations.

In the evaluation of deformation, the key post-test parameter commonly analyzed is the maximum diametric strain. Figure 6(a) presents an example of a cladding segment following a LOCA burst test, highlighting the distinct balloon morphology frequently observed in Zr claddings. As depicted in Figure 6(a), the cladding ballooning transpires in a nodal fashion, with hoop strain diminishing on either side of the apex. This geometry is constrained by the adjacent cladding material, with hoop strain receding along the axial direction on both sides of the balloon center.

To describe the balloon geometry, the cross-section is often approximated as a circle, with an axially varying diameter. Figure 6(b) showcases a light-optical micrograph of two sections of a Zircaloy cladding after testing. The outer section was taken from the center of the balloon region, while the inner section was taken from the bottom of the sample, distant from burst. Consequently, the section from the burst region maintains a primarily circular shape, although significant deviation is noticeable nearer to the rupture site. Additionally, local strain environments surrounding the cladding section are not entirely captured by parameters like diametric strain.

The maximum diametric strain, measured at the center of the balloon, has been extensively employed as a useful characterization for the entire balloon geometry, offering insights into the extent of ballooning and its potential implications on safety considerations such as coolant flow obstruction.

Evaluating diametric strain in Zr alloys can be quite complex. Figure 5(b) from Powers and Meyers [30] presents maximum diametric strains against burst temperature for transient testing

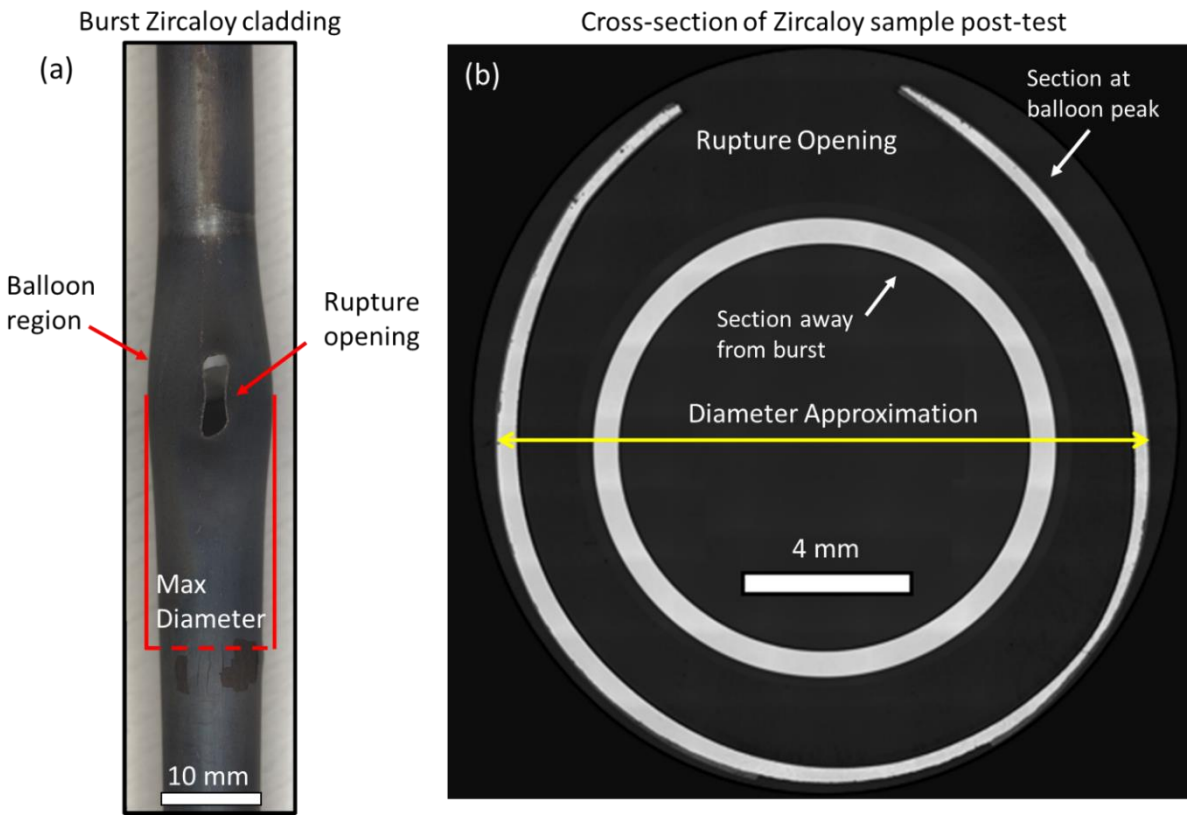

Figure 6. (a) Image of a Zircaloy cladding post-burst test, exemplifying the characteristic balloon geometry. (b) Light-optical micrographs of sections at and away from the center of the balloon region illustrating the usefulness of approximating the cross-section as a circle.

with a range of heating rates in a steam environment. In the temperature range relevant to LOCA conditions, diametric strain exhibits multiple "superplastic" peaks. The two lowest temperature peaks occur near phase transitions: the first one appears close to the α to α + β transition, and another at the α + β to β transition. A third peak is observed entirely within the β phase. Furthermore, there is a significant dependence on both heating rate and environment. Although not shown here, it has been demonstrated that oxygen concentration can reduce diametric strain model predictions, particularly in the β phase [33].

The burst testing performed by Chapman and others involved experiments aimed at establishing baseline behavior for fresh cladding materials in the absence of fuel and irradiation environments. In a real LOCA scenario, irradiation damage and the presence of fuel could influence cladding behavior. Experiments such as those conducted at ORNL's out-of-reactor hot cell facilities with irradiated specimens and fuel present are crucial to safety analysis and assessing the applicability of un-irradiated testing.

1.2.3: The Severe Accident Test Station and standard simulated LOCA burst testing

The renewed interest in burst testing is driven by two primary factors: (1) the need to qualify new Accident Tolerant Fuel (ATF) claddings, developed in response to the Fukushima accident in 2011, and (2) the assessment of existing Zr claddings for approval of higher burnup limits to extend fuel cycle length and efficiency. The latter requires addressing safety concerns related to fuel fragmentation, relocation, and dispersal (FFRD) [34]. Chapter 2 discusses motivations for testing ATF claddings and provides current experimental summaries, while Chapter 5 covers renewed burst testing of bare Zr alloys related to FFRD and modeling gaps.

Burst testing is currently being pursued systematically by only a few international institutions, such as the French Atomic Energy Commission (CEA), the Korean Atomic Energy Research Institute (KAERI), and ORNL. More information on recent testing by these institutions can be found in Chapter 3. This section high-lights the standard burst testing carried out at ORNL since 2013.

The Severe Accident Test Station (SATS) at ORNL was established to assess new cladding materials using burst testing after the 2011 Fukushima Daiichi accident. Standard SATS testing simulates a LB-LOCA scenario, in accordance with NRC regulation 10.CFR§50.46. A detailed

description of SATS is available in reference [35], and a general schematic of SATS from Massey et al. [36] is shown in Figure 7.

For a standard SATS LOCA test, cladding segments (~30 cm or 12" in length) are secured with Swagelok fittings at both ends, and an alumina filler rod is inserted to simulate fuel volume and thermal mass. The top fitting connects to a high-pressure gas line, with a transducer continuously monitoring the internal pressure. Four type S thermocouples (TCs) are then attached to the cladding using Pt-30% Rh wire. Two TCs are placed at the center of the cladding, 180º apart, while the other two TCs are attached ~5 cm on either side of the cladding center.

The cladding train is then secured in a 50 mm diameter quartz tube, which is then placed into an 8-kW infrared (IR) furnace that is used to heat the claddings via a pre-programmed regime controlled by LabView. The standard SATS simulated LOCA profile is again found in Figure 4. To ensure proper sealing, the cladding is first pressurized and examined for 10 min at 100 ºC. Steam is flowed over the surface of the claddings throughout the entirety of the test. The claddings are then heated to 300 ºC at 5 ºC/s, held for 300 s to further check for proper sealing and establish a stable environment before proceeding. The samples are subsequently heated from 300 - 1200 ºC again at 5 ºC/s and held again for 300 s to observe high temperature steam oxidation. Burst always occurs during the 300-1200 ºC temperature ramp. After the 300 s hold at 1200 ºC, the claddings are allowed to cool in steam to 600 ºC, where they are quenched in room temperature distilled water.

During the 300-1200 ºC temperature ramp a drop in pressure, blue curve in Figure 4, indicates the cladding has burst. At this point in time, the TC reading closest to rupture and pressure are recorded and taken as the burst temperature and burst pressure. Burst engineering hoop stresses are then calculated using the thin-walled approximation for a cylinder shown in Eq. 2,

$$\sigma_H = \frac{PR}{h}, \tag{2}$$

where σ_H is the hoop stress (MPa), P is the burst pressure (MPa), R is the as-received mean radius (mm), and h is the initial wall thickness of the cladding (mm). The burst engineering hoop stress is calculated for conventional comparison against burst temperature seen in previous publications of burst testing [29,36–38].

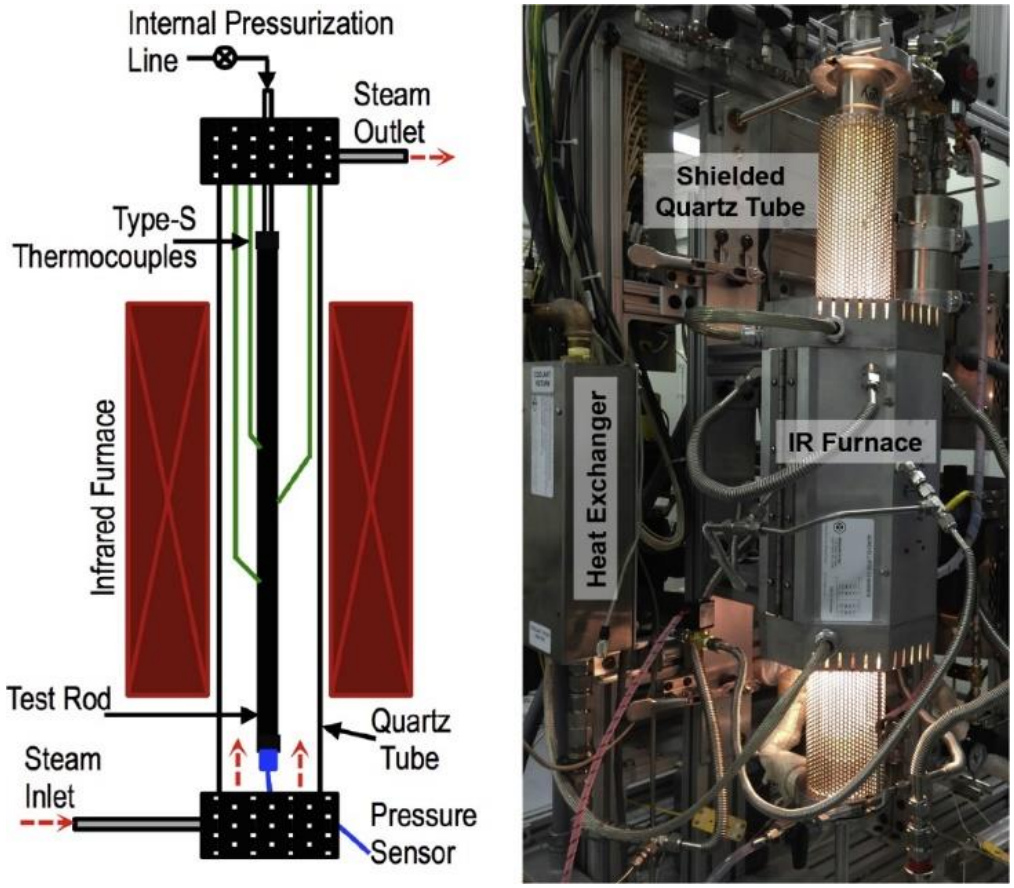

Figure 7. A schematic of the SATS furnace from Massey et al. [36] is shown on the left. A real-life image of SATS in use during a test is shown on the right. Reproduced with permission from Elsevier.

1.2.4: Reflection on standard burst testing and recent SATS improvements

Standard SATS burst testing, along with historic efforts, yields essential *ex-situ* data crucial for comparing the behavior of incumbent and newer material systems, as well as establishing safety limits. Figure 8 illustrates the utility of this data by showing plots of burst engineering hoop stress and burst temperature for Zry-4 and 2nd generation FeCrAl. As the data suggests, the 2nd generation FeCrAl maintains integrity under higher temperatures and given loading/stress conditions, indicating increased accident tolerance and potential for extension into a LOCA transient.

Although *ex-situ* characterization from burst testing is vital for evaluating cladding behavior, *ex-situ* parameters are coarse in nature and susceptible to experimental variations. Deformation parameters, such as maximum diametric strain, provide a general understanding of cladding balloon characteristics, but offer limited insight into material behavior from the initial to post-burst state. Moreover, local strain developments such as demonstrated in Figure 6(b), are not captured.

The geometry of the balloon is influenced by multiple factors beyond the resolution of diametric strain. Chung and Kassner [15] studied Zry-4 and showed strong dependencies of ballooning on not only the presence of alumina filler rods but also the form. Sectioned pellets, intended to represent fuel stacks and induce non-uniform heating, resulted in multiple balloons and significant bending. In contrast, solid filler rods or "mandrels" constrained axial contraction during ballooning and reduced bending. Local temperature gradients also have a profound effect on the final diametric strain values. Consequently, conventional ex-situ testing, although an effective comparative tool, has limitations in predicting performance during a real LOCA.

The integration of real-time, nodal temperature, pressure, and strain data during burst testing could offer a deeper understanding of cladding behavior, reducing reliance on global post-test parameters. From a developed material model, experimental variations such as local temperature distribution can be accounted for in finite element modeling suites such as BISON [39]. These high-fidelity models are vital for assessing advances in LWR operation, like high burnup extension with incumbent Zr or implementation accident tolerant fuel (ATF) systems.

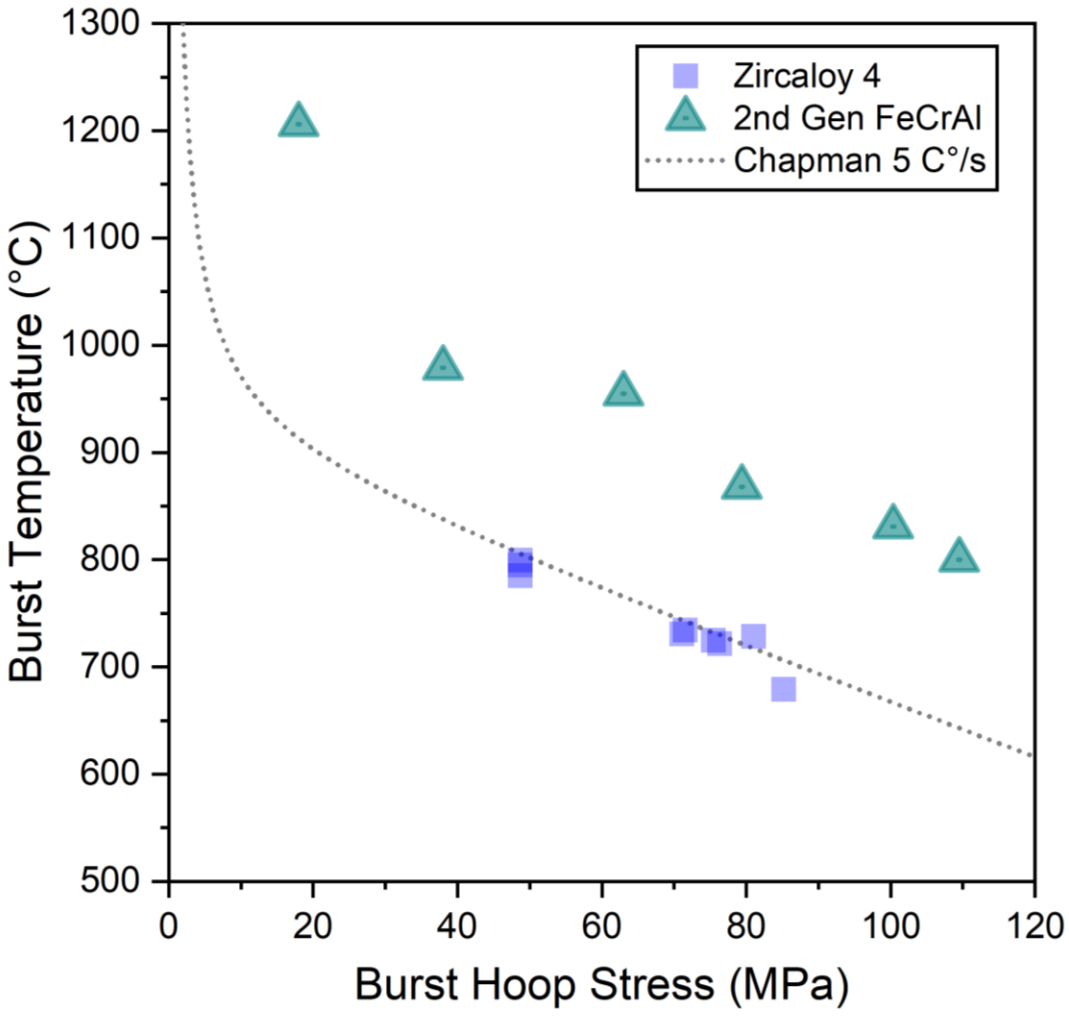

Figure 8. Burst hoop stress and temperature of Zircaloy-4 and 2nd generation FeCrAl compared to the historical Chapman correlation [27,28].

Chapter 2: Accident Tolerant Fuel Claddings and Previous Burst Testing Efforts

Chapter Foreword

In this section, the motivation for accident tolerant fuel (ATF) claddings is examined, with a focus on two near-term candidates for reactor implementation: (1) Cr-coated Zr and (2) FeCrAl alloys. A literature review of burst testing efforts for these ATF selections is provided. Transient burst testing performed of both Cr-coated Zr and FeCrAl alloys at ORNL is discussed in the subsequent two chapters. This sets the foundation for following chapters that explore recent conventional testing using the SATS. Whereas testing of SiC-based claddings, a long-term ATF concept, has been conducted at ORNL [40], it is not included in this dissertation.

Section 2.1: Motivation for ATF Claddings and Candidate Systems

2.1.1: Fukushima nuclear disaster as a driver for ATF materials

On March 11, 2011, a magnitude 9.0 earthquake struck approximately 130 km east of the Oshika Peninsula of Tohoku in Japan. This event generated a tsunami that measured 40 meters above sea level upon reaching land and penetrated up to 6 km inland [41]. The combined impact of the earthquake and tsunami caused tens of thousands of deaths, destruction of towns, and extensive damage to infrastructure [41,42].

In response to the earthquake, Tokyo Electric Power Company immediately shut down three boiling BWRs at the Fukushima Daiichi power plant and four BWRs at the Fukushima Daini power plant. After a SCRAM, reactors rely on ECCS to maintain coolant flow and remove decay heat. However, due to the power grid interruption and disabled backup generators at the Fukushima Daiichi plant, the ECCS failed to operate, resulting in a station blackout (SBO). The decay heat then drove up temperatures, gradually boiling off residual water in the core.

Exposed to high-temperature steam, the Zr alloy fuel rods rapidly oxidized, releasing heat and hydrogen gas. The highly exothermic oxidation reaction significantly contributed to the power output in the core [5], worsening the accident conditions. The buildup of hydrogen gas eventually led to explosions in Units 1, 3, and 4 at Fukushima Daiichi, resulting in the dispersal of nuclear material, displacement of communities, and substantial monetary costs that are still being addressed.

The Fukushima disaster had long-lasting and detrimental impacts on the nuclear industry. Public perception of nuclear power was negatively affected [43], existing reactors shutdown, and construction of new power plants halted or canceled [44]. It is expected to take decades and billions of dollars to fully decommission and clean up [45]. As such, the Fukushima SBO highlights the importance of preparing for severe accident conditions alongside DB. Such beyond design-basis accidents (BDBA) are evaluated on probability of occurrence. While a DB-LOCA has never occurred in a LWR [5], severe accidents such as Three Mile Island and the Fukushima disaster were expected to have a probability of occurrence of 1 in 100,000 reactor-years of operation [46]. Yet, as Terrani [5] asserted, two BDBA have occurred in the past ~40 years.

After the Fukushima disaster, the nuclear community sought to passively improve reactor safety by choosing material systems that reduce the effects of claddings on the severity of the accident conditions. New material systems are currently being pursued to replace incumbent Zr alloys. These materials are expected to improve both accident resilience and operational performance. While the Fukushima Disaster was a BDBA, new cladding materials need to be evaluated during DB-LOCAs. Consequently, LOCA burst testing efforts have been renewed to characterize the behavior of new cladding system.

2.1.2: General goals of Accident Tolerant Fuel systems

The Fukushima Daiichi SBO prompted the nuclear community to develop ATF materials and fuel systems that exceed current safety and performance standards. Given the significant role hydrogen production and oxidation heat played in the Fukushima SBO, the primary objective for any Zr cladding replacement is to reduce steam oxidation kinetics, specifically by at least 100 times [47]. Candidate cladding materials should also exhibit similar or improved mechanical response, such as strength, deformation, and post-failure fuel and fission product retention. Figure 9 from Zinkle et al. [48] further details ATF cladding goals.

Improving oxidation behavior is the foremost goal of ATF claddings. Oxidation kinetics should be slower, and the oxides formed must remain stable under both accident scenarios and normal operating conditions. Chromia, alumina, and silica are the three main oxide candidates that satisfy high-temperature steam resistance criteria. Figure 10 from Pint et al. [47] presents parabolic rate constants in steam versus inverse temperature, demonstrating that these oxides achieve the goal of 100x reduction in oxidation kinetics.

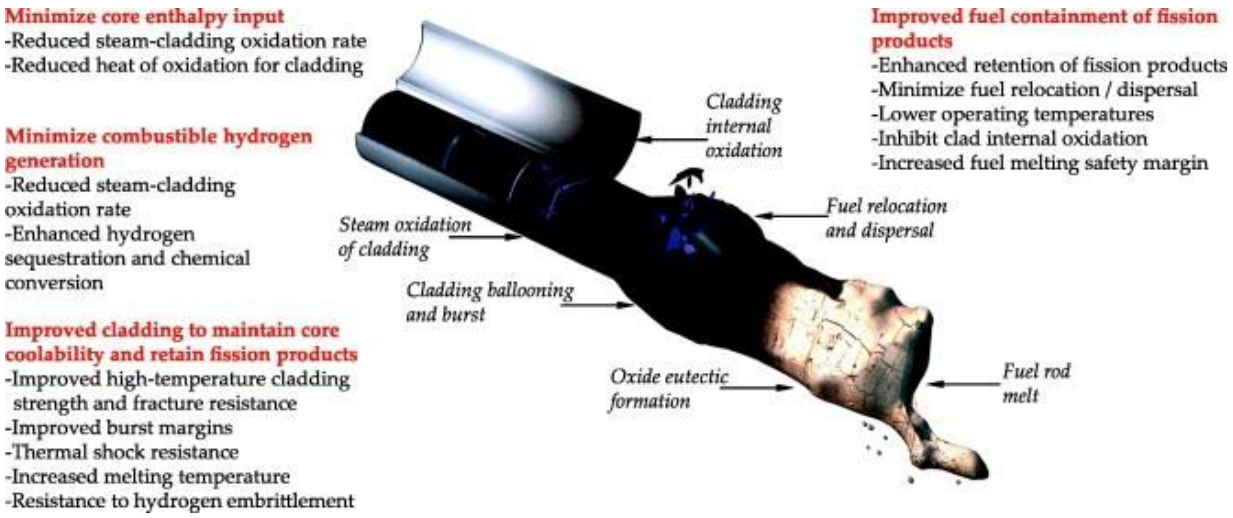

Figure 9. Illustration from Zinkle et al. [48] detailing goals beyond improvement in oxidation and deformation behavior. Reproduced with permission from Elsevier.

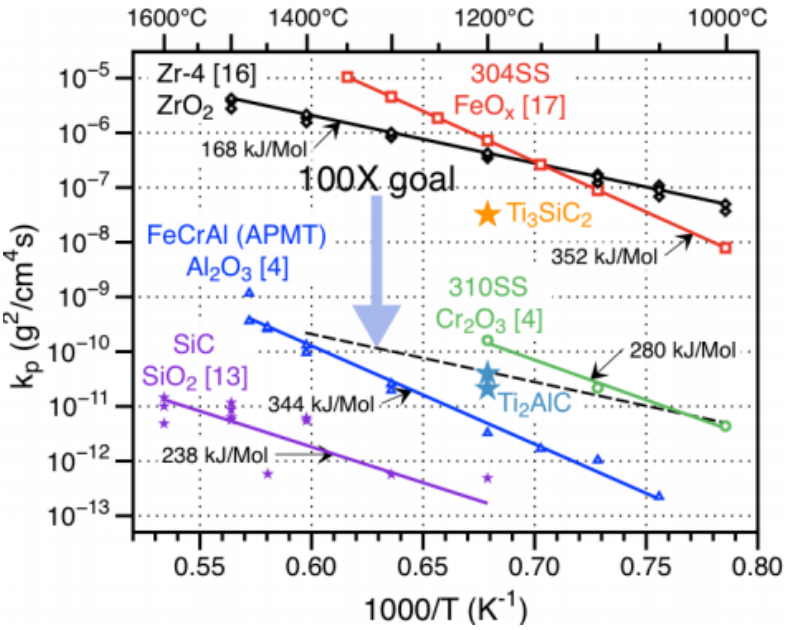

Figure 10. Plot of parabolic rate constants in high temperature steam from Pint et al. [47] of ATF cladding concepts (silica, alumina, and chromia formers). Reproduced with permission from Springer Nature.

There are two possible methods for improving nuclear system safety from a cladding perspective: either by completely replacing Zirconium or by applying a protective coating. The latter is considered a short-term solution, while replacement materials are being developed for mid- and long-term implementation.

2.1.3: Candidate systems for ATF claddings

Extensive research has been conducted on various potential coatings for Zr claddings, including Cr [49–51], CrN [52,53] , and MAX-phase compounds [54,55]. To be effective, a coating must strongly adhere to the cladding at operating temperatures [48] (~280-350 °C) and maintain the structural integrity of the coating-cladding system in accident conditions. Matching thermophysical properties, such as thermal expansion coefficient, is necessary to avoid spallation [48]. Ideally, the selected coating should also increase high-temperature strength and reduce Zr cladding ballooning.

In recent years, the focus has shifted to Cr coatings due to their superior high-temperature steam oxidation resistance [49,56], hydrothermal corrosion resistance at operating conditions [50], neutron irradiation stability [57], and potential for improved mechanical performance [50,58]. Initially developed to reduce grid-to-rod fretting [5,59], metallic Cr coating are currently being assessed for their performance under accident conditions. Studies on high-temperature steam oxidation behavior [49,50,56] indicate that Cr coatings can effectively mitigate ZrO_2 formation and remain stable during accident conditions. Experiments on the burst behavior of Cr-coated systems featuring varied deposition methods and thicknesses (15-80 um), have demonstrated reduced ballooning strain and potential improvements in strength [49,58,60]. However, due to neutronic considerations, thinner coatings (5-30 um) are being pursued that have negligible impact on operating efficiency [61].

The medium- and long-term goal for enhancing reactor safety involves completely replacing Zr alloys. General Electric and ORNL [62] developed alumina-forming ferritic Fe-Cr-Al alloys, with down-selection leading to alloys like C26M (Fe-12Cr-6Al-2Mo-0.03Y-0.2Si) based on considerations of high-temperature steam oxidation resistance [63–66] and improved mechanical behavior [36,67–69]. The main drawback for FeCrAl alloys is the neutronic penalty, necessitating thinner claddings, more fuel, and/or possibly higher enrichment >5%, [70,71]. Fuel bundles with FeCrAl claddings are estimated to cost 15-25% more than Zr alloy-clad bundles.

SiC ceramic matrix composite (CMC) claddings are being considered for long-term replacement of Zr due to unparalleled high temperature steam oxidation behavior (Figure 10), high temperature strength [72,73], and favorable neutronics [61]. Due to the timeframe associated with SiC CMCs, limited burst testing has been conducted and therefore not presented.

Section 2.2: The State of ATF LOCA Burst Testing

2.2.1: Previous ex-situ burst testing of FeCrAl Claddings

In 2016, Massey et al. [36] performed simulated LOCA burst testing on two 1st generation FeCrAl alloys (T35Y2 and B154Y), Zircaloys, and 304 stainless steel (SS) using the SATS facility at ORNL. The claddings were subjected to the standard LOCA test described in Chapter 1 and quenched at 800 ºC in distilled water rather than 600 °C. To compare against burst data, they conducted two creep tests on Zircaloy-4 (Zry-4) and 2nd generation FeCrAl (C35MN) at 800 ºC with stresses of 20 and 26 MPa, respectively.

Figure 11 from Massey et al. [36] reports the 1st generation FeCrAl burst stress and pressure versus burst temperature data in Figure 11(a) and Figure 11(b), respectively. Data for Zircaloy (Zry-2) and Zry-4 were also presented for reference. The red and black lines represent empirical burst hoop stress models for Zircaloys and 304 stainless steel (SS), respectively. The burst stress predictions presented in Figure 11(a) were converted to burst pressure in Figure 11(b) using cladding thickness. Their results demonstrated the strength improvements of 1st generation FeCrAl over Zircaloys. Figure 11(b) also reveals that 1st generation FeCrAl withstood similar internal loading conditions at lower temperatures due to the thinner cladding walls used for FeCrAl to account for neutronic considerations. Creep testing of C35MN indicated significantly higher creep resistance of FeCrAl alloys compared to Zry-4. The creep behavior of 2nd generation FeCrAl as well as modeling of 304 SS led Massey et al. to conclude that the burst behavior of wrought Fe-based alloys is minimally dependent on creep. Limited LOCA burst testing results on 2nd generation FeCrAl alloys, like C26M, is available in the literature. Transient burst testing of C26M was performed for this dissertation work and will be discussed in depth in a subsequent chapter.

Joshi et al. [74] conducted isothermal creep burst testing on 2nd generation C26M at temperatures of 480-650 ºC. A video camera was used to accurately capture rupture time and determine diametric strain. Joshi et al. [74] found two main behaviors: (1) opening geometry was either “pinholes” or large, “direct open ups” and (2) the power-law creep regime broke down at a

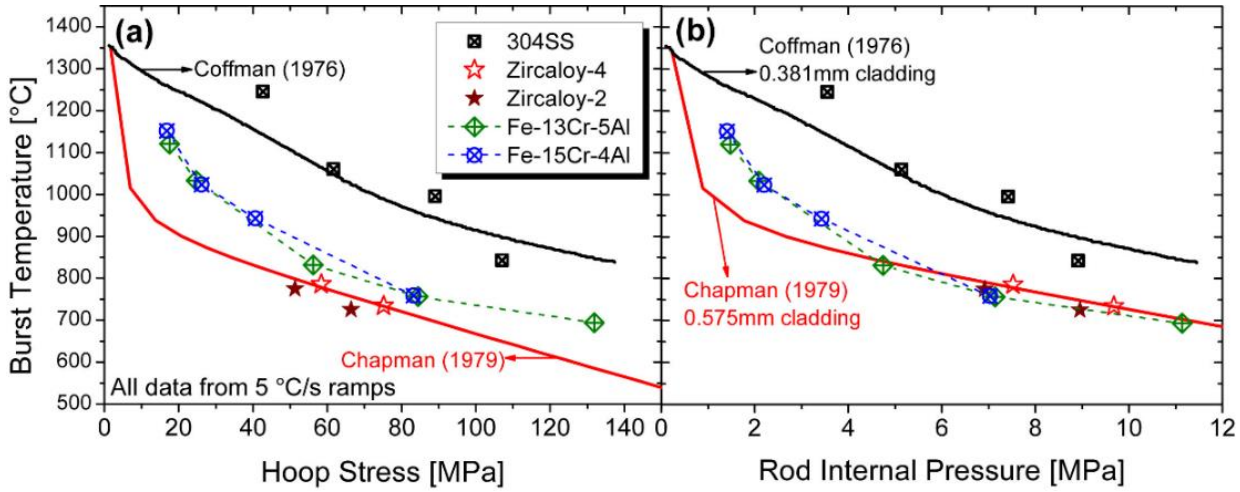

Figure 11. Plots of burst temperature vs hoop stress, 4(a), and burst temperature vs burst pressure, 4(b), for Zry-2, Zry-4, 1st generation FeCrAl T35Y2 and B154Y, and 304 SS from Massey et al. [36]. Reproduced with permission from Elsevier.

critically applied stress. The former was associated with a change in fracture mechanisms while the latter indicated sub-grain boundary break downs. Notably, no filler rods were employed to simulate fuel volume. Without a filler rod, the gas occupies a larger volume for a given pressure, meaning more energy is available during depressurization to develop the rupture opening.

Kane et al. [75] performed "saw-tooth" testing on C26M FeCrAl, 316 SS, and Zircaloy-2 to simulate cyclic dry-out conditions during anticipated transients without SCRAM (ATWS) and anticipated operation occurrences (AOOs). The cladding materials were internally loaded and subjected to repeated rapid transients, 14-17 ºC/s, from 300-650 ºC, 300-700 ºC, and 300-800 ºC. As an example, Figure 12 shows the imposed temperature and engineering hoop stress profile for a 2nd generation C26M cladding. They found that C26M withstood more cycles at higher hoop stresses for the same transients, indicating greater resistance to fatigue. These results support Massey et al.'s [36] findings on the possibly minimal impact of creep on the high temperature behavior of wrought FeCrAl alloys. As such, these findings suggest plasticity-based modeling could be sufficient for describing wrought FeCrAl behavior. *In-situ* data from burst testing could then validate this finding and provide reference failure conditions.

2.2.2: Previous ex-situ burst testing of Cr coated claddings

Burst and creep testing has been conducted on Cr coatings with varying thicknesses and deposition methods, generally indicating improved mechanical performance. In 2015, Kim et al. [49] performed ramp test at a heating rate of 14 ºC/s on partially coated samples in a steam environment. The coating thickness reported was ~80 μm, deposited using a physical vapor deposition (PVD) method via 3D laser coating technology. However, due to deposition method limitations, the specimens were only partially coated. The claddings only burst in uncoated regions during ramp testing, and ballooning in Cr-coated regions was reduced. In addition to burst testing, Kim et al. [49] performed hardness testing of the Cr coating and into the substrate, seeing a ~60 Hv difference between the two. Ring compression and tensile testing was also performed, with Cr coated specimens showing similar strain profiles to bare reference specimens, but again demonstrating increased strength. Kim et al. [49] therefore concluded the difference in behavior across testing could be due to general increased strength. They also indicated that microstructural effects associated with a Zr-Cr interdiffusion zone (IDZ) could influence behavior. However, the idea of "general strength" is vague, and no in-depth follow up was conducted to explore

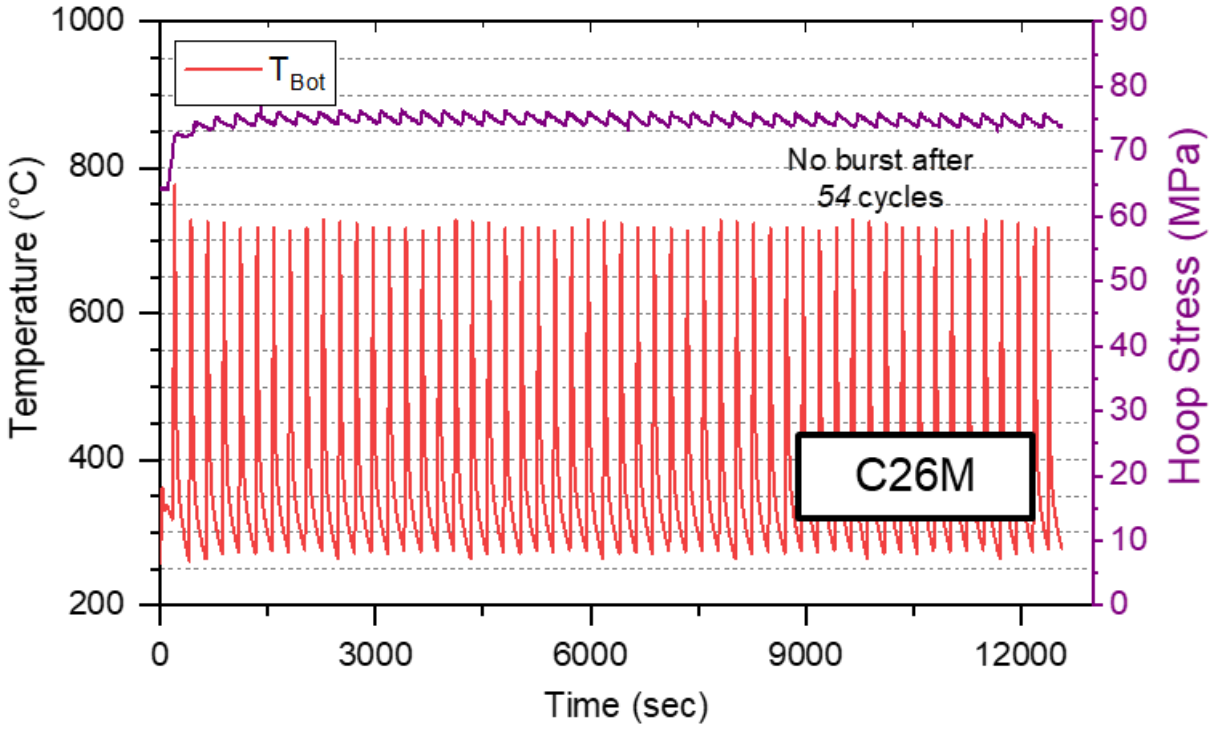

Figure 12. Plot of hoop stress and cladding surface temperature vs time for burst testing simulating cyclic dry out transients from Kane et al. [75] . The author of this dissertation was involved in this publication.

mechanisms for improvement. Due to neutronic and operational considerations [61] an 80 µm coating is not an economical option. Therefore, the community has focused on thinner claddings, ~5-30 µm.

In 2016, Park et al. [60] conducted simulated LOCA testing on Zr cladding with ~30 µm thick coatings, applied via cold spray techniques. The coated claddings were subjected to a temperature ramp from 300-1200 ºC at a heating rate of 5 ºC/s in a steam environment and held at 1200 °C for 5 minutes. Two burst tests were performed with internal pressures of ~8 MPa consisting of a bare and coated sample. The Cr coated sample burst at ~840 ºC and the bare sample burst at ~755 ºC. They also saw a ~20% reduction in maximum diametric strain for the coated samples, as well as reduction in opening geometry. While these improvements were noted, Park et al. [60] did not posit underlying mechanisms for the improvement. This work still was integral in establishing that thinner coatings (~20-30 um) have the potential to improve burst characteristics. However, experimental variations such as azimuthal thermal gradients were not reported which could impact the comparisons of diametric strain and rupture geometry.

In 2017, Brachet et al. [58] conducted both ramp and creep burst testing on M5 claddings with 10-15 µm thick coats deposited via PVD methods. The Cr coating was consistent and dense with a strong bond to the substrate. The EDGAR facility, equipped with *in-situ* laser deformation measurement capabilities, was utilized to characterize the materials behavior. A 10-15 µm coating extended time to rupture by ~150 s as well as reduced maximum circumferential strain by ~40% in creep testing. Preliminary results were discussed for ramp testing with heating rates ranging from 1 ºC/s to 25 ºC/s and internal pressures from 1 to 10 MPa. Brachet et al. [58] found, based on the limited testing conducted at that time, that balloon sizes were generally smaller for Cr coated samples and that burst temperatures were comparable or slightly above those of bare samples. However, no follow up publication detailing the ramp burst testing is available in the literature.

Brachet et al. posited the improvements in mechanical behavior, particularly in creep testing, cannot be explained by the increased thickness of the system from the coating alone. In a subsequent publication, Brachet et al. [51] notes that the mechanical properties at operational conditions for Cr is not significantly different than industrial Zr alloys, thus a coating is not likely to greatly affect mechanical behavior during operation. This posit then frames the notion of an "inherent" strengthening mechanism exclusive to high temperatures. As will be elaborated on later,

steady state creep plays a vital role in the behavior of Zr alloys during LOCA models. If a Cr coating interacts with high temperature creep performance, it is possible this influence is responsible for improved burst behavior.

In 2019, Chalupová et al. [76] performed similar creep burst testing based on temperature peaks that are expected in water-water energetic reactors (WWERS). They used Zr-1Nb alloys with ~15 µm thick coatings applied via magnetron sputtering and subjected the claddings to temperatures between 600-1100 ºC with internal pressures ranging from 1 to 10 MPa. The cladding samples were initially pressurized, then loaded into a pre-heated furnace and monitored until failure. Chalupová et al. [76] also concluded that a Cr coating led to improvements in high temperature creep behavior such as increases in time to burst and reduction in ballooning. However, no fundamental understanding was gained as to why the Cr coatings improved creep behavior.

Recently, Ridley et al. [77] performed burst testing of Cr coated Zry-4 deposited via high impulse magnetron sputtering (HiPIMS) using the SATS. The results from this testing are combined with analysis of Cr-coated Zirlo, also performed using SATS, in subsequent chapters. Two Cr coated Zry-4 systems were tested: (1) denoted "Cr#1" where the surface roughness of Zr cladding substrate created through-cracking and (2) labeled "Cr#2" where the samples were polished before application, and no through cracking was observed. Generally, the well adhered Cr#2 coating demonstrated consistent improvements in burst temperature, while Cr#1 did not. Analysis will be expanded on these systems in Chapter 3.

2.2.3: Potential mechanisms for Cr coating influence on Zr

Cr coatings have, at least preliminarily, been shown to improve rupture opening geometry, reduce creep rates, lower diametric strain, and increase burst temperatures across a wide range of Cr coated Zr systems. However, the inherent strengthening mechanism at high temperatures is not well understood. It should be noted not all these benefits are realized the same for every Cr coating-Zr system, demonstrating the variability of performance from system to system. This point will be elaborated further in Chapter 3 when discussing ORNL ex-situ testing.

From a mechanical perspective, the coatings account for < 4% of the coating-cladding system thickness and exist at the ambient outer surface. Remarkably, these thin coatings are clearly

impacting the bulk substrate behavior. It is reasonable to assume any influence of the coating is due to interfacial interactions, be it mechanical or resulting from chemical influences. The thin-walled hoop stress approximation is an excellent choice for conventional comparisons of strength of claddings. However, this approximation ignores nuances of the stress-state across the cladding. A more appropriate description produces stress as a function of radial position given by Eq .3,

$$\sigma_\theta = \frac{a^2 b^2 P}{(b^2 - a^2) r^2}, \tag{3}$$

where a is the inner radius (mm), b is the outer radius (mm), P is the gauge pressure (MPa), and r is the radial position of interest (mm), and σ_θ is the hoop stress at that radial position (MPa). Reflecting on Eq. 3, the stress state in a cylindrical structure under loading is higher near inner interface, i.e., away from the Cr coating. If temperature is truly uniform across a cladding during testing, it is likely failure initiates near or at the inner surface. Cr coatings, if improving burst/failure temperatures, is then affecting the behavior of the cladding away from the interface.

This analysis oversimplifies the complex mechanisms underlying clad failure but was presented for perspective. Clad failure typically ensues following substantial plastic deformation, characterized by moderate ballooning and thinning of the clad wall. Beyond these initial stages, there are other post-yield deformation and fracture processes, often inadequately modeled in general materials science and engineering, that demand further attention. For instance, if the stronger Cr coating strongly adheres to the Zr cladding, the stress state at the Cr/Zr interface will deviate from what is predicted by Eq. 3. The adherent properties of the Cr coating could introduce additional stress factors, modifying the behavior of the clad and possibly influencing the onset and progression of failure. Thus, a more nuanced analysis is required to fully capture the intricacies of these interactions and their implications for clad integrity.

Residual stress can be found in the Cr coating dependent on deposition, with compressive stresses commonly ranging from a few ten to hundreds of MPa in magnitude [51,78]. Brachet et al. believed the compressive stresses could influence mechanical behavior of the cladding-coating system. If a residual compressive stress is responsible for improvements, it is possible that a shifted threshold stress must be reached before ballooning/failure can occur. In terms of a chemical interaction, diffusion rates are increased at high temperatures promoting the expansion of an interdiffusion zone (IDZ). Ribis et al. [79] performed an in-depth analysis of the as-received

interface, reasoning that understanding the IDZ is valuable to assessing its effect on adherence and mechanical behavior. For a PVD coated M5 cladding, they found the IDZ comprised of a Laves phase Zr $(Fe,Cr)_2$ with C14 and C15 structures present. It is possible this hard intermetallic region grows during a LOCA transient, further affecting the mechanical behavior of the system of the entire system.

It is also possible that both posited mechanisms play roles in the improved mechanical behavior of Cr coated systems. For example, an ambient intermetallic compound is more brittle and stronger than the metallic cladding underneath possibly inhibiting ductility and subsequent ballooning. A residual compressive stress could increase burst temperature, i.e., delay burst by effectively lowering the net stress induced by internal loading. As such, residual stress could serve to improve burst temperatures, but minimally affect the ballooning process.

In-situ data could better help understand the balance of mechanisms responsible for improved burst characteristics. By synchronizing time, temperature, strain, and load, a more fundamental comparison of Cr coated claddings to bare reference can be drawn. As such, a framework built around gathering *in-situ* data is valuable to investigating Cr coating behavior and ultimately directing further optimization.

Chapter 3: Ex-situ Burst Testing of Cr-coated Zirconium alloys

Chapter Foreword

This chapter presents an investigation into the LOCA behavior of Cr-coated Zr alloys using conventional *ex-situ* SATS burst testing, building a foundation for comparing burst behaviors between bare and Cr coated Zr alloys using *in-situ* measurement techniques. It thus strengthens the motivation for the development of an accelerated *in-situ* characterization framework and is relevant to results later in the dissertation.

The research presented in this section has been published in two separate articles in the Journal of Nuclear Materials and the Annals of Nuclear Energy. The article on Cr-coated Zirlo [80] is titled "Burst and oxidation behavior of Cr-coated Zirlo during simulated LOCA testing" and was published in the Journal of Nuclear Materials, Vol. 564, 153679. The second publication [77], titled "Effects of Cr/Zircaloy-4 coating qualities for enhanced accident tolerant fuel cladding," can be found in the Annals of Nuclear Energy, Vol. 188, 109799. By combining the analysis from both articles, this chapter provides a comprehensive assessment of Cr-coated Zr cladding behavior during simulated LOCAs. Although the data and figures from the original publications are reproduced, the writing has been significantly modified to offer a more relevant discussion of using *in-situ* techniques to further investigate behavior of Cr-coated Zr claddings.

Three Cr coated Zr systems were evaluated using burst testing: (1) SRA Zry-4 with a rough surface finish and ~5 μm Cr coating deposited via HiPIMS, (2) polished SRA Zry-4 with a ~6-7 μm HiPIMS Cr coating, and (3) Zirlo with a 4.40 μm Cr coating deposited via Direct Current Magnetron Sputtering (DCMS). These coated materials, along with their bare counterparts, were subjected to the standard SATS LOCA test with a heating rate of 5 °C/s described in Chapter 1.

This chapter compares the performance of Cr coated claddings presenting burst strength, balloon deformation, and rupture geometry alongside oxide analysis to evaluate thin coating performance. This investigation seeks to underscore the subtle differences in performance of Cr-coated Zr systems, considering factors such as deposition method, surface roughness, coating thickness, and underlying material. It also emphasizes the broad spectrum of performance of Cr coatings, cautioning against overarching generalizations about coating behavior. This chapter

concludes by identifying the knowledge gaps unaddressed by *ex-situ* burst testing and positing the further experimental resolution that can be gained from *in-situ* techniques.

Section 3.1: METHODS AND MATERIALS

3.1.1: Cr coated systems and deposition parameters

Two distinct Cr coated Zr systems are presented in this chapter on *ex-situ* burst testing: (1) DCMS coated Zirlo and (2) HiPIMS coated Zry-4. The behavior of two batches of HiPIMS coating are compared in this chapter: (1) Cr#1, which consisted of a ~5 µm Cr-coating on Zry-4 with a rough surface finish prior to deposition, and (2) Cr#2, a ~6-7 µm Cr-coating on Zry-4, but with a polished surface prior to deposition. A Mahr MarTalk profilometer was utilized to measure surface roughness of the Zry-4 claddings before and after polishing. The rough Zry-4 substrates for Cr#1 had an average surface roughness, R_{ave}, of 0.36 µm and a max roughness, R_{max}, of 4.89 µm. The Cr#2 Zry-4 polished substrate had a R_{ave} of 0.10 µm and a R_{max} of 1.05 µm. The SRA Zry-4 used for both Cr#1 and Cr#2 came from the same batch, mitigating variations related to processing methods and initial ingot chemistry. Coating thickness and as-received geometry of the systems are presented in Table 3. The HiPIMS coatings were deposited by Acree Technologies.

Prior to HiPIMS deposition a plasma precleaning step was performed to prepare the surface of the claddings for 60 min. Cr#1 was deposited at a -20 V bias with a sample temperature of 100 °C. Cr#2 was first deposited with a -1000 V bias for 10 min, followed by a -100 V bias for the rest of the deposition process. Peak temperature for Cr#2 samples was 200 °C. No treatment of the coated claddings was performed before performing burst testing.

The specimens were subjected to the standard SATS LOCA test described in Chapter 1, heated at a rate of 5 °C/s in a steam environment and held for 5 min at a 1200 °C isotherm. To compare length dependence and conserve material, shortened segments were utilized for the Cr#2 testing, specifically 152.4 mm (6”), Table 3. The bare Zry-4 reference tests were also performed with shortened lengths.

Optical scans of the claddings were obtained using Keyence VR-3000 series microscope. Burst opening geometry was then characterized using these scans. Maximum diametric strain was recorded for the specimens using digital calipers. Post-test, the claddings were sectioned, mounted in epoxy, and polished with colloidal silica to investigate coating and oxide structure near and

Table 3. Sample geometry and coating thickness for Cr coated and bare samples.

Cladding Material	Coating Thickness (μm)	Outer Diameter (mm)	Wall-thickness (mm)	Cladding Length (mm)
Bare Zirlo	0	9.49	0.610	304.8
Cr-coated Zirlo	4.40 ± 0.24	9.49	0.614	304.8
Bare Zry-4	0	9.5	0.56	304.8 and 152.4
Cr#1 on Zry-4	4.8 ± 0.2	9.5	0.56	304.8
Cr#2 on Zry-4	6.8 ± 0.5	9.5	0.56	152.4

away from the burst region. The cross-sections were taken from the center of the balloon region. A Tescan MIRA3 SEM was utilized to perform EDS measurements and microscopy of the post-test cross-sections.

3.1.2: As-received coating characterization

The possibility for improvements in high-temperature mechanical and steam oxidation behavior relies heavily on a well-adhered coating, free from substantial delamination or through-cracking. Figure 13, recreated from Ridley et al. [77] presents the surface roughness of the Zry-4 tubes (a) before and (b) after polishing. The corresponding HiPIMS coatings are shown in Figure 13(c) and Figure 13(d) for the rough Cr#1 and polished Cr#2 surfaces, respectively. It is evident the rougher substrate resulted in a coating with pre-test delamination and through-cracking. From a mechanical perspective, this could undermine any potential benefits of the coating, such as effects of residual compressive stress, due to poor interfacial quality. From a steam oxidation resistance standpoint, through-cracking could provide pathways for oxygen to reach the underlying Zr substrate, thus compromising the effectiveness of a Cr barrier. If the formation of a Laves phase (a Cr-Zr interdiffusion layer) is responsible for improved mechanical behavior, oxidation could degrade this boundary.

A similar SEM micrograph of the as-received Cr-coated Zirlo specimen is presented in Figure 14, displaying a well-adhered coating. Notably, the long columnar grains are oriented radially, characteristic of PVD techniques.

Section 3.2: EXPERIMENTAL RESULTS

3.2.1: Conventional burst strength characterization

Figure 15 depicts the burst hoop stress and temperature for all three of Cr coated systems and their bare counterparts. Due to material constraints, further replicate testing was not possible, necessitating selection of a range of initial pressures for preliminary comparison of burst behavior. Table 4 presents the burst criteria associated with these tests. Bare Zirlo is denoted by orange circles, while Cr-coated Zirlo samples are represented by purple diamonds. Green triangles correspond to Cr#1, and red squares to Cr#2. Bare SRA Zry-4 is indicated by yellow stars. The empirical Chapman model [27,30] for Zircaloys with a 5 °C/s heating rate serves as a reference (black line).

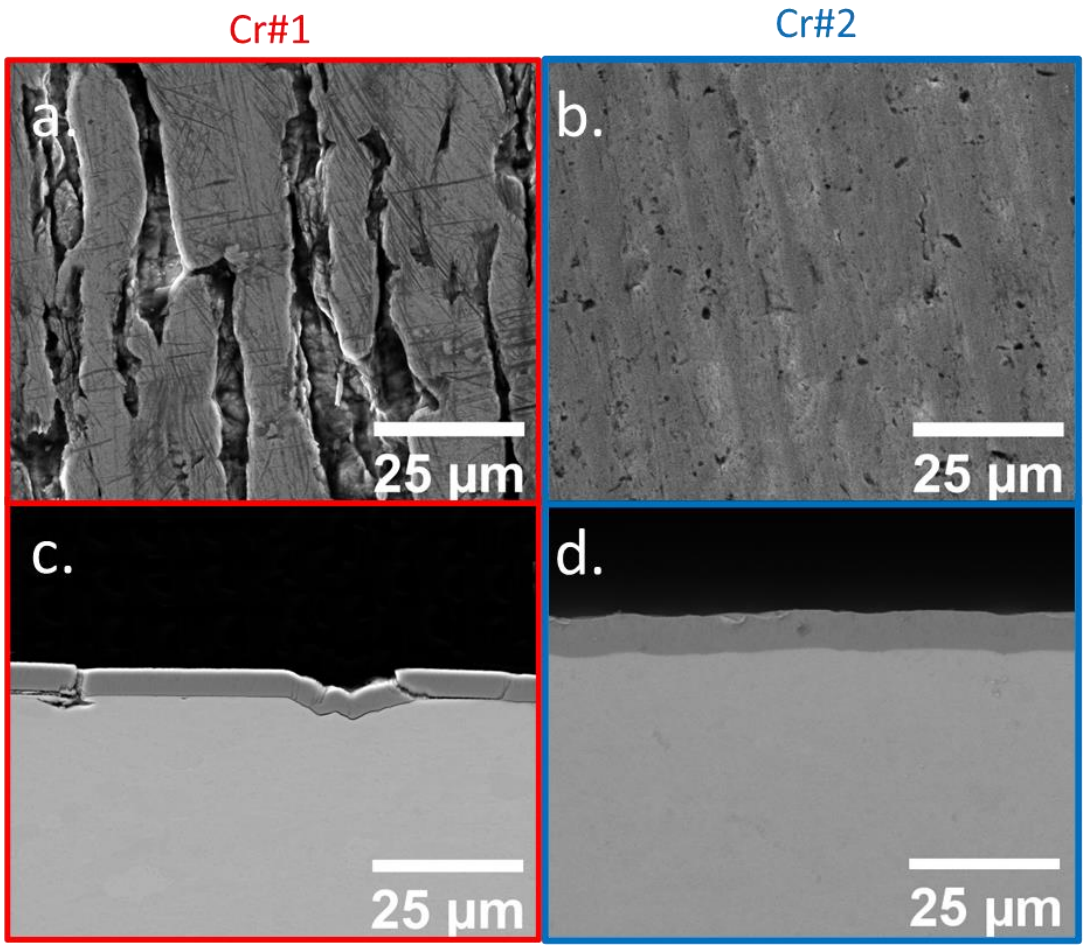

Figure 13.(a) Surface roughness of the SRA Zry-4 before polishing and (b) after polishing. (c) Cr#1 coating interface after deposition onto the unpolished surface, showing through-cracking and delamination. (d) Cr#2 coating interface on the pre-polished surface demonstrating a well-adhered coating with minimal through-cracking.

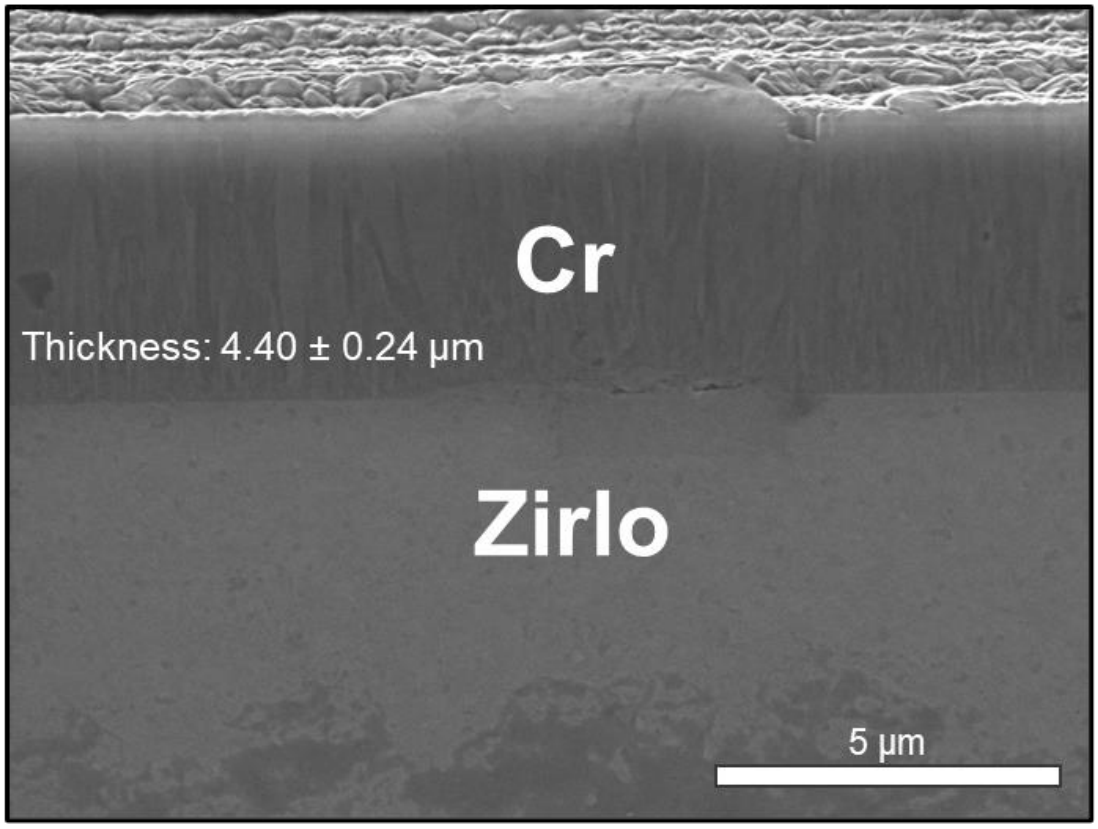

Figure 14. SEM micrograph of a cross-section from the base of a Cr-coated Zirlo cladding prior to testing.

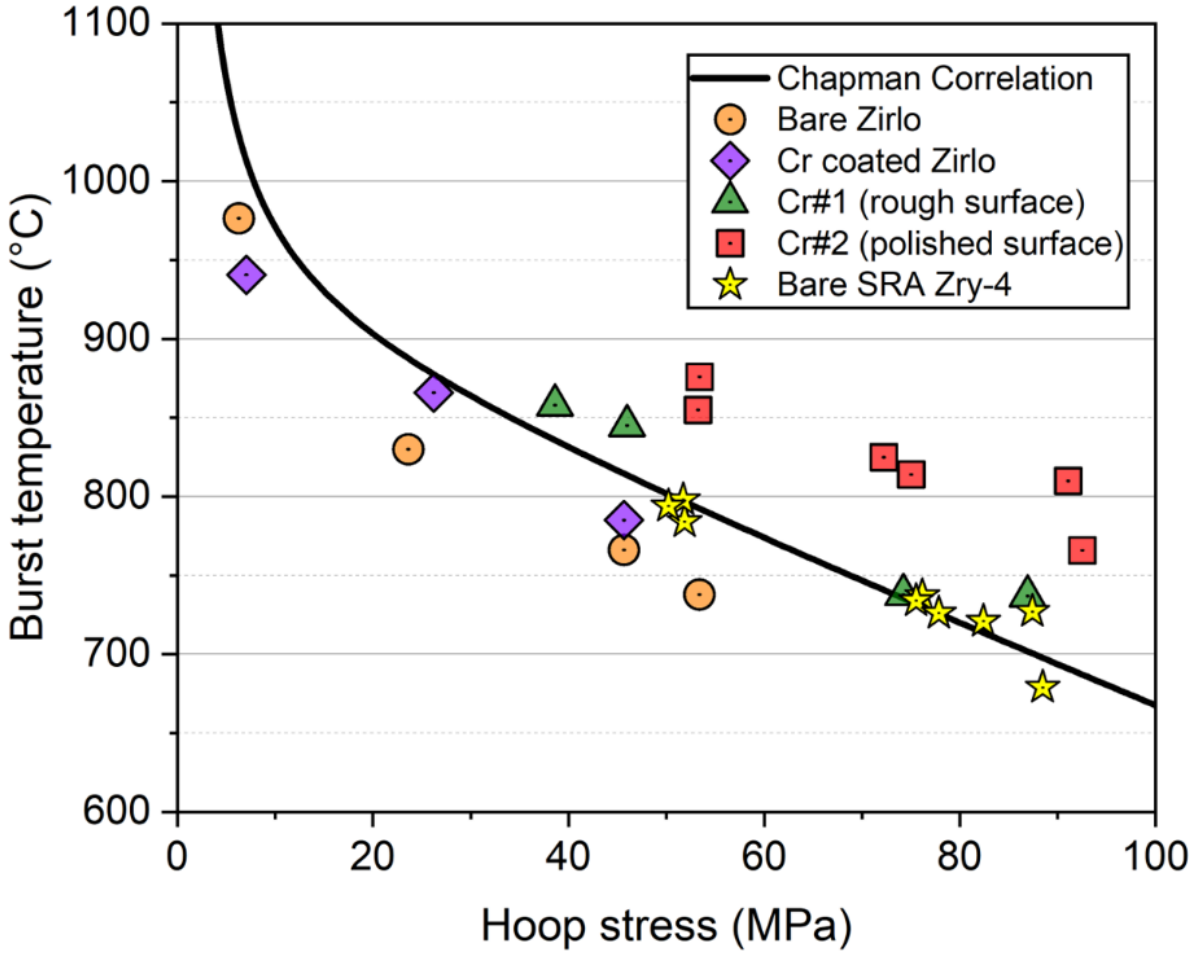

Figure 15. Burst temperature and hoop stress of all systems presented in this chapter.

Table 4. Burst criteria for all bare and Cr coated Zr testing presented in this chapter

Cladding Material	Burst Temperature (°C)	Burst Pressure (MPA)	Burst Hoop Stress (MPa)
Bare Zirlo	747	7.88	57.4
	766	6.74	49.1
	835	3.49	25.4
	977	0.929	6.76
Cr coated Zirlo	808	6.69	48.3
	867	3.87	28.0
	941	1.04	7.54
Bare Zry-4 (152.4 mm)	727	10.97	87.6
	721	10.34	82.5
	737	9.56	76.7
	734	9.48	75.7
	784	6.51	52.0
	798	6.49	51.8
Bare Zry-4 (304.8 mm)	11.10	679	88.6
	9.77	726	78.0
	6.30	794	50.3
Cr#1 Zry-4	737	10.89	86.9
	738	9.30	74.2
	845	5.76	46.0
	858	4.84	38.6

Considering Zirlo at an initial pressure of ~1 MPa, the Cr-coated sample burst at a temperature 36 °C lower than the corresponding bare cladding. Conversely, at ~3.4 MPa and ~5.9 MPa, the Cr-coated Zirlo withstood temperatures 32 °C and 42 °C higher, respectively, than the bare cladding. This suggests that a 4.4 μm thick Cr-coating, deposited by DCMS, might marginally enhance burst temperatures at higher stresses. It should be noted that this variation could also be attributed to experimental error, necessitating future testing with repeat testing and expanded loading conditions.

Examining the HiPIMS coated Zry-4, Cr#1 (high surface roughness) had a possibly marginal impact on burst temperature, especially in comparison to Cr#2. The Cr#1 testing overlapped with the reference bare Zry-4 testing at higher hoop stresses. Though no directly comparable bare tests are available for the two Cr#1 tests at lower pressures, the burst temperatures were ~20-30 °C higher than the reference Chapman correlation. It is possible that Cr#1 exhibited improved burst temperatures at lower pressures due to the coatings actually having integrity for these samples. Only one as-received sample was inspected, shown in Figure 13. It is conceivable that the through-cracking and subsequent compromising of the Cr coating was not present for all cladding sections. Given that sections for testing were taken from various parts of a parent rod, coating integrity might have only been compromised in regions where samples for the higher stress tests were taken. This discussion will be more relevant when considering the SEM analysis of the Cr coatings after testing in a subsequent section.

In contrast, Cr#2 successfully increased burst temperatures by ~60-80 °C compared to bare Zry-4 for all tested specimens. Regardless of the Cr#1 sample-to-sample coating integrity, it is apparent that surface roughness may play an important role in the accident behavior of Cr coated alloys. If the lower pressure samples did improve burst temperature, the discrepancy could also be related to the difference in deposition parameters, specifically the bias voltage and sample temperature during deposition.

3.2.2: Ballooning and deformation

Figure 16 presents optical images of burst Zirlo claddings initially pressurized to ~1 MPa, ~3.4 MPa, and ~5.9 MPa. Bare samples are shown in Figure 16(a), (c), and (e), while Cr-coated samples are depicted in Figure 16(b), (d), and (f). No discernible differences in the ballooning profiles between coated and bare samples at the same initial pressures can be observed visually.

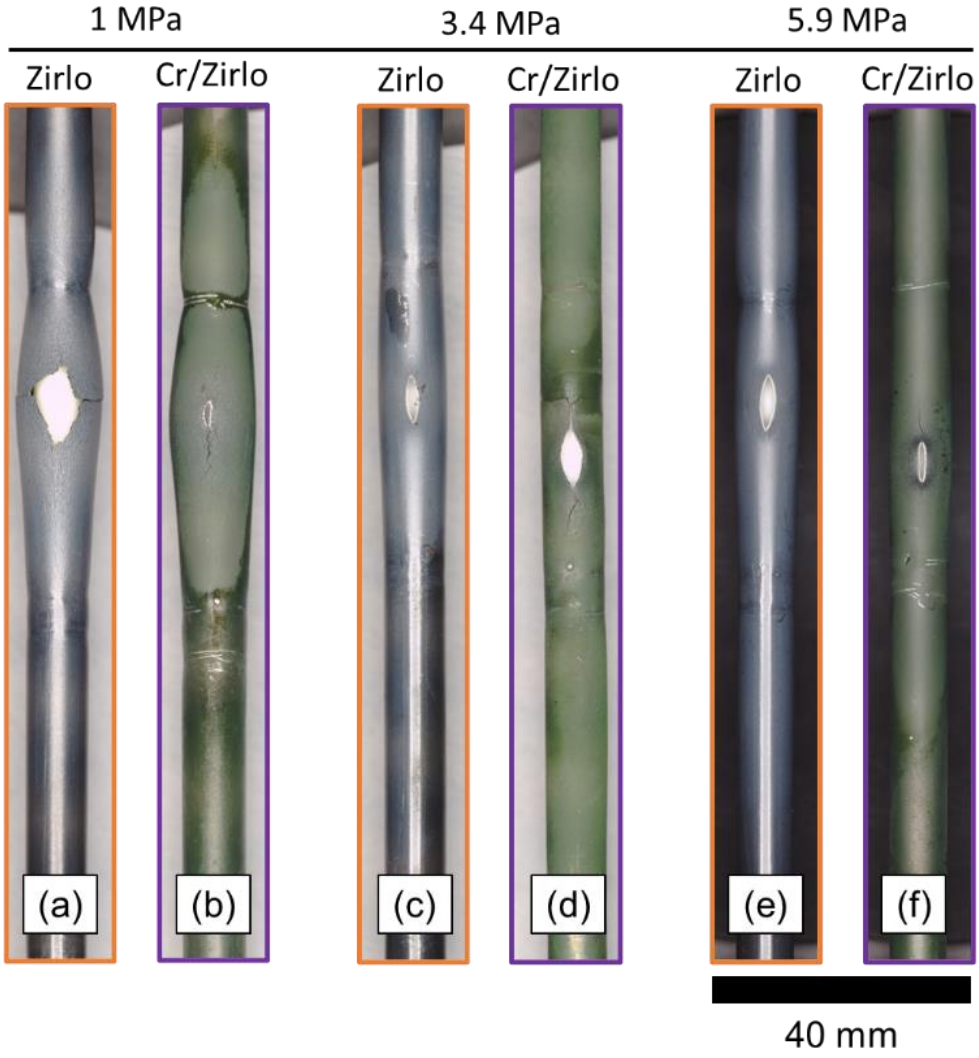

Figure 16. Optical macrographs of burst Zirlo and Cr-coated Zirlo at initial pressures of (a,b) 1 MPa, (c,d) 3.4 MPa, and (e,f) 5.9 MPa. The 1 MPa initial pressure bare Zirlo sample has significantly larger opening than the comparable Cr-coated sample. The large opening in (a) formed during post-test handling due to severe embrittlement of the cladding.

To quantitatively assess differences in ballooning, diametric strain profiles for claddings that had initial pressures of ~1 MPa and ~3.4 MPa are presented in Figure 17(a) and Figure 17(b), respectively. The small drops on either side of the large peaks in Figure 17(a) and Figure 17(b) are attributed to constriction from the Pt-Rh wire securing the thermocouples. These strain profiles display similar maximum diametric strain values and profile forms for corresponding initial internal pressures. Comparable results were obtained for the diametric strain of samples with ~5.9 MPa initial pressure. If anything, the Cr coated samples demonstrate slightly increased diametric strain. Based on the limited testing performed, it appears that the 4.4 μm Cr-coating does not significantly impact ballooning during LOCA burst testing, contrary to previous literature findings.

Figure 18 presents optical images of the HiPIMS coated samples after testing for samples with burst pressures of ~9.4 MPa. Bare Zry-4 samples are depicted in Figure 18(a) and (b), while Cr#1 and Cr#2 are presented in Figure 18(c) and (d), respectively. A visual assessment of Figure 18 reveals that the Cr#1 sample exhibited a ballooning profile more in line with the bare samples. In contrast, the Cr#2 sample, which increased burst temperatures by almost 75 °C, demonstrated a more substantial balloon and opening. Despite the similar final load, the enhanced burst temperature in the Cr#2 sample led to less favorable balloon characteristics. As the Cr#2 sample burst later during the transient, it sustained the load for a longer duration at elevated temperatures, possibly responsible for the increased ballooning. Burst pressure might not be the best comparison, as burst temperatures were increased by ~60-80 °C.

Burst temperature could be a better comparison between coated and bare systems. However, it is important to note that the correlation between burst temperature and final diametric strain is complex, especially considering the super-plastic peaks characteristic of Zircaloys (Figure 5, Chapter 1). It is possible that the Cr#2 samples have similar superplastic deformation behavior dependent on burst temperature. Therefore, increasing burst temperature could shift diametric strain along a supposed peak, resulting in higher strain.

The diametric strain profiles of samples Cr#1 and Cr#2 were analyzed in comparison with the reference Zry-4. Maximum diametric strain for each sample is depicted against burst temperature and pressure in Figure 19(a) and Figure 19(b), respectively. Figure 19(a) incorporates a solid line derived from NUREG 0630 [30], a curve initially developed by Chung and Kassner [15] at Argonne National Laboratory (ANL). The α and α + β regions are denoted to differentiate

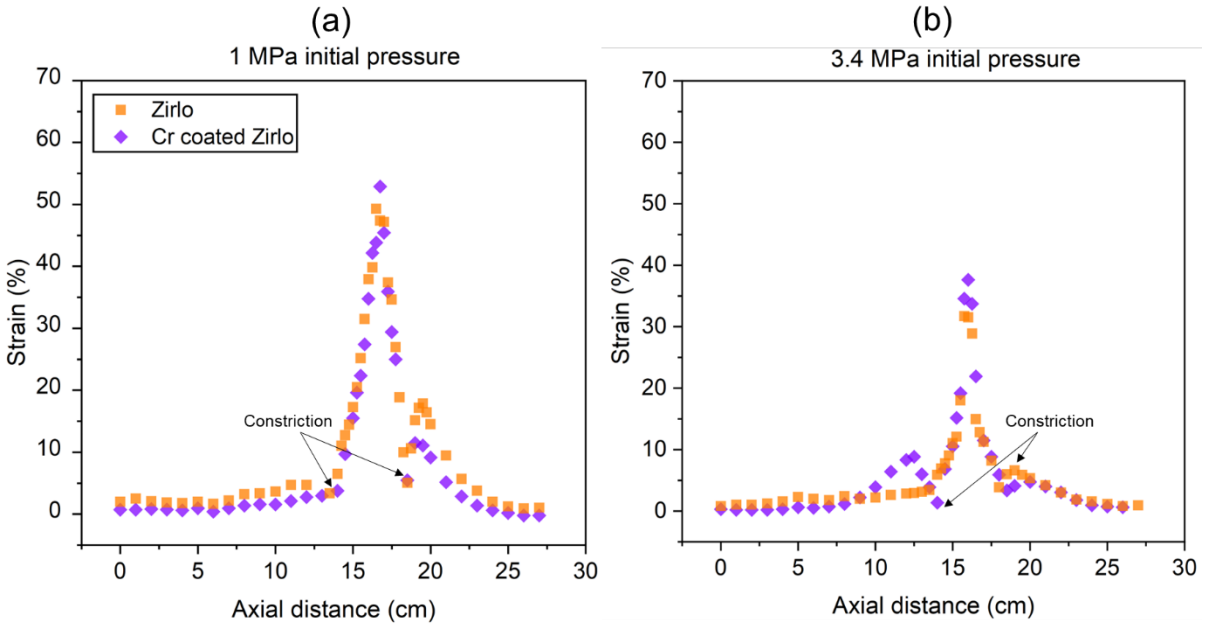

Figure 17. Post-burst diametrical strain measurements along cladding axial distance for Zirlo (orange squares) and Cr-coated Zirlo (purple diamonds) at initial pressures of (a) ~1 MPa and (b) ~3.4 MPa. The black arrows indicate the axial location where constriction from the Pt-Rh wire that secured the thermocouples occurred.



Figure 18. Optical scans of claddings that failed at ~9.5 MPa burst pressure. (a) and (b) present 300 mm and 150 mm length bare Zry-4 claddings, respectively. (c) Cr#1 and (d) Cr#2 samples after testing.

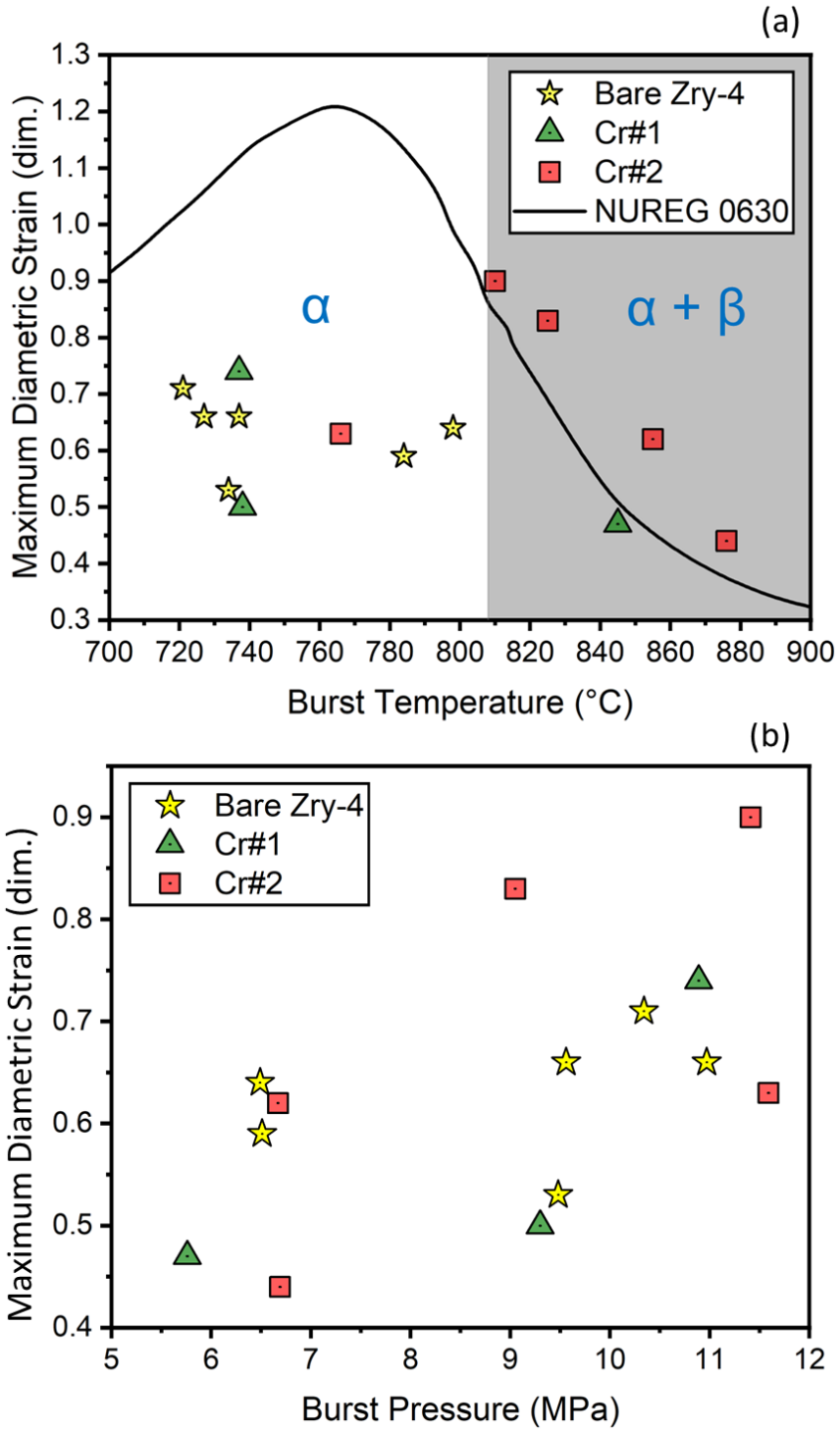

Figure 19. Maximum diametric strain as a function of (a) burst temperature and (b) burst pressure. The units on the y axis of "dim." represent the dimensionless quantity of mm/mm.

behavior of the phases. It should be noted that the ANL curve is one of few available in NUREG 0630, however, it was chosen due to fidelity of experimental conditions (single rod heated at 5 °C/s in steam) and quality of testing. The exact position and magnitude of superplastic peaks is not consistent across available models; thus, this serves as a qualitative comparison.

In the α phase region, the maximum diametric strain for both Cr#1 and Cr#2 aligned with the reference Zry-4. Notably, the maximum diametric strain remained relatively consistent across the burst temperature range within the α-phase for all Zr systems. In comparison to the qualitative ANL curve, diametric strains from this testing in the α-phase were significantly lower. Potential reasons for this discrepancy could be experimental variability, material condition, testing apparatus differences, or azimuthal temperature gradients which are known to influence post-test diametric strain [15].

The initial test pressures were selected to encourage failure in the α phase based on bare Zr behavior. To ensure consistent load conditions, the same fill-pressures were used for the Cr coated samples. However, a ~60 – 80 °C increase in burst temperatures caused most Cr#2 specimens and the lowest-pressure Cr#1 test to fail near or within the α+β phase. Phase stability, strongly influenced by composition, is not exactly known for this Zry-4 batch but was taken from Miquet et al. [9] for this analysis. As such, this discussion serves as a more qualitative assessment. Given the Cr coating barrier during the transient, it is possible that oxygen introduction via the steam environment into the substrate is reduced, resulting in differing phase boundaries during a LOCA test compared to the bare counterpart.

A distinct increase in maximum diametric strain at the qualitative phase boundary is evident in Figure 19(a), exemplified by jump in strain between the Cr#2 sample that burst at ~770 and ~810 °C. Beyond this qualitative phase boundary, Cr#2 specimens display a decreasing trend akin to the superplastic peak from ANL curve for Zircaloys. The lowest pressure Cr#1 test, a sample that possibly increased burst temperature, also exhibited lower diametric strain consistent with this trend. These observations suggest a potential superplastic peak for the Cr-coated Zry-4 samples. Combining this with the observation of increased burst temperatures, it is possible that the Cr coatings delay burst, rather than alter the underlying cladding behavior. Without comparative tests for bare Zry-4 claddings, this remains a conjecture as the observed peak might be a result of experimental error and sample variability. A comprehensive matrix encompassing a

wide range of loading conditions is necessary to validate any superplastic peaks for these coated systems. Additionally, this data set was constrained to limited testing by material availability, which emphasizes the need for accelerated qualification methods that reduce the number of tests necessary to investigate postulates such as this.

3.2.3: Opening geometry analysis

Figure 20 presents higher magnification optical images of the burst regions for the Zirlo samples with initial pressures of ~3.4 and ~5.9 MPa. The bare claddings, represented in Figure 20 (a) and Figure 20(b), displayed typical lenticular openings. On the other hand, Cr-coated Zirlo claddings shown in Figure 20(c) and Figure 20(d) demonstrated similar opening shapes but with through-wall cracks noticeable near the rupture ends across all samples. This might suggest a transition from ductile fracture during the initial stages of rupture development to brittle fracture at the end. Alternatively, these cracks could have formed during the quench at 600 °C, well after the burst, due to thermally induced stresses. Though the standard LOCA test is utilized to evaluate coating performance, the 1200°C hold and subsequent quench add a layer of complexity to deciphering the coating effects near burst occurs. Further testing of Cr coated Zr in this dissertation, particularly with DIC techniques, will not utilize the 1200 °C hold and quench sequence.

Figure 21 presents the burst opening area and length against hoop stress in Figure 21(a) and Figure 21(b), respectively, for the Zirlo samples. In general, both bare and Cr-coated samples exhibit comparable opening areas and lengths. The Cr-coated sample with an initial pressure of ~3.4 MPa demonstrated a larger opening area and length than the respective bare sample, while the Cr-coated cladding with an initial pressure of ~5.9 MPa exhibited a smaller area and length than the corresponding bare cladding. It should be noted that the ~1 MPa initial pressure bare Zirlo sample, as depicted in Figure 16(a), fractured during handling and is therefore not reported.

A parallel analysis was conducted for the HiPIMS coated Zry-4. Figure 22(a) and Figure 22(b) present the burst opening area for the bare Zry-4 reference, Cr#1, and Cr#2 against burst temperature and pressure, respectively. Both Cr#1 and Cr#2 displayed significant variability in burst opening area compared to the bare reference. The bare Zry-4 showed a monotonic decrease in opening size with increasing burst temperature, a trend not visible in Cr#1 and Cr#2 due to their considerable scatter. Overall, Cr#1 and Cr#2 samples featured larger opening areas than the bare

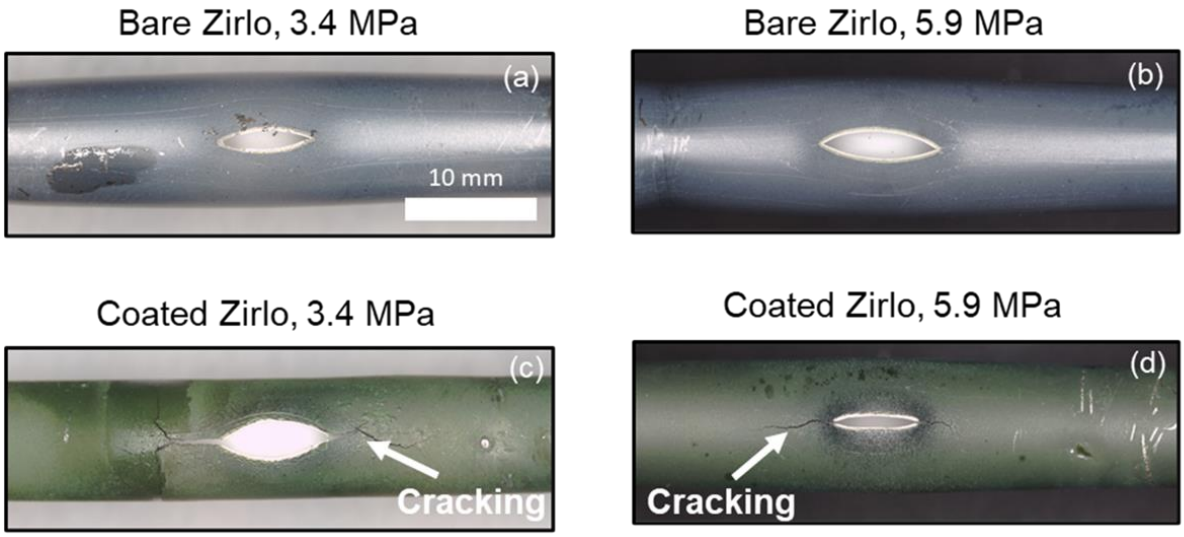

Figure 20. Higher magnification optical images of the burst regions for claddings that had ~3.4 and ~5.9 MPa initial pressures. The bare samples are shown in (a) and (b), the Cr-coated samples are shown in (c) and (d). Through-wall cracks can be seen at both ends of the opening for the Cr coated samples.

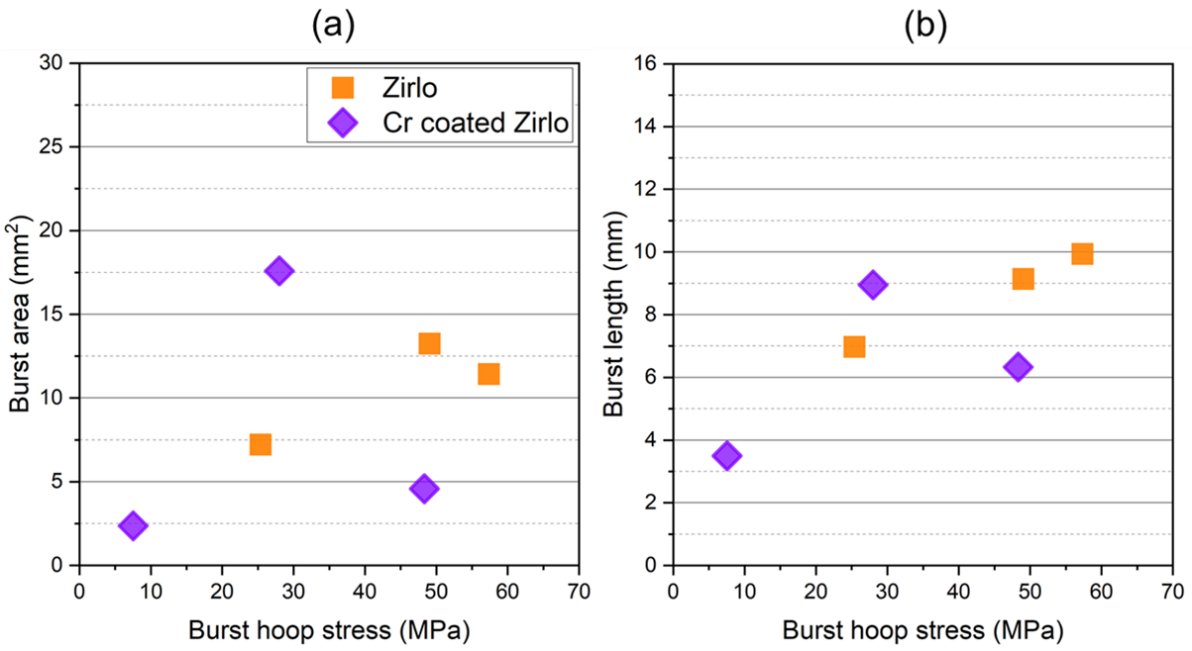

Figure 21. (a) Burst opening area and (b) burst opening length versus hoop stress for Cr-coated and bare Zirlo.

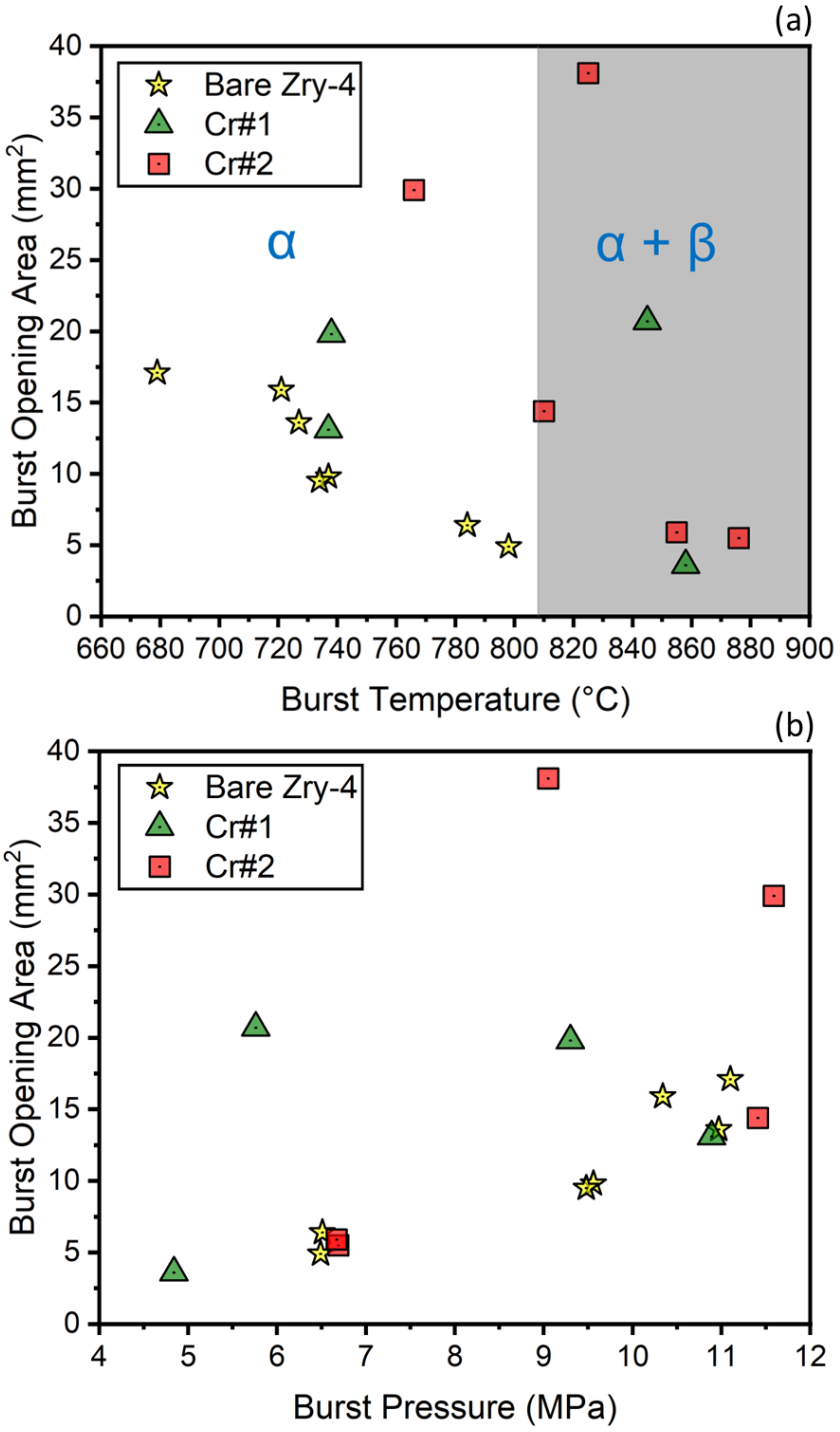

Figure 22. Burst opening area as a function (a) burst temperature and (b) burst pressure.

Zry-4, an observation that deviates from previous literature on Cr-coated burst testing. However, it is important to note that most of the Cr#2 samples and one Cr#1 test failed near or in the α + β region. Further testing with initial pressures accounting for a 60-80 °C increase in burst temperature is necessary. These preliminary results indicate that the Cr coatings show greater burst openings; however, additional testing is required to draw definitive conclusions.

3.2.4: Oxidation analysis of regions opposite from burst

Cross-sections were taken from the bare and Cr-coated Zirlo claddings subjected to an initial pressure of ~1 MPa, specifically from center of the balloon region and presented in Figure 23. Figure 23(a) and Figure 23(c) present light optical micrographs of the entire specimen cross-sections. The Cr-coated cladding, as shown in Figure 23(c), exhibited cracks resulting from post-test handling and mounting. Both bare and coated Zirlo claddings showed a significant decrease in wall thickness at the burst tips, suggesting high levels of strain. Conversely, regions situated ~180° from the burst demonstrated considerably less wall-thinning and strain. Figure 23(b) and Figure 23(d) present higher magnification micrographs centered around the regions ~180° from the burst for the bare and coated samples, respectively.

The bare cladding displayed extensive ZrO_2 formation on both the inner diameter (ID) and outer diameter (OD) in the region opposite burst, measuring 57.3 ± 6.8 and 37.4 ± 1.4 μm in thickness, respectively. However, for the coated sample, as shown in Figure 23(d), ZrO_2 formation was entirely absent on the OD in regions 180° from the burst for the Cr coated sample. This observation suggests that the Cr coating effectively protected the cladding from oxidation in these areas, satisfying the major criteria for an ATF cladding concept.

Figure 24(a) presents a higher magnification BSE micrograph of the lower strain region opposite the burst region from the Cr-coated Zirlo sample subjected to an initial pressure of ~1 MPa (as shown in Figure 23). A Cr_2O_3 layer was present on the ambient surface of the cladding, with a residual Cr layer underneath. A Zr-Cr IDZ formed between the residual Cr-coating and the Zr substrate. Figure 24(b) provides an EDS line scan through all three reaction layers.

Detailed statistics of the reaction layers formed in the region opposite rupture for the coated and bare samples are provided in Figure 25(a) and Figure 25(b), respectively, using box and whisker plots. The thicknesses of the Cr_2O_3, residual Cr, and Zr-Cr IDZ layers were measured to

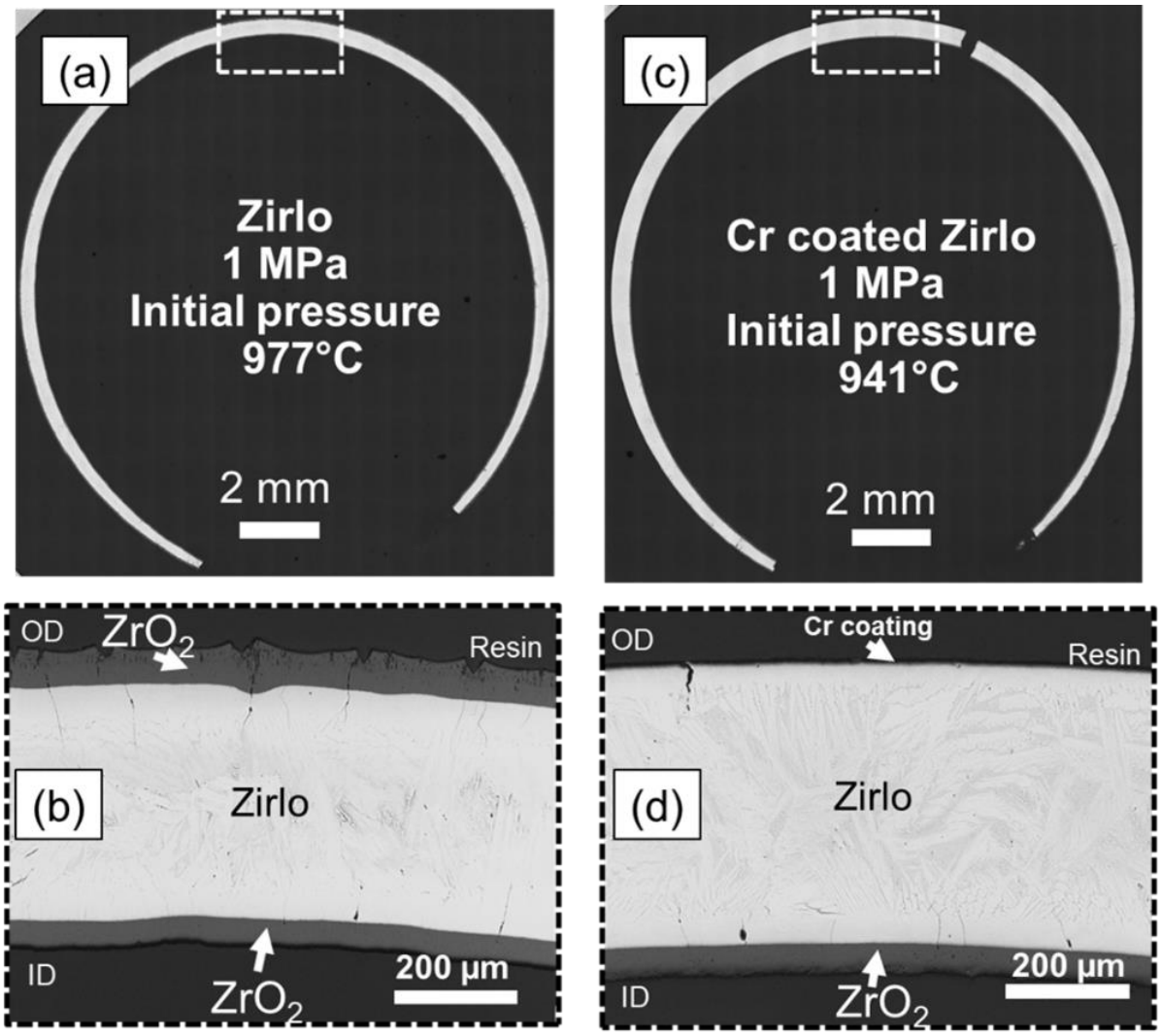

Figure 23. Cross-sectional optical macrograph taken from the burst region of Zirlo (1 MPa initial pressure) and (b) higher magnification micrograph of region opposite burst opening, indicated by dashed box. (c) Similar macrograph taken from burst region of Cr-coated Zirlo (1 MPa initial pressure) and (d) higher magnification micrograph taken from region opposite burst, also indicated by dashed box.

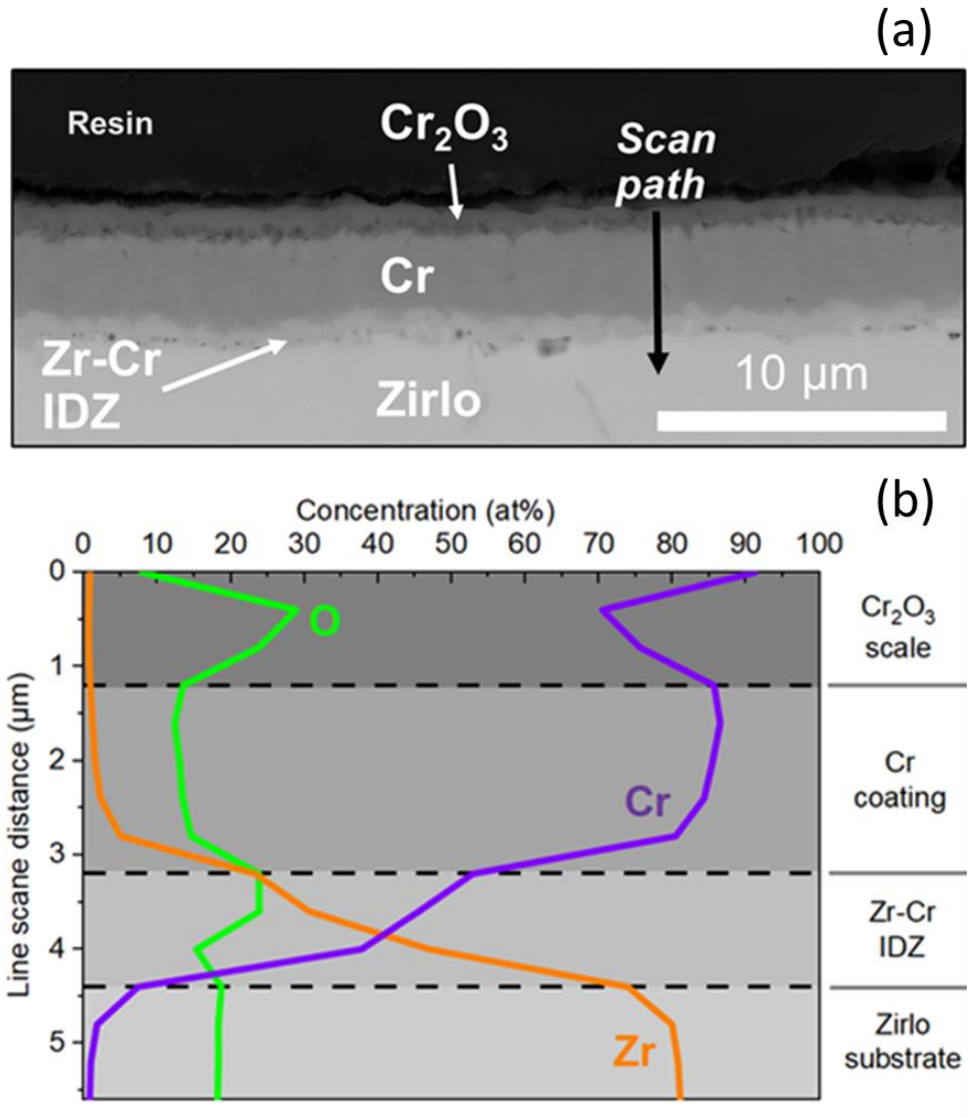

Figure 24. BSE micrograph of the Cr-Zirlo interface taken in a region opposite burst (1 MPa initial pressure). (b) EDS line scan across the reaction layers. This micrograph is representative of reaction products formed in lower strain regions opposite burst.

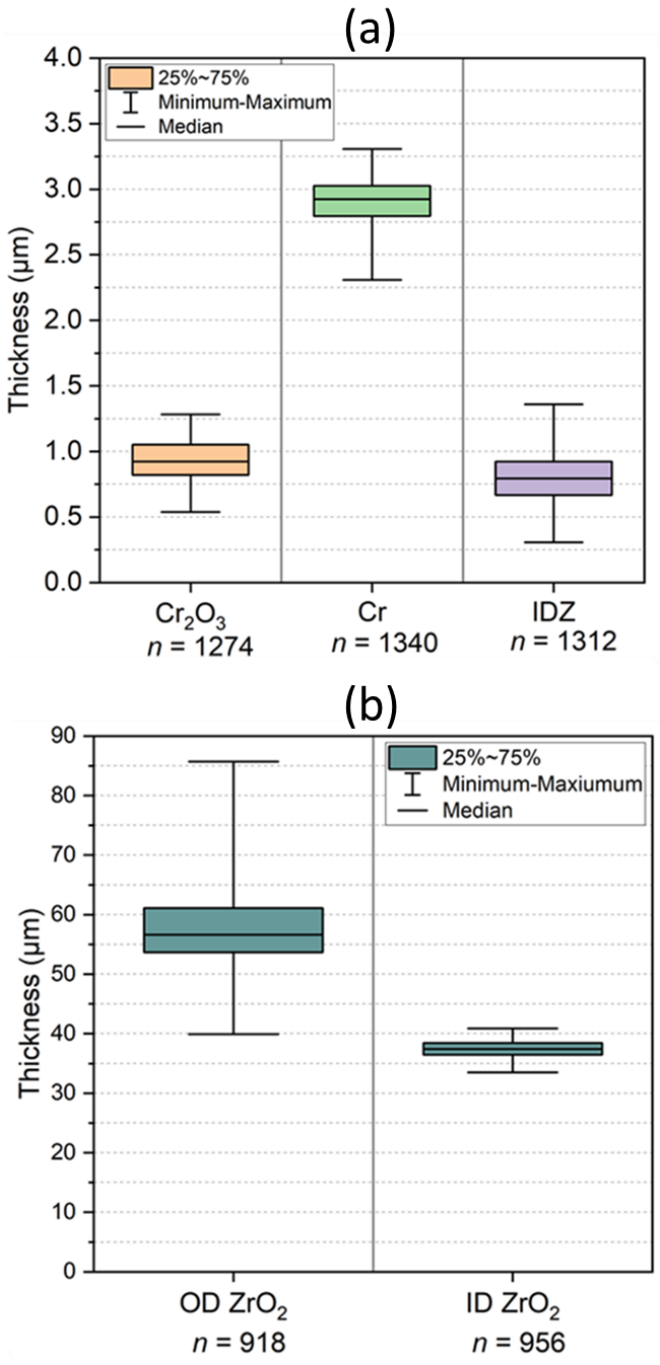

Figure 25. Thickness data of reaction layers found in lower strain regions opposite burst from Figure 24 and (b) oxide scale thickness data from the micrograph in Figure 23. “n” represents the number of measurements.

be 0.94 ± 0.15 µm, 2.90 ± 0.18 µm, and 0.81 ± 0.20 µm, respectively. The presence of these layers, especially the Cr_2O_3 and the residual Cr layer, suggest that the Cr coating in this region maintained its integrity during the simulated LOCA testing. These measurements were performed using the ORNL developed Size of Oxidation Feature from Image Analysis (SOFIA) software, publicly available on GitHub [81].

A similar analysis was conducted for the HiPIMS coatings, as reported by Ridley et al., and a brief discussion of the findings is included here. For a more in-depth exploration of Cr coating and IDZ formation, please refer to the publication. Figure 26 presents a SEM image and corresponding EDS maps of a region away the burst opening for the Cr#1 sample subjected to an initial pressure of 5.52 MPa. This sample is one of the Cr#1 claddings that potentially enhanced burst temperature, as illustrated in Figure 15. A similar structure of Cr_2O_3, residual Cr coating, Cr-Zr IDZ, and Zr substrate are found. Porosity at the oxide-coating interface was again observed. Most significantly, no ZrO_2 formation was detected in the oxide structure, again implying effective protection. Fe and Cr segregation can also be seen in the substrate.

SEM/EDS results for the higher pressure 8.27 MPa Cr#1 sample that did not improve burst behavior, presented in Figure 27, reveal that the coating was not protective in this instance. The region analyzed was again ~180 ° from the burst opening. Despite Cr_2O_3 formation being observed on the specimen surface, a substantial 70 µm ZrO_2 scale of formed under the residual Cr coating, signifying oxidant transport through the coating. Notably, a Cr-Zr IDZ zone was not detected, and the Cr layer was reduced compared to the 5.52 MPa sample.

These observations suggest that potential pre-cracking due to surface roughness present for some of the Cr#1 samples created short-circuit pathways for oxidation, rendering the 8.27 MPa sample coating ineffective compared to the 5.52 MPa test. Conversely, these findings raise the possibility that at higher pressures, the stress state for the Cr#1 coating was sufficient to generate cracks distant from the burst region during testing. Regardless, this high-lights the importance of coating quality and surface roughness in preserving the protective properties of the Cr coating under LOCA conditions.

Figure 28 presents a similar pairing of an SEM image and EDS maps of a region away from the burst region for a Cr#2 sample pressurized to 5.52 MPa. Similar to the post-test analysis of Cr#1 in Figure 26, the structure indicates that the coating provided effective protection during

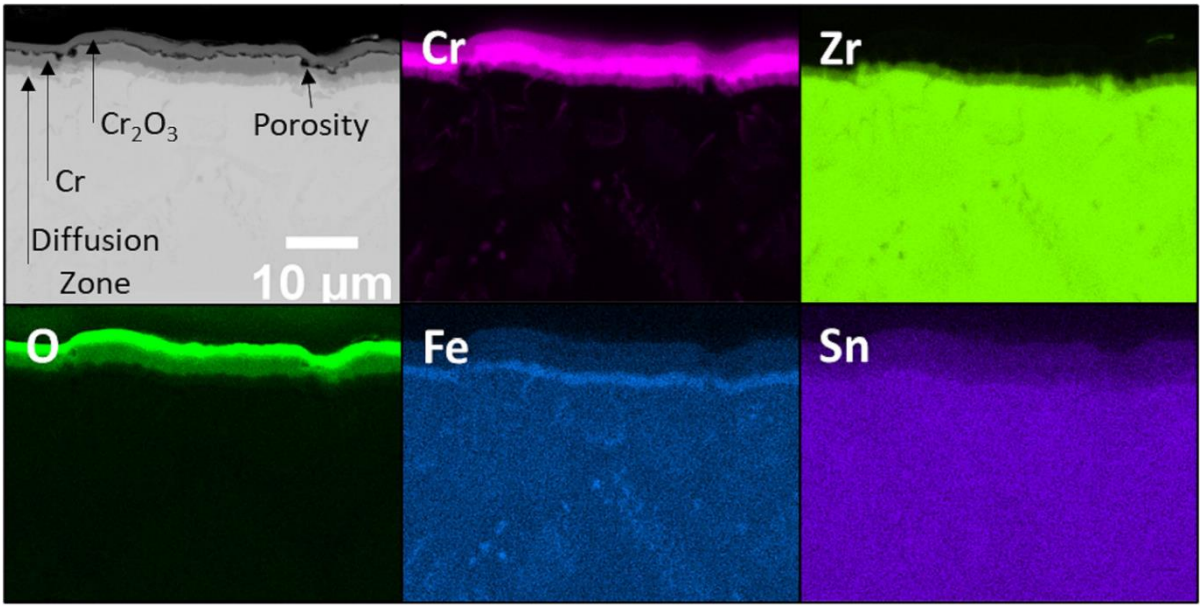

Figure 26. EDS maps of the region away from burst for the Cr#1 sample initially pressurized to 5.52 MPa.

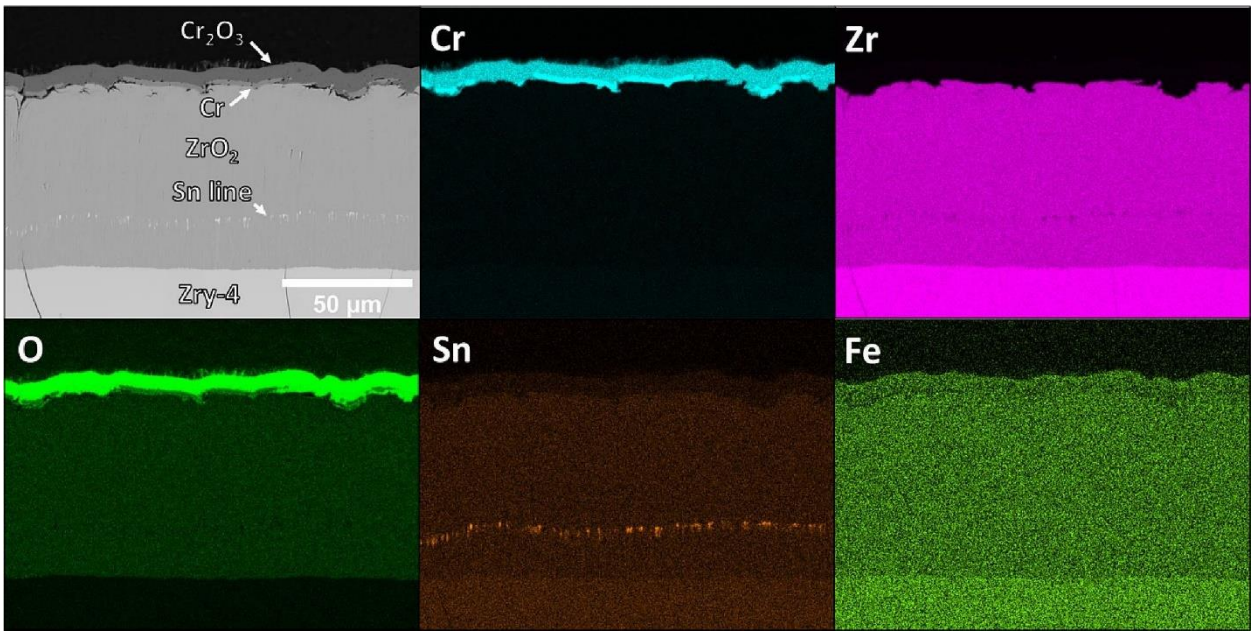

Figure 27. EDS mapping for the region away from burst of the Cr#1 sample initially pressurized to 8.27 MPa.

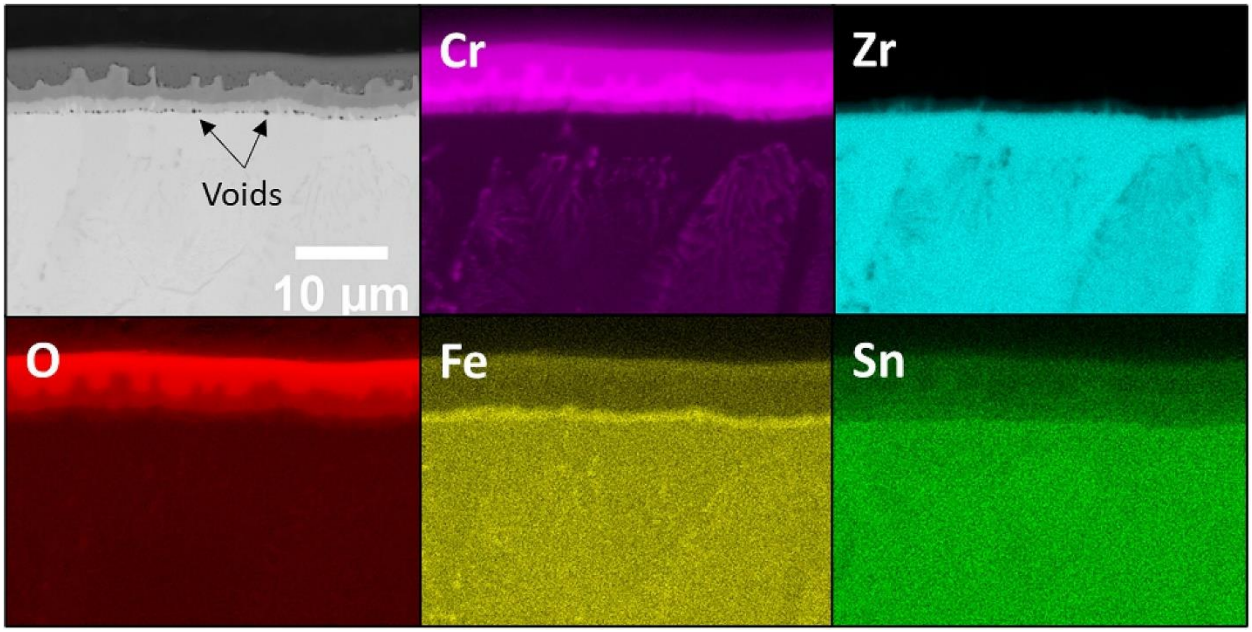

Figure 28. EDS mapping of the region away from burst for the Cr#2 sample initially pressurized to 5.52 MPa

high-temperature steam exposure. A notable difference is the reduced porosity at the oxide-residual coating interface for the Cr#2 sample. However, porosity/voids were found at the IDZ-Zr interface for this sample. Furthermore, the oxide-coating interface reveals a rough texture, with substantial local fluctuations in oxide thickness. Despite these variations, the coating's integrity was maintained in this region away from the burst opening. Again, the formation of Fe and Cr-rich precipitates in the Zr substrate is evident, which possibly formed during the quench after the 1200 °C hold. All the electron microscopy analyses discussed in this section were conducted in regions as far away from the burst location as possible, areas that were subjected to the lowest strain compared to those proximal to the rupture point. As will be shown in the following section, coating integrity was naturally compromised in the regions near the burst opening.

3.2.5: Oxidation analysis of regions of high strain

In regions closer to the burst opening, where strain is higher, the oxidation behavior of the Cr-coated cladding differed from that in lower strain regions ~180° from the burst. Figure 29(a) presents a stitched optical macrograph of the burst tip for a Cr-coated Zirlo sample (~1 MPa initial pressure), showing that the Cr-coating did not deter the formation of ZrO_2 in these higher strain areas. A substantial amount of ZrO_2, ~ 50-60 µm thick, formed on both the OD and ID near the burst tips. As the distance from the burst tip increased, the formation of ZrO_2 on the OD gradually diminished until no oxide was readily observable, presenting a structure similar to that in Figure 23. This suggests that the local strain and stress history plays a direct role in the effectiveness of the Cr-coating in mitigating oxidation and ZrO_2 formation.

The relationship between oxide formation and strain was quantified by examining residual wall-thickness and the thickness of the ZrO_2 along the Cr-coated Zirlo cross-section in Figure 29(a). “Wall-strain” was calculated using Eq. 4,

$$\varepsilon_{wall} = \frac{h-h_0}{h_0}, \quad (4)$$

where ε_{wall} is wall-strain, h is the unconsumed metallic wall-thickness after testing, and h_0 is the pre-transient wall-thickness. Given that the majority of ZrO_2 formation occurred during the 300-second hold at 1200 °C after burst, the metal consumption was adjusted to account for oxide thickness on both the OD and ID using the Pilling-Bedworth ratio [82]. The corrected metal consumption was then added to the measurements of the unconsumed wall-thickness, providing a

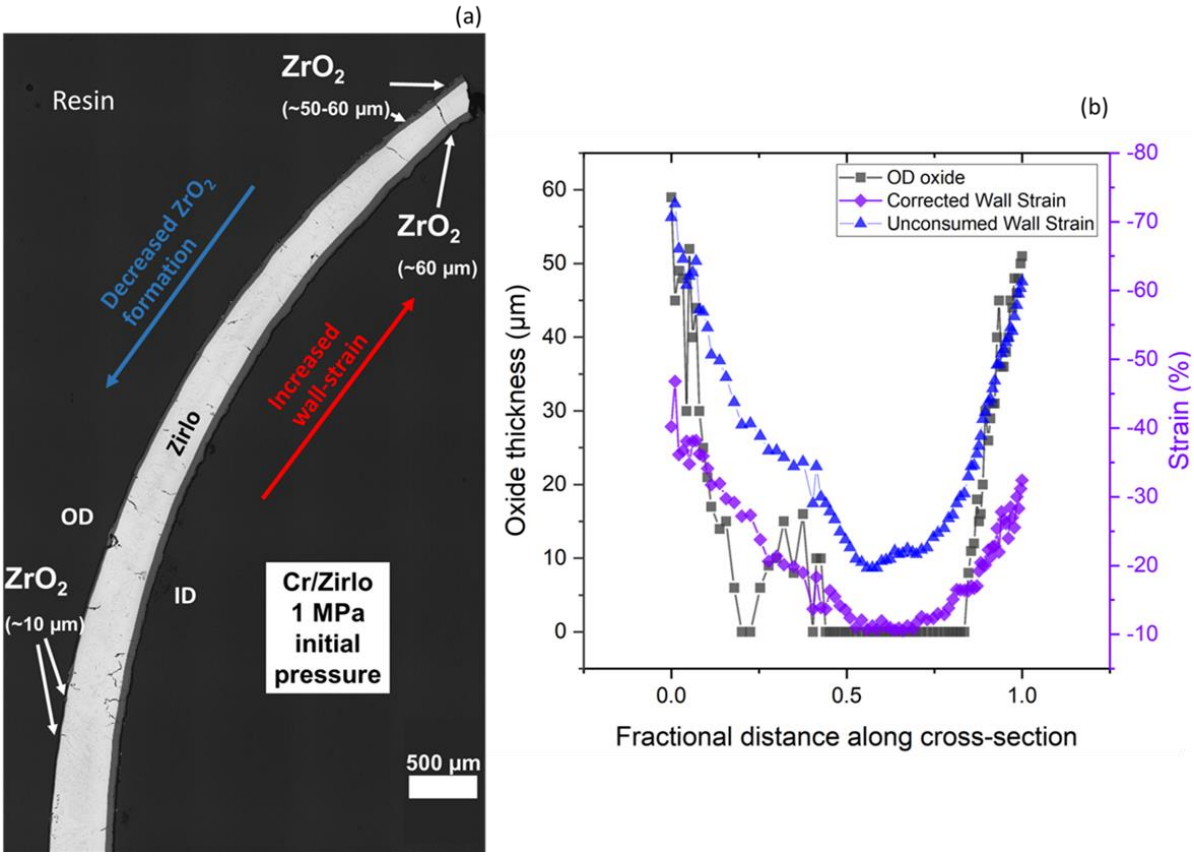

Figure 29. (a) Optical macrograph of the burst tip of a Cr-coated Zirlo sample (1 MPa initial pressure) showing the tapering of zirconia formation away from the burst region. (b) OD oxide thickness and wall-strain versus fractional distance along the cross-section. 0 and 1 fractional distance represent either end of the cross-section, i.e., the burst tips. Unconsumed wall-strain values, blue triangles, were calculated using the residual metal thickness after oxidation/testing. Corrected wall-strain values, purple diamonds, were calculated by adding the thickness of metal lost due to oxidation to the unconsumed metal thickness. Metal consumption was determined using the Pilling-Bedworth ratio [82].

more accurate depiction of wall-thickness along the cross-section immediately after burst.

Figure 29(b) presents the unconsumed wall-strain (blue triangles), the corrected wall-strain (purple diamonds), and the OD oxide thickness (grey squares) along the Cr-coated cross-section. In this figure, the burst tips are denoted as 0 and 1 in terms of fractional distance. At the point opposite the burst opening, the absolute value of wall-strain (|εwall|) reached a minimum and no ZrO_2 formation was observed on the coated OD ZrO_2 formation started around this minimum, beginning where |εwall| reached approximately 15%. Moving towards the burst region, both the |εwall| and the thickness of OD ZrO_2 increase, reaching their maximum values near the opening, thus demonstrating a relationship between the two. This observation agrees confirms that the effectiveness of the Cr-coating in preventing ZrO_2 formation is closely tied to the local strain conditions, with higher strain resulting in more extensive ZrO_2 formation. Additionally, the data presented in Figure 29(b) could imply the presence of a strain threshold for this coating system effectiveness.

Figure 30 provides higher magnification BSE micrographs and EDS elemental maps of Cr, Zr, and O, aiding in further examination of the coating behavior near the burst region. Figure 30(a) reveals two distinct structures in areas near the burst: (1) regions of partially consumed coating and (2) regions of fully consumed coating. In areas where Cr is fully consumed, large through-cracking formed in the Cr_2O_3 layer, coinciding with a thicker underlying ZrO_2 scale. Figure 30(b) shows a higher magnification micrograph focused on a region of partially consumed Cr. A visible crack through the residual Cr-coating, connecting the Cr_2O_3 and underlying ZrO_2 formation, is apparent. The EDS maps shown in Figure 30(c), (d), and (e) confirm the presence of O and Zr in the through-crack, while Cr is notably absent.

In regions of intermediate wall-strain, located between the area ~180° from the rupture and the burst tips, areas of accelerated localized corrosion were found on the OD, presented in Figure 31, indicating the coating failed but to a lesser degree. In other words, the spacing between developed through cracks was possibly greater in this region compared to the burst opening. This further indicates that the effectiveness of the Cr-coating in mitigating ZrO_2 formation is contingent on the local strain conditions.

The HiPIMS Cr#2 coating exhibited a similar ambient structure near the burst region/opening as the Zirlo samples, as shown in Figure 32. The SEM images and corresponding

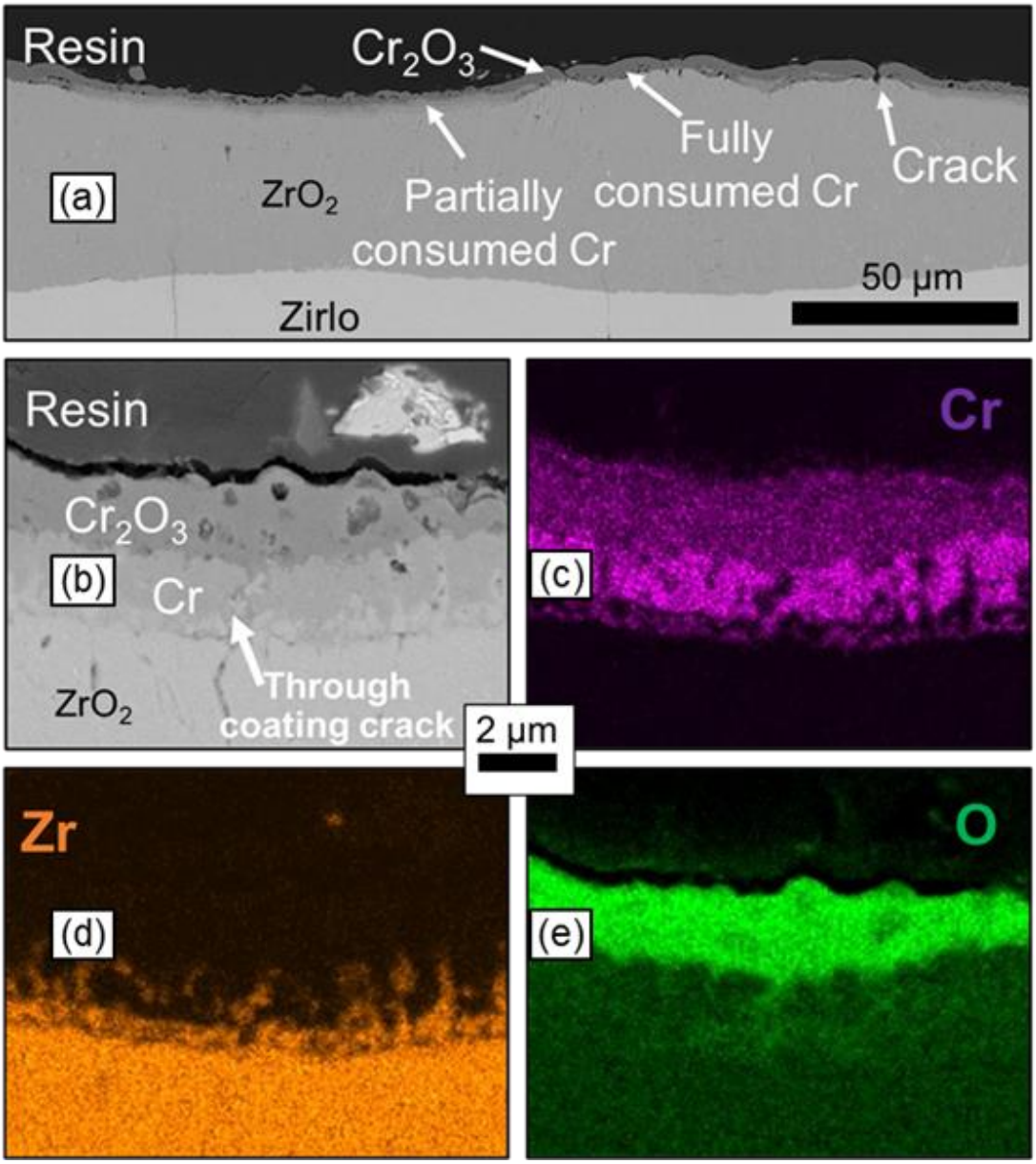

Figure 30. (a) BSE micrograph of the oxide scales that form in the burst tip vicinity. (b) Higher magnification BSE micrograph representative of regions where the Cr-coating was partially consumed, and associated (C) Cr, (d) Zr, and (e) O elemental maps.

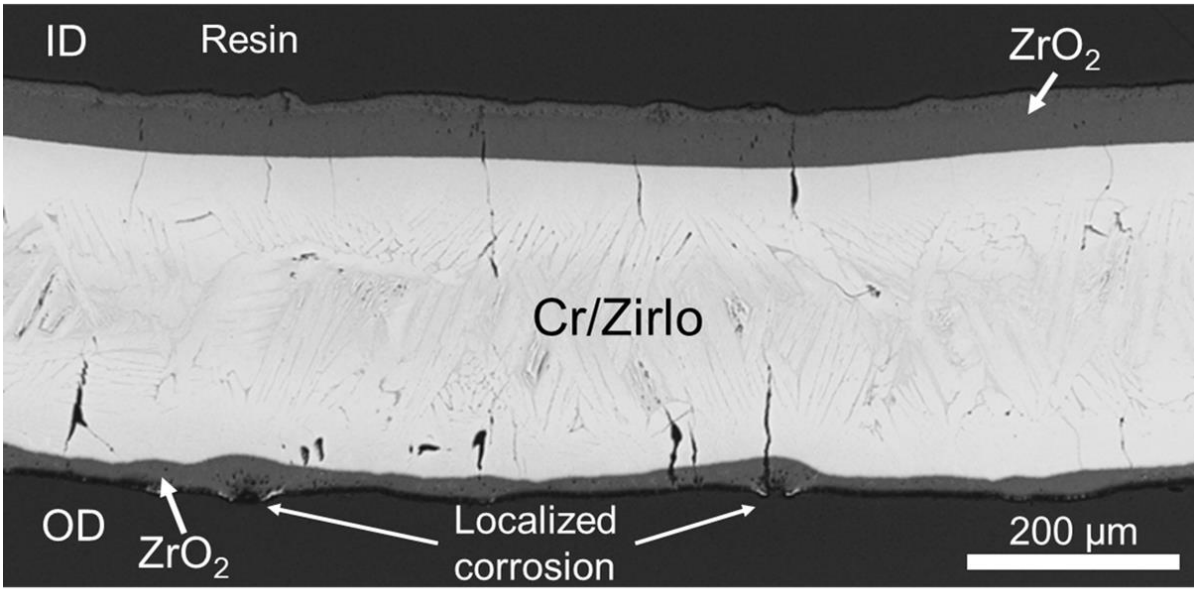

Figure 31. Higher magnification micrograph of a region of intermediate wall-strain, illustrating the areas of localized corrosion.

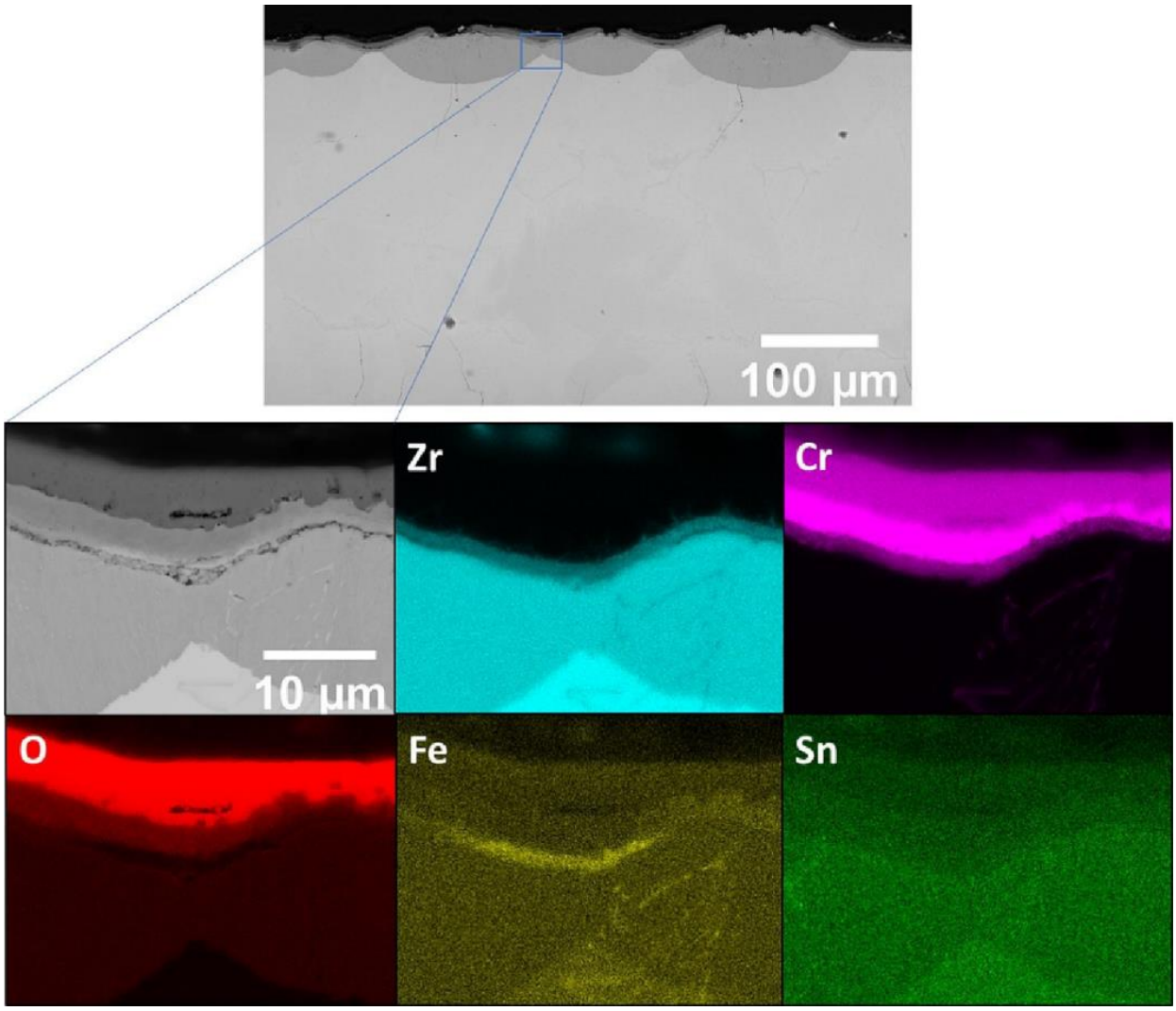

Figure 32. EDS mapping of the region near the burst vicinity for the Cr#2 sample initially pressurized to 5.52 MPa

EDS maps of the region near burst for the Cr#2 test, pressurized to 5.52 MPa (polished surface) exhibit the same nodular corrosion structure associated with crack formation. However, the nodular corrosion appears to be more localized, with distinguishable "scallop" structures present. From Figure 32 it is clear the Cr coating/Cr_2O_3 was absent from the top of these nodes. Ridley et al. posited that the volume expansion associated with ZrO_2 formation in the cracked regions elevated the coating and eventually led to delamination. Yet, in comparison to the Zirlo analysis Cr#2 showed improved mitigation of ZrO_2 formation.

Section 3.3: DISCUSSION

3.3.1: Effect of thin coatings on burst strength

At higher burst pressures/stresses, a 4.4 µm Cr-coating increased burst temperatures compared to bare Zirlo, as shown in Figure 15.. However, the lower initial pressure coated sample, ~1 MPa, exhibited a lower burst temperature. These findings are reasonably consistent with preliminary results from Brachet et al.'s [58] ramp testing of M5 claddings with 10-15 µm coatings, where comparable or slightly higher burst temperatures were observed. As such, a 4.4 µm thick Cr-coating deposited by DCMS possibly provided some improvement in burst temperatures at higher internal stresses. However, it is possible this observation is skewed due to minimal testing and lack of repeat data points. As such, these findings are preliminary and further experimentation is necessary.

Analysis of the Cr#1 results indicate the effect of surface roughness on coating performance. However, it is possible that the Cr#1 lower pressure tests demonstrated improved burst behavior due to an intact coating before testing for these samples. This was further supported by comparing the reaction products of the 5.52 and 8.27 MPa Cr#1 fill pressure tests, where the former demonstrated a post-test coating structure away from the burst region comparable to the structure of Cr#2 testing that improved burst temperatures. The 8.27 MPa Cr#1 sample showed extensive ZrO_2 formation opposite of the rupture site, indicating either: (1) the coating integrity was compromised for this sample or (2) the higher-pressure test resulted in coating failure. Regardless, it is evident that Cr#2 demonstrated more consistent performance increases.

The ~6-7 µm Cr#2 coating drastically improved burst temperatures compared to bare Zry-4 and Cr#1. Given the similar thickness of all coated systems, Table 3, it is demonstrated that the coating deposition process and parameters have a significant effect on burst behavior

improvement. Compared to DCMS, HiPIMS methods utilize greater powers during pulses resulting in a much denser film with better adhesion. As such, these qualities could directly relate to the comparative performance increase for Cr#2 in relation to the coated Zirlo. However, the substrate Zr alloys were not the same making this comparison inconclusive. Considering Cr#1 (lower pressure samples that possibly increased burst performance) vs. Cr#2, the difference in bias and greater operating temperature could relate to the relative performance gains. Conversely, it is possible that there is some thickness threshold near ~5 μm where drastic benefits occur for the coated Zirlo and Cr#1. Therefore, optimization of coating thickness and process parameters is necessary for each deposition method and Cr coating system.

This discussion underscores the nuances associated with Cr coating performance. While many uncertainties remain in terms of exact coating microstructure and processing effects, there were clear differences across the coating systems. As such, these observations from *ex-situ* testing demonstrate that overarching claims about the impacts of a Cr coating, especially in terms of increasing burst temperature, should be limited. Minimal characterization of the coating was performed in this work as this was a preliminary injunction. Further investigation of coatings such as Cr#2 is necessary to determine the mechanism for improvement such as IDZ formation or residual stress impacts. Future efforts are currently planned to investigate the process-property-performance relationship of coatings building off the Cr#2 deposition process but are beyond the scope of this dissertation.

3.3.2: Lack of reduction in diametric strain from thin Cr coatings

Maximum diametric strain as well as the ballooning shape of the profiles were similar between the experimental data for bare and Cr-coated systems. Zirlo in this limited testing showed no reduction in diametric strain, and possibly slightly greater values for the Cr coated samples. The Cr#2 coating, although showing a significant improvement in burst temperatures, demonstrated comparable or potentially worse ballooning and rupture characteristics. Preliminarily, no diametric reduction effect was found for any of the < 10 μm Cr coatings. The lack of reduction to diametric strain does not align with previous ramp testing [49,60,58,83] of thicker coatings, where significant reduction in ballooning and rupture size was observed.

There may be a thickness threshold where Cr-coatings provide a benefit of reduced deformation seen in literature. This threshold is likely reliant on deposition method and parameters.

A thickness effect does not support the notion that an IDZ or an inherent strengthening of the cladding is responsible for improved performance. From onset until burst, the IDZ expansion during a LOCA transient for a 6-7 μm and a > 10 μm thick coatings should not be substantially different. This consideration is even more stark when comparing the ~5 μm Cr#1 low pressure samples that possibly improved burst temperature and the 6-7 μm Cr#2 results. A thicker coating provides more material and possibly greater residual stress imparted on the cladding. Thinner coatings may fail at lower loads/strain, compromising benefits for the remainder of the ballooning process. As such, this could explain why Cr#2 increased burst temperature but did not reduce diametric strain. However, this explanation does not consider the effects of increased burst temperature on the microstructure/phase region or the complex behavior of bare Zr alloys.

Due to the increased burst temperatures, most of the Cr#2 tests and one Cr#1 sample failed in or near the α + β phase region. Diametric strain in the α phase region was not affected by the Cr#1 and Cr#2 HiPIMS coatings, Figure 19, and was relatively consistent across the low temperature phase. Near the nominal α + β phase boundary, Cr#2 demonstrated a trend in diametric strain with burst temperature similar to a characteristic super-plastic peak of Zr. This could suggest that the thin Cr coating served to delay the onset of ballooning and burst, rather than altering the bulk behavior itself. If such a posit is true, thin Cr coatings could result in higher diametric strains for the sample load conditions as seen in this work. For example, conditions could be such that the burst temperature is now at a top of one of the super-plastic peaks. Inversely, Cr coatings could by the same logic result in a lower diametric strain. This thought experiment neglects in-service and chemical influences discussed in the next section. Extensive further testing with bare Zry-4 failure in this region and replicate testing is necessary to address effects of experimental error and validate this trend for the SATS experimental setup. Such efforts could yield a curve akin to the ANL curve specific to the SRA Zry-4 material and SATS.

It is worth noting that the ANL curve presented in Figure 19 was generated from testing using direct electrical heating, while ORNL SATS testing relies on external IR heating. With external heat sources, claddings balloon toward the heat source, likely causing an increase in temperature during the final stages. This might result in lower total strain as the rapid temperature increase would promote failure and exacerbate any existing temperature gradients. Also, this could worsen any temperature gradients already present. In contrast, samples with other heating methods

do not balloon towards the heat source, possibly leading to lower heating rates during the final stages. Having more time to reach a critical failure temperature could potentially cause the cladding to balloon more. It should also be noted, the ANL trendline is not the only historic model of diametric strain and burst temperature. However, the ANL single rod testing with a well-controlled environment represents a high-fidelity comparison case, specifically with a heating rate of 5 °C/s.

Azimuthal gradients are known to play a significant role in the total diametric strain after testing. Rosinger et al. [33] and Erbacher et al. [26] both showed a strong influence of azimuthal temperature difference on total diametric strain for Zr alloys. A sharp decrease in diameter is found as the gradient increases. For current SATS testing, a global parameter such as diametric strain may not be the best measure of comparison. However, in-situ strain data synchronized with temperature and loading would provide a much more fundamental understanding of the coating effects.

Observations such as a potential super-plastic peak are crucial for evaluating Cr coating performance and understanding its safety limitations. It is important to note that all data presented here represents findings from ex-situ, end-of-life evaluations. In-situ data during the deformation process, as produced by the framework in this dissertation, is essential for a more comprehensive assessment of the observed differences in behavior and to better understand the underlying mechanisms at play. Correlation of stress, temperature, and strain to a given point could alleviate the uncertainties associated with experimental error by providing a thermomechanical connection between the as-received and post-test state. For Cr coatings, this could provide better insight into the effect of the Cr coating on the bulk behavior during the test, rather than relying on speculation based on initial and final diametric strain.

3.3.3: Effect of Cr coating on rupture geometry

Preliminarily, the coating did not minimize the post-test opening geometry. It is possible that the Cr coated samples resulted in larger burst openings for a given burst pressure. Given the scatter present for Cr#1 and Cr#2, further investigation is needed to draw definitive conclusions. However, since most of the Cr#2 samples failed in the $\alpha + \beta$ range, a direct comparison of opening size with burst temperature/pressure may not be possible. This observation does not align with literature findings on deformation behavior of Cr coated claddings, which suggests that there may

be other factors at play that were not captured in this preliminary analysis. More comprehensive testing and analysis, possibly including adjustments to coating thickness or deposition process, are required to better understand the observed discrepancies with the literature.

3.3.4: A critique of generalized statements about improved burst behavior from as-received testing

All testing presented in this section was performed on Cr coated and bare material in the as-received condition. This material condition is not representative of all cladding states in a reactor. Generally, one third of the fuel assemblies are replaced at the end of 18-24 month fuel cycle in an LWR. As such the claddings in an older fuel assembly could be subjected to operational considerations such as hydrothermal corrosion and irradiation effects on the order of 5-6 years. Therefore, cladding condition theoretically includes a range from as-received to end-of-life during a fuel cycle. Yet, much of the literature (although sparse) makes sweeping claims about effects of the Cr coatings in LOCA conditions. As shown in this chapter, the enhancements from a Cr coating are dependent on many factors such as coating thickness, integrity, and deposition parameters. Even compared to broad literature claims, these observations were divergent particularly in terms of coating effects on rupture geometry and diametric strain.

Cr coatings can impart a residual compressive stress, with the magnitude dependent on the deposition method [51,78,84]. If residual stress is responsible for the clear improvements in burst temperature, but possibly causes a delay in ballooning postulated for Cr#2, it is uncertain this improvement would be present after significant time in reactor. The residual stress in the coating could be degraded by time at operational temperature (~300 °C) via irradiation creep or through effects of hydrothermal corrosion. Further testing specifically looking at the evolution of residual stress with temperature is necessary, such as use of a synchrotron. Another avenue would be to perform autoclave testing for staggered amounts of time to simulate reactor environments and then perform burst testing.

Cr coatings are expected to act as an effective barrier to both oxidation and oxygen ingress during the cladding lifetime. Oxygen concentration as a result could be lowered in the bulk of the underlying Zr alloy. Similarly, any oxygen ingress into cladding during a LOCA transient would be mitigated by the barrier coating. Creep testing of Zircaloy-4 by Chow et al. [85] from 650 to 1400 °C found that homogenized oxygen reduced creep rates of both the α and β phases, with a

greater effect on β phase. Rosinger et al. [33] subsequently produced a model that accounted for these effects that predicted considerably lower diametric strains in the β phase. While further investigation is needed, it is possible that the Cr coating oxygen barrier could led to higher strains in reactor service. As such, making definitive, general conclusions about the effect of a Cr coating during a LOCA from this as-received material testing or other limited testing is premature.

3.3.5: Cr coating integrity near and away from the burst region

As expected, an adherent Cr-coating reduced ZrO_2 formation compared to bare Zirlo and Zry-4 claddings with complete mitigation in lower strain regions away from the burst during the simulated LOCA. The coating integrity for all coating systems was compromised in regions of intermediate and high strain, demonstrated by the development of cracks and extensive ZrO_2 formation under the residual coating and ambient Cr_2O_3. As through-coating cracking was not observed in the as-received condition for Cr coated Zirlo and Cr#2, Figure 14, ballooning and burst likely caused these developments. Additionally, the Cr-coat was consumed from both interfaces.

The varying presence of ZrO_2 on the Zirlo samples, Figure 29, indicates coating failure occurred along much of the OD, where for ~1/2 of the cladding cross-section ZrO_2 formation was ≥10 μm. The observed relationship between OD ZrO_2 thickness and wall-strain for the coated Zirlo, Figure 29(b), indicates that where $|\varepsilon_{wall}| \geq \sim 15$ %, the Cr-coating failed. As such, this indicates a possible strain threshold for coating failure.

Observation of the oxide in intermediate wall-strain regions for all coated systems revealed localized formation of ZrO_2. More distinct "scallops" were found for the Cr#2 samples, with lower total ZrO_2 formed compared to the Cr coated Zirlo analysis. The structure of these localized corrosion areas resembles the "nodular ZrO_2 spots" reported by Brachet et al. [51] during steam oxidation testing of coated Zircaloy-4 samples with pre-cracking. It is possible that regions of higher strain formed more cracks. With more short-circuit pathways, local oxidation rates would be higher, explaining the association of wall-strain and ZrO_2 thickness.

The "wall-strain" presented in this study is not a typical measurement associated with the stress state in thin-walled tube geometry and is intended as a proxy for other more rigorous valuations such as axial, radial, or hoop strain during deformation. As such, the correlation of strain with coating failure where $|\varepsilon_{wall}| \geq \sim 15$ % is only for wall-strain, and the possible effects of

strain-rate are not represented. Also, the wall-strain along the circumference was non-uniform, evidenced by the asymmetric deformation shown on either side of the minimum in Figure 29(b). Non-uniform strain/strain rate and thermal gradients could influence coating failure.

Despite the partial protection in intermediate and high wall-strain regions, Cr coatings still demonstrated improvements in steam oxidation resistance relative to bare claddings during simulated LOCA conditions for all Cr-Zr cladding systems. Therefore, for all Cr-Zr cladding systems, a < 10 μm coating demonstrated improvements in steam oxidation resistance relative to bare claddings during simulated LOCA conditions. However, a more complete study of the critical Cr-coating thickness is needed to determine statistically significant improvements in burst and oxidation behavior, such that the optimum coating thickness can be evaluated based on a cost-benefit analysis of both normal operating and accident condition performance.

3.3.6: Reaction product formation in regions of complete mitigation

Previous research [86–89] on Cr-coated Zr systems in 1200 °C steam environments and considerations of the Zr-Cr phase diagram [90] suggest the IDZ most likely comprises a $ZrCr_2$ intermetallic. For the Cr-coated Zirlo and Cr#2, pores were observed at the Zr-IDZ interface as well as the Cr-Cr_2O_3 interface, as shown in Figure 24(a). Notably, in the regions where Cr#1 demonstrated protection, voids were only found at the Cr-Cr_2O_3 interface.

Hu et al. [86] observed large voids in the Zr substrate at the Zr-IDZ interface, associated with Cr and Sn segregation. Brachet et al. [87] suggested these pores are Kirkendall voids, with cavities at the Cr-Cr_2O_3 interface resulting from outward cationic diffusion [91], while cavities at the Zr-IDZ boundary resulted from vacancy flux arising from differences in solubility and diffusivity between the Cr-coating and Zr substrate.

The reason for the presence of porosity only at one interface in the case of the 5.52 MPa Cr#1 sample in Figure 26 is unclear, particularly considering that this was one of the Cr#1 samples that potentially exhibited an intact, adherent coating. The absence of voids near the IDZ implies a relative balance of Cr and Zr flux in this region. However, comparing the SEM micrographs of Cr#1 and Cr#2, Figure 26 and Figure 28, the porosity found for Cr#1 at the Cr-Cr_2O_3 was greater than that of Cr#2. The primary structural difference between Cr#1 and Cr#2 was surface roughness, suggesting that a rough interface could enhance diffusion to the extent that inward Cr

flux from this interface balances the outward Zr flux. While the Cr_2O_3 layer remained intact for the entire 5.52 MPa Cr#1 sample in the region away from the burst location, it is possible that during an LOCA, porosity might reach a level where the oxide spalls off. This analysis is qualitative and further investigation into separate effects is necessary.

3.3.7: Insights to be gained from in-situ strain data

The lack of impact on diametric strain and possible super-plastic peak for Cr#2 suggests that the Cr coating primarily serves to delay the onset of burst rather than alter the burst mechanism itself. This finding is in stark contrast to previous literature testing. However, as discussed above the lack of data and effects of an azimuthal temperature gradient present in SATS testing limit the ability to draw a definitive conclusion. In-situ strain data would be valuable by providing a more comprehensive understanding of how a thin Cr coating improves burst temperatures but not final diametric strain. This postulated delaying effect could be attributed to the presence of a compressive stress exerted by the coating, which needs to be overcome before the material fails.

Additionally, the coating's post-test structure, in both near and away from the burst region, remained relatively similar for the Zirlo and HiPIMS Cr#2 coatings, further supporting this observation. However, the 1200 °C for 5 min exposure makes this finding inconclusive. Testing would need to be stopped right after burst to correlate coating structure at burst with performance. Cracking of the coating due to strain is a critical factor that could be better understood through in-situ strain measurements during the tests. These measurements could help establish correlations between local strain, coating behavior, and the observed improvements in burst temperatures.

Section 3.5: CONCLUSIONS

Simulated LOCA burst testing at a heating rate of 5 °C/s was performed on Cr-coated and bare Zr claddings, focusing on three different thin coatings and their effects on burst behavior. The 4.4 µm DCMS coating on Zirlo possibly increased burst temperature at higher pressures, yet it had no discernable effect on balloon behavior or rupture geometry. The 4.8 µm Cr#1 HiPIMS coating was deposited on a rough cladding substrate, which affected the consistency of improved burst behavior. This coating showed an enhanced burst temperature at lower pressures, a finding supported by SEM comparisons between the low-pressure Cr#1 and Cr#2 samples that explicitly elevated the burst temperature.

The Cr#2 HiPIMS coated system consistently improved burst temperatures by ~60-80 °C over bare Zry-4. However, its balloon geometry and rupture size were comparable, if not worse, to the bare reference. A simplistic comparison of final diametric strain with burst temperature or pressure is not adequate given the increase in the former for comparable initial loading conditions. Predominantly, Cr#2 samples failed within the α + β phase, displaying a peak similar to the superplastic behavior characteristic of bare Zry-4. This observation suggests that the thin Cr#2 coating may have delayed failure, as opposed to altering the ballooning process.

The results from this testing of thin coatings are in stark contrast to significant reduction of ballooning in the literature for coatings greater than 10 μm. However, given experimental uncertainties present such as microstructural characterization of the coatings and residual stress, the fundamental mechanisms for these observed variation and differences cannot be concluded. Yet, *in-situ* thermomechanical data would be useful in further resolving the effect of the coating on balloon formation, in conjunction with microstructural characterization of subsequently developed Cr coated systems.

Chapter 4: Ex-situ Burst testing of Down-selected C26M FeCrAl

Chapter foreword

This chapter presents the results of conventional *ex-situ* burst testing on a down-selected FeCrAl alloy and Zircaloy-2 claddings as a reference. The research detailed in the following sections has been previously published in the Journal of Nuclear Materials Volume 557 153242, under the title "Strength and rupture geometry of un-irradiated C26M FeCrAl under LOCA burst testing conditions" [38]. The content of the manuscript has been further edited and refined for the purpose of this dissertation.

The purpose of this chapter is to demonstrate the value of data collected from *ex-situ* SATS testing, while also high-lighting the benefits of a framework with *in-situ* measurement capabilities. As such, the following provides in-depth analysis of *ex-situ* FeCrAl data and suggests specific areas of improved resolution from *in-situ* data. This chapter concludes with reference to modeling work, in which the author was involved, that utilized tensile and burst testing data presented in the manuscript. The modeling efforts present a direct use case of the framework to provide necessary *in-situ* data and accelerate qualification and understanding of ATF materials.

Ferritic iron-chromium-aluminum (FeCrAl) alloys, a promising candidate for accident tolerant fuel, are being considered as potential replacements for the incumbent Zr- based claddings. Nuclear grade FeCrAl alloys are marked by superior high temperature mechanical behavior and exceptional steam oxidation resistance, both of which enhance safety margins during accident scenarios.

This chapter compares the behavior of three un-irradiated, commercially fabricated cladding materials under simulated LOCA conditions at a heating rate of 5 °C/s: (1) T35Y2, a 1st generation nuclear-grade FeCrAl alloy, (2) C26M, a 2nd generation nuclear-grade FeCrAl cladding, and (3) Zircaloy-2, a historic alloy used in BWRs. Compared to Zircaloy-2, both FeCrAl alloys demonstrated an improved mechanical strength and steam oxidation resistance.

C26M claddings exhibited superior accident tolerance with higher burst temperatures at all tested stresses, reduced oxide formation, limited ballooning, and preferable fuel retention behavior in terms of burst opening area and length. Furthermore, high-temperature tensile data for C26M is presented and compared against findings from burst testing.

For both un-irradiated FeCrAl alloys, it was found that a distinct “threshold” burst stress signified the transition between small and large openings. Higher threshold hoop stresses were associated with higher uniaxial strength for the FeCrAl alloys, indicating that tensile data, rather than creep data, could be useful for predicting rupture size and assessing fuel dispersal concerns.

Section 4.1: INTRODUCTION

C26M is a 2nd generation FeCrAl alloy with a nominal composition of Fe-12Cr-6Al-2Mo-0.2Si-0.03Y, representing a promising ATF cladding concept. Designed to balance fabricability, strength, and ductility, C26M retains excellent steam oxidation resistance and minimizes radiation embrittlement [67,92]. Strength improvements over 1st generation FeCrAl were achieved through Mo and Si additions and an optimized processing route, resulting in a partially recrystallized microstructure. Additionally, the Cr content is reduced from ~20 to 12 wt.% compared to conventional high-temperature FeCrAl alloys to limit irradiation-induced embrittlement [93].

Previous studies have shown that nuclear-grade FeCrAl alloys exhibit superior mechanical [36,67,68,75] and steam oxidation [63–66,94,95] properties compared to Zr alloys. However, due in part to neutronic constraints, FeCrAl claddings are expected to be significantly thinner than their Zr-based counterparts [96,70,71]. Thus, it is critical to evaluate FeCrAl cladding behavior under standard LOCA ramp testing [18,27,30,36], in accordance with U.S. Nuclear Regulatory Commission regulation 10CFR§50.46. Understanding the mechanical response of FeCrAl, particularly in terms of fuel dispersal and ballooning concerns, is also needed to fully assess the cladding’s ability to extend burnup beyond 62 gigawatt-days per metric ton of uranium (GWd/MTU) [34,97].

This chapter characterizes the rupture size, burst strength, and deformation behavior of un-irradiated C26M claddings during a simulated large-break LOCA, comparing the results against previously reported data for 1st generation T35Y2 [36,98]. Zircaloy-2 (Zry-2), a historical BWR cladding, is used as a baseline for comparison with both FeCrAl variants.

Burst opening area and length measurements, in conjunction with microstructural characterization of burst claddings, are employed to assess fuel retention capabilities. High-temperature uniaxial tensile data is also presented, and the use of tensile data, rather than creep data, for predicting mechanical response during LOCA burst testing is discussed.

This work is a stout representation of the characterization of ATF concepts that results from *ex-situ* LOCA testing, setting the foundation for improvements in understanding from *in-situ* techniques. Thus, it is presented to strengthen the motivation for development of the *in-situ* framework in this dissertation. Towards the end of the chapter, a model is presented that leverages tensile and burst data of C26M and successfully predicts burst temperature, emphasizing the value of *in-situ* DIC data in generating thermomechanical data for modeling campaigns of ATF claddings.

Section 4.2: METHODS AND MATERIALS

The SATS at ORNL was employed to conduct burst testing of 2nd generation C26M FeCrAl using the standard ramp rate LOCA procedures [36,27,30,18], adhering to the LOCA testing protocol delineated in Chapter 1. Burst data for 1st generation T35Y2 FeCrAl reported by Massey et al. [36] is also presented for comparison. Table 5 presents the measured compositions of the FeCrAl claddings, while Table 6 reports the cladding geometry for both C26M and T35Y2. C26M cladding samples were obtained from Heat #17025001, previously described and labeled as "C26M2" in other literature studies [92,99,74].

Post-burst, the claddings were cross-sectioned, mounted in epoxy, and polished with colloidal silica. Cross-sections were taken from the base of the tubes, where deformation was minimal, and the burst centerline [36]. A Tescan MIRA3 Scanning Electron Microscope (SEM) operating at 10 keV was employed to perform back-scatter electron (BSE) imaging on the cross-sections. Electron back-scatter diffraction (EBSD) maps of the base tube cross-sections were generated using the same Tescan SEM, operating at 30 kV. A Keyence model VR-3100 structured light scanning microscope was used to image the claddings and rupture opening. The burst opening length was determined as a straight line from end to end of the opening using ImageJ. Circumferential deformation, wall thickness, and oxide thickness were also measured using ImageJ.

In addition to burst testing, axial tensile tests were conducted on fresh C26M tube samples from room temperature (RT) to 800 ºC. This was done to compare with previous tensile data from the 1st generation FeCrAl alloys and burst criteria. Axial tube tensile specimens were created via wire electrical discharge machining (EDM) using a dual gauge design with a gauge length and width of 4 mm and 2 mm, respectively. Figure 33 shows a CAD rendering of the tensile rig and

Table 5. Chemical composition in weight % of FeCrAl alloys.

ALLOY	Fe	Cr	Al	Mo	Si	Y	Other
C26M **[98]**	82.26	13.15	4.44	<0.01	<0.01	0.012	0.002 C, <0.01 Nb
T35Y2 **[67]**	bal.	12.2	6.1	2.04	0.20	0.04	<0.01 C, <0.005 S

Table 6. Pre-transient geometry for C26M and T35Y2 [67] claddings.

ALLOY	Wall-thickness (mm)	Inner Diameter (mm)	Outer Diameter (mm)	Source
C26M	0.38	9.52	10.28	Present Study
T35Y2	0.385	8.73	9.50	Massey et al. [36]

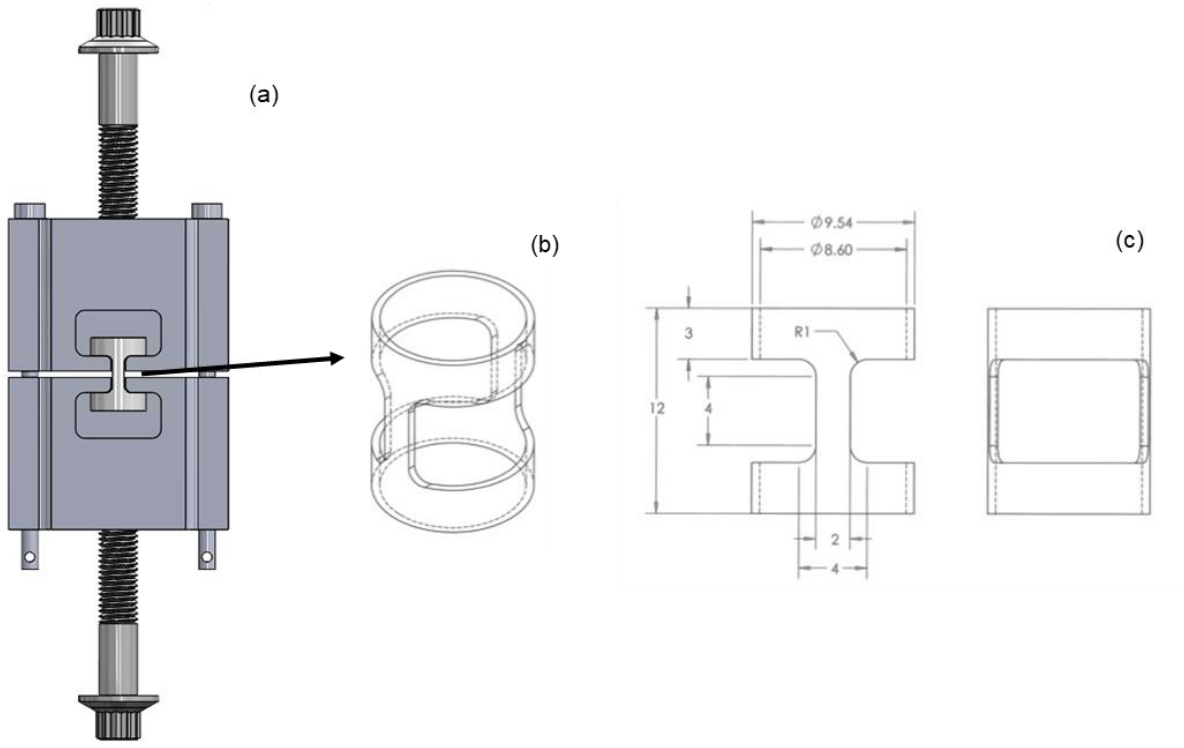

Figure 33. Shown above is a solid works rendering of the extensometer (a), an illustration of the tube specimen (b), and the dimension specifications of tube specimen (c) used for tensile testing in this study. The units of (c) are in mm.

technical diagrams of the axial tube specimens. All tests were performed in air using a strain rate of 10^{-3} s^{-1} after holding at the desired test temperature for 10 minutes to ensure temperature homogeneity. Results of similar axial tensile testing methods for Fe-based claddings can be found elsewhere [100,101].

Section 4.3: EXPERIMENTAL RESULTS

4.3.1: Burst behavior and tensile strength

Table 7 and Figure 34(a) present the burst engineering hoop stress and corresponding burst temperature for C26M, T35Y2, and Zry-2, represented in blue, green, and red, respectively. The empirical model based on burst data from Chapman [27,28], developed by Powers and Meyer [30] for Zircaloys, is shown in gray in Figure 34(a). See Chapter 1 for further details on the empirical model.

C26M demonstrated higher temperature resistance, withstanding ~200 ºC greater temperatures than Zry-2 and ~100 ºC higher than T35Y2. T35Y2, in turn, outperformed Zry-2 by ~100-150 ºC The Zry-2 burst data aligns well with Chapman's 5 ºC/s ramp rate curve, particularly at elevated temperatures. Due to ample material availability, Zry-2 underwent replicate testing that yielded a low spread of burst stress and pressures, indicating that the current burst testing is highly reproducible for Zry-2 assuming identical mechanical properties between samples.

Figure 34(b) illustrates the relationship between burst pressure and temperature. It is essential to differentiate between hoop stress and burst pressure, as nuclear-grade FeCrAl claddings are thinner than Zr claddings due to neutronic constraints [74,98,99] and will experience higher engineering hoop stresses at the same pressures. Nevertheless, burst pressure follows a trend similar to burst hoop stress. At identical internal pressures, C26M burst at temperatures ~150 ºC higher than Zry-2 and 100 ºC higher than T35Y2. In the absence of the strengthening additions found in C26M, T35Y2 outperformed Zry-2 at elevated temperatures but burst at similar pressures at lower temperatures. Table 8 presents the results of tensile testing from RT to 800 °C, while Figure 35 (a) and Figure 35(b) compare the ultimate tensile strength (UTS) and yield strength (YS) of C26M and T35Y2 [67], respectively. C26M exhibited higher UTS values across the entire temperature range. The YS of both FeCrAl alloys appears to overlap at approximately 700 ºC; however, this may be an artifact of the large gap in T35Y2 data between 550 and 750 ºC and the line connecting them.

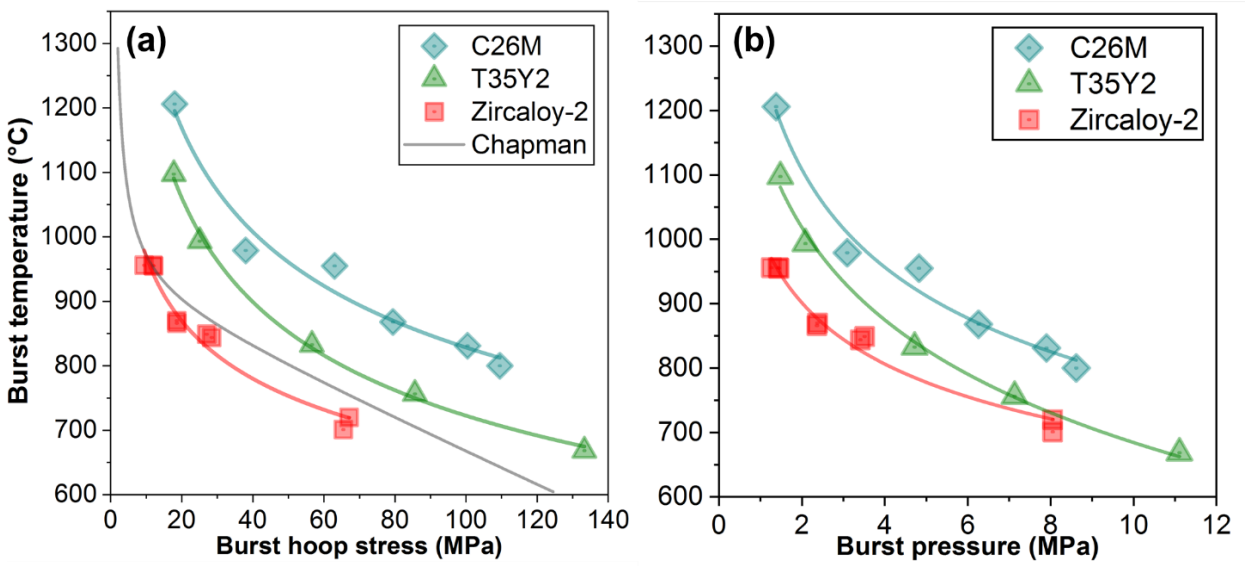

Figure 34. Burst temperature and burst engineering hoop stress curves for all test claddings are shown in (a). C26M is shown in blue, T35Y2 in green, and Zry-2 in red. A ramp-rate dependent model for Zircaloys by Powers and Meyer [30] using burst data collected by Chapman [27] is shown in grey. Figure 34(b) uses the same color scheme to represent burst temperature and burst pressure curves.

Table 7. Burst temperature and hoop stress data for all three materials. Burst hoop stress was calculated using burst pressure.

ALLOY	Burst Temperature (°C)	Burst hoop Stress (MPA)	Source
C26M	800	110	Present work
	831	100	
	868	80	
	955	63	
	979	38	
	1206	18	
T35Y2	668	132	Massey et al. [36]
	756	85	
	833	57	
	993	25	
	1097	18	
Zry-2	701	65	Present work
	720	67	
	844	28	
	849	27	
	866	19	
	870	19	
	955	12	
	956	12	

Table 8. Tensile data from C26M from tube geometry testing: yield strength (YS), elongation at yield (YE), ultimate tensile strength (UTS), uniform elongation (UE), and total elongation (TE). Commas separate values from different tests at the same temperature.

Temperature (°C)	YS (MPa)	YE (%)	UTS (MPa)	UE (%)	TE (%)
20	(542, 583)	(6.1, 6.5)	(773, 780)	(12, 13.3)	(22.1, 22.6)
200	(516, 531)	(5.7, 5.7)	(644, 653)	(10.5, 10.8)	(13.5, 13.7)
400	(452, 458)	(4.6, 4.8)	(603, 609)	(11.6, 12.5)	(14.4, 14.4)
500	(379, 394)	(4.3, 4.4)	(501, 501)	(12.0, 12.2)	(25.1, 33.1)
600	(178, 181)	(2.4, 3.9)	(245, 249)	(12.1, 12.2)	(65.1, 65.4)
700	(68, 80)	(1.5, 1.7)	(101, 115)	(13.1, 16.6)	(94.8, 96.1)
800	(39, 40)	(1.2, 1.3)	(44, 45)	(12.2, 15.6)	(92.9, 96.5)

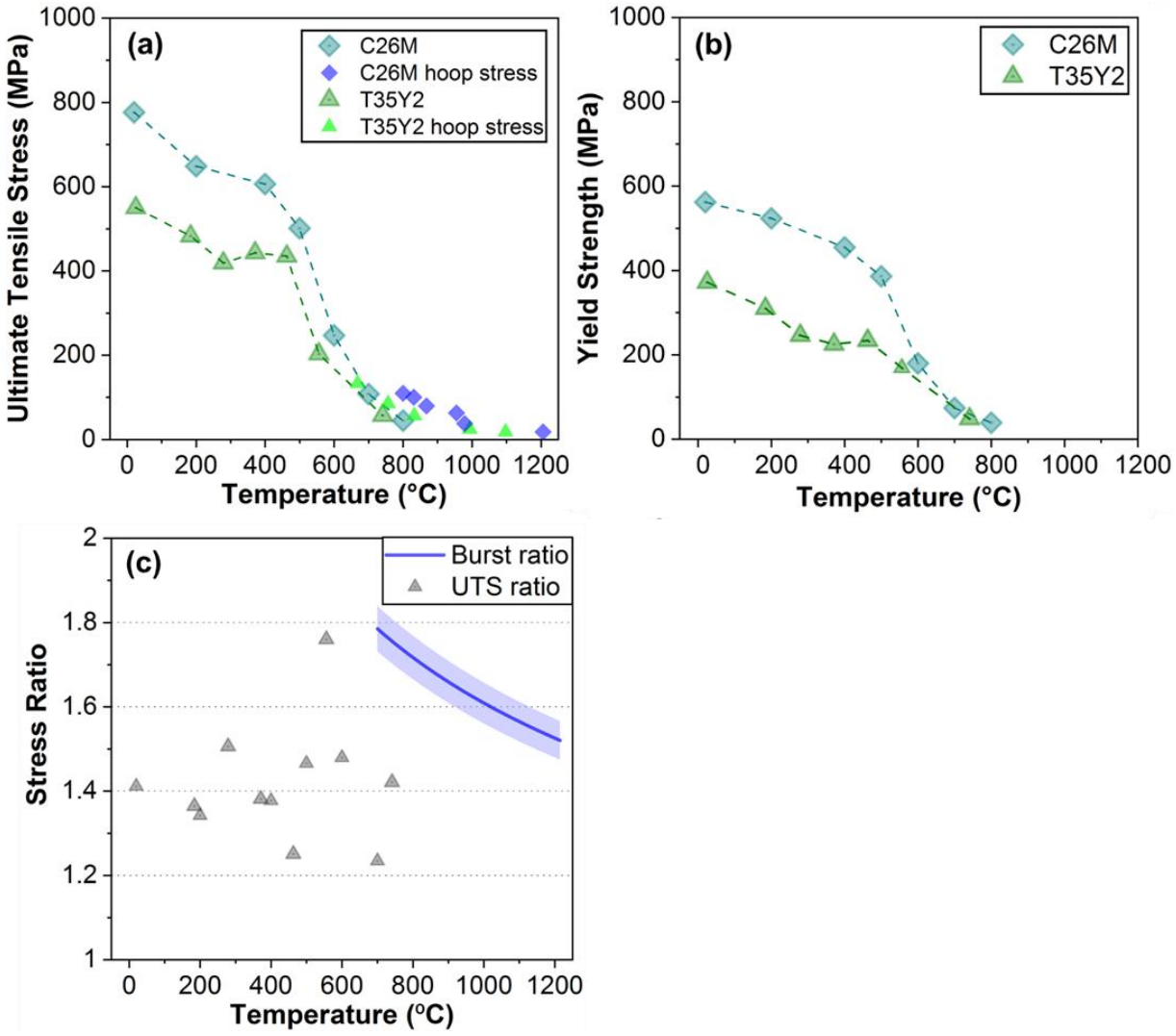

Figure 35. Ultimate tensile strength, (a), and yield strength, (b), vs temperature data for C26M and T35Y2. The C26M to T35Y2 ratio of UTS values is reported in (c), alongside the ratio of the burst curves from Figure 34 . Data points in Figure 35(a) and Figure 35(b) represent the averages of YS and UTS from Table 4. Since the tensile testing temperatures were not the same, the UTS ratio was calculated by comparing the C26M and T35Y2 data points to the interpolated curve of the other alloy. The burst ratio was determined by taking the ratio of the simple allometric fits shown in Figure 34(a). The shaded region around the burst ratio line indicates the authors' degree of confidence. In (a), the smaller blue diamonds and green triangles are burst hoop stress data from Figure 34(a) for C26M and T35Y2, respectively.

It is important to note that the C26M tensile testing was conducted on axial tube specimens. Ring geometry testing, which differs from axial tube geometry, could yield different results and may be more representative of cladding burst in the hoop direction.

Additionally, the C26M and T35Y2 samples were in the cold-drawn and annealed conditions, respectively. Cold-working effects might contribute to the relatively high tensile performance of C26M at lower temperatures. Recrystallization of the alloy could be promoted above ~700 ºC, resulting in reduced cold-work strengthening. This consideration is crucial when comparing tensile and burst data, as the lowest burst temperatures for 1st and 2nd generation FeCrAl are near ~700 ºC.

To compare the results of mechanical strength testing for the FeCrAl alloys, the C26M to T35Y2 ratio of the UTS curves, Figure 35(a), and the ratio of the burst curves, Figure 34, were determined and reported in Figure 35(c). Between RT and 700 ºC, the UTS ratio had a low value of 1.23 and a high of 1.76, with an average value of 1.41 ± 0.13. The burst ratio decreased from 1.79 at 700 ºC to 1.52 at 1200 ºC. While the temperature ranges of mechanical testing and burst do not overlap, the UTS and burst ratios are roughly consistent.

4.3.2: Microstructure characterization

The grain structure of the alloys was analyzed using EBSD maps generated for C26M and T35Y2, as shown in Figure 36 and Figure 37 , respectively. Cross sections at the ends of the full-length tubes were utilized for this analysis. Unlike the regions where burst occurred, which reached ~1200 °C, the ends of the tubes experienced temperatures of ~700°C. As such, these sections are not directly comparable to the burst region but still provide a comparison of microstructural effects.

C26M had an average grain size of 89 ± 52 μm from 51 grains, in line with reports from Gigax et al. [99]. T35Y2 had an average grain size of 45 ± 33 μm from 146 grains, consistent with a previous study [67]. These results indicate that T35Y2 samples possess smaller grains, on average, compared to C26M claddings ($t(64.62) = 5.66$, $p < 0.001$).

EBSD analysis revealed that both cross-sections of the alloys exhibit fully recrystallized grain structures, as evidenced by the negligible kernel average misorientation (KAM) gradients within each grain (Figure 36 and Figure 37). This suggests that extensive dislocation networks are not the reason for C26M's superior strength performance compared to T35Y2. However, some

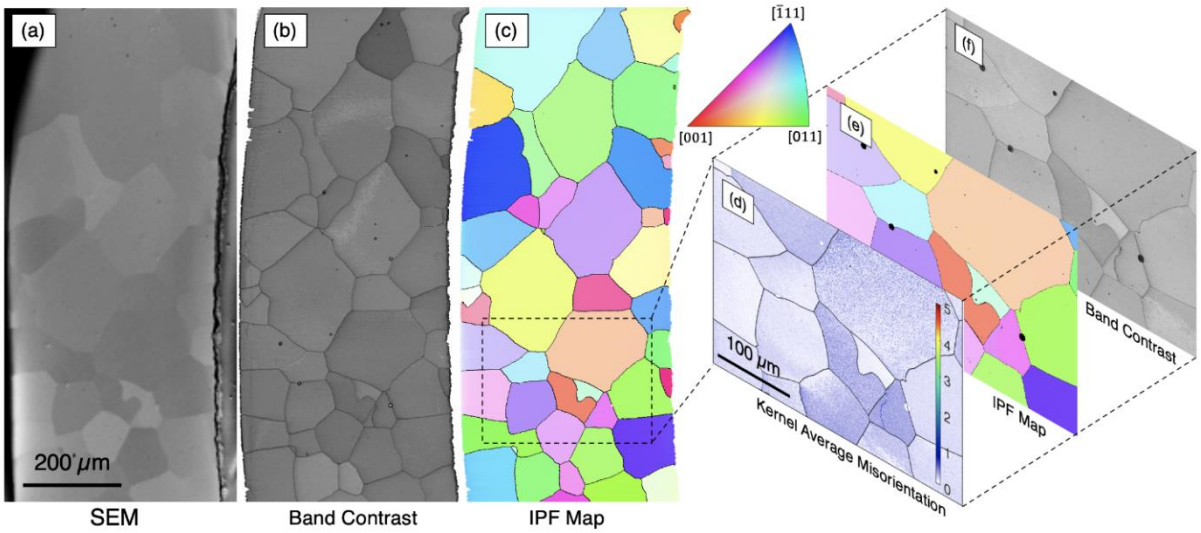

Figure 36. EBSD map of a C26M cladding cross-section. The sample was taken from the ends of the full-length tube, where temperature was much colder than the burst region. Figure 36(a) shows a SEM image, Figure 36(b) a band contrast image, and Figure 36(c) an inverse pole figure (IPF) map. Figure 36 (d)-(f) focuses on a smaller section of the cladding, and are a KAM map, IPF map, and a band contrast image.

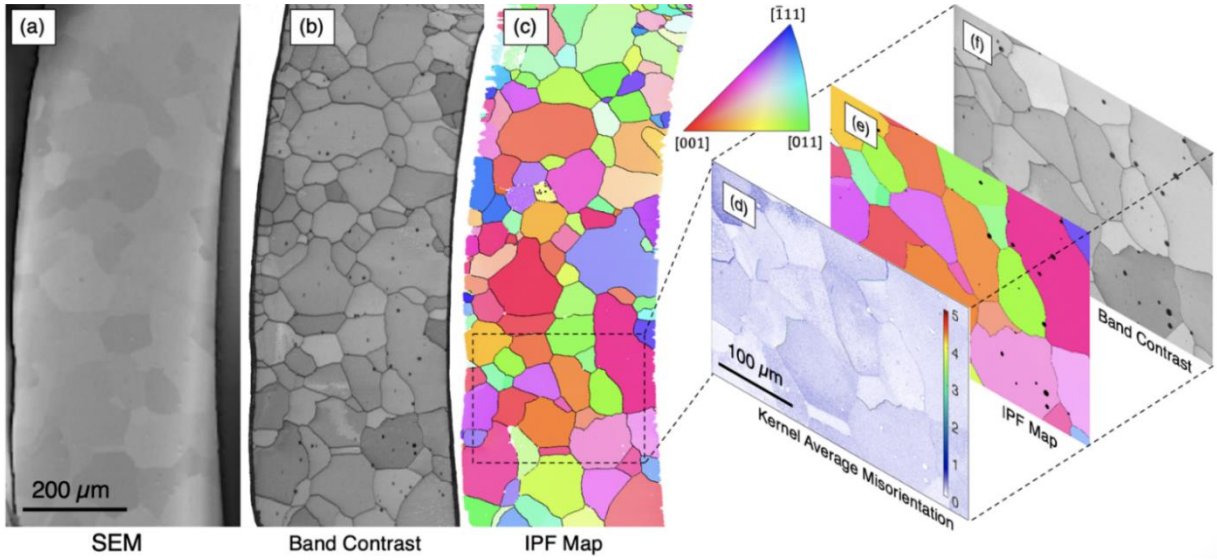

Figure 37. EBSD map of T35Y2 cross-section from the end of the full-length tube, where temperature was much colder than the burst region. Figure 37(a) shows a SEM image, Figure 37(b) a band contrast image, and Figure 37 (c) an inverse pole figure (IPF) map. Figure 37(d)-(f) focuses on a smaller section of the cladding, and are a KAM map, IPF map, and a band contrast image.

dislocations may have been annihilated during the LOCA testing. T35Y2 has smaller grains, implying that any Hall-Petch strengthening would favor it. Therefore, the improvements in high-temperature strength can be attributed to higher Al, Mo, and Si solid solution strengthening in C26M [67] .

4.3.3: Ex-situ Cladding deformation

Circumferential strain profiles along the axial direction are shown for burst claddings with C26M (blue) in Figure 38(a), T35Y2 (green) in Figure *38*(b), and Zry-2 (red) in Figure *38*(c). The area under the curve in the burst region was calculated to quantify the cladding expansion (CE) of the burst area. Integration was performed on 5 cm regions centered on the burst openings and is reported in units of percent strain-cm alongside their respective profiles Figure 38. FeCrAl alloys exhibited less ballooning than Zry-2 for all similar burst hoop stresses and temperatures.

Stitched cross-sectional optical micrographs of C26M and Zry-2 claddings that burst at 63 and 65 MPa, respectively, are displayed in Figure 39, in comparison to T35Y2 cross-sections in Figure 6 of Massey et al.'s previous testing [36]. C26M is shown in Figure 39(a) and Zry-2 in Figure *39*(b). The inner cross-sections were taken from the base of the tubes where deformation was minimal, and the outer cross-sections were taken from areas of approximately largest deformation. Wall thickness measurements were made along the burst cross-sections for both samples in Figure 39, as well as the available micrograph for T35Y2 [36]. Wall thinning was normalized to the undeformed wall thickness and is reported in Figure 40 against the fractional distance around the cross-section. The ends of the profiles, 0 and 1 fractional distance, each represent a burst tip and are given a 0 fractional wall-thickness. Due to significant zirconia formation during the 300 s hold at 1200 °C, an additional wall thickness strain line corrected for Zry-2 oxidation is presented. Metal consumption was accounted for by taking the thickness of the oxide layer at points around the cross-section and then using the Pilling-Bedworth ratio to compute the metal consumed. Steam oxidation rates of T35Y2 and C26M were low, and no correction was needed. This correction more accurately reflects the wall thickness strain immediately after burst.

The two FeCrAl curves in Figure 40 are starkly different in form from Zry-2. As Zry-2 deformation during LOCA transients is assumed to be dominated by creep [18,19,102], this could imply lower creep effects for both FeCrAl alloys. The FeCrAl curves showed rapid drops near the burst tips, i.e., the ends of the profile. Higher magnification SEM micrographs of the burst tips for

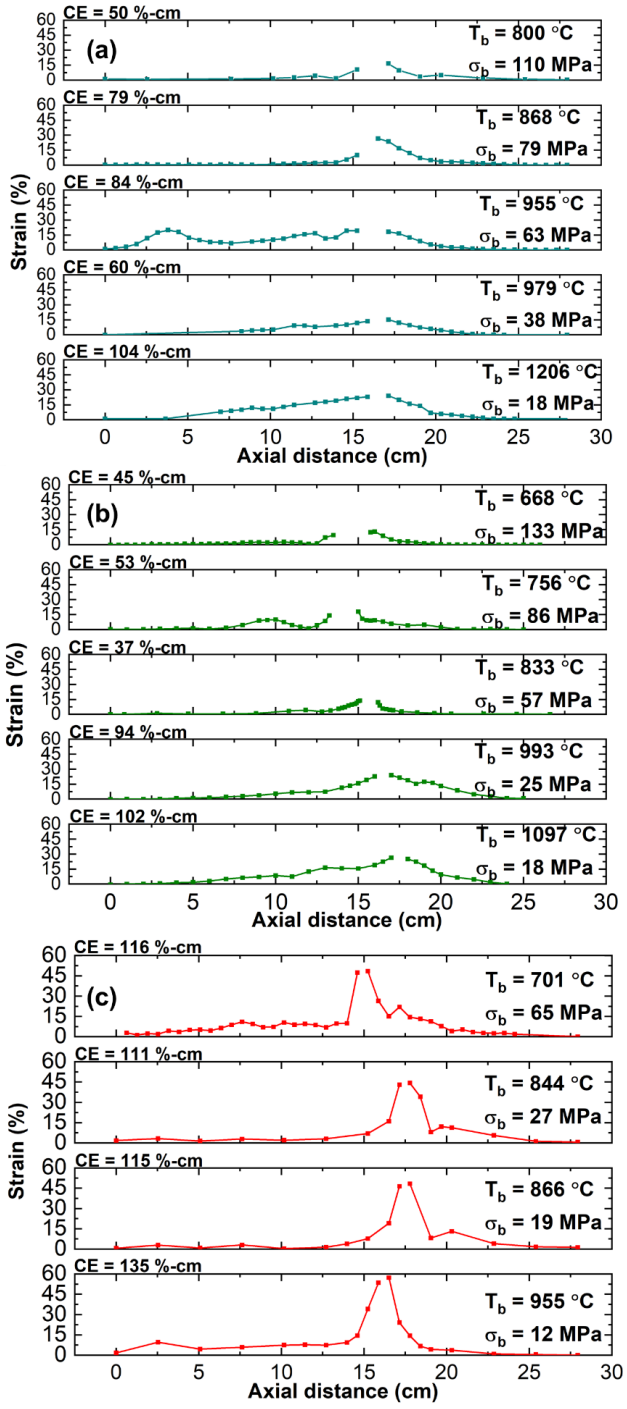

Figure 38. Ballooning profiles with circumferential strain vs. distance along the axial direction of burst claddings. C26M is shown in (a), T35Y2 in (b), and Zry-2 in (c). T_b represents the burst temperature and σ_b is burst hoop stress for the sample. Cladding expansion (CE) was computed using integration of the 5 cm region center on the burst area to quantify ballooning, and is presented in units of %-cm.

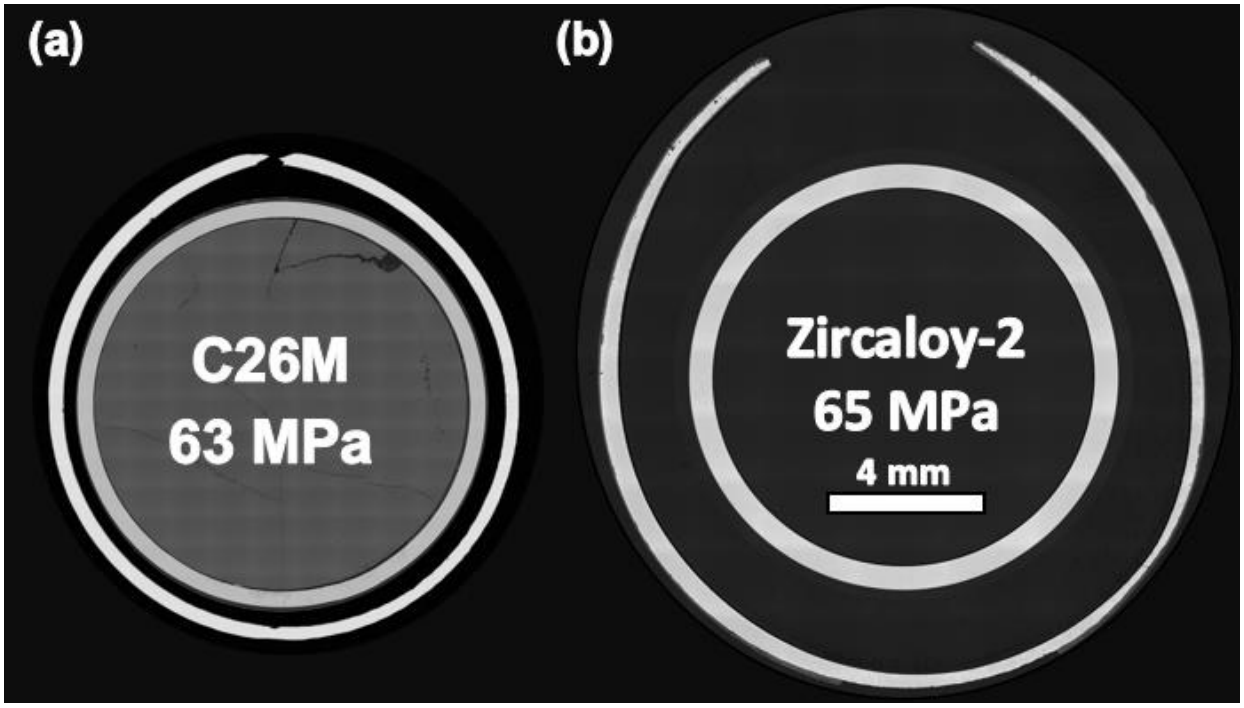

Figure 39. Optical macrographs of C26M and Zry-2 cross-sections from samples that burst at ~60 MPa hoop stress. The inner cross-sections are from regions away from the burst area, where minimal deformation occurred, and the outer cross-sections are from regions of approximately largest burst deformation. The grey region inside the cladding seen in (a) is the alumina filler rod that was not possible to remove post burst. A similar illustration for T35Y2 can be found in Figure 6(c) of Massey et al.'s previous manuscript [36].

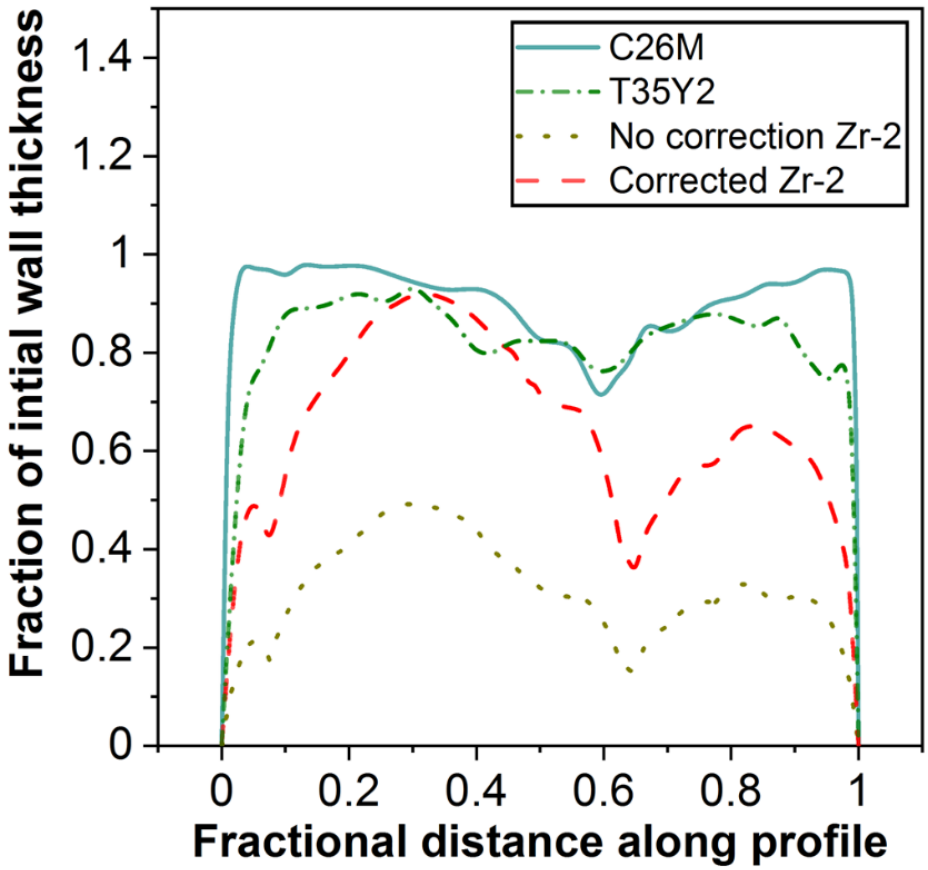

Figure 40. Curves illustrating wall-thinning for samples around ~60MPa burst hoop stress. C26M is shown in blue, T35Y2 shown in green, and the metal consumption corrected and raw Zry-2 wall-thickness shown in red and gold respectively. The metal loss correction was applied to Zry-2 to get a notion of thinning before extensive oxidation. Deformation occurred before Zr corrosion in steam would be significant, as the sample burst at ~750 ºC.

all three claddings are shown in Figure 41. The rapidly narrowing ends on the two FeCrAl alloys, Figure 41(a) and Figure 41(b), visually indicates ductile overload, reminiscent of necking failure in uniaxial tensile testing [103,104]. The ends of Zr claddings, Figure 41(c), were embrittled and oxidized and tended to break off after testing, evidenced by the unoxidized cladding near the tip. In order to study the fracture surface properly, the experiment should be stopped after burst to avoid the 1200°C isotherm steam oxidation.

The reduced steam oxidation kinetics of FeCrAl alloys is qualitatively shown in Figure 41. C26M oxide scales were ~0.5-1 μm thick, while T35Y2 oxides scales had a thickness ranging from ~2-6 μm. The differences between 1st and 2nd generation FeCrAl oxide thickness is not expected based on previous steam oxidation testing [105]. Other factors such as surface roughness could contribute to thicker than predicted oxides. Regardless, Zry-2 claddings had significantly larger oxide scales than both FeCrAl alloys with thicknesses 54 ± 1 μm.

4.3.4: Burst opening characterization

Critical to fuel retention, the relationship between burst opening area and burst engineering hoop stress for C26M, T35Y2, and Zry-2 is shown in Figure 42(a), and opening length is also plotted against burst hoop stress in Figure *42*(b). At all similar hoop stresses, C26M burst area was smaller than T35Y2 and Zry-2. For C26M (blue), burst area remained relatively constant up to ~100 MPa, above which burst area rapidly increased. To illustrate this transition, openings for C26M claddings that burst at 80, 100, and 110 MPa are shown in Figure 43. Images showing a similar transition for T35Y2 at lower hoop stresses was reported by Massey et al. [36]. In Figure 42(a), a data point is missing for T35Y2 at ~57 MPa (burst area was not determined prior to cladding sectioning). However, looking at the cross sections reported by Massey et al. [36], the transition to large openings occurred at hoop stresses ≤ 57 MPa for T35Y2, which is significantly lower than the ~100 MPa transition for C26M.

Opening length follows a similar trend to area for C26M, seen in Figure 42(b), except that the length appears to initiate a rapid increase around ~80 MPa hoop stress, compared to the burst area increase observed after ~100 MPa. Similar to burst area, T35Y2 transitioned to larger opening lengths at lower hoop stresses than C26M.

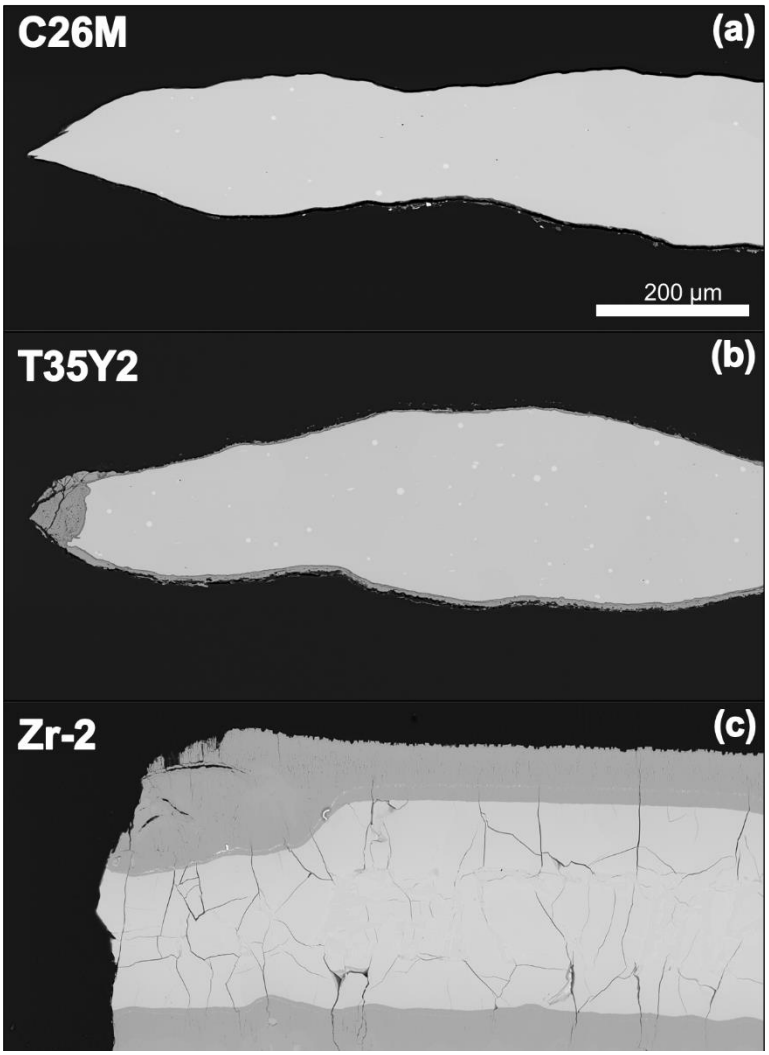

Figure 41. BSE micrographs of the burst tips for the ~60 MPa burst hoop stress samples. C26M shown in (a), T35Y2 shown in (b), and Zry-2 shown in (c).

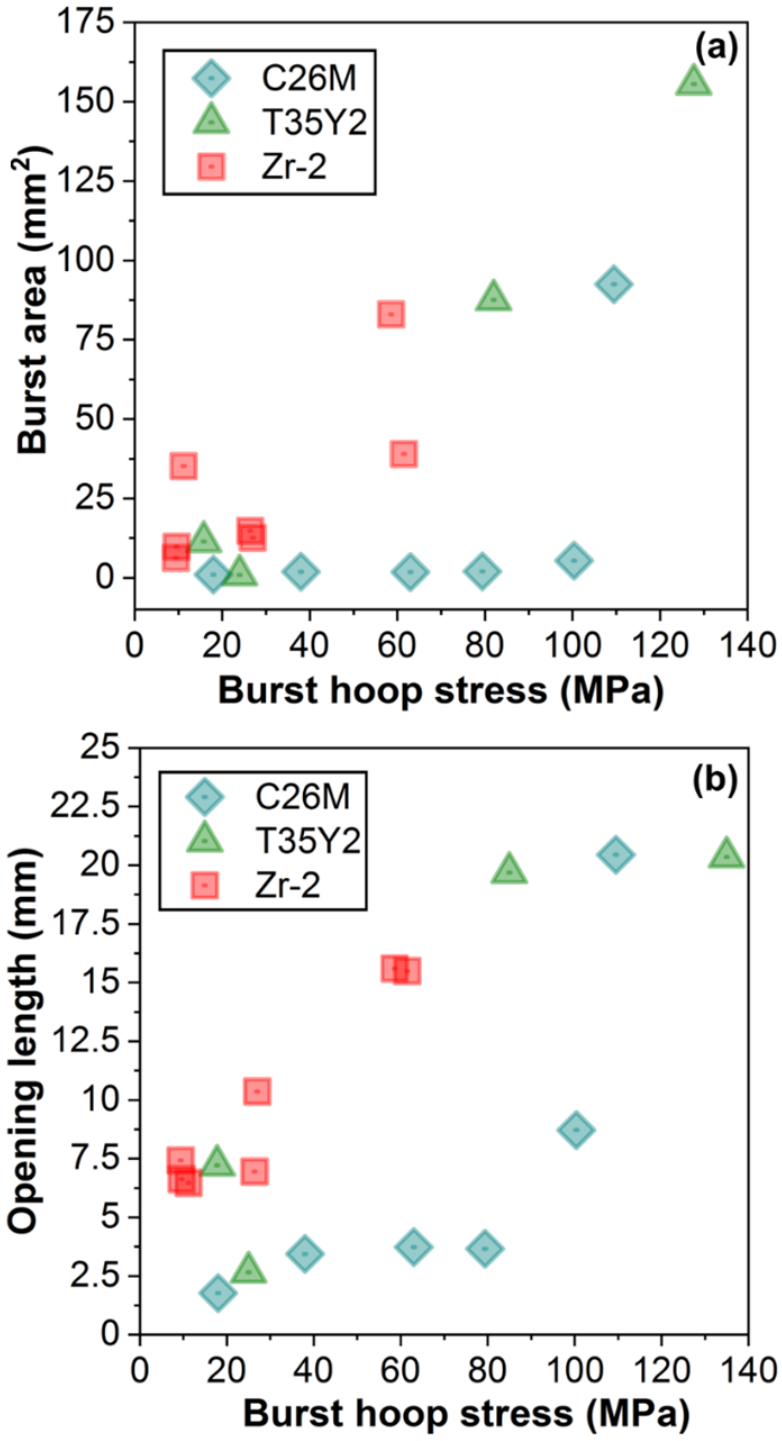

Figure 42. Burst area vs hoop stress for all claddings tested is shown in (a) and burst opening length vs hoop stress is shown in (b). C26M is shown in blue, T35Y2 in green, and Zry-2 in red.

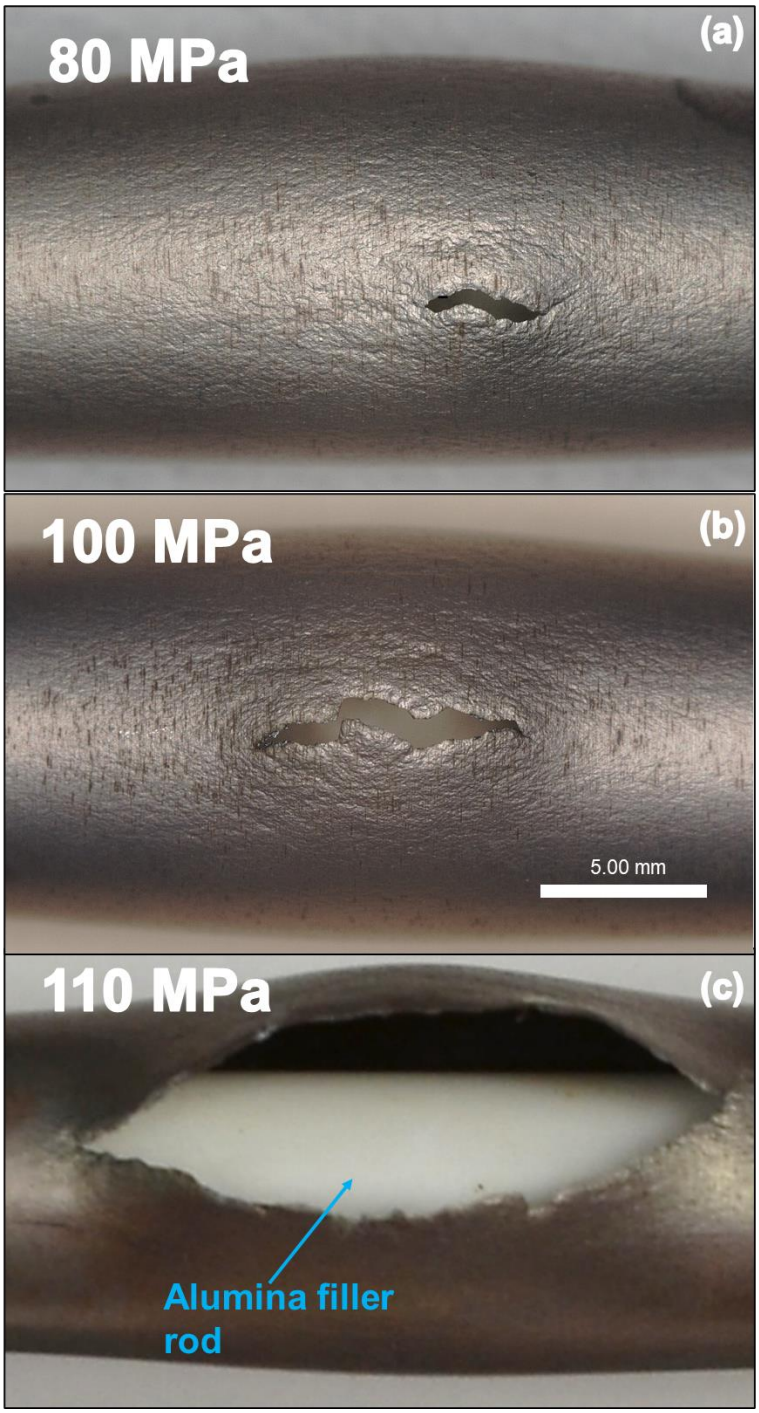

Figure 43. Images of C26M claddings that burst at 80, 100, and 110 MPa hoop stress illustrating the development of the opening and transition in burst area ~100 MPa.

Replicate testing of Zry-2 yielded a wide spread of burst openings, with an approximately linear correlation (R^2 = 0.548) between hoop stress and burst area, Figure 42(a). Opening length of Zry-2 exhibited much lower scattering that increased linearly with hoop stress (R^2 = 0.920), Figure 42(b). This discrepancy indicates the association of, but not direct relationship between characteristics of burst opening geometry.

Section 4.4: DISCUSSION

4.4.1: Conventional burst characterization

C26M exhibited significantly higher burst temperatures for a given hoop stress, ~100 ºC greater than T35Y2 and ~200 ºC higher than Zry-2. However, comparing these materials based on burst pressure is more appropriate due to dimensional differences. Even so, for a given burst pressure, C26M improved burst temperatures by a smaller yet substantial margin, as shown in Figure 34. Considering the comparable grain sizes and microstructures between the FeCrAl generations depicted in Figure 36 and Figure 37, the strengthening of C26M is likely attributable to compositional changes, such as the addition of Al, Mo, and Si.

C26M also exhibited lower maximum diametric strains, indicating reduced localized ballooning compared to Zry-2. However, when assessing a global measure of ballooning, such as the CE displayed in Figure 38, the total deformation of the claddings appears more comparable. Nevertheless, increased localized ballooning is undesirable due to considerations like fuel relocation and potential direct blockage of coolant supply.

4.4.2: Proposed mechanisms of rupture formation, dynamics, and relation to tensile properties

Understanding the transition from small to large burst openings could be integral to assessing fuel dispersal and coolant blockage risks of FeCrAl. Three distinct deformation mechanisms occur during burst. First, critical burst hoop stresses are reached, and plastic instability begins, causing localized necking and failure, directly resulting in the initial burst opening. Second, at this instantaneous point of failure, tips of the opening would experience a concentrated stress from the internal pressure, similar to a pre-existing crack.

If the temperature dependent fracture toughness is exceeded, the opening would continually propagate outwards, leading to larger burst lengths. Between 80 MPa and 100 MPa hoop stress for C26M, Figure 42(b) and Figure 43, fast fracture began but the crack was arrested

before significant deformation occurred. Therefore, fast fracture occurs before the burst area transition after ~100 MPa. The initiation, propagation, and arrest of the opening could be similar to that described by Hahn et al. [106] or Maxey et al. [107] for pre-existing cracks in pressurized cylinders. Hahn et al. [106] determined extension criteria for high and low to medium toughness materials. Both descriptions were related to flow stress.

For the third deformation mechanism, residual pressure and escaping gas applies a stress on the burst edges, bending them if yield conditions are met. Significant bending of burst edges has been noted in other pipe fracture scenarios [108–110]. If the edges bend outward enough, the opening area increases allowing for rapid decompression. Ives et al. [111] noted sudden decompression and rapid bending of the burst edges after a certain crack length was achieved in running ductile fracture testing. The second and third mechanisms happen at the same time as well as affect each other. Folias [108] demonstrated that the driving force at the crack tip in pressurized cylinders is influenced by the bending of the edges.

Reasonable similarity of the UTS ratio, 1.41 ± 0.13 from Figure 35(c), and the burst hoop stress ratio, ~1.52-1.79, indicates a connection between tensile parameters and burst criteria in LOCA transients for wrought Fe-based alloys, as described by Massey et al. [36]. Therefore, tensile data may be a suitable predictor for burst strength for FeCrAl alloys, even at temperatures where creep contributions could become significant. Additionally, the T35Y2 small-to-large opening transition is reasonably assumed to occur at ~57 MPa, while the C26M threshold stress is ~100 MPa. Higher tensile strength is associated with a higher burst area transition stress, indicating uniaxial tensile strength could also be a reliable proxy for predicting the small-to-large opening transitions and relative potential for fuel dispersal of FeCrAl claddings during a LOCA. Unfortunately, this data set is limited because only a limited number of candidate compositions were fabricated into cladding. Barring significant microstructure influences, uniaxial strength may be a potential proxy to consider when predicting burst opening geometry and fuel dispersal risks in LOCA scenarios.

There are undoubtably important parameters not accounted for in this study of wrought FeCrAl that could affect burst strength and opening characteristics such as the irradiation dose and microstructure. A comparison of FeCrAl variants with drastically different microstructures, such as higher strength ODS FeCrAl [112], would be useful.

4.4.3: Impacts of thermal gradients, microstructure, and irradiation

The effects of the thermal gradient within the IR furnace should be considered, as temperature differences could impact ballooning and burst [29]. As stated in the experimental section, four thermocouples spanning the center ~10 cm of the cladding specimen were used. Examples of gradients present during testing are reported for C26M burst at 100 and 38 MPa in Figure 44(a) and Figure 44(b), respectively, and are representative of the general range of gradients for a SATS test.

The thermal gradients for two Zry-2 samples that both burst at 19 MPa and ~870 ºC are also shown in Figure 44(c) and Figure 44(d) to compare gradient effects on burst conditions. For all burst tests, the 300-1200 ºC ramp corresponded to the highest temperature differences. Evidence of circumferential thermal gradients were present in wall-thinning measurements in Figure 40, around ~0.6 of the fractional profile. The thinning of all three samples at this point could indicate a competing location for failure.

At first glance the reported gradients would be anticipated to result in inconsistent burst temperatures/pressures. However, the replicate testing of Zry-2 (Figure 34) yielded highly reproducible burst data. Therefore, while varying thermal gradients are present during testing, they appear to have limited effect on burst pressure and temperature for that material. Future work will be specifically aimed at measuring cladding thermal gradients and assessing the impact on burst geometry.

Microstructural differences between alloys could promote a change in the strength ratio and burst area transition relationships discussed above. Features such as grain size, grain shape, and the presence of precipitates would impact the mechanical response at high temperature, especially in relation to creep and grain boundary decohesion. This could drastically change relative burst strength reflected in conventional comparisons like engineering hoop stress using pre-transient geometry, Figure 34(a). Processing routes could also create a grain shape that allows for easier extension of the initial opening, i.e., the second mode above. Therefore, while tensile data could be useful for assessing burst strength and predicting rupture geometry, microstructure differences could play an important role. The analysis in the present study was conducted for alloys that exhibited similar microstructure form, Figure 36 and Figure 37. Uniaxial strength and its

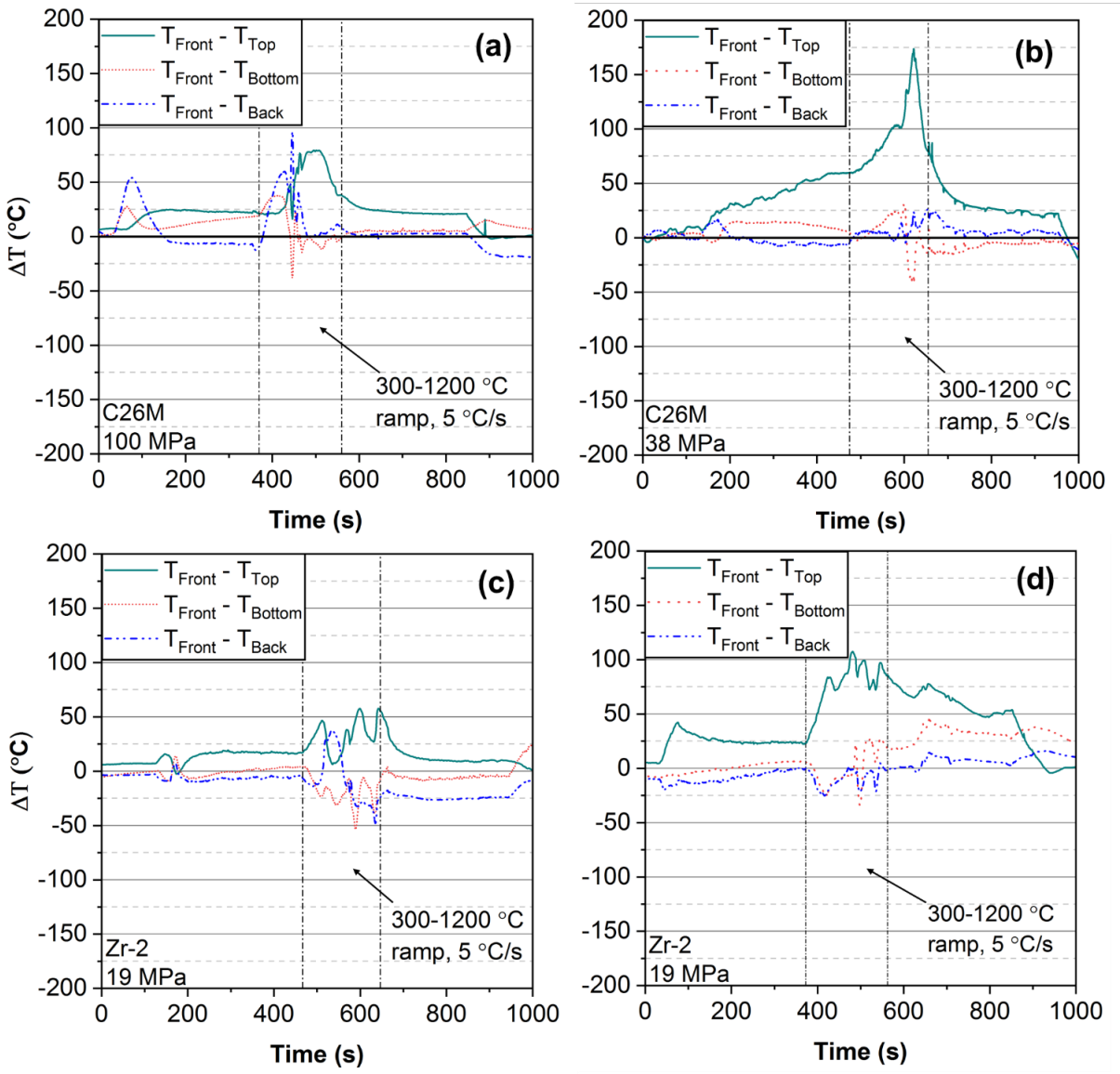

Figure 44. Thermal gradients during burst testing of C26M for a burst hoop stress of (a) 100 MPa, and (b) 38 MPa, measured across the four thermocouples. The thermal gradients for two Zry-2 samples that burst at 19 MPa and ~870 °C are shown in (c) and (d). For all gradients, the thermocouple reading is subtracted from the center-front thermocouple reading. T_{Front} represents the temperature reading from the center-front thermocouple, T_{Back} represents the temperature reading from the center-back thermocouple, T_{Top} is the temperature reading from the top thermocouple, 5 cm from the center, and T_{Bottom} is the temperature reading from the bottom thermocouple also 5 cm from the center, where both T_{Top} and T_{Bottom} are situated on the frontside of the cladding.

relation to burst criteria and the small-to-large opening transitions is valid only for these alloys. Again, an extensive effort would be needed to fabricate cladding with different microstructures to study this issue.

Finally, the samples in this chapter were in the un-irradiated condition. Irradiation hardening effects in FeCrAl alloys is related to dislocation network formation and precipitation, with the degree of hardening dependent on dose, composition, and initial microstructure [113]. Irradiations of C26M cladding in commercial reactors have been completed and other trials are in progress. Post irradiation burst testing may be possible. It is possible that FeCrAl claddings could be irradiated to the point where the ductile failure modes above are irrelevant and uniaxial strength is no longer a suitable proxy for opening characteristics. This is especially important to consider, as fuel dispersal concerns are related to extended service and high burnups.

4.4.4: Proposed benefits from an in-situ burst framework for modeling campaigns

The opening dynamics described above could be further explored using *in-situ* data. As detailed in Chapter 2, Joshi et al. [74] observed similar discrepancies in opening size from *in-situ* creep testing. They noticed the formation of "pinhole" and "direct open up" ruptures correlated with the position of the data point in relation to the general Monkman-Grant relation trend during their C26M testing. Pinhole openings were associated with lower strain rates for a given rupture time, appearing to the left of the trend line, while direct open-up ruptures formed at higher strain rates.

The transition from small to large openings shown in this work was linked with higher stresses, and possibly greater strain rates. Consequently, strain and strain-rate measurements from DIC near the rupture opening might give insight to this phenomenon, which is evident across both creep and transient burst testing. *In-situ* data could be instrumental in understanding the conditions that facilitate larger openings, thereby addressing concerns regarding fuel dispersal. Moreover, DIC data could contribute significantly to modeling and understanding the ballooning process leading up to rupture. Sweet et al. [114] recently utilized the BISON framework to model the burst behavior of C26M, comparing the results with the testing outlined in this chapter. Creep data for C26M was not available, so models for a previous iterations of 2nd generation alloys were used as inputs. This is a reasonable assumption given the similar alloy composition and the expectation that creep deformation will not be significant until higher temperatures. Material failure and

plasticity behavior were defined using the tensile data of C26M described in this chapter. Plasticity models were implemented by interpolating between stress-strain curves at testing temperatures and extrapolating beyond 800 °C.

The initial model underpredicted the burst temperature and hoop stress. This suggested that softening and microstructural effects might have influenced the higher temperature tensile tests (700 and 800 °C) due to the 10-minute hold for temperature homogeneity. As a result, testing was repeated at 700 and 800 °C with loading initiated as soon as the target temperature was reached.

Figure 45 displays the plastic portion of the C26M tensile curves presenting the initial testing with a 10 min hold in solid lines and the new 700 and 800 °C tests in dashed lines. A comparison of the plastic sections reveals a significant effect on strength (particularly for the 800 °C test) and ductility (especially for the 700 °C test) when the test was initiated upon reaching the target temperature. This high-temperature plasticity data is crucial for modeling LOCA performance, as behavior was extrapolated past these points. Substituting these tensile tests profoundly impacted the predicted burst criteria, demonstrated by Figure 46.

This data is presented to emphasize two key points: (1) ensuring the model inputs accurately represents the material condition, and (2) the possible efficacy of standard mechanical testing and plasticity models in predicting burst behavior for wrought FeCrAl. Sweet et al.'s modeling effort underscores the need to account for the influence of LOCA transients on microstructural behavior and high-lights the nuance required when applying tensile data to burst scenarios. This principle is not exclusive to the FeCrAl system; it likely also applies to other cladding materials such as Zr alloys and coated systems. While these predictions of failure were accurate, no *in-situ* transient burst testing data has been collected for comparison against plasticity and creep-based strain predictions for C26M.

Burst testing of C26M FeCrAl with the application of *in-situ* DIC techniques would yield *in-situ* strain data for comparison against models generated from tensile testing and creep data. While a complete test matrix is not presented in this dissertation, an *in-situ* framework has explicit value for validating the use of conventional mechanical testing to model wrought FeCrAl burst behavior.

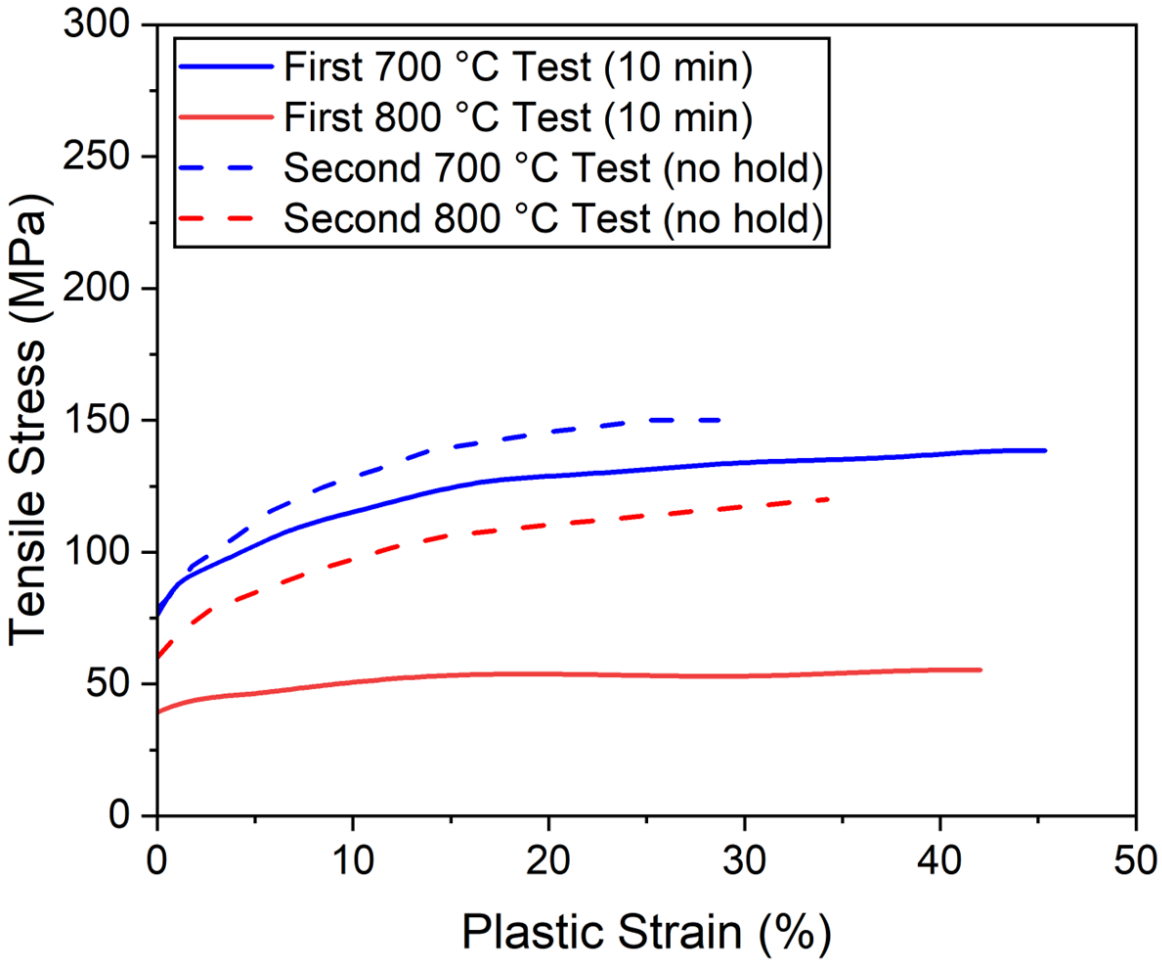

Figure 45. Plastic portions of the uniaxial tensile testing at 700 and 800 °C where samples were held for 10 min at temperature prior to starting the test (solid lines) and updated curves at 700 and 800 °C curves where the tensile test was initiated once reaching temperature (dashed lines). The samples were loaded in uniaxial tension along the axial direction using the dual gauge geometry described in this chapter. Data generated by Caleb Massey and reported by Sweet et al. [114]. The author of this dissertation was a co-author for this work.

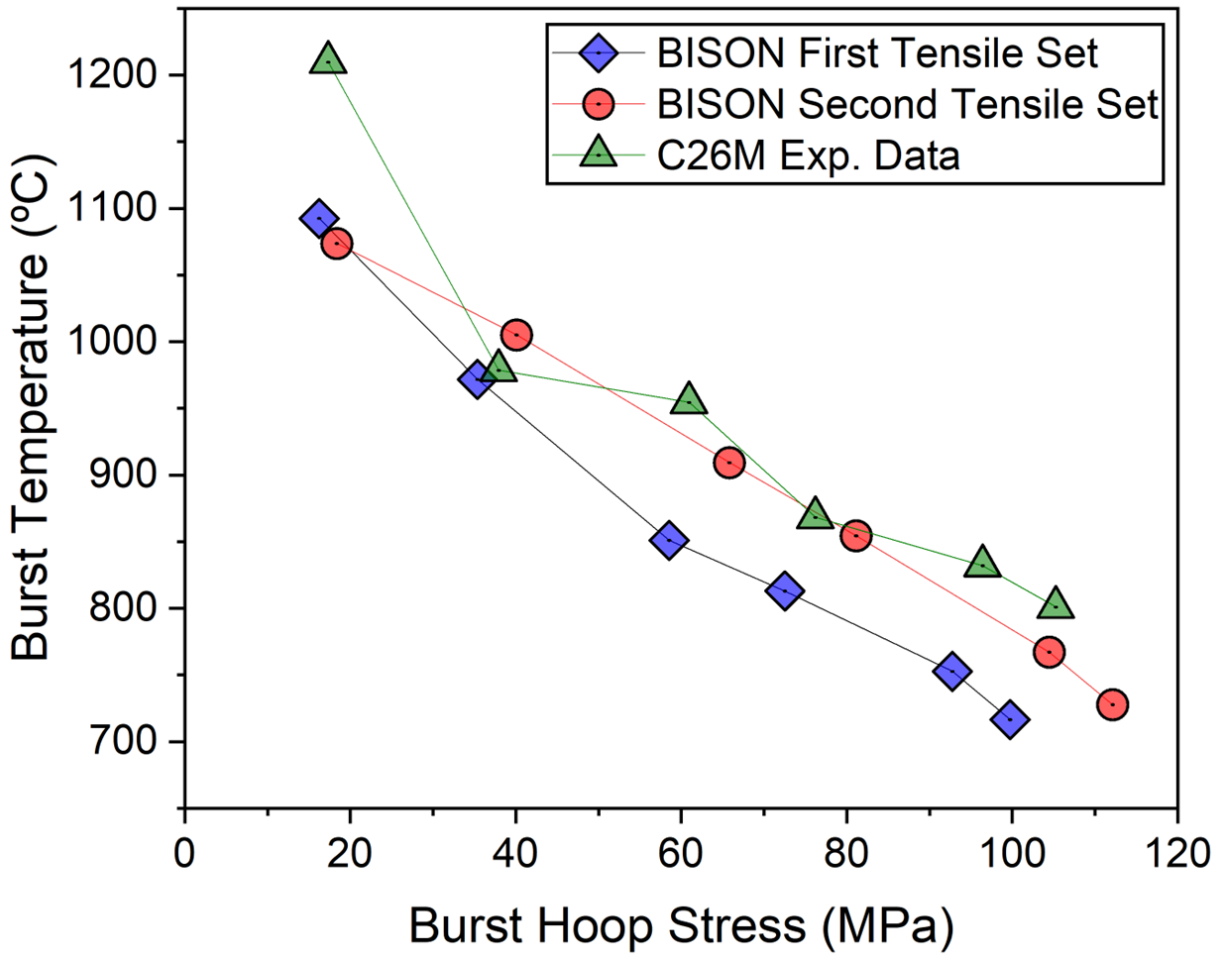

Figure 46. Sweet et al.'s [114] burst criteria predictions using the tensile data where all samples were held for 10 min at temperature prior to initiating the tensile tests and updated predictions with the 700 and 800 °C tests where testing was started immediately after reaching temperature. Burst hoop stress represents the hoop stress portion of the biaxial stress at failure. Modeling data produced by Ryan Sweet and replotted here.

Section 4.5: CONCLUSIONS

Burst testing under standard simulated LOCA conditions, at a heating rate of 5 ºC/s, was conducted on un-irradiated second generation (C26M) FeCrAl and Zry-2 claddings. This testing was compared to previously reported first generation FeCrAl (T35Y2). FeCrAl alloys displayed significantly less ballooning during testing compared to Zry-2, indicating a lower potential for coolant blockage. As expected, C26M burst at significantly higher temperatures, ~100 C greater compared to T35Y2 and ~200 °C higher than Zry-2. C26M also demonstrated preferable burst opening behavior compared to Zry-2 and T35Y2 in terms of opening area and length, with minimal values for both until higher hoop stresses. Both FeCrAl alloys exhibited a threshold hoop stress that differentiated between small and large burst openings. The ratio of these threshold stresses (~1.52-1.79) closely aligns with the ratio of UTS (~1.41 ±0.13). Barring significant microstructure influences, uniaxial strength is thus a potential proxy to consider when predicting burst opening geometry and fuel dispersal risks in LOCA scenarios.

The discussion also established the motivation for integrating *in-situ* strain measurements into burst testing. This *in-situ* framework could explore observations from *ex-situ* testing of FeCrAl. Specifically, strain and strain rate data could offer insight into the small or large openings demonstrated in both transient LOCA and creep testing. An opportunity was also identified for *in-situ* strain data to further validate models that have been successful in predicting burst criteria using tensile data. Thus, the value of an *in-situ* framework is affirmed, and the potential for accelerating qualification of ATF claddings is established.

Chapter 5: LOCA Modeling Gaps in Zr alloys and High Burn-up Concerns

Chapter Foreword

The major goal of developing the in-situ framework was to expedite the qualification process of new ATF cladding materials. However, initial testing of current Zr alloys is pertinent for two main reasons: (1) the extensive testing database and deployment of these incumbent claddings and (2) existing modeling gaps associated with Zr alloys in the α phase, which is relevant for safety analysis involving high-burnup extension. Before discussing testing of Zr alloys, it is essential to understand the current and historical models of LOCA behavior.

The reasons for improving Zr alloy modeling in relation to higher burnup conditions and fuel fragmentation, relocation, and dispersal (FFRD) are outlined in this chapter. Conventional descriptions of Zr alloy LOCA burst behavior are detailed, specifically in the α phase, and the modeling input into the BISON finite element code is reviewed. BISON modeling is the reference frame for this work given the developing role of the code in current research efforts. The inaccuracies present are exposed, and misrepresentation of anisotropy is posited. The discussion thus prepares the stage for a deeper investigation into Zr alloys and the mechanisms of deformation during a LOCA test.

Section 5.1: High burnup extension and Zr LOCA behavior

The nuclear industry is working towards raising peak average burnup levels from the current limit of 62 GWd/MTU to over 75 GWd/MTU [34], in order to extend fuel cycles and enhance economic efficiency. However, this objective also poses potential safety challenges. As burnup levels increase, fuel pellets are further degraded due to irradiation damage. This degradation could potentially lead to severe fragmentation, or even pulverization, of the fuel during a LOCA [115]. The fragmented fuel may relocate within the cladding during a LOCA, exacerbating the severity of the accident. Furthermore, these fragments could be ejected during post-rupture decompression, spreading radioactive material throughout the reactor systems. Therefore, with the push for higher burnup levels, it is crucial for the industry to manage these risks, ensuring reactor safety remains paramount.

In late 2021, the U.S. NRC issued a research interpretation letter (RIL) [116], drawing attention to the criticality of understanding FFRD risks. The specific areas highlighted by the NRC RIL included:

(1) Empirical thresholds for fine fragmentation of fuel pellets
(2) Local cladding strain thresholds below which fuel relocation is minimized
(3) Examination of the mass of dispersible fuel as a function of burnup
(4) Evidence of significant transient fission gas release (tFGR) during LOCA conditions that would impact cladding burst behavior
(5) Establishing a range of packing fraction for non-dispersed fuel in the balloon region

Improving models for incumbent Zr alloys is imperative, given that many of the FFRD concerns are associated with cladding behavior. Most characterization efforts for Zircaloys have focused on behavior in the α + β and β phase regions (above ~810 °C), given historic burnup levels and the 1204 °C limit in U.S. NRC regulation 10. §50.46. With higher average burnup fuel pellets, the resulting higher internal pressure and contribution from tFGR could result in cladding failure in the α phase region. Consequently, recent burst testing efforts have been dedicated to developing higher fidelity models in the α phase under high-burnup LOCA conditions.

Traditional LOCA models for Zr alloys [18,102,19] assume that steady-state creep is the principal factor influencing deformation, i.e., rely on creep descriptions where strain rate stabilizes at a minimum value under constant conditions. However, LOCAs are inherently dynamic, not reflective of steady-state conditions. Seminal developers of the steady-state model noted this gap [18,117], citing their model's lack of consideration for primary and tertiary creep, as well as non-creep, time-independent plasticity. Recent attempts to incorporate these elements encountered convergence issues [118]. As a result, current efforts still fully rely on creep assumptions.

The steady-state creep behavior of Zr alloys can be described by the Five Power Law (FPL) for class M alloys. The general phenomenological form of the FPL steady-state creep is presented by Eq. 5,

$$\frac{d}{dt}\varepsilon_{ss} = A_0\sigma^n \exp\left(-\frac{Q}{RT}\right), \quad (5)$$

where A_o is the structure coefficient, σ is the applied stress, n is the stress exponent, Q is the activation energy, R is the universal gas constant, and T is absolute temperature. This equation represents the simplest form of the FPL, excluding considerations for grain size, modulus normalization, threshold stress, and so forth. Three FPL models are common in LOCA modeling: (1) the default Erbacher model [18], (2) the Kaddour model [119], and (3) the Donaldson model [120]. Each will be discussed; however, the Erbacher model will be examined in greater detail due to historic relevance and standard use in modeling efforts.

For operational conditions, two distinct creep correlations are implemented in BISON modules: (1) the Hayes and Kassner model [121], which accounts for secondary thermal creep , and (2) the Limback-Anderson model [122] that incorporates expressions for primary and secondary creep as well as irradiation induced creep. To simulate a LOCA, the Limback-Andersson model [122] is used for creep rates below 700 K. One of the high-temperature creep models, detailed subsequently, is implemented past 900 K. An interpolation of the Limback-Andersson model [122] and the high-temperature model is used for temperatures between 700 and 900 K.

Section 5.2: Historic and Contemporary Zr LOCA Models

5.2.1: Erbacher model and anisotropy considerations

The Erbacher model, presented in Table 9, consolidates test results from multiple sources [18,32,117,123]. Rosinger et al. [123] conducted isothermal axial creep testing on cladding, applying a constant load in the axial direction for temperatures ranging from 667 to 1600 °C and stresses from 0.9-100 MPa. While not directly stated, other authors [117] denote that Rosinger et al. [123] tested RXA Zry-4. The exact heat treatment is unknown. Rosinger et al.'s testing concluded either after 10 minutes had passed or once a 15% strain had been achieved.

The structure coefficient, A, derived for the axial direction can be utilized to calculate the equivalent value for the hoop direction using Eq. 6 [124],

$$A_\theta = \left(\frac{F+G}{4} + H\right)^{\frac{n-1}{2}} (0.5F + H)(F + G)^{\frac{-(n+1)}{2}} A_z, \quad (6)$$

where A_θ is the structure coefficient in the hoop direction, A_z is the structure coefficient in the axial direction, n is the stress exponent, and G, H, and F are the Hill parameters. Hence, knowledge

Table 9. BISON model parameters for LOCA strain calculations for the α, α +β, and β phases [125].

Zircaloy Phase	Creep Rate Regime	A (MPa^{-n} s^{-1})	Q (J/mol)	n
α phase	—	8737	$3.24e5 + 24.69(T - 923.15)$	5.89
Mixed α − β phase	$\dot{\epsilon}_{eff} \leq 3e-3$	0.24	1.02366e5	2.33
Mixed α − β phase	$\dot{\epsilon}_{eff} \geq 3e-3$	Interpolation	Interpolation	Interpolation
β phase	—	7.9	1.41919e5	3.78

of the anisotropic Hill factors is integral for application of such data sets and highlights the effects of anisotropy on creep-based modeling.

There are two concerns with the testing performed by Rosinger et al. [123] in terms of application to LOCA behavior: (1) testing was halted after a relatively low strain value (15%) compared to historically observed burst diametric strains, and (2) assumptions about Hill parameters are implicit in calculating the strain rate in the hoop direction. For (1), strain could become significant to the point where deformation mechanisms change, plastic instability is initiated, or power-law breakdown occurs. If creep is indeed the primary factor during LOCAs, testing with a low strain threshold could misrepresent the latter stages of ballooning where most of the deformation occurs.

For (2), Hill parameter inputs can have significant impact on predictions of final strain. The impact of such inputs on burst strain and temperature calculations was demonstrated by Suman's [126] modelling efforts for a high heating rate of 40 °C/s. Suman modeled the behavior of as-received, β-annealed, α-annealed, and isotropic claddings. Table 10 below summarizes the Hill parameters for the respective conditions. The as-received and α-annealed models, the most anisotropic cases, exhibited burst strains ~30-40% lower than the more isotropic cases in the α and α+β phases. Naturally, convergence of the predicted strain occurred in the β phase due the inherently isotropic bcc structure.

This discussion of Hill parameters high-lights the importance of anisotropy in modeling efforts. Though Zry-4 for reactors must adhere to ASTM standards, discrepancies in processing histories could partly explain variances in behavior. Moreover, as suggested by Hayes and Kassner [121], variations in chemical composition and variances in microstructure for nominal recrystallized of stress relieved heat treatments could influence observed differences in strain rates between different creep tests of "Zircaloy-4". Using a generalized set of parameters for all Zry-4, such as those employed in BISON, may not be the best approach.

The developers of the Erbacher model, which was compiled for analysis by Neitzel et al. [117], were well aware of the effects of anisotropy. Regarding Hill parameters, Neitzel et al. [117] state: “In Section 3.2 it was shown that the anisotropy of the Zircaloy can significantly change the burst temperature in the α-Zr region. Unfortunately, knowledge of the anisotropic factors is very limited. In this work we arbitrarily chose the values of F = 0.924, G = 0.374 and H = 0.192 for the

Table 10. Hill parameters for a range of metallurgical conditions of α-phase Zry-4 modeled by Suman [126].

Metallurgical Condition	F	G	H
As-received	0.773	0.532	0.195
α-annealed	0.956	0.322	0.222
β-annealed	0.572	0.418	0.510
Isotropic	0.5	0.5	0.5

anisotropic factors". The model developers recognized the importance of anisotropy yet assumed constancy across the low temperature phase, implying a constant A value across the domain.

Certain studies have revealed that Hill parameters measured at room temperature (RT) are not applicable at higher temperatures. For instance, Rosinger et al. [127] in 1982 and Choi et al. [124] in 2021 found that the Hill factors tended towards isotropy (F = G = H = 0.5) at 800 °C during creep testing. This shift could signify changes in the microstructure related to higher temperatures, such as recrystallization or activation of more slip planes. More recently, Kamerman and Nelson [128] performed strain-controlled burst testing of Zry-4 at RT, 150°C, 275°C, 400°C, and 525°C to investigate multiaxial plastic behavior and measure Hill parameters. Metallurgical condition of the tubing was not presented but reported to adhere to ASTM B353-12 for tubing not intended for cladding use. The samples were held at the target temperature for 3 hours before testing began. They found that texture-related anisotropy was present at room temperature, but minimized starting at 400 °C. This lower thermal boundary is considerably below typical temperatures for recrystallization annealing processes, implying that a different mechanism might be responsible for the more isotropic behavior in the α phase. As discussed in Chapter 1, the dominant deformation modes/slip systems of Zr are temperature dependent. Therefore, it is possible that more slip planes are activated at LOCA relevant temperatures, leading the cladding towards effectively isotropic behavior, as suggested by Rosinger et al. [127]. Hill parameters are explicit in the strength coefficient, A, and as such, the predicted dimensional strains (hoop, axial, radial) could vary throughout a LOCA in the low temperature phase.

Another critical assumption in the Erbacher model is that n (stress exponent) and Q (activation energy) are relatively constant in the α phase at LOCA relevant temperatures. However, the validity of this assumption is questionable, as many other class M alloy systems do not demonstrate this behavior. Hayes and Kassner [121] conducted a literature review of Zr alloy creep behavior in the α phase from 300 to 850 °C, noting the sudden drop in creep activation energy near 650 °C for pure Zr. Previous literature referenced in their review suggested that Zr and its alloys never reach a true steady-state, as well as the stress exponent and activation energy continually change with stress [129,130]. Although this claim is questionable and requires significant investigation.

5.2.2: The Donaldson Model

Donaldson et al. [120] performed isothermal, internally loaded creep testing of Zircaloy-4 sourced from three manufacturers: Westinghouse, Wolverine, and Sandvik. The metallurgical condition (SRA or RXA) was not specified. The tubing length was 76 cm in length and tested in the as-received condition. In the α phase, testing was performed from 700 °C to 800 °C and stresses from 12 to 65 MPa. The heating rate was not specified, yet claddings were held at the target temperature for 15 minutes before pressurization. Creep data was captured by measuring diameter change at the mid-point of the cladding section using a laser gauge. Donaldson et al. [120] utilized a variant of the FPL equation modified by the shear modulus and temperature,

$$\dot{\varepsilon}_{hoop} = \frac{A*G}{T} * (\frac{\sigma_{hoop}}{G})^n e^{\frac{-Q}{RT}}, \quad (7)$$

where A is the structure constant, G is the temperature dependent shear modulus, T is the absolute temperature in K, Q is the activation energy, and R is the universal gas constant. Parameters were determined via multi-linear regression to produce best fits to Eq. 7. From these fits, the model parameters shown in Table 11 were determined, explicitly defined in terms of the hoop direction. Donaldson et al. [120] noted that the specimens from Westinghouse and Wolverine displayed similar behaviors, while the Sandvik tubing demonstrated superior creep strength. The ZryCreepLOCAUpdate BISON module only incorporates the model generated for the Westinghouse samples.

5.2.3: The Kaddour Model

The most recent established model, the Kaddour model, was developed in 2004 at Ecole des Mines Paris. Kaddour et al. [119] performed creep testing on Zr-1Nb and Zry-4 cladding sections loaded along the axial direction. The Zry-4 cladding segments were in the SRA condition with equiaxed grains with a mean size of 8 μm. Note, equiaxed grains are not typical for the SRA condition. The applied stress levels were modulated, first incrementally increased, then decreased, in effort to observe effects on the microstructure. Testing was performed under vacuum and heated using a radiative furnace. Kaddour et al. [119] evaluated creep behavior across the three phase regions (α, α + β, and β). However, the low temperature α-Zr phase model is discussed due to the relevance to high-burnup LOCA modeling and the focus of this dissertation. While not directly stated in the manuscript, testing was performed at temperatures ranging from ~600 – 1000 °C.

Table 11. Parameters from the Donaldson model for Zry-4 in the α phase

Parameter	Westinghouse	Wolverine	Sandvik (NRU)
A (MPa^{-n-} s^{-1})	$4.43 \cdot 10^{23}$	$1.83 \cdot 10^{23}$	$6.54 \cdot 10^{22}$
n (dim.)	5.31 ± 0.06	5.42 ± 0.02	4.94 ± 0.09
Q (kJ/mol)	266.8 ±14.0	272.2 ±12.0	294.0 ±16.0

From this work, deformation mechanism maps for both alloys were created and compared to literature on pure Zr from Sargent and Ashby [131]. It should be noted that Sargent and Ashby developed their maps base on pure Zr with a grain size of 100 μm. Kaddour et al. [119] used another variant of the FPL creep equation that is again distinct from the Erbacher and Donaldson models. The Kaddour model has the following temperature compensated form of Eq. 8,

$$\dot{\varepsilon} = \frac{A}{T}\sigma^n e^{\frac{-Q}{RT}} \quad (8)$$

Parameters associated with the fit for Zry-4 are presented in Table 12. Two distinct regimes dependent on stress were found associated with diffusion (n ~ 1) and most likely dislocation creep (n ~ 5). The authors also noted that the creep behavior was not affected by thermal or loading history, i.e., the varying loading had no measurable effect on creep rates.

As the model was generated using tensile data from the axial direction, Hill parameters are again necessary to determine parameters for the hoop direction. These parameters were not reported by Kaddour et al. [119]. However, Massih [19] utilized Hill parameters of F = 0.956, G = 0.304, and H = 0.240 to define factors for the hoop direction when comparing the outputs from this model.

5.2.4: Failure criteria for LOCA models

Plasticity models are available, such as the empirical relation from Geelhood et al. [132] at Pacific Northwestern National Laboratory. However, much of the data was developed for use in dry-cask modeling applications. Similarly, convergence issues can arise in BISON computations when including plasticity models into LOCA modeling efforts [125]. The role of plasticity will be discussed in a subsequent section.

Failure criteria constitute a critical aspect of LOCA modeling and producing accurate behavior predictions. Failure is determined based on two distinct criteria that can be applied separately or together. The first criterion is an overstress criterion where a failure stress based on the empirical model shown in Eq. 9,

$$\sigma_b = a * \exp(-bT) * \exp\left[-\left(\frac{\eta-\eta_0}{9.5*10^{-4}}\right)^2\right] \quad (9)$$

where σ_b is the burst hoop stress, a and b are experimental constants, T is the absolute temperature, n_0 is the initial oxygen concentration in the cladding, and n is the current oxygen concentration.

Table 12. Parameters generated from Kaddour et al. [119] for Zry-4 in the α phase.

Stress Regime	A ($K \cdot MPa^{-n} \cdot s^{-1}$)	n	Q (kJ/mol)
$\sigma \leq 15$ MPa	$1.00 \cdot 10^6$	1.3	190
$\sigma > 15$ MPa	$1.63 \cdot 10^8$	5.0	316

The second criterion is based on strain rate, where failure occurs once a rate of 2.78 %/s is reached. This understanding of material failure adds significant value to the modeling of LOCA scenarios, enabling more accurate predictions of the cladding behavior.

5.2.5: Comparison of high temperature creep models and a critique of general models for Zircaloys

Strain rate predictions for a given hoop stress at 650 and 700 °C from the three models are presented in a log-log plot in Figure 47. Hill parameters utilized by Massih [19] were assumed to predict behavior in the hoop direction for the Kaddour and Erbacher models. The models show general overlap in predicted strain rates. This is particularly true at higher hoop stresses. However, considering lower stresses the curves differ by a factor of ~1.5 - 3 times. Therefore, the choice of model could affect model predictions, on top of anisotropic factors. Such sensitivity between models developed for "Zircaloy-4" should be accounted for in modeling use. Only Kaddour et al. reported metallurgical condition and grain size. None of the three models above declare the exact alloy composition or processing routes. This notion of generalization extends beyond specific alloys as high temperature creep models described are broadly applied to Zircaloys. As in, these high temperature models do not factor in discrepancies between types of Zircaloy.

Zirconium alloys intended for cladding use are required to adhere to the range of composition in ASTM B811-13, yet considerable variations can be present from individual manufacturers in terms of alloying elements and processing. The role of this compositional variation was considered by Hayes and Kassner [121] when reflecting on differences in the creep strength between literature data for Zircaloys. Hayes and Kassner also noted a difference in behavior between metallurgical states of Zry-4, namely CWSR, cold-worked (CW), and RXA. The creep strength and stress exponent of the RXA material was higher in the intermediate stress regime (relevant to LOCAs) than compared to the CW or CWSR Zry-4. Hayes and Kassner posited that this difference could be related to recrystallization effects in the CW/CWSR material that occurred early during testing in the literature studies. However, the inverse behavior was true for Zry-2, with the CW and CWSR having higher creep strength. These nuances in behavior highlight the broad range of factors that influence creep behavior in Zr alloys. As such, general models encompassing all Zircaloys or alloys with varying compositions and metallurgical states is subject to inherent misrepresentation.

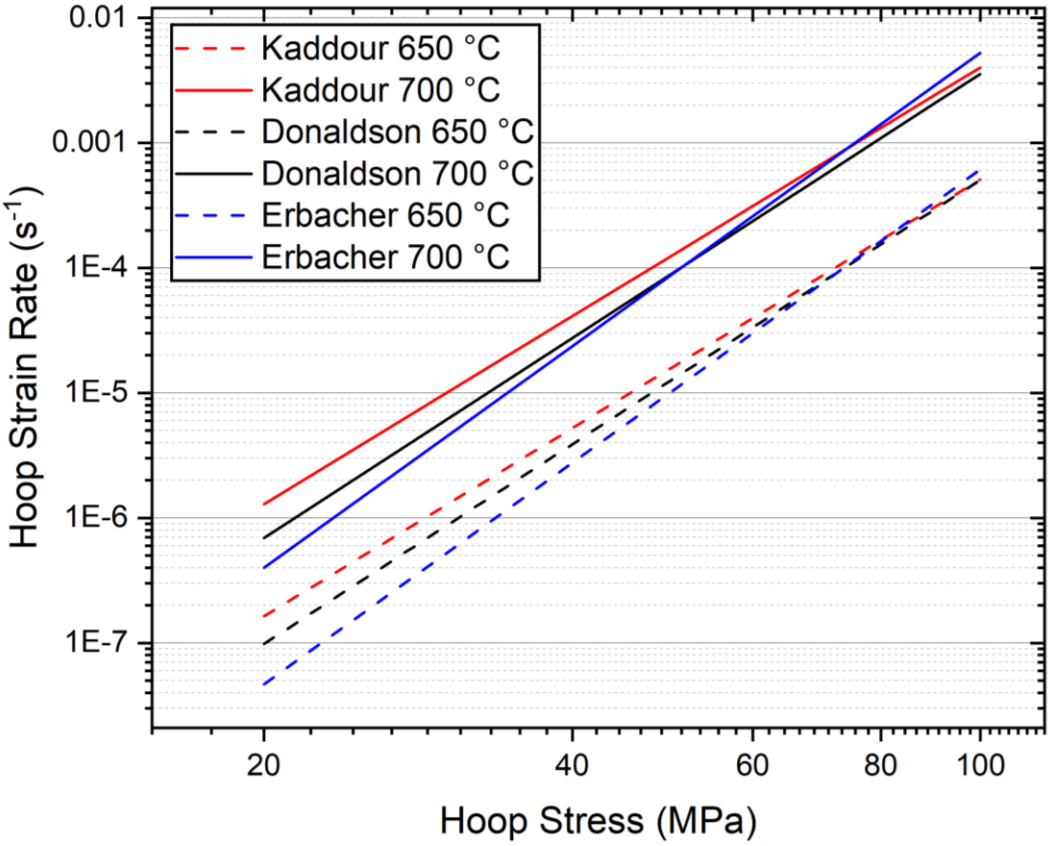

Figure 47. Comparison of the models in the ZryCreepLOCAUpdate module in BISON at 650 °C and 700 °C. The solid and dashed lines represent isotropic and anisotropic versions of the models, respectively.

This variation was also demonstrated by the work performed with the Donaldson model. Donaldson et al. [120] tested three separate reactor grade "Zircaloy-4" heats that adhered to industry standards. Yet despite the noted similar behavior of Wolverine and Westinghouse tubing, considerably different parameters were determined. However, compared to the Sandvik Zry-4, the Westinghouse and Wolverine claddings demonstrated considerably lower creep strength.

If a steady state creep-based approach to LOCA modeling is used it could be pertinent to develop creep models for tubing from a specific source/processing route. Even then, uncertainty associated with manufacturing could play a significant role. Note, all of the models presented were determined in either a vacuum or an inert environment. While oxygen concentration and oxide formation are expected to have a more significant impact on the β phase behavior [33,85], it should still be considered.

Section 5.3: BISON Modeling of Zircaloys

5.3.1: Preliminary comparison of BISON predictions to literature data

The performance of BISON modeling compared to *in-situ* data from this dissertation will be presented in a subsequent chapter. A more general comparison of BISON model predictions to experimental results is presently discussed, as it highlights the gap in model predictive capabilities. This capability is critical in safety analysis and design criteria for high burnup applications.

A plot from Capps et al. [133] comparing the percent difference of *in-situ* experimental data with the BISON predicted strain from 300- 825 °C for a few transiently heated burst tests is shown in Figure 48. Note that Zry-4 is expected to be in the α phase at these temperatures and is relevant to high burnup considerations. Capps et al. [133] utilized the Erbacher model discussed previously. The inability of current models implemented in BISON to predict strain with inaccuracies up to ~300% difference is evident from this data.

5.3.2: Handling of anisotropy in BISON models

The current implementation of anisotropy in BISON might partially contribute to the inaccuracies observed in modeling predictions. In some BISON modules, Hill parameters are used to calculate the effective structure constant which is further used in effective stress/strain rate computations in the Erbacher model. However, as of this writing, BISON employs isotropic calculations of inelastic strain [134]. This means that while anisotropy is considered when

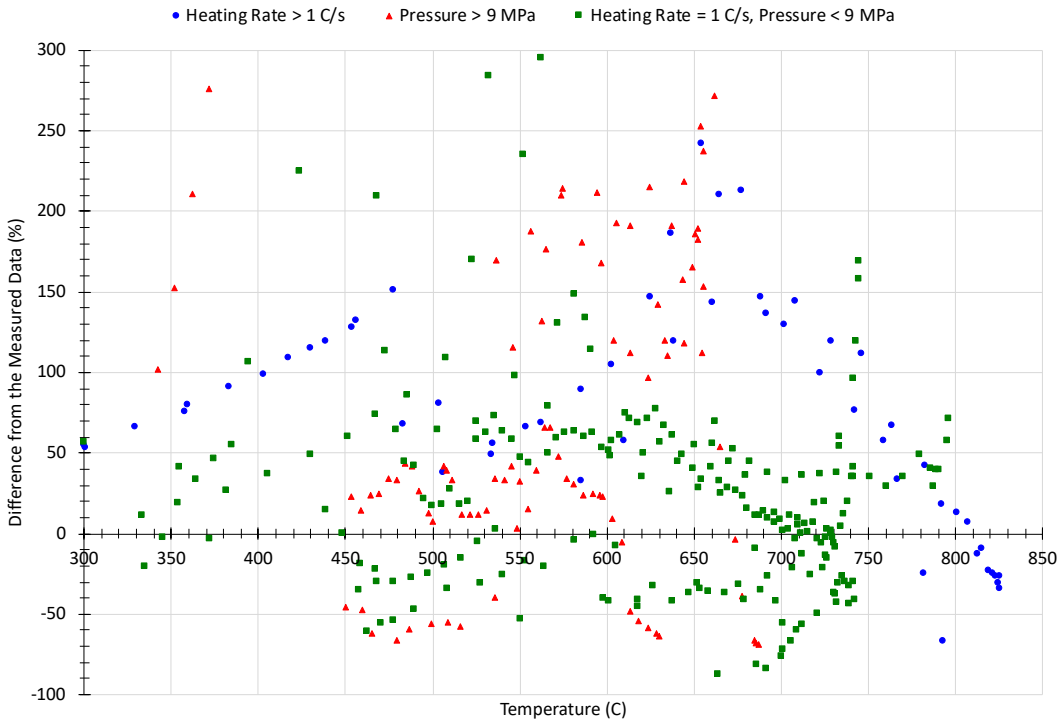

Figure 48. Difference of measured strain from predicted strain by BISON for a range of temperatures in the α phase [133].

developing model parameters for an effective framework, it is not accounted for during inelastic strain calculations. It is plausible that this could lead to an overestimation of hoop strain and an underestimation of axial strain during a LOCA event. This potential issue has been identified by the BISON development team, detailed in a milestone report by Recuero et al. [134] that incorporates considerations of anisotropy specifically for Zry-4.

Nevertheless, this is one of the many possible influences on modeling accuracy discussed in this chapter, such as material condition (SRA/RXA) and grain size. It is essential to recognize and evaluate these potential factors holistically to improve the overall reliability of models for LOCA scenarios.

5.3.3: Summary of BISON modeling of Zircaloys

The models reviewed above each offer valuable insights into potential sources of error in modeling efforts. One key takeaway is the critical role of Hill parameters in correctly using data from axial testing to predict hoop strain behavior, as demonstrated by the Erbacher and Kaddour models. The emphasis is often on hoop strain due to its greater magnitudes and implications for in-bundle effects on coolant flow during a LOCA. However, if the goal is to develop a truly representative model, accurate prediction of axial or radial strain behavior is paramount. No matter the testing method, understanding and applying the anisotropic state of the material is necessary. This proposition is far from trivial, given evidence suggesting that Hill parameters are not constant with temperature. Still, the temporal aspect of this evolution is often neglected and may be relevant on the time scales of a LOCA. Such observations underscore the need for models that delve beyond empirical relations and macro-scale descriptions of deformation and instead investigate the relationship between microstructural changes and cladding behavior.

Beyond uncertainties within individual data sets, variations among different “Zircaloy-4” samples could also impact the applicability of the models. Differences in processing and chemical composition between manufacturers could account for some of the variation between models, as suggested by Hayes and Kassner [121]. Thus, to achieve accurate predictions necessary for advancing efficiency thresholds, claddings may need to be assessed on a manufacturer-by-manufacturer basis. These sources of uncertainty are starkly manifested in the inability of current models implemented in BISON to accurately predict the deformation behavior of Zry-4, as shown in Figure 48. While modern Zr-Nb alloys such as Zirlo and M5 are widely used today,

investigations into Zry-4 are still relevant for incumbent systems and build the foundation for investigation into newer alloys.

It is crucial to keep in mind that the basis of LOCA modeling efforts is the steady-state creep assumption. This assumption applies the empirical toolset and descriptions developed for constant temperature and mechanical states to a fundamentally dynamic setting. As such, modeling efforts could benefit from extending the steady-state creep dependence to incorporate visco-plastic descriptions and even primary or tertiary creep. Granted, processes such as tertiary creep or plastic instability are notoriously challenging to capture, even phenomenologically. Nevertheless, it is possible to evaluate the validity of the steady-state creep assumption by synchronizing pressure, strain, and temperature during a simulated LOCA. Therefore, Zr alloys serve as an excellent demonstration case for the *in-situ* framework developed in this dissertation.

Section 5.4: Role of time independent plasticity in LOCA behavior

5.4.1: Instability criterion

The role of time-independent plasticity-based mechanisms in LOCA deformation behavior have been ignored for two reasons: (1) historic development of models based on creep and (2) recent integration of plasticity considerations into BISON modeling resulting in convergence issues when utilized in conjunction with creep descriptions [125]. Consequently, contemporary LOCA modeling efforts tend to depend on secondary creep, using power law-based phenomenological descriptions discussed above. However, factors such as time-independent strain behavior beyond yielding, strain hardening, and the non-uniform strain tied to plastic instability probably significantly influence the balloon and burst behavior.

The purpose of the present section is to outline the potential avenues for modeling behavior after instability onset, including its limitations. While a brief introduction to general principles is included, it should be noted that modeling post-necking behavior is of current interest across a broad array of domains. Experimentally, as will be shown later, considering post-necking behavior in ballooning may be vital for developing accurate LOCA modeling efforts.

At a certain point in ramped stress profiles typified in constant strain rate tensile tests or LOCA cladding ballooning phenomena, the effect of work hardening becomes inadequate to counteract the softening from area reduction, resulting in strain localization or “necking,” where

deformation behavior turns unstable. This localization or necking process manifests in two potential forms: diffuse necking, where non-uniformity is widespread across the necked region and may lead to fracture [103]; and localized necking, typified by a constricted band of local strain in the necked region, often the site of fracture.

In 1952, Swift [135] developed a criterion for the initiation of diffuse necking under biaxial stress conditions based on the maximum load principle of Considère [136] . That same year, Hill [137] extended the work of Considère to predict the onset of localized necking. These criteria have become integral in thin metal sheet manufacturing, forming the basis for commonly used forming limit diagrams [138–141]. Given the similarity in biaxial stress states and applications to high temperatures, frameworks developed for thin sheets may serve as benchmarks for qualitatively probing plastic instability in LOCA conditions. Marciniak and Kuczynksi [142] developed further criteria for thin sheets by assuming a matrix that behaves uniformly, and a small zone or "defect" that experiences non-uniform deformation due to geometric effects. As deformation continues, the strain in the defect area rises more quickly than in the matrix, resulting in localized thinning. Larsson et al. [143] implemented the local defect principle in finite element modeling for pressurized testing of aluminum and copper tubing at room temperature, following Tveegard et al.'s methodology [144]. Assuming an initial defect of 0.01 mm resulted in bifurcation into diffuse necking at the defect location near the maximum load of the test samples, effectively demonstrating applicability to internally loaded tubing.

If the balloon process is driven by plastic instability, application of such criteria to cladding behavior under LOCA conditions could be useful for predicting the ballooning onset. However, the practicality of applying these criteria, derived from constitutive models of conventional mechanical testing, are complicated by the transient heating characteristic of LOCA scenarios. These criteria fundamentally hinge on factors such as material hardening, where the increased resistance to plastic deformation may be countered by thermal softening effects due to a rise in temperature. While instability criteria might be employed to anticipate the beginning of ballooning, the descriptions of deformation behavior become considerably more intricate with the loss of uniformity in the strain field. This complexity is not captured in any current model of multiaxial flow localization; further research and tailored modeling is necessary to accurately capture the nuanced interplay between thermal effects and material behavior in LOCA conditions.

5.4.2: Loss of uniformity, variability in necking, and short falls of analytical methods

True stress-strain curves obtained from standard tensile tests offer valuable insights into strain hardening up to the point of instability. Beyond this stage, material parameters derived from measurement systems like extensometers become unreliable, stemming from the loss of strain uniformity. Additionally, the onset of diffuse necking compromises the assumption of plastic flow incompressibility due to material damage.

The localization of flow and the formation of a necked region are frequently influenced by the sample's geometry and loading configuration. For instance, a simple uniaxial test sample, such as a flat and rectangular thin tensile bar, undergoes reduction in both width and thickness during necking. The deformation here is asymmetric. Conversely, a cylindrical specimen, being circular in cross-section, exhibits symmetrical reduction in diameter at a specific axial point during necking. This symmetry enables a decrease in diameter across the entire circumference, culminating in a conical necking region within a triaxial stress state.

Analytical descriptions of stress and strain within the necked region are feasible, as illustrated by Bridgman's work [145,146] on necking in cylindrical tensile bars under uniaxial tension, taking into account the neck's geometry. However, these descriptions must be handled cautiously and individually [147], as it often proves challenging to account for the evolving geometries of the neck. Owing to these analytical complexities, contemporary efforts to characterize the necked region typically employ extrapolation or parameter determination methods, coupled with full strain fields and finite element analysis. Such approaches recognize the intricate interplay between geometry and material properties, aiming to provide a more nuanced understanding of deformation behavior under various loading conditions.

5.4.3: Utilization of damage and hardening models post-necking

This section introduces conventional empirical forms used in modeling post-necking behavior. Typical approaches incorporate hardening and/or damage models to capture the complex phenomena occurring after necking.

The simplest method to approximate post-necking stress-strain relationships is to extrapolate hardening behavior gathered from data preceding the maximum load. However,

predictions relying on pre-necking data extending far into the diffuse necking phase are speculative and strongly influenced by the chosen empirical hardening rule [147].

A frequently employed empirical plasticity description for high temperatures and strain rates is the Johnson-Cook (JC) model [148], which is particularly apt for modeling collision or impact conditions [149,150]. This model is introduced due to its explicit consideration of temperature, potentially rendering it useful for LOCA conditions compared to simpler plasticity models such as those by Swift or Voce. The constitutive equation for the JC model is given by,

$$\sigma = \left[A + B\varepsilon_p^n\right]\left[1 + Cln\frac{\dot{\varepsilon_p}}{\dot{\varepsilon_{p0}}}\right][1 - T^{*m}], \tag{10}$$

$$T^* = \frac{T - T_0}{T_m - T_0}, \tag{11}$$

where A, B, C, n, and m are material constants, ε_p is the plastic strain, $\dot{\varepsilon_p}$ is the plastic strain rate, $\dot{\varepsilon_{p0}}$ is the reference plastic strain rate, T is the deformation temperature, T_0 is the reference deformation temperature, and T_m is the melting temperature. The bracketed expressions represent isotropic strain hardening, strain rate effects, and temperature softening, respectively.

Plastic instability and necking are typically accompanied by material damage, with void growth and coalescence eventually leading to fracture. Damage is often incorporated into modeling efforts alongside hardening laws to predict material failure. Alongside the JC plasticity model, there is also the commonly utilized JC damage model for predicting failure in FEM, expressed as:

$$\varepsilon_f = \left[D_1 + D_2 e^{D_3\sigma^*}\right]\left[1 + D_4 ln\dot{\varepsilon}_p^*\right][1 + D_5 T^*] \tag{12}$$

where D_1 through D_5 are material-dependent damage parameters, ε_f is the strain at failure, and σ^* is the measure of stress triaxiality. Damage can be defined by the sum of increments relative to the computed failure strain, where failure occurs when $D \geq 1$. Research by Hanock and Mackenzie [151] found that strain to failure is heavily dependent on the stress state, emphasizing the significance of damage parameters D_1 through D_3 in the JC damage model [152].

The JC models are empirical macroscale models that do not account for damage on lower length scales. The advantage of the JC model is in fact the purely empirical coefficients derived from tensile testing. An alternative approach was developed by Gurson [153], who formulated a yield criterion for porous ductile materials considering the volume fraction of voids. Gurson's

model connects the void presence to the loss of load-carrying capacity and predicts the initiation and growth of damage. Subsequent work by Tvergaard and Needleman [154,155] extended Gurson's model to capture not only void growth but also void nucleation and coalescence, leading to the Gurson-Tveegard-Needleman (GTN) model. This provides a more nuanced description of ductile failure, portraying the entire process from inception to final failure, and represents a vital formulation in the field of damage mechanics.

5.4.3: Potential application to LOCA modeling

The plasticity model for Zircaloys, implemented in BISON [125], was initially developed by Geelhood et al. [132] at Pacific Northwest National Laboratory (PNNL) for the U.S. Department of Energy. Specifically developed for dry cask storage applications, this model was later extended to encompass high-temperature behavior, with correlations based on SRA data relevant to conditions up to approximately 482 °C.

Plasticity behavior beyond this temperature was derived from a figure published for the Prometra database [156], which did not report the supporting data. This lack of concrete data led Geelhood et al. to caution against the extension of their correlation to higher temperatures. Consequently, for LOCA-relevant temperatures, a significant investigation into Zircaloy's behavior may be necessary. This includes detailed studies related to specific material processing and microstructure, which would be instrumental in further developing the models discussed above.

Beyond the uncertainties inherent in current models, the extrapolation of hardening processes beyond the point of instability often falls short in accurately capturing complex post-necking behavior, especially at large strains. This complexity is heavily influenced by the particular choice of material and hardening laws. For instance, Dumand and Mohr [157] demonstrated that applying the Swift hardening law to high-strength steels led to poor agreement with large strain behavior in finite element modeling (FEM). Conversely, Sung et al. [158] found that the combination of Voce and Hollomon hardening laws yielded FEM results that were consistent with tensile data up to failure for dual-phase steels. This result led the authors to suggest that damage and void growth might not play significant roles in the tensile failure of the alloys tested. These examples highlight the varied and often limited success of extrapolation in the post-necking domain.

Proper FEM analysis for post-necking necessitates extensive experimental comparisons and significant attention to mesh management. Predicting the precise location of diffuse necking in uniformly cross-sectioned samples is notoriously difficult [147], frequently necessitating the use of a pre-placed notch in the mesh. Moreover, validation of post-necking behavior often requires the utilization of tapered or notched samples in experimental setups to pre-identify the necking region [147,159,160]. Factors related to mesh configuration [161,162] can also influence predictions at large strains. Adaptive meshing in the region of interest is commonly applied to refine mesh size to handle large strains [163,164].

In summary, relying on predetermined hardening parameters presents challenges due to the inherent complexities of strain localization. Though hardening models can be extrapolated to some degree, their applicability, especially at larger strains, is often ambiguous. Moreover, a hardening behavior that proves effective under one set of loading conditions may fail under others.

Applying these concepts to LOCA scenarios further complicates matters. The transient nature of LOCA conditions means that claddings are subject to dynamic changes in both loading and temperature, differing fundamentally from conventional tensile tests where strain rate and displacement are prescribed. In fact, changes in internal loading and strain rate are a direct result from the rising temperature. The standard strain and strain rate hardening behavior may lack relevance or even be overshadowed by thermal softening. Furthermore, the broad range of heating rates in LOCA testing (~1-100 °C/s) may result in varied applicability of plasticity parameters. As such, more nuanced models that extend beyond conventional hardening and damage descriptors will likely be essential to faithfully represent LOCA behavior.

While initial modeling efforts may benefit from the application and extrapolation of existing parameters, coupled with refined mesh strategies, modern approaches often employ inverse analysis methods. These methods aim to derive complete system solutions and determine parameters based on full-field strain characterization, thereby providing a more holistic understanding of sample behavior.

5.4.4: Finite element inverse and virtual field method

The finite element inverse method (FEIM) is a procedure whereby experimental results inform the parameters or characteristics of a given model. This method is particularly useful when

model parameters are challenging to measure directly or are unknown a priori. The common approach involves running simulations for various parameter sets, then contrasting the simulated results with experimental data. The parameters minimizing an objective function are regarded as the most probable to be accurate. FEIM has seen widespread application across various domains [165–167], but in reference to post-instability deformation this method utilizes full field strain data to determine hardening parameters for a given hardening model. It should be noted the computation time associated with this method is cumbersome, and the dependability of a finite element model is greatly influenced by the type of analysis, the domain and time discretization, as well as the interpretation of boundary conditions and the modeling of specimen geometry [168].

An alternative and growingly popular method is the virtual field method (VFM) [169,170]. Essentially, VFM employs the strain field derived from an experiment (usually through DIC or similar full-field measurement techniques) alongside an arbitrarily selected stress field (the "virtual field") to ascertain the best fit for material parameters. This 'virtual' approach utilizes mathematically convenient functions that satisfy the problem's boundary conditions, without representing any physical state of stress. VFM aims to find parameters that minimize the difference between internal (W_{int}) and external (W_{ext}) work, expressed as:

$$W_{int} = -\int \sigma_{ij} {\varepsilon_{ij}}^* dV \tag{13}$$

$$W_{ext} = \int T_i u_i^* dS \tag{14}$$

where V is the given volume, T_i is the tractions applied on the surface S, ${\varepsilon_{ij}}^*$ is the virtual strain, σ_{ij} is the internal stress, and u_i^* is the virtual displacement. This description is pertinent to small strain theory, where finite strain theory definitions are available [171]. VFM's chief advantage lies in its ability to gather information across the entire region of interest, rather than just at a single point. Coppieters et al. [168], for example, successfully employed VFM to extend the Swift and Voce hardening models to DC05 steel during uniaxial tensile testing. However, they noted inconsistencies between results from different testing configurations, emphasizing the method's sensitivity.

This section's discourse sought to briefly review both the potential value and limitations of possibilities to model behavior after instability onset. The role of post-necking in ballooning may be vital in LOCA testing, as revealed later in the experimental section. The challenge is to either

extrapolate hardening behavior and include damage mechanics in FEM—applicability being case-specific—or to leverage full-field experimental data with inverse methods.

Inverse methods, while powerful, entail solving an optimization problem, which may confront issues regarding solution uniqueness and stability. Multiple parameter sets might yield similar experimental data alignments, and minor input variations can lead to substantial output alterations. Strain, displacement, and loading are the known variables from this framework, with stress needed to be determined. Also, any constitutive model in FEIM or VFM will inevitably rest on assumptions, such as isotropic hardening, even though the actual material may display kinematic or mixed hardening. The anisotropic behavior of materials such as cladding in the α-Zr phase will also necessitate further consideration.

Utilization of the VFM holds direct relevance to this dissertation's framework, especially considering the integration of DIC into SATS. Implementing such methods requires meticulously refined methodology with minimized error levels. The experimental work in this dissertation will not utilize VFM due to current and past limitations of techniques. However, moving forward, the ultimate objective should encompass refining methodologies and incorporating both VFM and possibly FEIM for comparative purposes, to derive comprehensive descriptions of the ballooning process.

Chapter 6: *In-situ* Experimental Techniques and Augmentations to SATS

Chapter Foreword

This chapter presents a brief background of the *in-situ* techniques incorporated into SATS as well as experimental configurations for subsequent testing in this dissertation. The fundamentals of DIC and infrared thermography (IRT) are examined and their implications for burst testing are discussed. SATS testing has seen the utilization of multiple iterations and variants of DIC, including both 2D and 3D DIC. The former was applied during the initial round of transient testing with in-situ measurements, to be described in Chapter 7. Understanding 3D DIC is also essential, as it is relevant to recent ATF experiments and the novel step-loaded isothermal testing that will be elaborated on in this chapter.

IRT was trial-tested in tandem with the 2D DIC iteration of the framework. However, challenges emerged when attempting to deconvolve the infrared radiation emitted from the SATS furnace environment and the samples. Consequently, IRT was discontinued in the 3D DIC work, but it could be reintroduced in the future after substantial adjustments. Despite these challenges, the application of IRT yielded valuable insights into temperature gradients. Emissivity values obtained were in alignment with the literature reports. This will be discussed in greater depth in the upcoming chapter.

Section 6.1: Background on In-situ Techniques

6.1.1: Fundamentals of digital image correlation

DIC techniques are an increasingly popular option for non-contact measurement of strain. DIC leverages cameras and image analysis methods to generate full-field strain during mechanical testing. DIC is a rich and diverse field with many algorithmic variants and image processing techniques. The intricacies related to matching functions, interpolation schemes, and other advanced aspects of DIC algorithms are numerous and far-reaching. For this dissertation, the focus will be on the practical applications of DIC and its role in the developed framework, without delving into the many aspects of DIC algorithm design and optimization. This focus aligns with the overall aim of the dissertation, which uses DIC as a tool for the purpose of investigating the LOCA behavior of cladding materials.

A simple illustration of a typical DIC setup from Zhao et al. [172] is presented in Figure 49(a). Each pixel in an image has an integer value assigned to it that ranges from 0 to 255. This is known as the "greyscale" value, with 0 denoting black and 255 signifying white. To facilitate the tracking process, a "speckle" pattern is typically applied to the surface under observation, resulting in the creation of unique, localized clusters of integers.

A region of interest (ROI) is divided into a grid of these localized clusters or "subsets" within a reference image. This can be seen in Figure 49(b), adopted from Zhao et al. [172], which shows an ROI subdivided into individual subsets. A DIC analysis software identifies the best match for the original subset in a subsequent image using a correlation function. Surface strain data can then be extracted via shape analysis of the subsets in that ROI. In effect, the subsets serve as digital strain gauges, enabling a detailed understanding of deformation and strain distribution throughout a mechanical test.

This experimental technique comes in two prominent forms: (1) 2-dimensional (2D) DIC, where only one camera/perspective is used to measure strain and (2) 3-dimensional (3D) DIC, which utilizes two cameras/perspectives. In 2D DIC, strain is only captured in the single image plane leading to possible error from out-of-plane displacement and rotation if a standard lens is used. An illustration in Figure 50 from Sutton et al. [173] demonstrates the effects from motion out of the image plane on perceived strain in 2D setups. The bias effects of 2D DIC can be mitigated by use of a telecentric lens, but the system can still be susceptible to rotation error. Additionally, telecentric lenses can be cost prohibitive.

3D DIC, or stereo-DIC, addresses the limitations of 2D DIC by utilizing two cameras placed at different perspectives. This additional dimension of measurement reduces errors associated with out-of-plane movements and adds a depth to the data collected, providing a more comprehensive strain profile of the sample. By comparing the images from the two cameras, the DIC software can track the displacements of a subset perpendicular to the image plane, adding a third dimension to the surface measurement.

It should be noted, however, that while 3D DIC provides a more accurate strain profile, it comes with increased complexity in setup and operation, and it generally requires more sophisticated (and costly) equipment compared to 2D DIC.

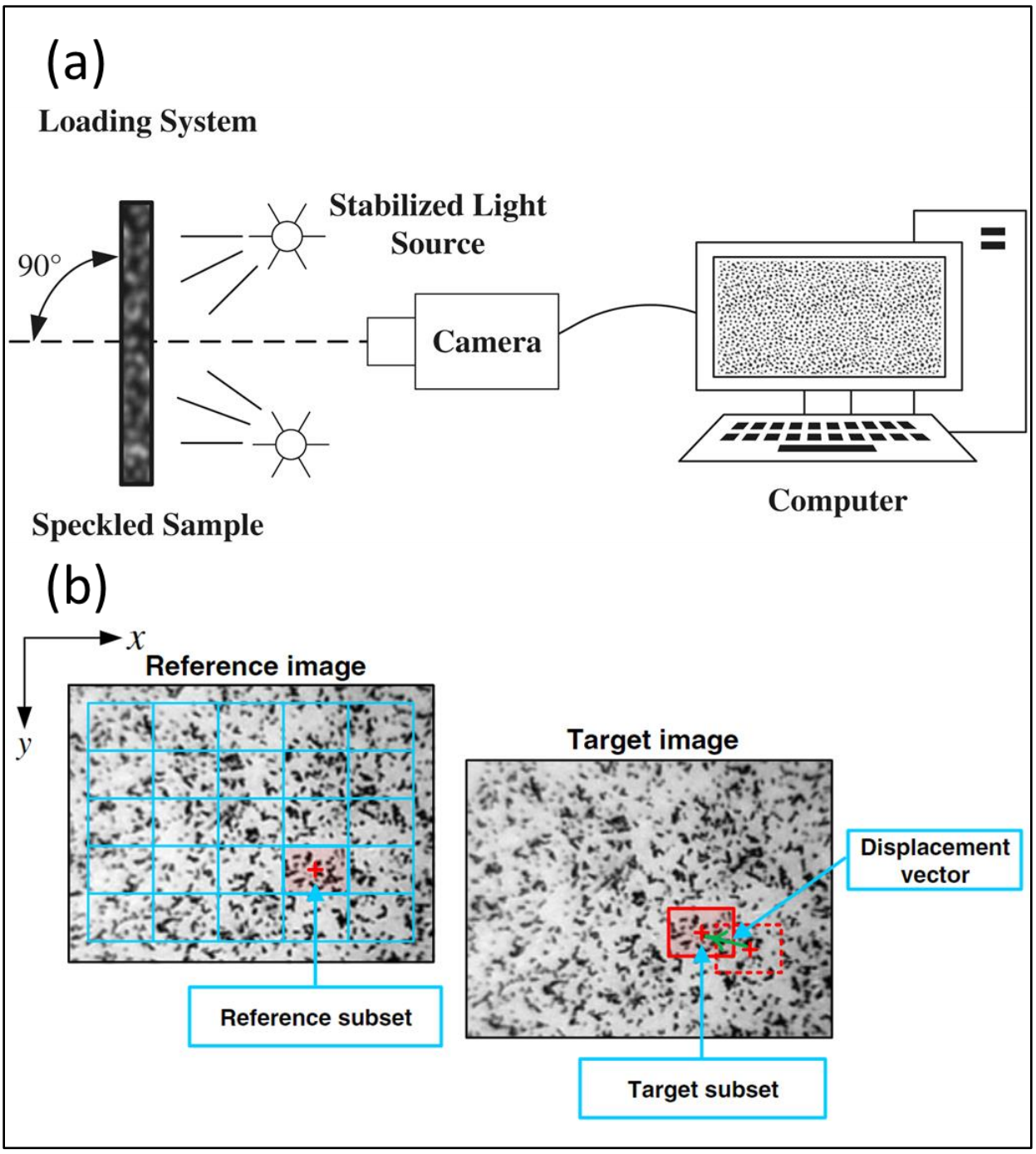

Figure 49. (a) Illustration from Zhao et al. [172] showing a typical 2D DIC setup. (b) Image of reference grid and subset displacement in subsequent image. Images reproduced based on a Creative Commons License.

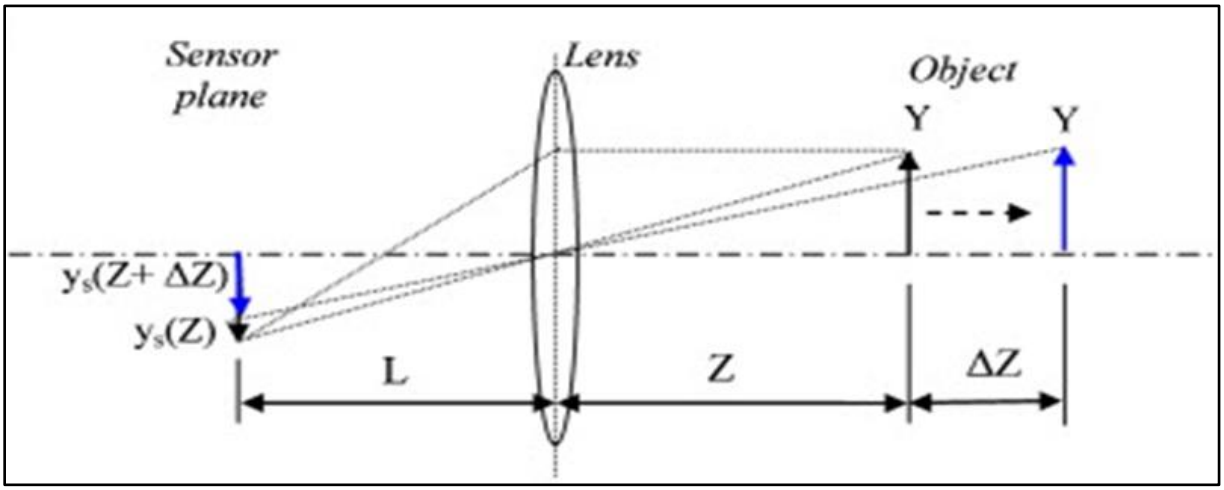

Figure 50. A simple ray diagram from Sutton et al. [173] illustrating how out-of-plane motion produces strain bias. Reproduced with permission from Elsevier.

Despite these challenges, the benefits of stereo-DIC in terms of improved measurement accuracy are often justified, especially in research applications where deformation is non-trivial such as burst testing. It should be noted that DIC techniques can extend even beyond these categorizations. Multiple stereo-DIC systems can be implemented for even more synchronized perspectives [174], or configurations with more than two cameras can be leveraged [175]. While these advanced setups can possibly provide fuller descriptions, they also require more setup procedures, lower experimental constraints, and more equipment.

The choice between 2D and 3D DIC largely depends on the specific requirements and constraints of the experiment. It is essential to consider the benefits and potential sources of error associated with each method and the specific test/specimens. For non-planar surfaces such as fuel cladding, 3D DIC can offer significant advantages by reducing errors associated with rotations and projections onto the image plane.

However, both methods have proven successful in different burst testing setups. Work by Campello et al. [176,177] with 2D DIC demonstrated effective calibration of optical effects to minimize uncertainties of in-plane measurements. Furthermore, Kane et al. [178–180] successfully applied 2D DIC with a telecentric lens to testing of Zry-4 in an air environment using the SATS facility, demonstrating the viability of this method in more constrained settings. 3D DIC, on the other hand, has been employed effectively in another unique burst testing setup, with Kim et al. [181] leveraging 3D DIC during burst testing of Zry-4 in an argon environment heated by an internal tungsten heater. While the choice of DIC method should be carefully considered, both 2D and 3D DIC offer valuable tools for measuring strain in burst testing scenarios. Both systems are successfully applied in this dissertation and in the literature, high-lighting the value of DIC to non-traditional characterization methods such as simulated LOCA burst testing.

6.1.2: Fundamentals of infrared thermography

Blackbody radiation is the characteristic electromagnetic radiation emitted due to an object's temperature and is a fundamental concept in engineering and applications of thermography. Planck's law, which describes the theoretical unique emission spectrum for a body at a specific temperature, underpins the use of thermography. In the context of accident scenarios, Figure 51 shows blackbody curves that correspond to relevant temperature ranges. A significant proportion of radiation emitted by a cladding at LOCA relevant temperatures falls within the short

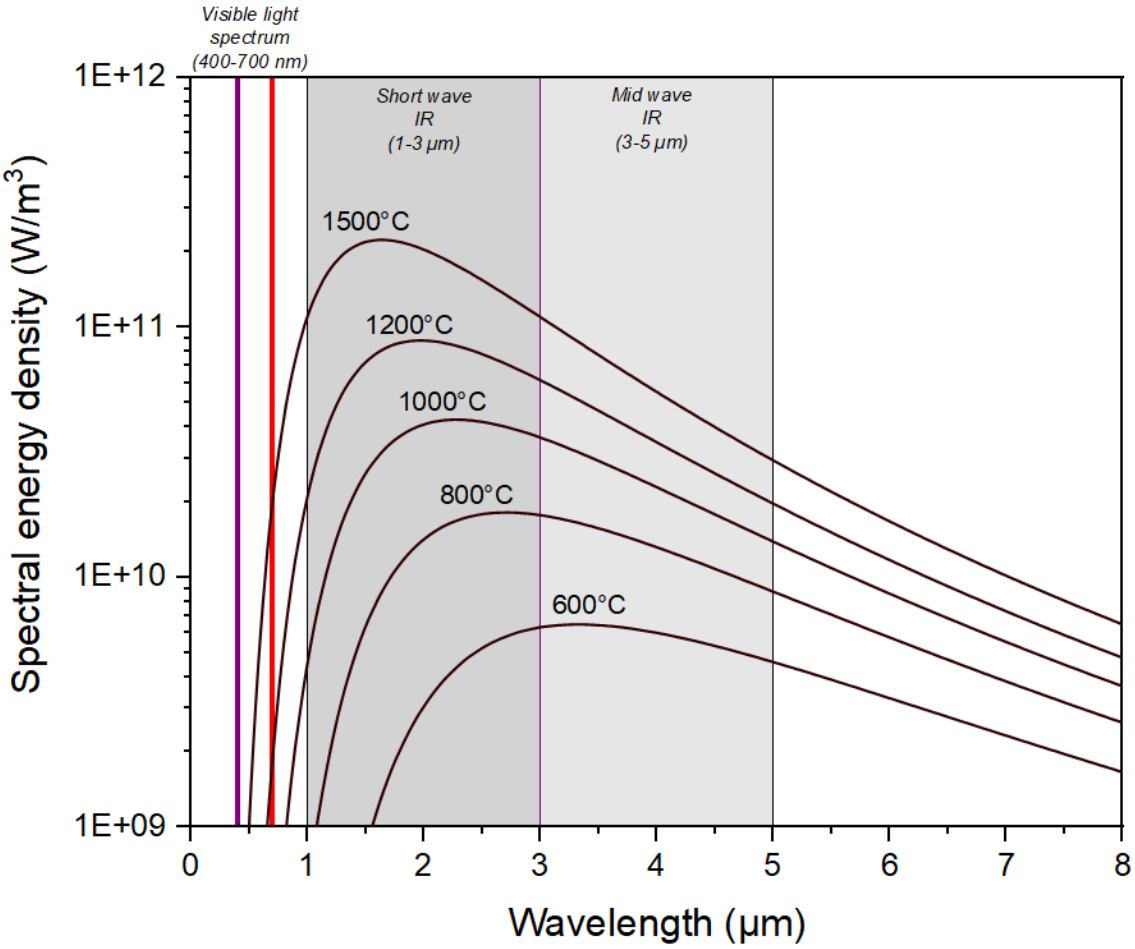

Figure 51. Spectral energy density for a given wavelength at a specified temperature. Black body curves from 600-1500 °C are plotted.

and mid-wave IR parts of the spectrum. Therefore, IRT would serve as a suitable tool for full-field temperature measurements of the cladding during testing. By differentiating the blackbody curves, Wien's law is derived that yields the wavelength of peak intensity for a given body. Concepts like Planck's and Wien's laws, from a granulated perspective, form the theoretical basis of thermography and IR cameras.

The ideal model of an emitting body is a "blackbody", characterized as a perfectly opaque material that absorbs all incident radiation and does not reflect any off or through the surface. In reality, materials behave like "graybodies", as illustrated in Figure 52, that reflect, transmit, absorb, and emit radiation to varying degrees The relative propensity of a material to perform these actions can be expressed through dimensionless coefficients. The emissivity coefficient (ε), for example, describes the relative power of a graybody compared to an ideal blackbody. Its value, ranging between 0 and 1, is defined as,

$$\varepsilon = \frac{P_g}{P_b}, \tag{15}$$

where P_g is the power emitted by the graybody and P_b represents that of a blackbody.

For incident radiation, photons are either absorbed, reflected, or transmitted. As such, the corresponding coefficients must satisfy the relation,

$$\alpha + \beta + \tau = 1, \tag{16}$$

where α is the absorption coefficient, β is the reflection coefficient, and τ is the transmission coefficient. It should be that all these parameters are dependent on factors like wavelength, temperature, and even direction. For metals, due to substantial absorption within a few μm of the surface, the transmission coefficient is effectively zero.

According to Kirchhoff's law of radiation, α and ε are equal when the body is in thermal equilibrium. While any application to LOCA burst testing is not in thermal equilibrium, this principle highlights the connection between a body's emissive and absorptive properties. Lower emissivity surfaces reflect more light, thereby complicating accurate temperature measurements. Understanding emissivity, along with its relation to reflection and absorption, is pivotal for accurate thermographic readings.

IR cameras estimate temperature by using incident radiation and relative intensities across various wavelengths to align emission spectra. However, without specific user input, these cameras

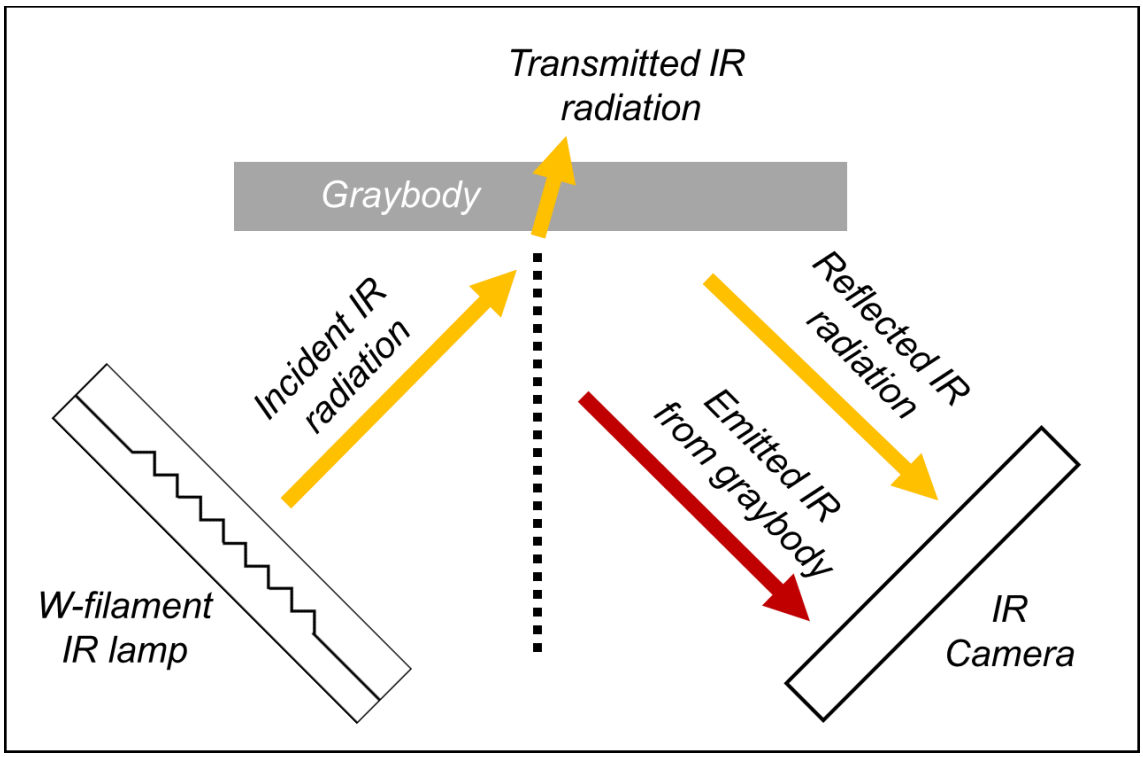

Figure 52. Illustration showing transmission, reflection, and emission of IR that occur when interacting with a material. Reflections off and emissions from the surface are recorded by the camera in summation.

cannot differentiate whether the radiation from a point is a result of body emission or reflection from an external source.

When an external source has a higher temperature, it emits more photons at shorter wavelengths, thereby causing a shift in the perceived spectrum. This reflected radiation can distort measurements, yielding apparent temperatures higher than the true value. Although in many thermographic applications these issues can generally be mitigated using the temperature of the external source, the unique conditions presented in SATS burst testing create a considerable challenge.

In terms of SATS testing, IR radiation is concentrated towards the chamber's center to heat the specimens. The tungsten filaments used for heating naturally have a higher temperature than the sample, and the aluminum chambers are designed to focus the IR towards the center Thus, the dual role of IR radiation; both for heating the samples and for temperature measurement, complicates the fidelity of temperature readings.

This challenge became evident when IRT was first incorporated into burst testing, prompting an early response in preliminary testing to address the issue. However, as will be elaborated upon in the following chapter discussing Zry-4 experiments, the solutions put into place did not completely resolve the issue. This discussion is necessary, given the modifications to the cladding train that arose from this phenomenon and its relevance in the interpretation of results.

Section 6.2: 2D DIC integration and experimental details

6.2.1: Physical integration of 2D DIC and IRT into the SATS

Substantial modifications to the SATS were made in order to incorporate DIC and thermography techniques. Initially, the standard SATS IR furnace was completely enclosed, without any line of sight to the claddings This necessitated the installation of a new furnace with two 2.54 cm viewports positioned 180° apart. Accommodating these viewports required a relocation of furnace elements, resulting in an X pattern formation. Figure 53 provides diagrams of both the standard and DIC-adapted furnaces, clearly illustrating the alterations made. The maximum angle between the chambers is 110°.

In addition to the modifications made to SATS, appropriate camera equipment was also needed for 2D DIC. To capture optical images for 2D DIC analysis, an Allied Vision GT6600

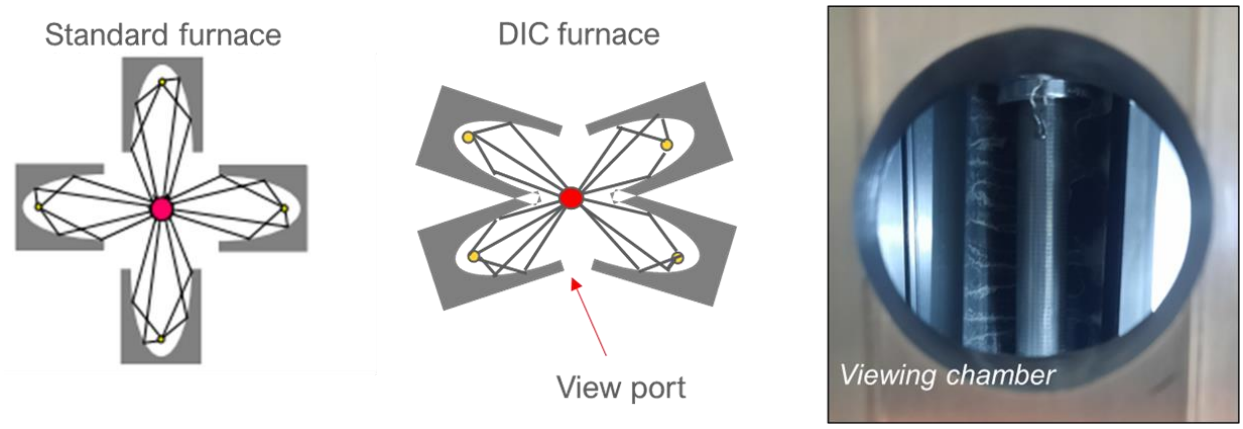

Figure 53. Illustrations of the standard SATS furnace, left, and DIC furnace, right. The deviation from filaments and elliptical chambers at 90º was needed to accommodate the view port for DIC and thermography applications.

camera equipped with a 24-megapixel matrix was employed. This camera supports dataflow rates up to 120 megabytes per second and a framerate of 4 fps [182]. To minimize error associated with out-of-plane motion, a telecentric lens was utilized. A FLIR E95 thermal camera with a 0.162-megapixel matrix was used to measure the temperature of the claddings.

Ensuring that both cameras view the same approximate perspective is critical for providing accurate thermomechanical data. Any significant discrepancy in the camera angles could result in measuring different sections of the cladding. As such, any conclusions drawn regarding the relationship between temperature gradients and non-uniform strain could be skewed.

Several iterations of a DIC/IRT camera setup were tested preliminarily. Figure 54 illustrates two of the iterations for 2D DIC and IRT. The first iteration, as depicted in Figure 54(a), utilized a mirror that reflects IR while remaining transparent to visible light, positioned at a 45º angle to the viewport. The DIC camera equipped with a telecentric lens was placed directly in line with the viewport, while the thermal camera was positioned at a 90º offset. To ensure the same perspective for IR measurements, the mirror was placed between the telecentric lens on the camera and the viewport. An actual image of the setup is found in the next chapter.

The first iteration of the optical setup utilized a mirror (Edmund Optics #64470), shown in

Figure 55(a). This mirror has an average reflection of 95% in the near infrared spectrum (750-1125 μm). However, at temperatures relevant to accident scenarios, the peak wavelength of emissions is not in the near infrared spectrum, as highlighted by the red curve in

Figure 55(b). Experimentally, reflection values at these accident-relevant temperatures were found to be around 10%. Thus, only 10% of the emitted IR radiation was reflected towards the camera. This significantly reduced the signal strength, resulting in suboptimal IR measurements.

As a result, the second iteration of the 2D DIC setup, illustrated in Figure 54(b), saw the removal of the IR mirror. In its place, an optical mirror was positioned at 45° to the viewport opening. The optical camera was positioned at a 90° angle to the viewport, with the optical mirror reflecting light towards it. To maintain approximately the same perspective, the IR camera was positioned at a slight off-angle relative to the opening.

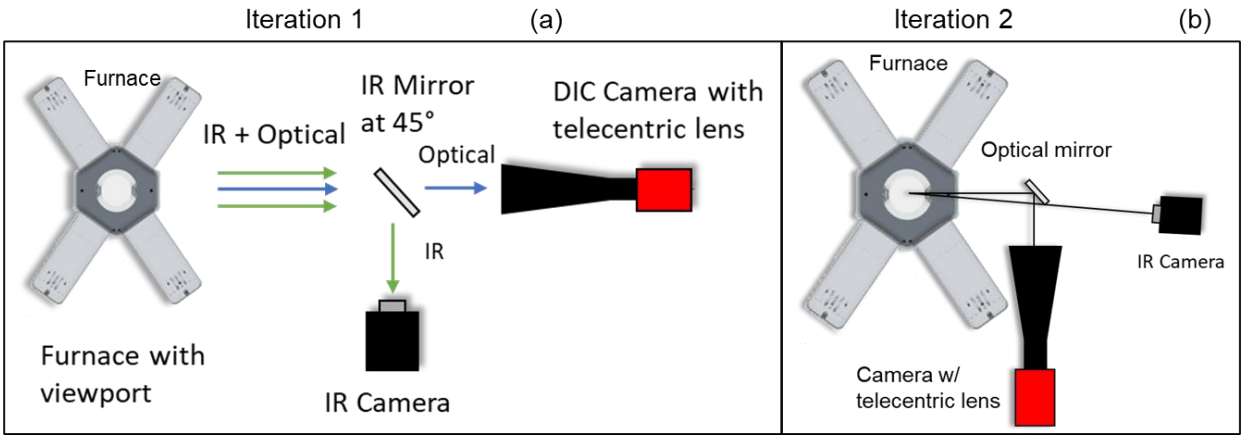

Figure 54. A top-down illustration of the integration of DIC and thermography to SATS testing. The mirror was placed at 45º to ensure the same perspective was seen by the DIC and thermal cameras.

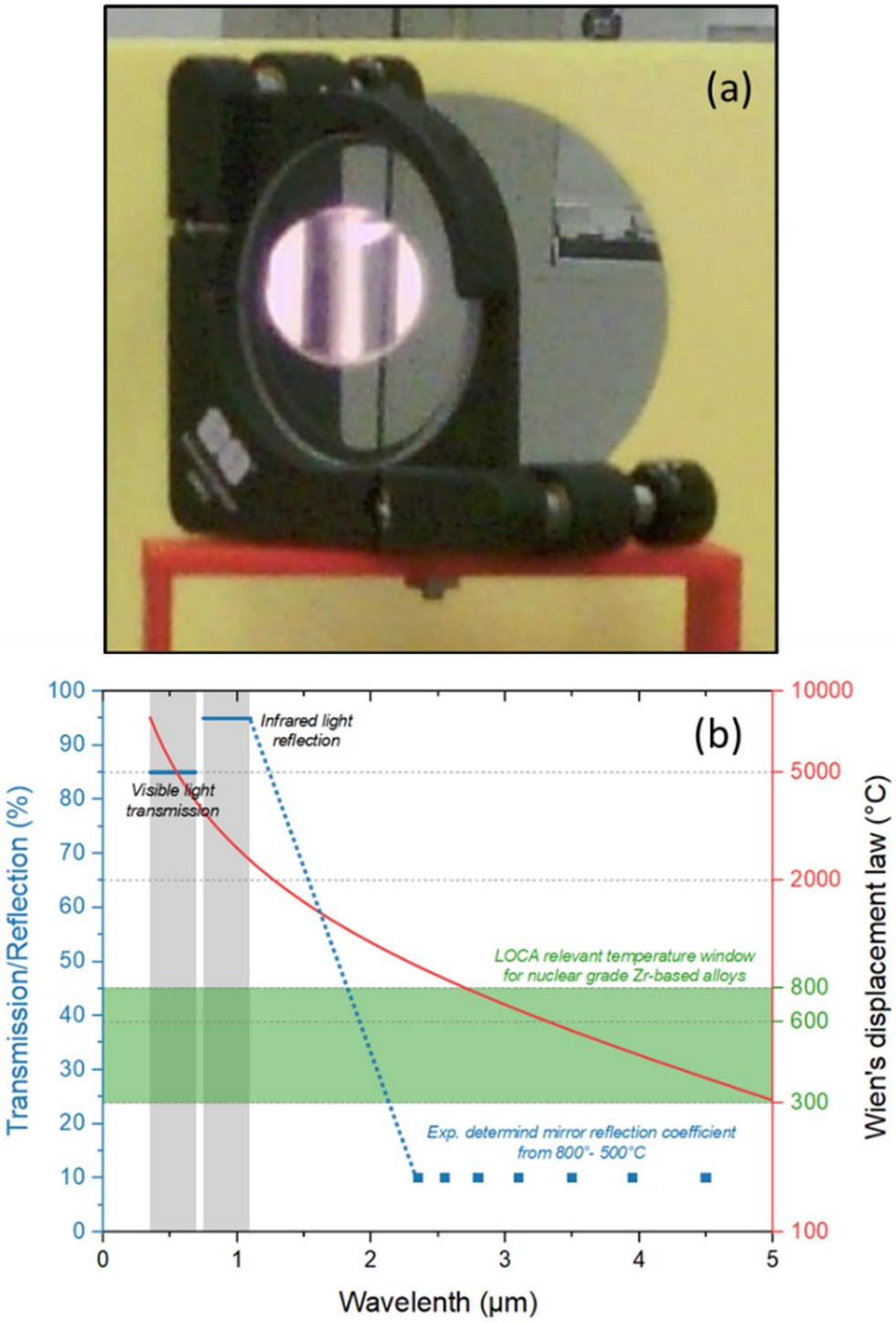

Figure 55. (a) Optical image of the mirror showing the perspective of the IR camera. (b) Plot demonstrating that the reflection of relevant wavelengths for LOCA temperatures is not strong.

6.2.2: Cladding train augmentations and 2D DIC patterning

Modifications to the cladding train assembly were also necessary. Initial 2D DIC burst tests were performed with full 30 cm segments. However, due to the limited size of the viewport (2.54 cm diameter) and minor variations in furnace output, burst events did not consistently occur within the camera's view. Initial attempts to address this issue were performed with 10.16 cm claddings, however, burst was still not centered. To definitively solve this issue, shorter 7.62 cm segments were employed, along with thick-walled 316 SS extensions, to ensure that the burst always occurs directly in view. Standard ramp testing confirmed that the use of smaller segments did not impact the burst strength, as shown in Figure 56.

For 2D DIC patterning, a laser-engraving method was chosen over conventional paint techniques, as the tests were originally planned to be conducted in steam. It was anticipated that a paint speckle pattern might interfere with oxidation kinetics and oxygen transport. Laser engraving involved etching 0.4 mm wide squares onto the cladding surface, positioned every 10 degrees and spaced 0.4 mm apart. Each row along the axial direction contained 60 squares. A LaserGear BOQX emitting 1062 nm wavelength photons and operating at 20 W was employed to apply the engraving pattern. However, later testing utilized an amorphous silica paint that allows steam transport. 3D DIC analysis was also hindered using a laser engraved pattern, further prompting the switch to paint patterning.

The average laser engraving depth ranged from 14-17 um (2-3% of cladding thickness), with the maximum engraving depth of 25 um (4% of cladding thickness) measured. Figure 57(a) depicts a scanning electron microscopy (SEM) image of the region opposite the burst for a laser engraved test.

To measure the surface height of the laser engraved cladding, a structured light scan was conducted using a Keyence VR-3000 microscope. Figure 57(b) presents a height profile along one side of the engraving from this scan, indicating a depth of ~17 μm. Debris is visible on either side of the engraving in Figure 57(a) and Figure 57(b), elevated above the nominal surface of the cladding.

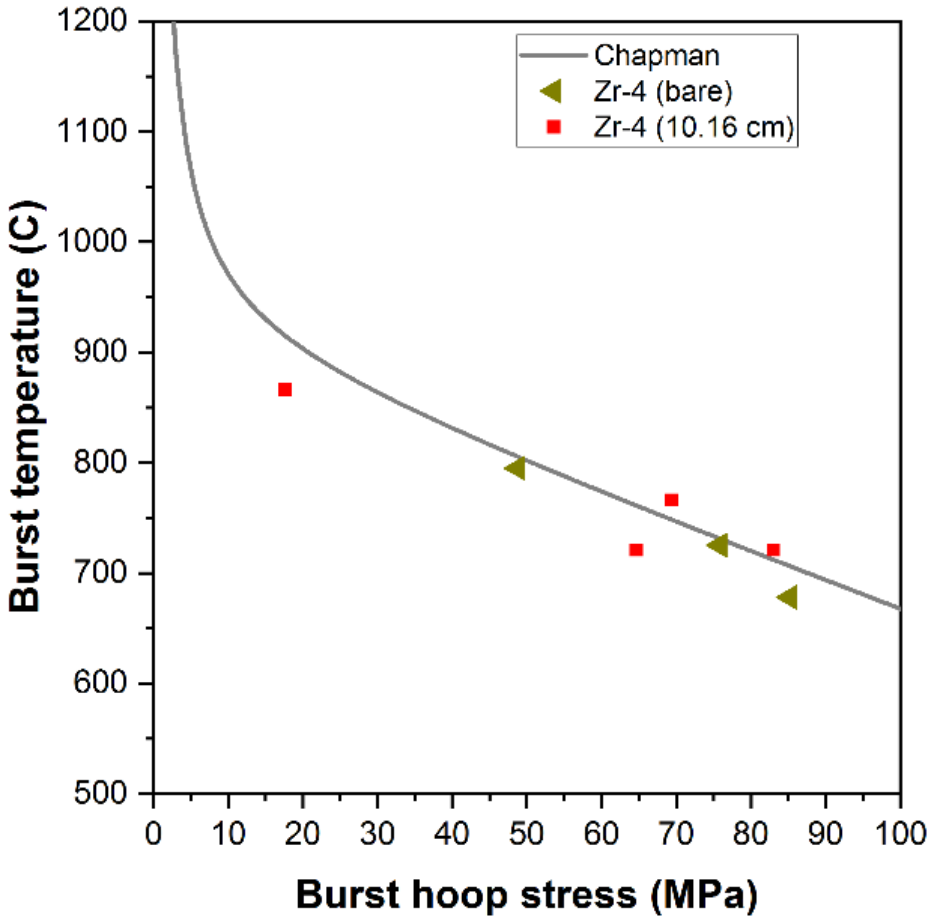

Figure 56. Burst hoop stress versus burst temperature for 10.16 cm and 30 cm segments of Zry-4. No effect on burst strength was discernable when smaller cladding segments were used.

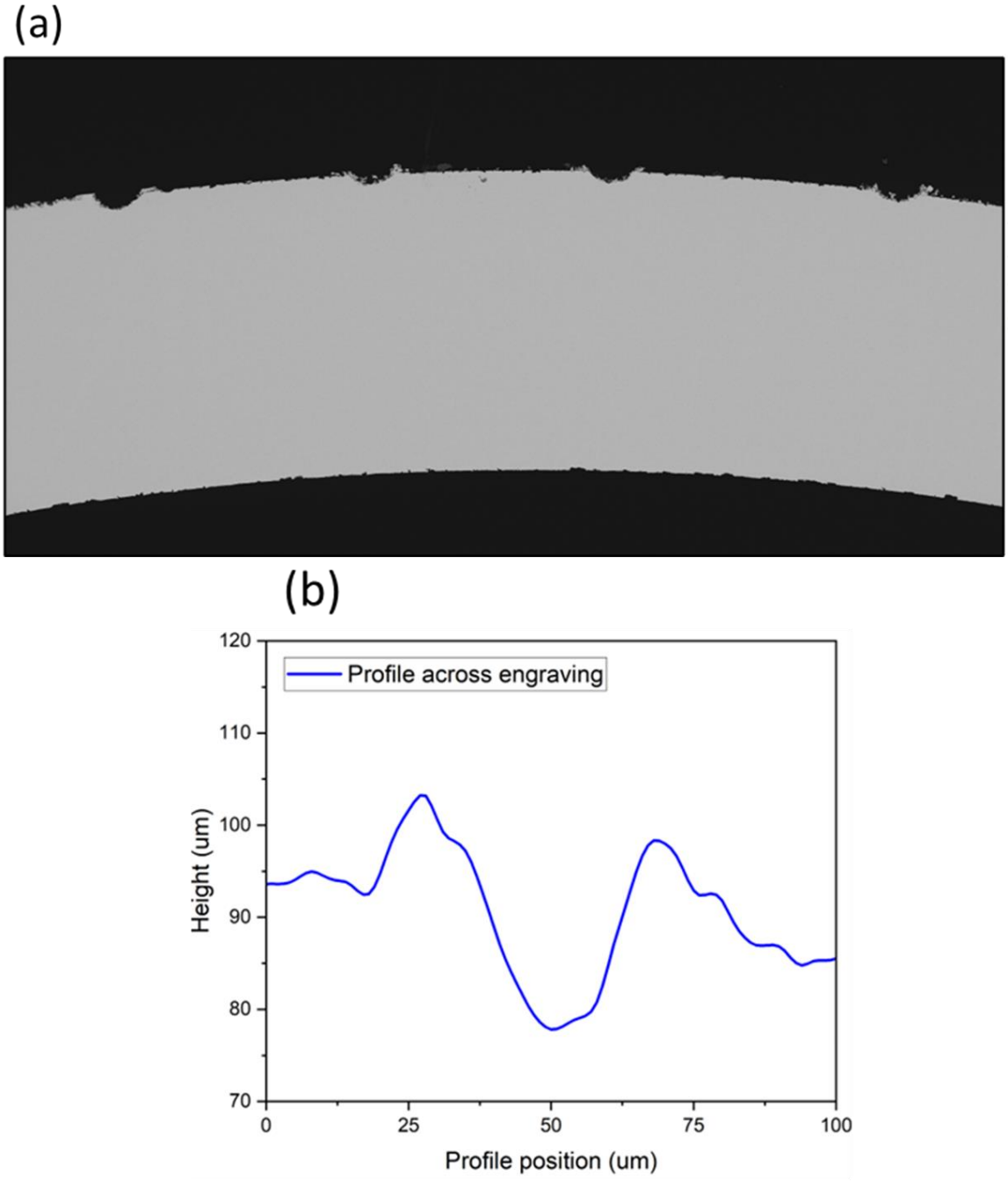

Figure 57. (a) SEM micrograph after a test from the side of the cladding opposite burst. (b) Profilometry results from the structured light scan, show the topology of an engraving that was 17 µm in depth.

6.2.3: Technical challenges in preliminary 2D DIC testing

Challenges arose when IR was used to heat the cladding segments and measure IR emissions simultaneously, as alluded to previously. Due to the low emissivity of unoxidized Zr approximately 0.2-0.32 [183,184], reflections from the tungsten filaments were observed on the cladding surface, as seen in Figure 58. These reflections skewed temperature readings towards higher values, increasing uncertainty.

The emissivity of oxidized Zry-4 is significantly higher, ranging from 0.86 to 0.91 [185].Since thermal emissions from any material are inherently a surface phenomenon, only a few microns of oxide formation are required to change the cladding's emissivity. This implies that the formation of an oxide layer formed during 2D DIC testing could largely mitigate the problem of reflections. Burgoyne et al. [186] found that the emissivity value of Zircaloys changed from approximately 0.27 in the as-received condition to nearly 0.85 with the formation of just a few microns of oxide. They further noted that Zircaloy materials become "opaque" after ~3 μm of zirconia is formed. A comparison of oxide scales and the determined emissivity from preliminary testing using 2D DIC and a laser-engraved pattern is presented in the next chapter.

The visible light emissions from the filaments posed another challenge, particularly for DIC pattern recognition. One of the fundamental principles of DIC is maintaining a stable light environment [182,187]. While there are computational methods available to account for changes in greyscale/pixel values, variation in or too much lighting of the surface pattern can reduce data quality. Changes in lighting alters the greyscale of a subsequent image, making tracking more difficult and less reliable. Oversaturation can wash out the pattern entirely, leading to complete data loss in those regions. For SATS LOCA testing, the power output from the furnace elements changes during the ramp leading to greater illumination. Additionally, as the cladding balloons the location of incident light on the cladding also changes. As such, the lighting environment is unstable, which led to drop in pattern tracking during preliminary testing. Figure 59 illustrates this issue where pattern recognition was maintained up to ~8 seconds before ballooning. However, once ballooning started, the changes in filament reflections led to pattern drop.

Two strategies were considered to address the issues of visible illumination instability and IR reflection. The first approach involved applying a speckle pattern using high emissivity paints to the cladding surface to substantially reduce IR reflections. This method, using black and white

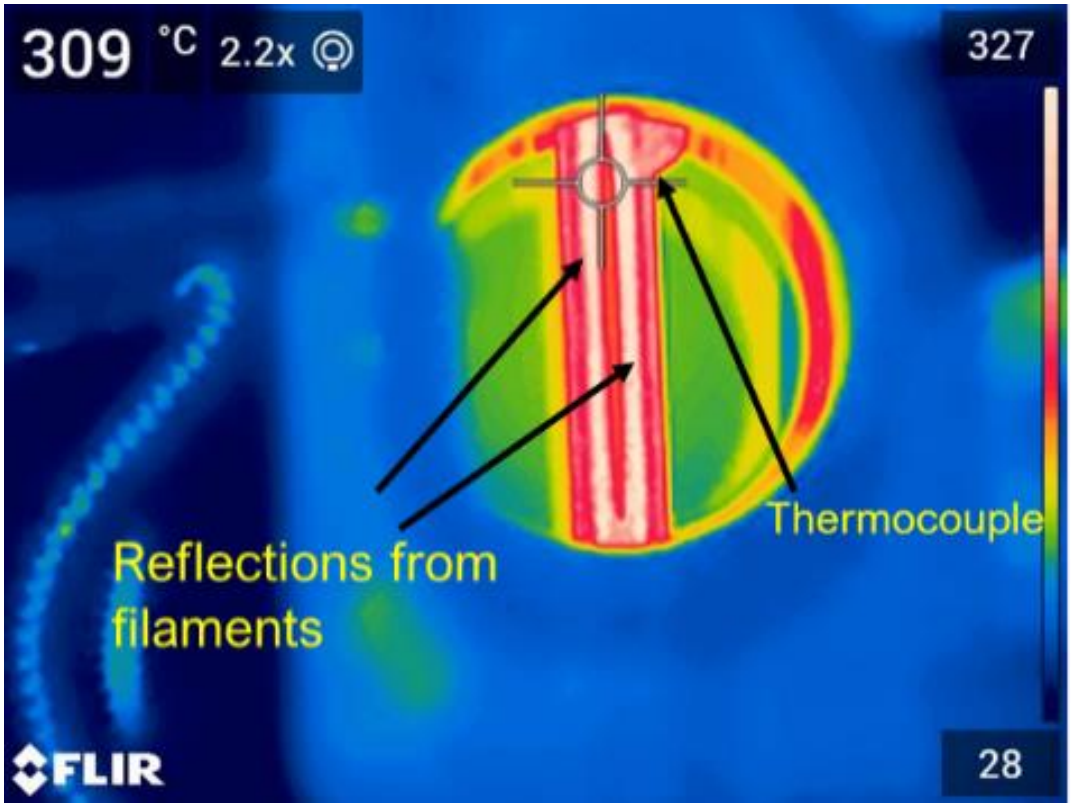

Figure 58. Thermal image of a unoxidized Zry-4 segment in the DIC furnace. The thin white lines on either side of the cladding center are reflections from the filaments in elliptical focusing chambers.

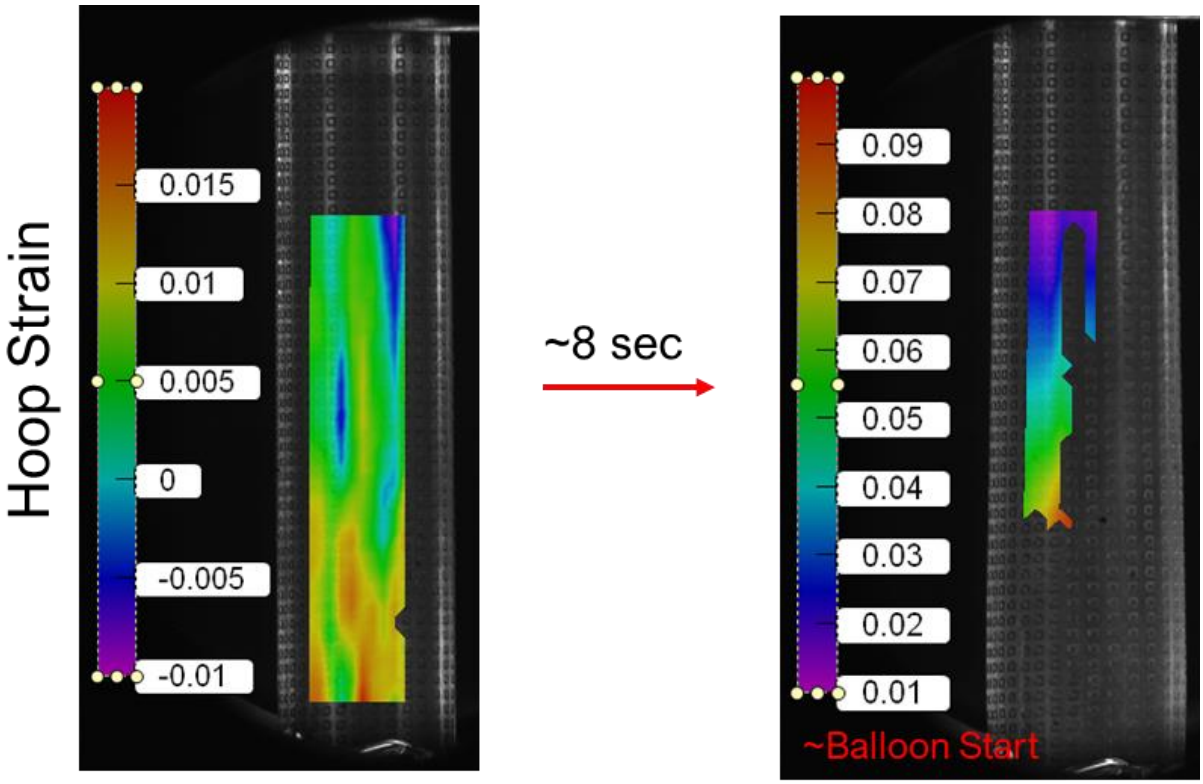

Figure 59. Optical images from the DIC camera of cladding segments ~8 s before burst, left, and just after burst began, right. The colored square on the left image is the DIC strain field, with minimal pattern drop. The image on the right shows severe pattern drop, owing to the ballooning of the cladding changing the angle of incident light from the filaments.

paint, would provide the consistent greyscale contrast needed for easier subset tracking. The long-term goal was to apply these techniques to steam environments.

A layer of paint approximately 25-50 µm thick could potentially obstruct steam oxidation [182] and alter the mechanical behavior of a Cr coating. While specialized amorphous silica paint was later discovered to allow steam oxidation to occur, this fact was not initially known, and 2D DIC testing was completed using laser engraving. Yet, given the engraving depth of ~14-17 µm (about 2% of cladding thickness) in current testing, if applied to Cr coatings of 5-30 µm, a significant reduction in coating material could occur. Therefore, shifting to amorphous silica paint had a dual benefit.

The second strategy involved blocking incident radiation, a method chosen for implementation as it avoided altering surface characteristics. A 7.62 cm long SiC "C" shell was made from a Hexoloy reaction tube to entirely encase the Zry-4 segment. Figure 60 shows images of the C shell integrated into the cladding train. With the high emissivity of SiC Hexoloy (~0.8-0.9) [188], the C shell absorbed most of the focused radiation from the filaments, effectively making it into a furnace element that reradiated and conducted the energy more uniformly. This led to an even temperature distribution on the cladding surface without reflections, as demonstrated in the thermal image of a cladding at approximately 527 °C with the SiC shell implemented, seen in Figure 61.

Unfortunately, the SiC shell's introduction negatively impacted the quality of temperature measurements. Resolving the cladding temperature became more challenging due to uniform heating and the higher temperatures of the SiC shell relative to the cladding, thus reducing the contrast between the two. As a result, resolving the cladding edges proved difficult.

One of the main concerns regarding the C shell's implementation was its effect on heating rate. However, the target heating rates inside were achieved within a margin of ± 0.1°C/s.

Section 6.3: 3D DIC transient and step loaded isothermal creep testing details

6.3.1: 3-dimensional DIC configuration for SATS testing

The implementation of 3D-DIC significantly improved in-situ strain measurements in terms of capturing the full balloon shape and process. The 2D-DIC method falls short in determining the full three-dimensional motion of the cladding surface during ballooning. Out-of-

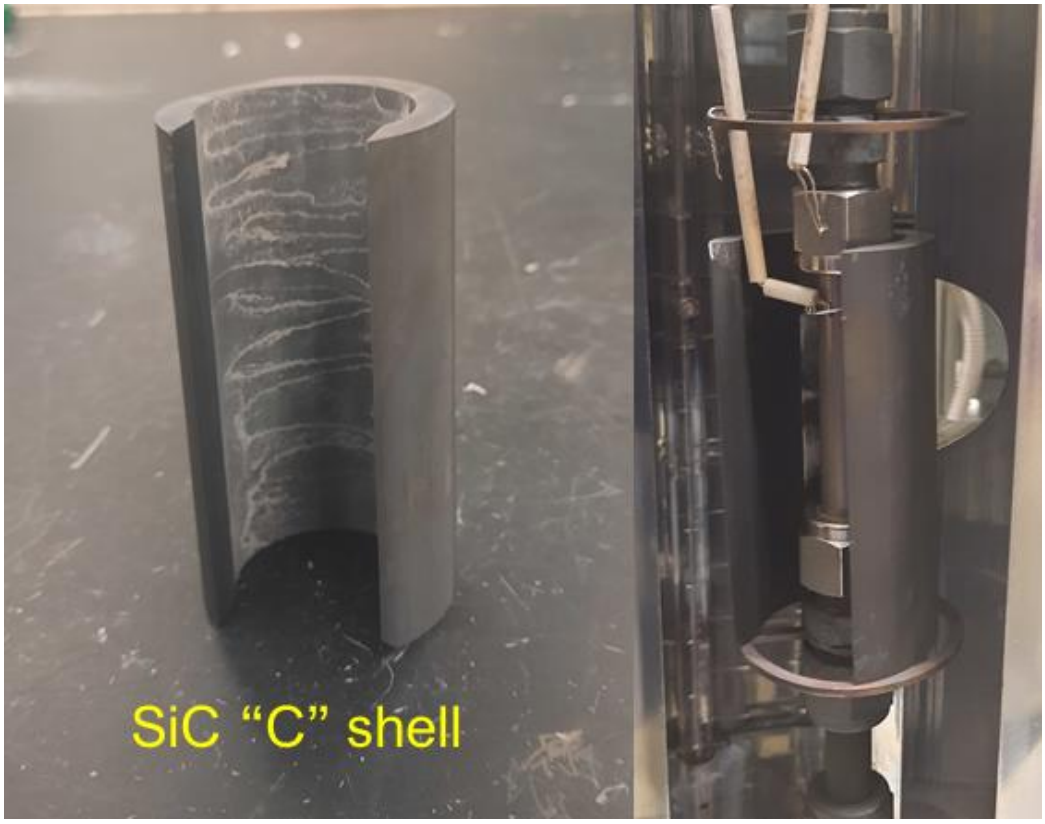

Figure 60. Image of the SiC Hexoloy “C” shell employed to block filament reflections.

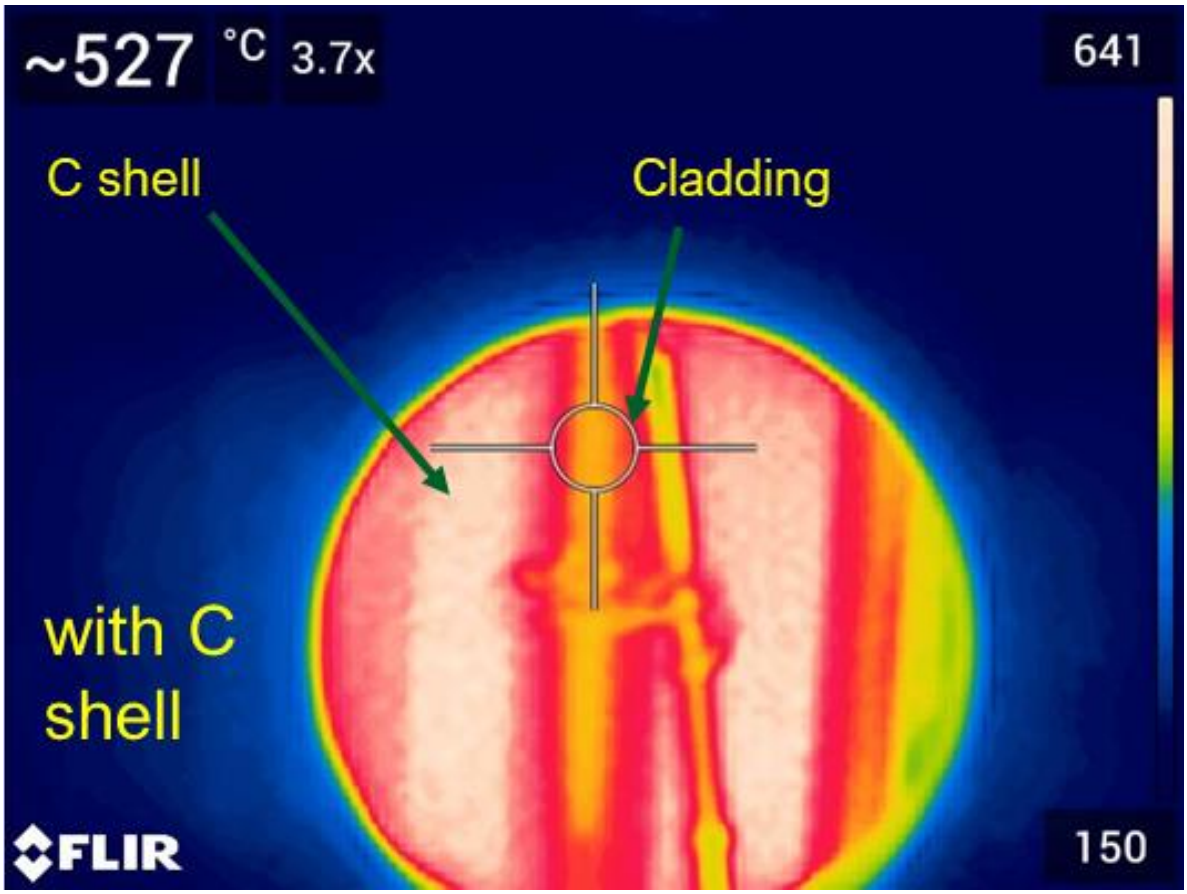

Figure 61. Thermal image from a test run with the C shell implemented. Uniform temperature gradients on the cladding surface are observed. However, resolution of the image was severely reduced due to the even temperature profile and the hotter C shell in the background.

plane rotation can introduce strain bias during burst testing, even when a telecentric lens is employed. While the error associated with 2D DIC can be lessened by limiting analysis to roughly planar regions or applying corrections (as was done in this dissertation and previous testing by Campello et al. [177]), 3D DIC has the potential to have higher fidelity. Additionally, 3D DIC enables reliable analysis of a larger portion of the cladding surface.

The general principles of DIC remain the same, but the comparison of two perspectives allows for the measurement of 3D displacement and strain. Figure 62(a) and Figure 62(b) show examples of the displacement measurements achievable by 3D DIC systems, as well as a strain map from a preliminary burst test, respectively. The data is from the frame immediately preceding burst and illustrates that the balloon geometry is captured.

A graphic of the 3D DIC setup is shown in Figure 63(a) and an image of the test setup is presented in Figure 63(b). Currently, a 3D DIC system from Correlated Solutions Inc. is integrated with the SATS system. Two 6-megapixel Grasshopper 3 cameras with blue light filters attached to the lens are positioned directly in front of the furnace opening. Blue light filters are necessary, as the light emitted by the tungsten filaments during testing could otherwise overwhelm the sensors. Blue lights are situated behind the camera to provide some level of stable lighting visible to the camera throughout the tests. The cameras are ~1 m away from the furnace center with the crossbar holding the cameras perpendicular to the furnace opening. A stereo angle of 20° is utilized for this setup due to the current viewport geometric constraints.

6.3.2: 3D DIC transient testing methods and augmentations

The application of 3D DIC to transient burst testing employed the setup detailed above and the general structure of the SATS experimental methods discussed in Chapter 1. Transient testing with 3D DIC integration followed similar pressure and temperature profiles to conventional SATS testing. Heating rates of 5 °C/s were used to heat the claddings to 300 °C for a 5-minute hold. After this hold, the claddings were ramped again at 5 °C/s until failure, at which point the furnace was shut off. Unlike conventional SATS testing, a 5-minute hold at 1200 °C was not applied. This modification aimed to assess cladding microstructure at failure temperatures. All 3D-DIC integrated transient testing was conducted in a steam environment.

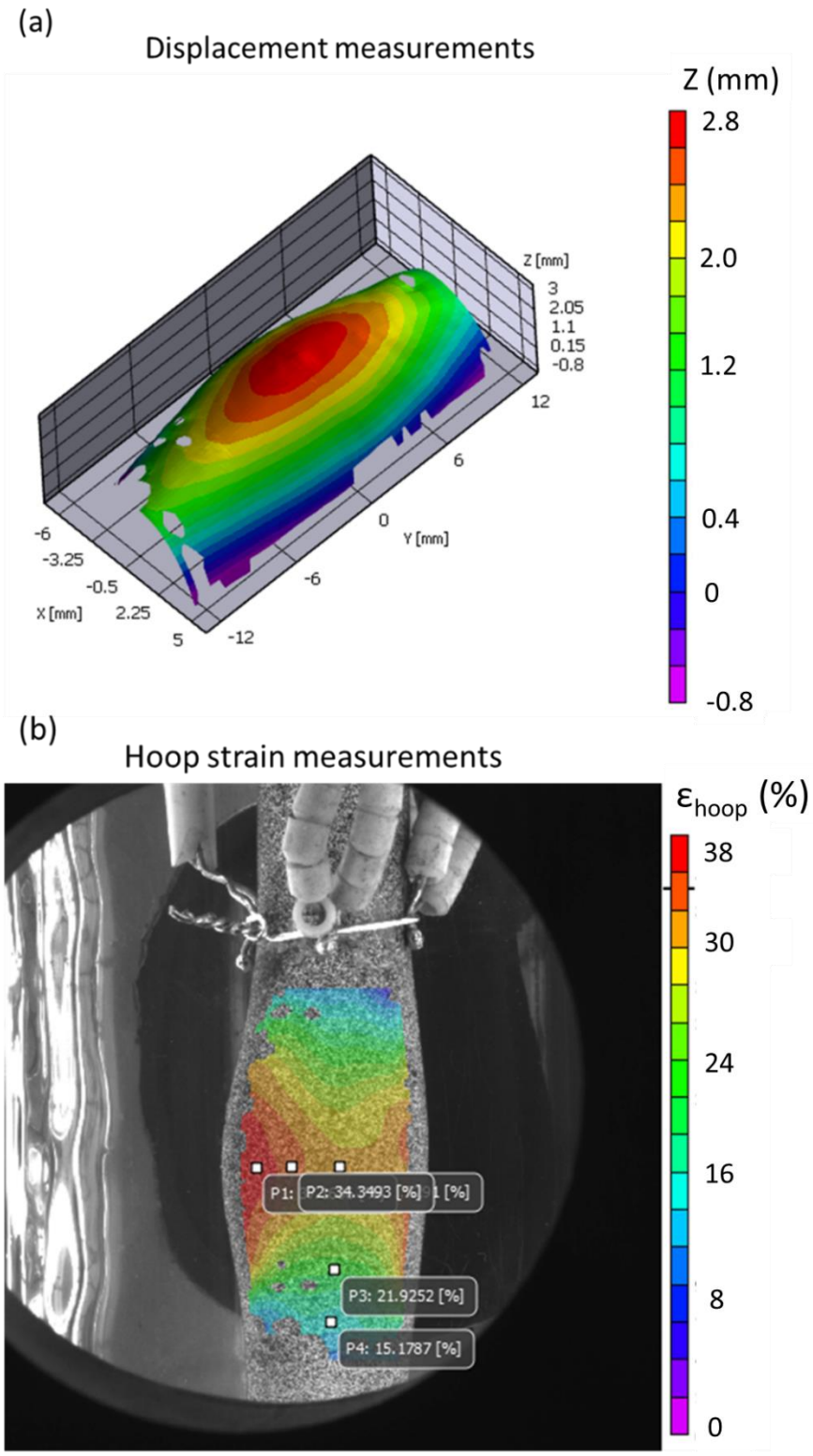

Figure 62. (a) 3D surface generated from a test near the final stages of ballooning. (b) Hoop strain measurements projected on the image from the same stage in ballooning.

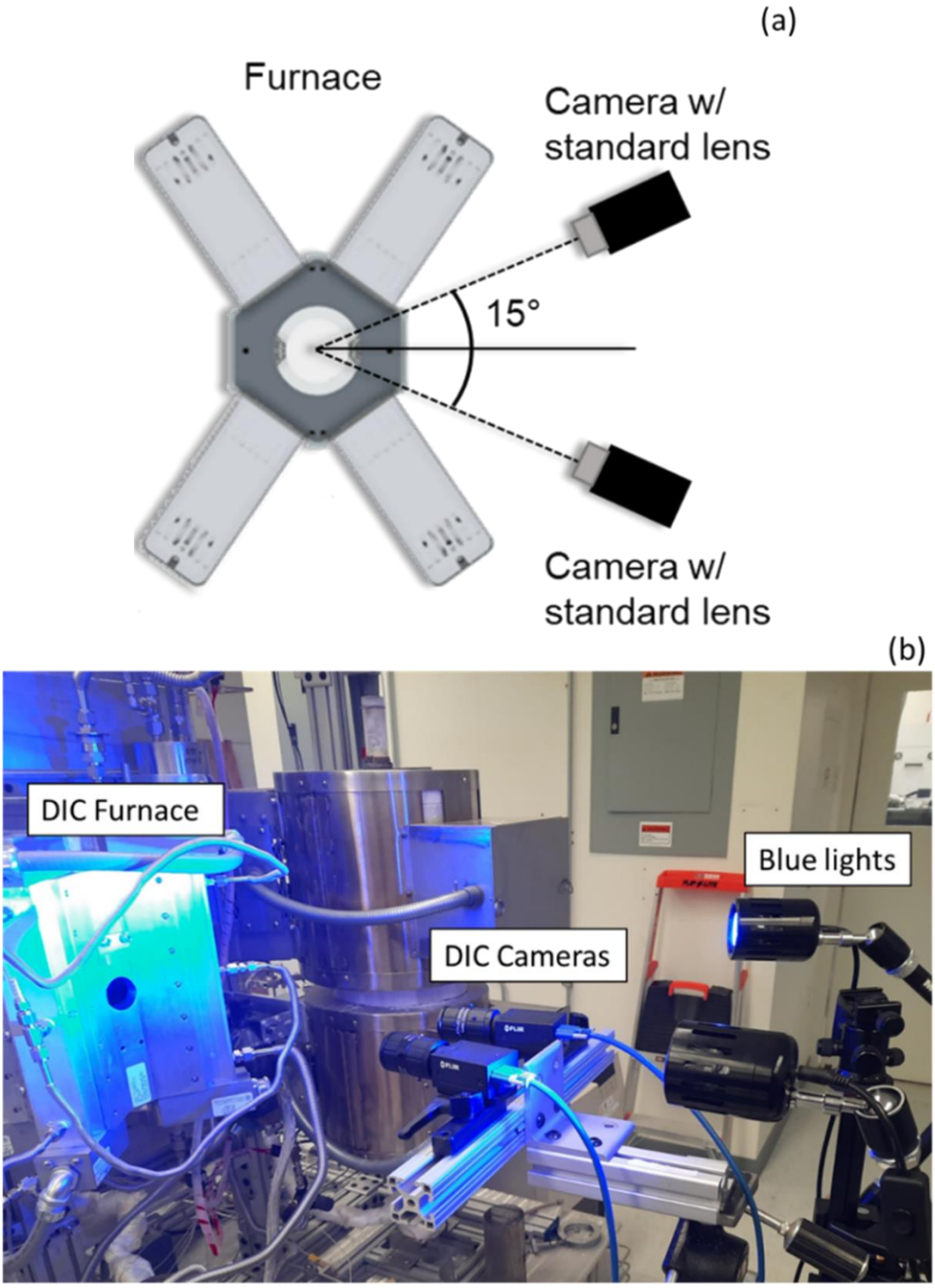

Figure 63. (a) Graphical illustration of the 3D DIC setup with two cameras at a stereo angle of ~20 °. (b) Photograph of the camera setup and lighting.

The claddings used in 3D-DIC integrated transient testing were coated with approximately 30 µm thick paint to create a speckle pattern. This paint allowed for steam transport, as evidenced by oxide formation, which will be further discussed in subsequent sections. Similar to the previous 2D DIC experiments, shortened segments of 11.4 cm (4.5”) claddings were used for transient testing with 3D DIC. To maintain specimen length in the furnace, 6.5 cm 304 stainless steel segments were placed on either side of the cladding. An 11.4 cm alumina filler rod was placed inside the cladding segment to simulate fuel volume and thermal mass. This change was made to minimize potential effects of compression fittings on thermal gradients and balloon development that are discussed in the next chapter.

Significant modifications were made to the thermocouple setup for the 3D-DIC integrated testing. In standard SATS testing, two thermocouples are positioned at the cladding's centerline of the 30 cm long segment, and two more thermocouples are placed ~50 mm above and below the centerline. Burst typically occurred between the centerline and adjacent thermocouples due to the constraint from the Pt-Rd wire used to attach the thermocouples. While this constraint had no impact on target parameters such as burst pressure and temperature, it prevented simultaneous measurement of temperature via thermocouples and strain from the cladding surface using DIC.

To address this issue, two thermocouples were placed 12 mm above the cladding centerline directly in view of the camera system and 180º from the viewport. For transient testing, an additional thermocouple was positioned near the midline of the cladding segment, approximately 45-60º from the other thermocouples. This configuration allowed for simultaneous temperature measurement and strain analysis using DIC. The burst parameters obtained from this setup were consistent with historical data and conventional SATS testing, as detailed in subsequent chapters.

6.3.3: 3D DIC isothermal creep testing

Isothermal creep testing is a significant addition within the accelerated SATS framework, allowing for more rapid creep model development and validation. Previously, such testing was not feasible due to the absence of in-situ strain measurement capabilities. To expedite qualification in this context, a modified approach called step-loading during isothermal burst testing was developed. The step-loading method involved incrementally increasing the pressure at predetermined time intervals while maintaining a constant temperature. This approach aimed to extract the stress exponent, n, at a specific temperature from a single creep test. Figure 64 provides

an example of the pressure history and associated strain data obtained from a 700 °C Zry-4 step-loaded test. Note the linear strain sections associated with the majority of each pressure step, characteristic of a steady-state. Within the paradigm of Zr cladding dependence on thermal creep, this technique could yield more accurate n values for use in modeling. This is particularly relevant as traditional models exhibit variations in the assumed stress exponent, as discussed in Chapter 5.

The cladding train configuration used in the isothermal burst testing was identical to that of the 3D DIC transient testing, with 304 stainless steel spacers placed on either side of the cladding segment. Temperature monitoring involved the placement of two thermocouples (TCs) positioned 12 mm above the cladding centerline. The TC responsible for controlling the furnace output was positioned directly in front of the viewport and cameras. Another TC, located 180 °C from the first TC, was placed at the back of the furnace to assess azimuthal temperature gradients. The test procedure began with heating the samples to 100 °C for a pressure check. Subsequently, the claddings were heated to 300 °C at a rate of 5 °C/s and held at that temperature for 5 minutes. The cladding trains were then further heated to the target temperature at the same rate of 5 °C/s. The samples were maintained at the target temperature for a specific duration before pressure was applied using Ar gas.

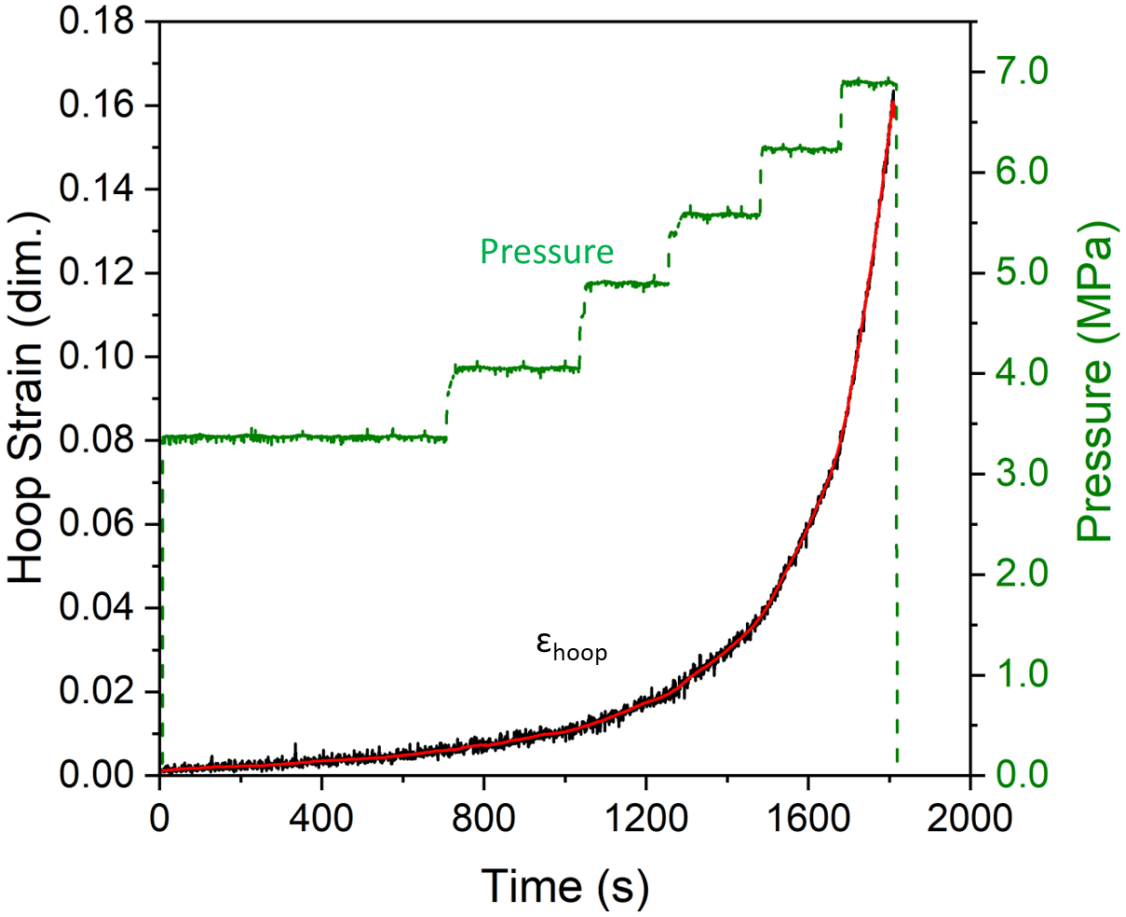

Figure 64. Example of a typical strain and pressure history from a SATS step-loaded isothermal creep test. The units of hoop strain "dim." represent the dimensionless quantity of mm/mm.

Chapter 7: Transient Testing of Zircaloy-4 with 2-dimensional DIC

Chapter Foreword

This chapter outlines the initial experiments incorporating 2D DIC into SATS testing, focusing on shortened segments of SRA Zry-4 to establish a baseline and verify the framework's validity. The investigation of the temperature dependence of Zry-4 and the traditional role of steady-state creep in Zr alloy LOCA behavior are highlighted. Distinct from traditional SATS testing, the heating rate is reduced to 1 ºC/s, and experiments are conducted in a laboratory air setting for reasons elaborated in previous sections.

A transition in temperature dependence was found for strain rate, with Arrhenius dependencies consisting of two segments. Activation energies were determined, with the average activation energy of the lower temperature regime found to be 328 ± 25 kJ/mol, in agreement with the ~320 kJ/mol used for conventional LOCA models. The higher temperature segment demonstrated increased activation energies as well as a dependence on whether the rupture formed in the analysis region. For tests where the rupture opening was away from analysis region, the average high temperature activation energy was 635 ±150 kJ/mol. For samples where the rupture opening was analyzed, the average activation energy was 1015 ± 179 kJ/mol. However, the high temperature activation energy is likely not representative of creep mechanisms and is treated as an apparent value. This is supported by comparison of the stress state for this high temperature segment to yield stress models, for which the data was well beyond, implying the high temperature deformation behavior is related to plastic instability.

This change in temperature dependence indicates a transition in deformation mechanism at the end of life, which has not yet been reported in the literature for Zr alloy LOCA behavior. Parameters at the transition points were analyzed to determine thresholds for this change in behavior. Final strain rates before rupture were also observed to be linearly dependent on both burst pressure and temperature, suggesting that a strain rate-based failure criterion may better describe Zr alloy cladding failure than a stress-based criterion.

Section 7.1: INTRODUCTION

Postulated design-basis accident scenarios in LWRs, such as a LOCA, subject nuclear fuel cladding materials to rapid thermal transients, dynamic internal loading, and high temperature

steam environments. During the transient, the Zr claddings typically balloon and burst as a result of the internal gas pressure (Helium and fission gas).

The nuclear community has long utilized "burst testing" as a means of assessing fuel cladding performance under accident conditions. The two prominent forms of burst testing are: (1) transient heating testing where pressurized claddings are heated at a specified heating rate [18,26,28,30,32] and (2) more conventional isothermal creep, constant loading burst testing [58,120,189]. Within transient testing (1), two additional subtypes of experiments are found: (a) isobaric testing where cladding samples are connected to a fixed pressure reservoir [18] and (b) constant-gas-inventory testing where the amount of gas present in the rod is fixed and pressure is allowed to vary with temperature [28,30]. The latter testing separates the effects of varying pressure on analysis while the former is more proto-typic of pressure conditions during an accident transient.

Conventional modeling efforts of Zr cladding burst behavior assume steady-state creep is dominant [18,33,125,133,190]. This assumption is a reasonable basis, as thermal creep rates for Zr alloys are significantly higher than other material concepts such as Fe-based alloys [191–193]. While LOCA transients subject claddings to inherently non-steady state conditions, application of power law creep has yielded reasonable results in historic [18,33] and modern efforts [133,191,194]. Current creep models assume the creep rate follows a power-law form with an Arrhenius temperature dependence. A general expression of the power-law description for effective strain rate is given by,

$$\dot{\varepsilon}_{eff} = A_{eff}\sigma_{eff}^{n}e^{\frac{-Q}{RT}}, \tag{17}$$

where $\dot{\varepsilon}_{eff}$ (s^{-1}) is the effective strain rate, A_{eff} ($MPa^{-n}s^{-1}$) is the structure constant, n is the stress constant, σ_{eff} (MPa) is the effective stress, Q (J/mol) is the activation energy, R (J/mol-K) is the gas constant, and T (K) is temperature. Such parameters are determined from traditional constant temperature and load creep testing [120,123].

The stress exponent for Zry-4 for LOCA relevant creep testing in the α-phase is found in the range of 4.94 – 5.89 [18,120,33,123]. Activation energies used in conventional LOCA models [18,33,125] are ~320 kJ/mol, in relative agreement with the self-diffusion activation energy [121] of Zr. If the Arrhenius temperature dependence explicit in the steady creep LOCA models is

accurate, real-time strain deformation data prior to and during ballooning should provide useful for model validation. More specifically, it should be possible to extract a consistent, Arrhenius temperature dependence of strain rate.

Confirmation of this temperature dependence necessitates simultaneous measurement of strain, strain rate, time, temperature, and pressure. Historic LOCA testing has typically focused on *ex-situ* parameters and failure criteria, i.e., end-of-life metrics. Relevant parameters such as burst pressure, burst temperature, rupture opening size, and post-test diametric strain have been critical for code validation and supporting safety basis. However, *in-situ* strain measurements are vital to refining material models and understanding, particularly when considering advances in LWR operational efficiency and safety.

Efforts are ongoing to extend burnup levels beyond a peak rod average burnup of 62 GWd/MTU to improve the economic efficiency of nuclear power plants. [34]. With higher burnup levels, severe degradation of the fuel pellets during a transient may occur [34,195], leading to concerns of fuel fragmentation, relocation, and dispersal. Additionally, the rod internal pressure is expected to be higher, increasing the possibility of cladding failure in the low-temperature (< 808 °C) anisotropic α-Zr phase [9,196]. Consequently, refinement of current LOCA models in the α-phase is necessary for reliably assessing safety concerns related to high burnup extension.

In-situ techniques were integrated into simulated LOCA burst testing and applied to Zry-4 claddings. The SATS at ORNL was out-fitted with DIC and IRT capabilities to provide thermomechanical data during a transiently heated burst test. From such data, novel insights into the LOCA behavior of Zr claddings were found. Moreover, this methodology has value for new ATF claddings and could significantly reduce testing needs for developing cladding concepts as a single test generates a statistically significant amount of data. For instance, a better understanding of bare Zr claddings enables a more rigorous investigation of Cr coating effects on LOCA performance. This testing serves a dual purpose: (1) refining understanding of incumbent Zr claddings and (2) validating this methodology for accelerating qualification of future materials during LOCA conditions.

Section: 7.2: EXPERIMENTAL METHODS

Transient burst testing in an air environment was conducted on SRA Zry-4 cladding segments using SATS. The nominal ingot chemistry provided by the manufacturer is presented in Table 13 in weight percent. EBSD analysis was conducted on an as-received cladding sample cross-sectioned perpendicular to the axial direction. Analysis was performed using a Tescan MIRA SEM operating at 30 kV. A band contrast and inverse pole figure for a 120 by 120 µm region are shown in Figure 65(a) and Figure 65(b). The step size for collection was 0.5 µm.

A bimodal grain size distribution can be seen in Figure 65, with a mixture of recovered (fine grain regions) and larger recrystallized grains. Figure 66 presents a distribution of the grain size recovered from EBSD analysis. A threshold minimum of 10 pixels was used to determine a grain, leading to an ~0.8 µm resolvable grain. In other words, the distribution does not reflect a significant portion of the microstructure by not incorporating sub-micron grains, yet still gives insight into the bimodal distribution. The grain size exhibited two peaks at 1 µm and 4 µm, with an average size of 3 µm. A map of band contrast overlaid with kernel average misorientation (KAM) is presented in Figure 67, showing the recrystallized grains in blue and the recovered grains in increasing KAM.

Pole figures for the {0001}, {10-10}, and {11-20} orientations are presented in Figure 68 to investigate the as-received texture. As the tube is only stress relieved and was not subject to a full recrystallization heat treatment, the tube retains its preferred grain orientation from the tube fabrication process. The two peaks offset by 30-45° from the center of the {0001} pole figure are indicative of the split basal texture, which is characteristic of Zr forming/rolling processes as discussed in Chapter 1.

The claddings had a nominal as-received outer diameter and wall-thickness of 9.5 mm and 0.575 mm, respectively. The testing presented in this section utilized the shortened cladding train configuration with a SiC shell, 2D DIC and IRT camera setup, and furnace configuration presented in Chapter 6, but a schematic of the setup is presented in Figure 69 again.

Eight burst tests in an air environment were completed to investigate the temperature dependence of SRA Zry-4, with internal pressures ranging from 6.2 to 15.1 MPa (Table 14). An 8 mm diameter alumina filler rod was also present inside the cladding segment to simulate fuel

Table 13. Ingot chemistry for SRA Zry-4 in weight percent.

Sn	Fe	Cr	C	O	Si	Zr
1.32	0.22	0.10	0.04	0.12	0.12	Balance

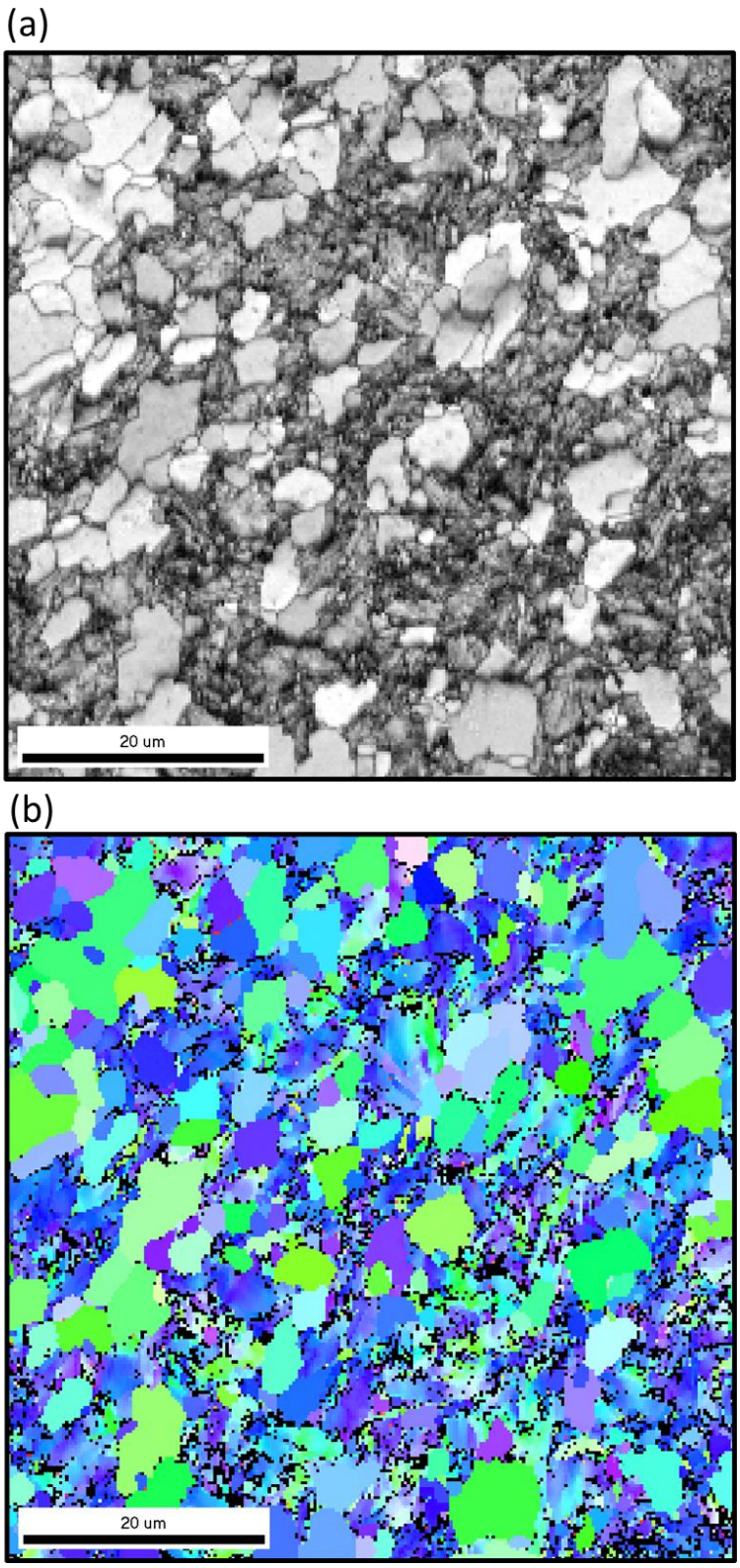

Figure 65. Band contrast (a) and IPF maps (b) of the SRA Zry-4. Courtesy of Caleb P. Massey.

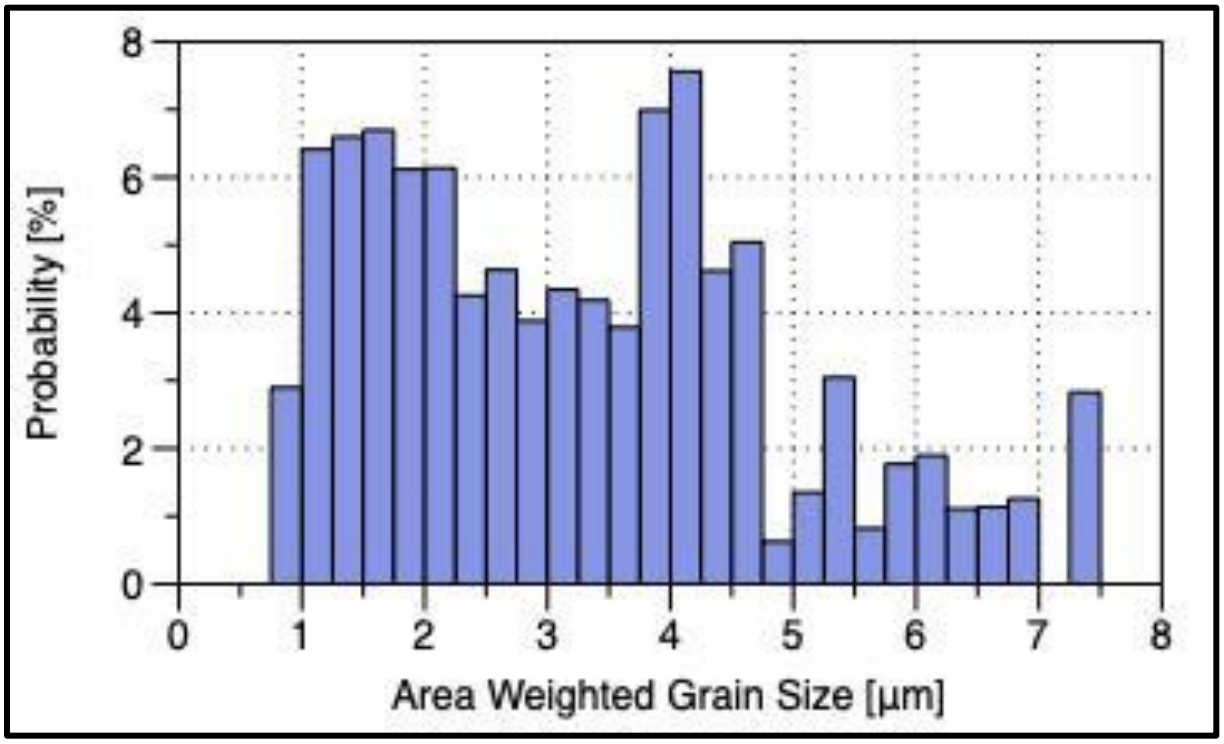

Figure 66. Grain size distribution for the tested SRA Zry-4. Courtesy of Caleb P. Massey.

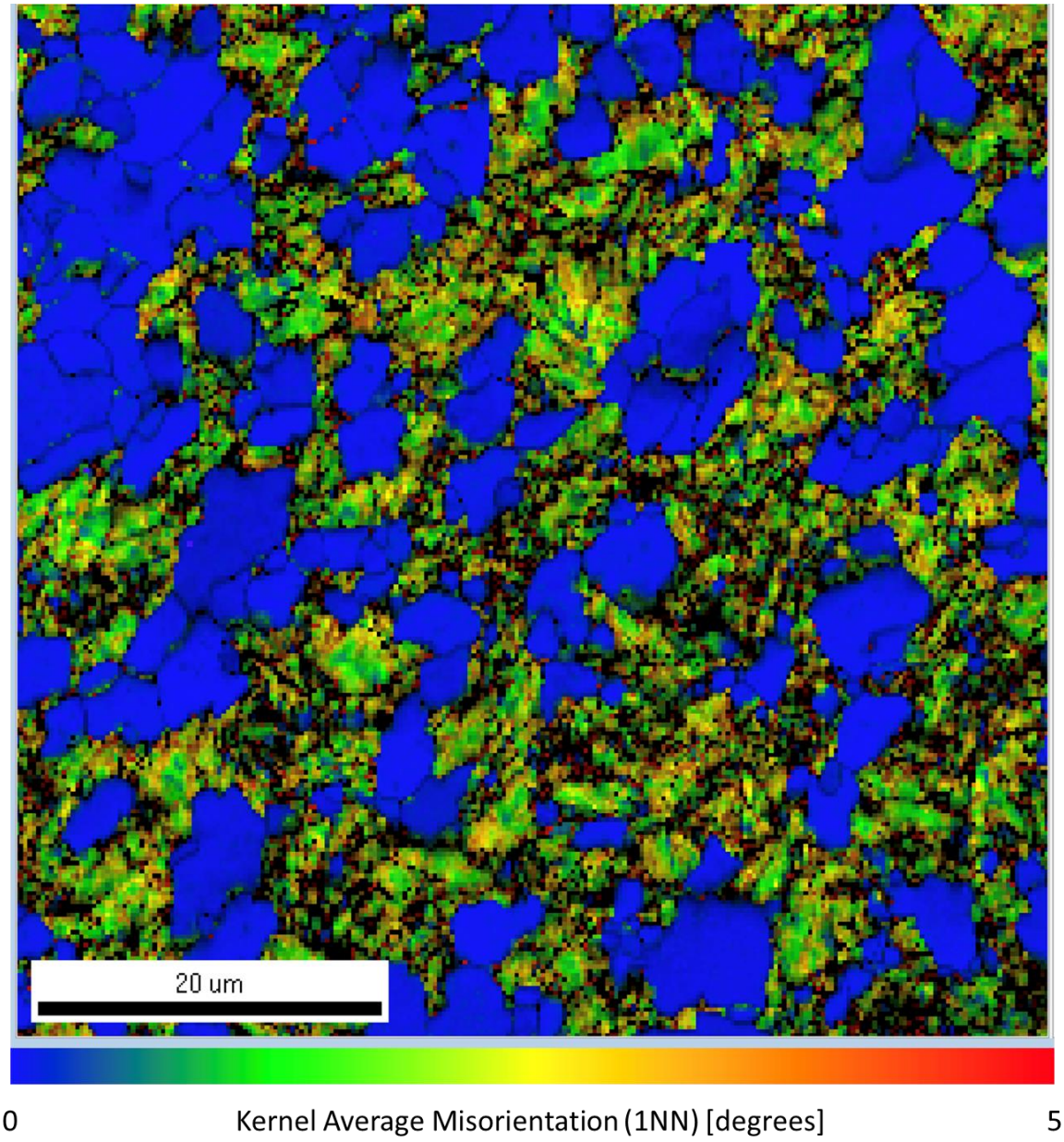

Figure 67. Band contrast map overlaid with KAM. Courtesy of Caleb P. Massey.

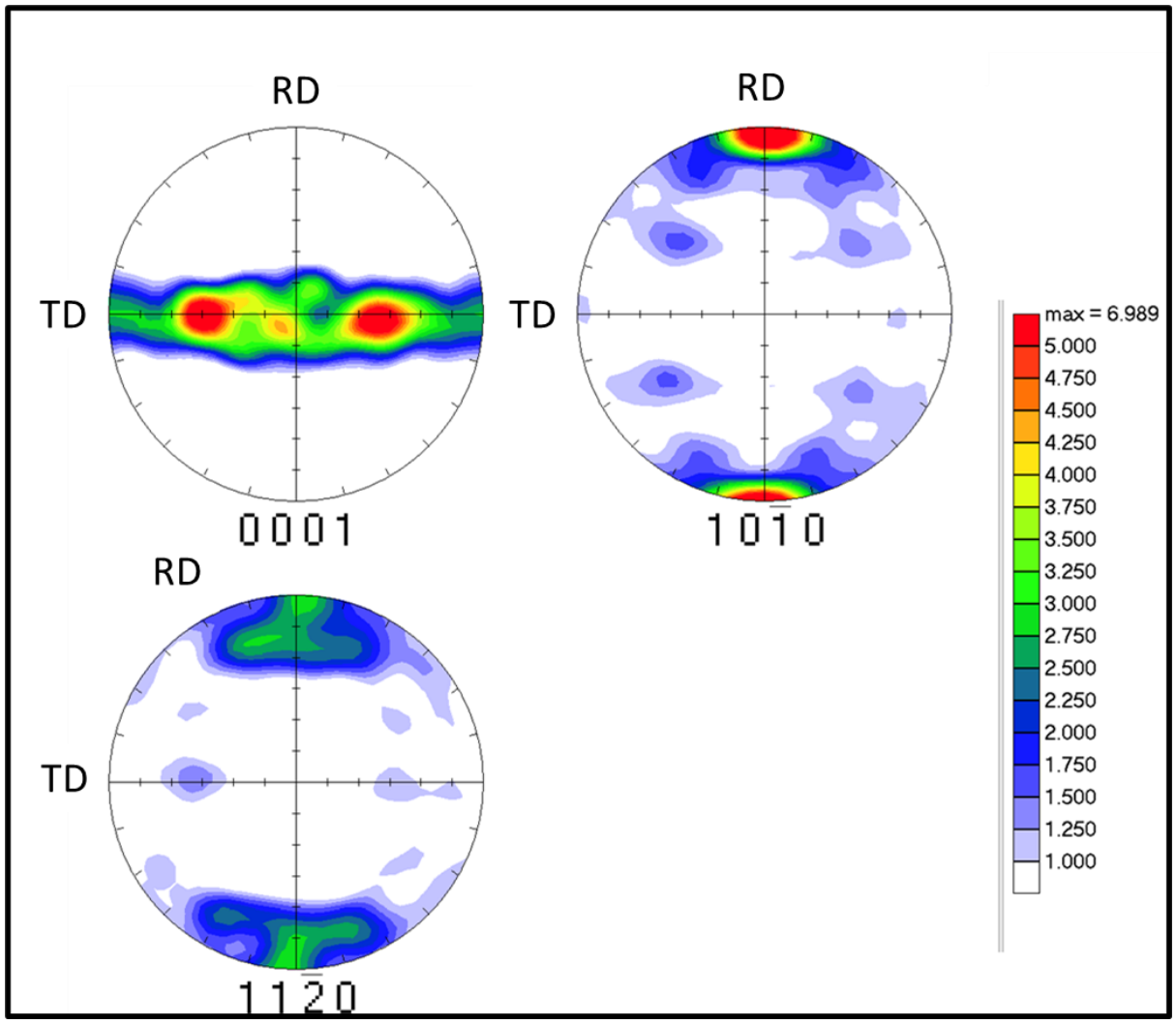

Figure 68. Pole figures for three {0001}, {10-10} and {11-20} orientations. RD and TD refer to the rolling and transverse directions, respectively. Courtesy of Caleb P. Massey.

Table 14. Test matrix, loading conditions, and burst data for all tests presented in this work. *Sample was repressurized at 300 °C to 14.8 MPa.

Internal pressure at RT (MPa)	Loading Condition (Open/Closed)	Front TC Ramp Rate (°C/s)	Front TC reading (°C)	Back TC reading (°C)	Burst Pressure (MPa)	Burst Location
6.2	Open	1.08	797	833	6.01	Back
6.2	Closed	0.99	738	777	7.63	Back
8.2	Open	0.98	751	761	7.97	Front
8.2	Closed	0.93	682	NA	10.36	Back
10.3	Open	0.92	687	721	10.11	Back
10.3	Closed	0.95	656	680	12.92	Between
15.1	Open	1.03	671	617	14.99	Front
15.1*	Closed	0.96	630	680	15.61	Front

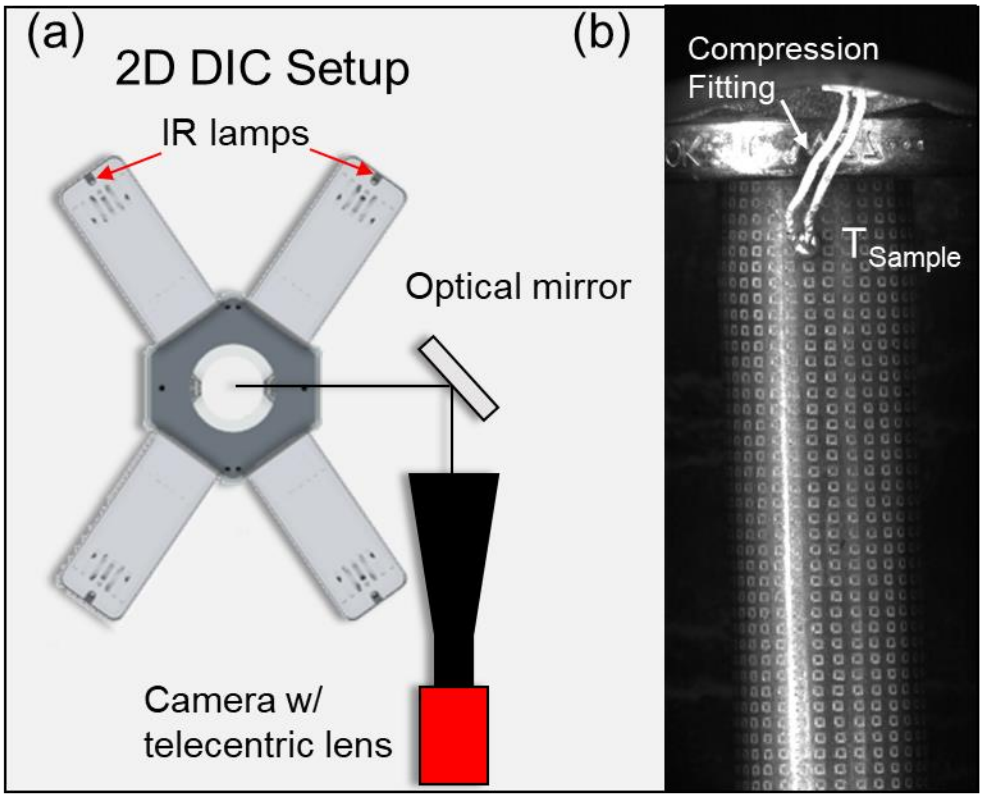

Figure 69. (a) Schematic of the furnace and optical setup. (b) Example image of a laser-engraved specimen.

volume and thermal mass. All cladding trains were loosely held in place on the bottom end, allowing for axial contraction/expansion.

Two distinct loading conditions were utilized: (a) “open valve” or isobaric testing where cladding samples are connected to a fixed pressure reservoir and (b) “closed valve” or constant-gas-inventory [30] testing where the amount of gas present in the rod is fixed and pressure is allowed to vary with temperature. An open and closed valve test was performed at each nominal pressure of 6.2, 8.2, 10.3 and 15.1 MPa, totaling eight tests. When heated to 300 °C before a transient, the initially 15.1 MPa at room temperature (RT) closed valve test reached internal pressures beyond the current safety limits for SATS. As such, it was depressurized to ~14.8 MPa before the test proceeded.

Three thermocouples (TCs) were present during testing, excluding one test (8.2 MPa closed valve) as indicated in Table 14. The TC controlling ($T_{Control}$) furnace power output was placed on the Swagelok compression fitting, outside the SiC shell that enclosed the cladding sample (see Chapter 6). Another TC (T_{Sample}) was placed 5 mm below the compression fitting and was in view of the DIC camera. The last TC (T_{Back}) was placed in the back of the furnace away from the viewport, 180° from T_{Sample}. Examples of the pressure and temperature histories for an open and closed burst test are shown in Figure 70(a) and Figure 70(b), respectively.

The claddings were initially pressurized at room temperature and heated to 100 °C to confirm no leaks were present. Then the samples were heated to 300 °C at 1°C/s and held for 5 min to ensure stable pressure and furnace conditions were achieved before a transient. After the hold at 300 °C, the claddings were heated at a rate of 1 °C/s until the claddings failed. The furnace was immediately shut off after burst and the claddings were allowed to air cool. Burst pressure and temperature was recorded and used to provide conventional metrics for comparison to historical models. Burst temperature was measured using the reading of the TC (front or back) closest to the burst region at the time of failure.

The presented DIC strain data was measured at the center of the balloon region, focused on an approximately planar section to mitigate the influence of out-of-plane rotation. An example of the DIC analysis region on the laser engraved pattern during ballooning is presented in Figure 71. The laser engraved pattern consisted of 0.4 mm wide squares onto the cladding surface, positioned every 10 degrees and spaced 0.4 mm apart. Each row along the axial direction contained

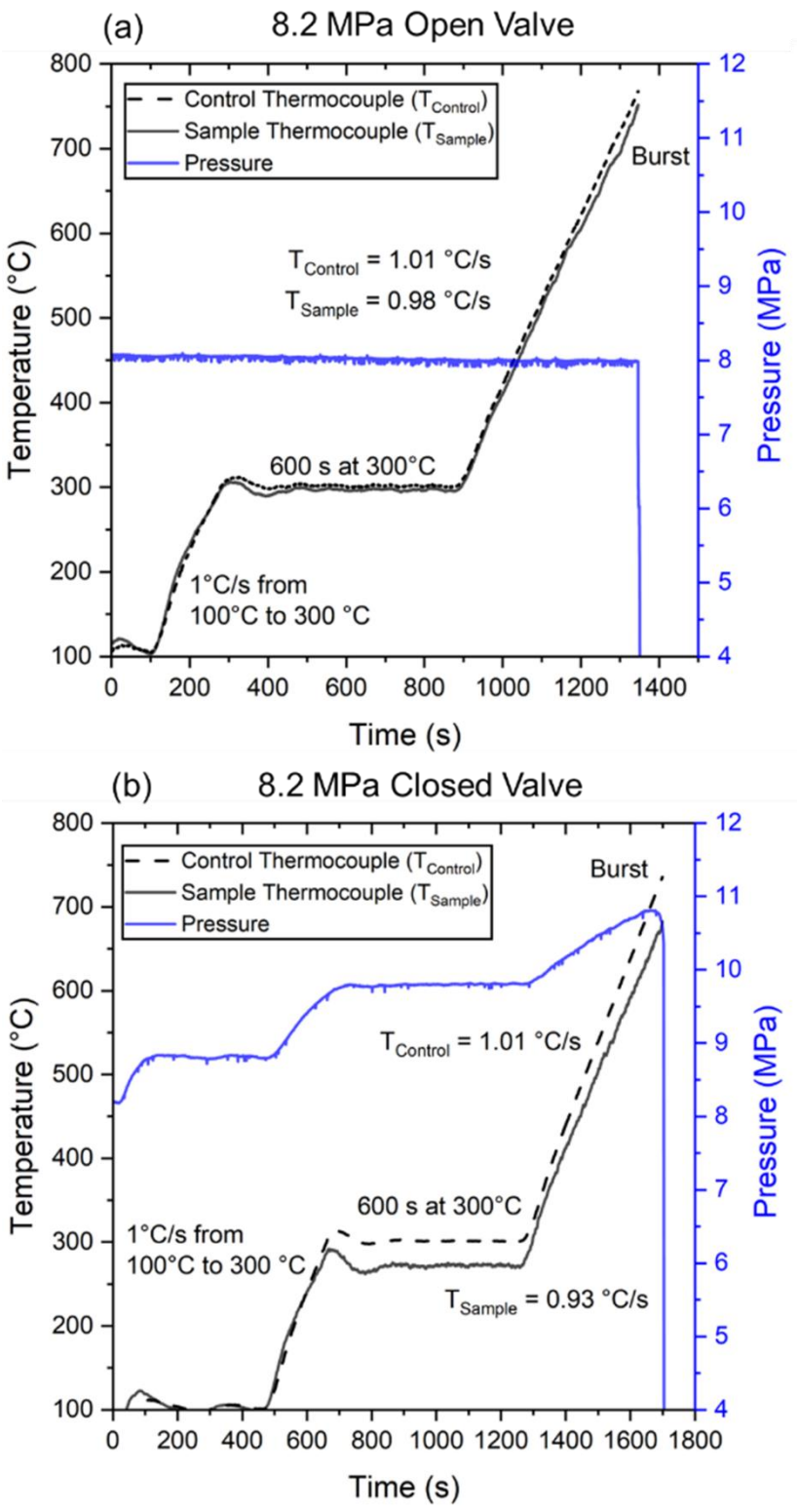

Figure 70. Example temperature and pressure histories for (a) open and (b) closed valve tests.

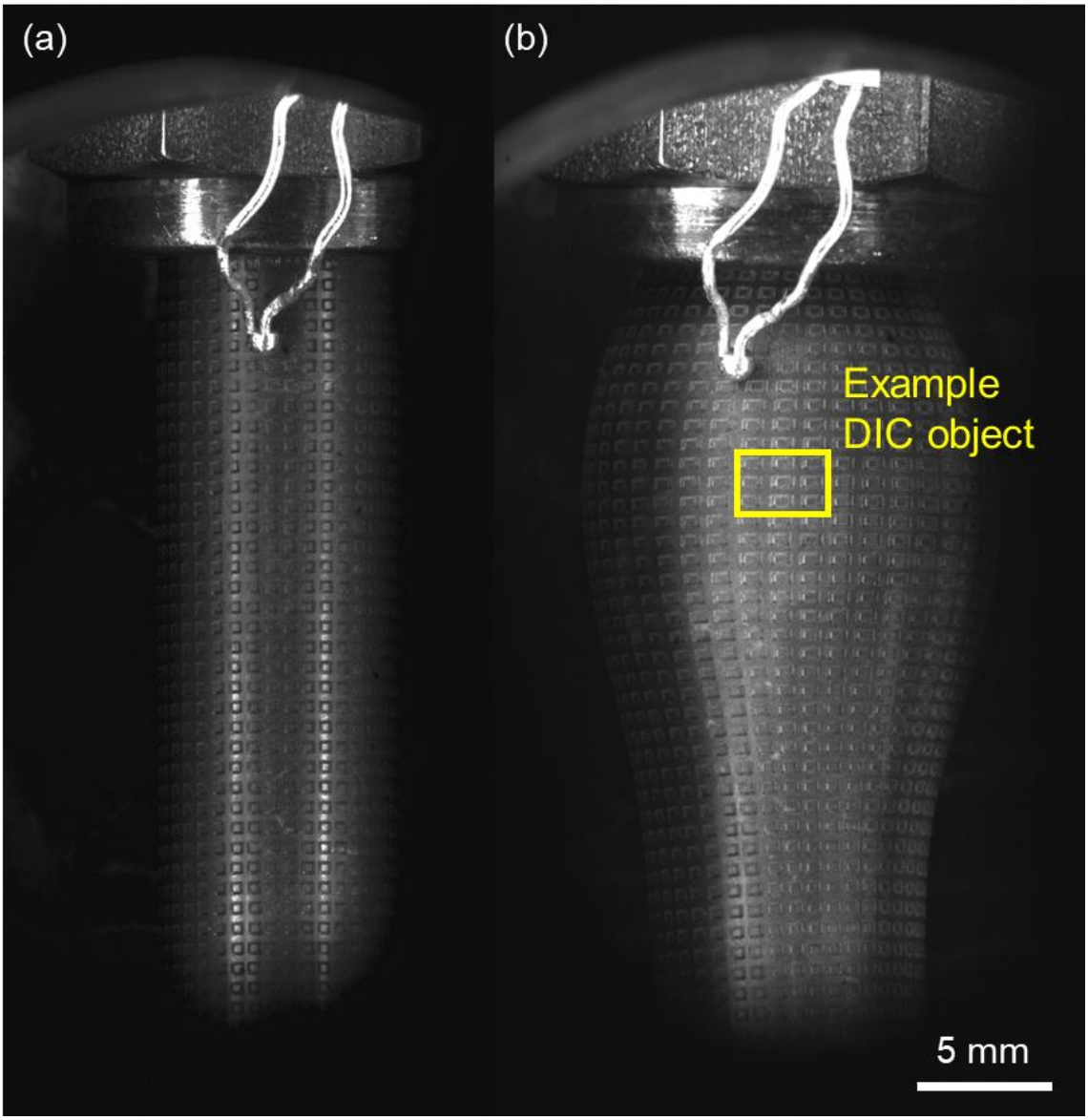

Figure 71. Image of a cladding specimen (a) before ballooning and (b) right before burst. The yellow square encompassing a 3 by 3 grid of laser engraved squares illustrates the location of and subset used for analysis.

60 squares. The depth of the engravings were ~14-17 μm.

All temperature correlations with DIC data were based on the reading of the TC in view, T_{Sample}. Hoop and axial train curves presented in this work are raw measurements from an in-house DIC software. Due to systematic noise brought about largely by heat waves in the furnace, all strain curves were smoothed using an adjacent averaging filter before numerical differentiation to determine strain rate. After testing, a VR-3100 Keyence structured light microscope was utilized for profilometry and determination of post-test diametric strain. Lastly, the samples were cross-sectioned at approximately the center of the balloon region and mounted in epoxy. Scanning electron microscopy was performed on the samples post-testing using the same Tescan MIRA3 to investigate oxide formation in the air environment and the laser engravings.

Section 7.3: RESULTS

7.3.1: In-situ Strain Comparison

Figure 72(a) and Figure 72(b) display the time-dependent hoop and axial true strain measurements for the open and closed valve tests, respectively. The tests conducted at pressures of 6.2, 8.2, 10.3, and 15.1 MPa are represented by black, green, blue, and purple lines, respectively. Since the strain measurements were taken at the center of the balloon region (Figure 71(b)), the location of rupture was taken into account during the analysis. In four out of the eight tests, the rupture occurred on the backside of the furnace, out of view of the camera. Therefore, the analysis was focused on the region opposite the rupture. For the 10.3 MPa open valve sample, the burst occurred between the two thermocouples, resulting in a rupture opening approximately 90° away from the camera view. The remaining three samples experienced rupture in view of the camera, allowing for analysis near or on the burst opening. Figure 73 provides a schematic illustration to clarify the relative orientation of the camera and rupture location. Figure 73(a) represents the orientation for samples that burst within the camera's view, while Figure 73(b) depicts the relative orientation for specimens where the rupture occurred outside the camera's view.

Significantly larger strains were observed for samples that burst in view of the camera, indicating the onset of non-uniform strains associated with failure. Dashed or dotted lines are used in Figure 72 to represent the samples that burst in view of the camera and distinguish them from other results. Generally, the axial strain was negative, with maximum magnitudes ranging from

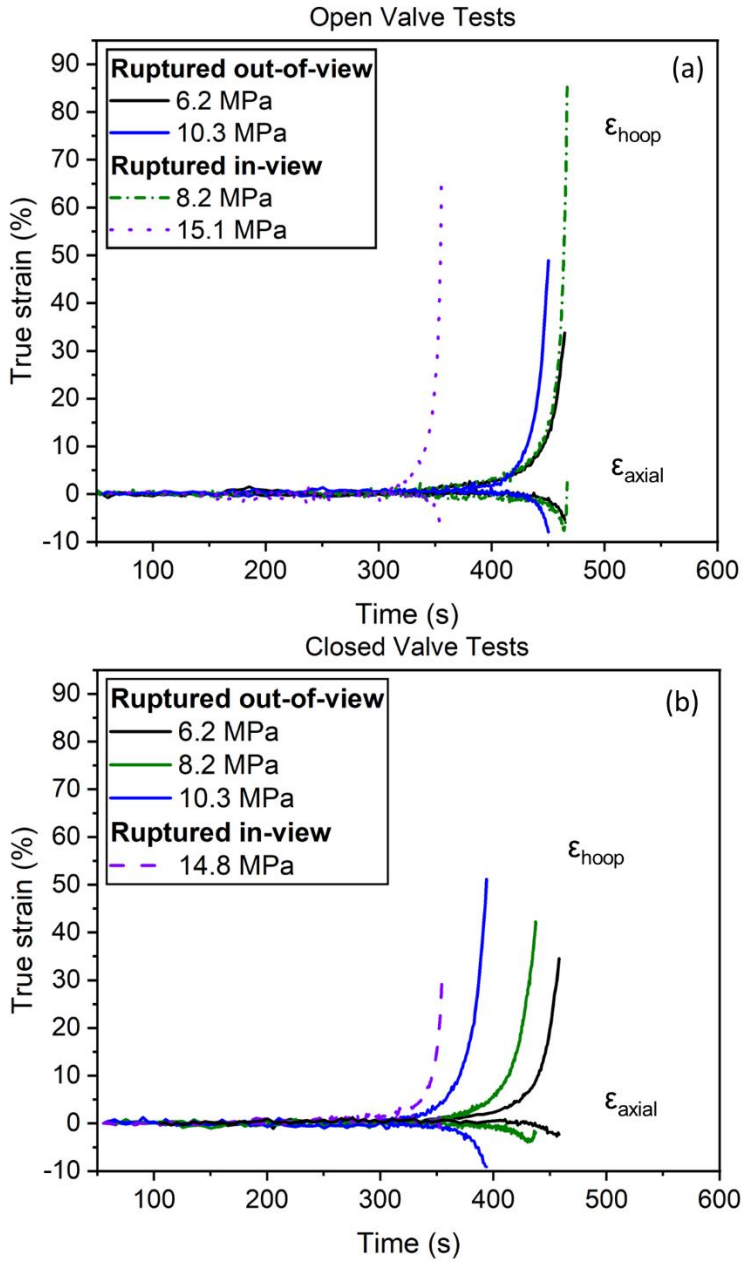

Figure 72. Hoop and axial strain-time curves for the (a) closed valve and (b) open valve tests. The dashed and dotted lines represent samples that burst in-view of the camera, meaning the strain measured was near the rupture location where large strains associated with failure are expected. The solid lines present strain from specimens that ruptured out-of-view of the cameras (~180°), leading to lower more uniform strain measurements.

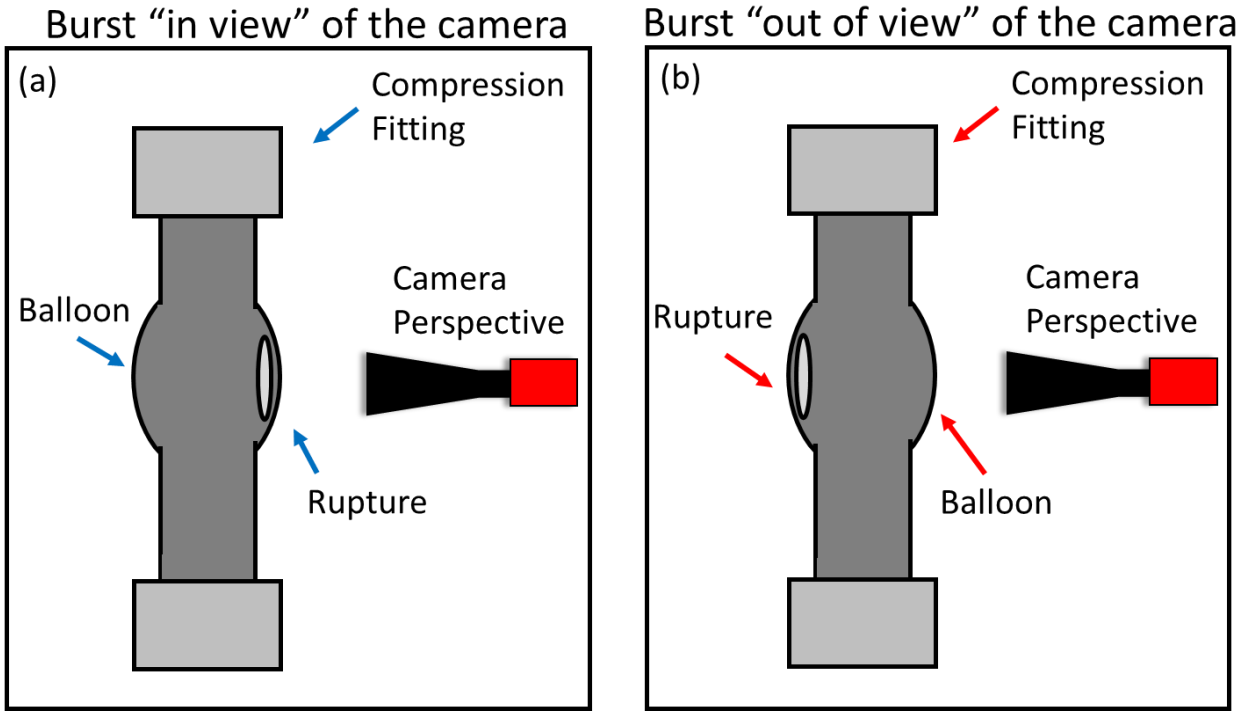

Figure 73. Illustrations of the relative orientations between the rupture opening and camera perspective for (a) specimens that burst “in-view” and (b) “out-of-view” of the camera.

approximately 2% to 8%. However, for the 8.2 MPa closed and open valve tests, Figure 72(a) and Figure 72(b), axial strain rapidly increases near the end of life. A positive final axial strain was measured for the 8.2 MPa closed valve test. This could indicate a transition to a state where the axial stress had a net positive deformation rate, rather than being dominated by constancy of volume considerations from the hoop strain. The remainder of the tests did not demonstrate this behavior.

The closed and open valve tests were pressurized to the same initial value at room temperature (RT), but towards the end of their lifetimes, the closed valve tests exhibited readings approximately 1.5 - 2.5 MPa higher than the open valve tests. Direct comparison of the strain curves between the two loading conditions with the same initial RT pressure is not possible. However, the pressure during ballooning of the 6.2 MPa closed valve test was comparable to 8.2 MPa open valve test. Figure 74 illustrates the hoop strain and pressure against time from the start of the 1 °C/s temperature ramp for these tests.

In Figure 74, the 6.2 MPa closed valve test is represented by the red curves, while the 8.2 MPa open valve test is represented by the black curves. The solid lines indicate the pressure, and the dashed lines represent the true hoop strain curves. Stars at the end of the strain curves indicate the final strain values. Since the 8.2 MPa open valve test burst in view of the camera, the latter portion of the strain measurements showed higher values due to the observation of non-uniform strain associated with failure. Regardless, the two tests showed considerable overlap particularly during the start of ballooning.

The exact onset of ballooning cannot be clearly defined based on the strain curves alone. Considering the 6.2 MPa closed valve curve around 370 s into the ramp, the rate of pressure change decreased and leveled off. This pressurization rate change is expected due to volume changes and coincided with the beginning of hoop strain increase. At approximately 433 s, the 6.2 MPa closed valve test reached a maximum pressure of 7.98 MPa, while the open valve test was pressurized to 8.00 MPa at the same point in the temperature ramp. It should be noted that a small pressure leak was present in the 8.2 MPa open valve test, resulting in a decrease of approximately 0.2 MPa in pressure from the moment of pressurization (around 1500 s). At around 433 s into the ramp, the strain curves showed similar hoop strain values of approximately 7%. After this point, the strain curves started to diverge. The volume increase due to ballooning for the constant gas inventory

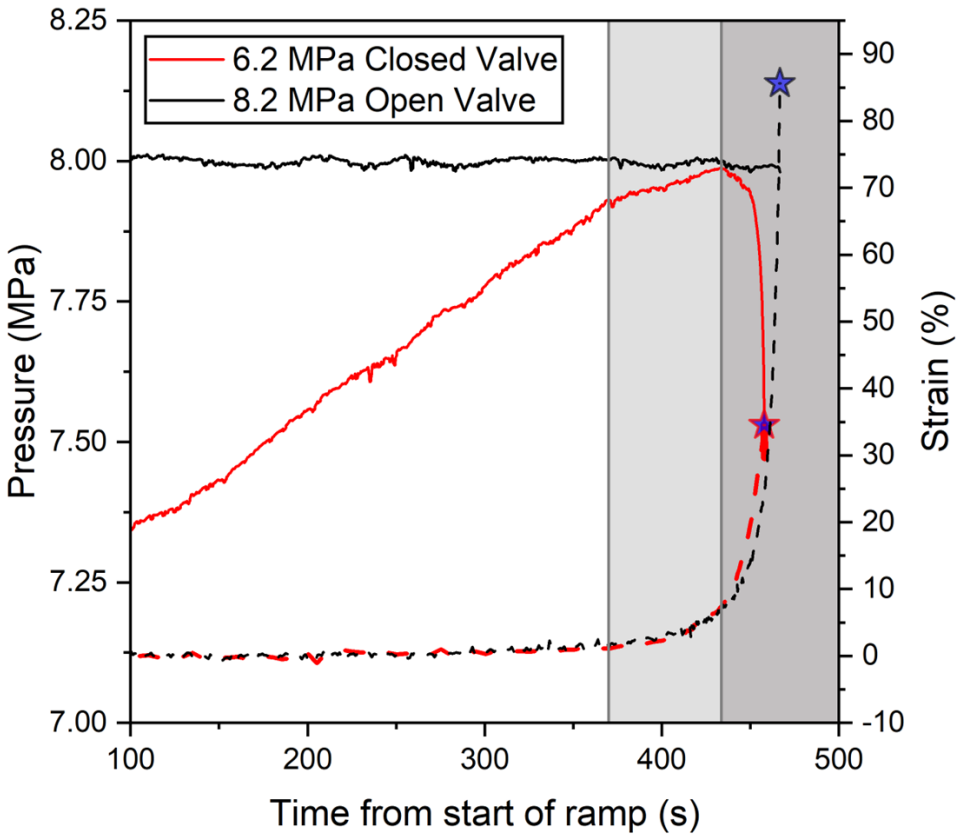

Figure 74. Strain and pressure against time for the 6.2 MPa closed valve and 8.2 MPa open valve tests.

test led to a corresponding decrease in pressure until the rupture occurred. While only the 6.2 MPa closed valve test is discussed in detail here, the tests with constant gas inventory showed similar relationships between pressurization and strain.

Strain-time considerations are not a complete description, as small variations in experimental heating rates can lead to shifts in the strain-time curves. A linear fit between the beginning of the ramp and time of burst are presented in Table 14 for all tests. The average heating rate was 0.98 ± 0.05 °C/s, with a maximum and minimum heating rate of 0.92 and 1.08 °C/s, respectively. A heating rate of 1 °C/s was prescribed to the system and generally achieved. Given the slow ramp rate a 0.1 C/s difference over the ~350-450 s duration of a test can produce differences in temperature ~35 – 45 °C difference at a given time after the ramp. For instance, comparing the 6.2 MPa and 8.2 MPa open valve tests (Figure 72), analyzing the time domain alone would lead to the conclusion that the samples behaved similarly despite the 2 MPa difference in pressurization. Yet, it is important to note that the 8.2 MPa open valve test failed at a temperature 82 °C lower and the temperature histories shifted accordingly.

Furthermore, variations in the starting temperatures of the samples were observed due to the influence of the SiC shell. The furnace power output during the test was controlled by the TC placed outside the SiC shell. Consequently, during the 300 °C hold before the ramp, the TC in view of the sample (T_{Sample}) indicated a lower temperature due to shielding, with a difference of approximately 20-30 °C. While heating rates of ~1 °C/s were achieved for the TCs in contact with the sample, differences in starting temperatures also contribute to the variations observed in the strain-time curves.

To illustrate the discrepancy between strain-time and strain-temperature comparisons, Figure 75 presents the hoop strain and temperature readings for the closed valve tests. The dashed lines represent claddings that burst in view of the camera. When the time axis is replaced with temperature, the strain overlap between the 6.2 MPa and 8.2 MPa tests in Figure 72(a) disappears, as shown in Figure 75. It should be noted that the strain-temperature curves may exhibit some noise due to experimental conditions in both the strain and temperature measurements. Thus, the strain curves may not appear as smooth in the temperature domain as they do in the time domain. Considering the combined effects of strain rate and temperature on deformation is valuable for investigating the assumption of Arrhenius temperature dependence. Evaluating the relationship

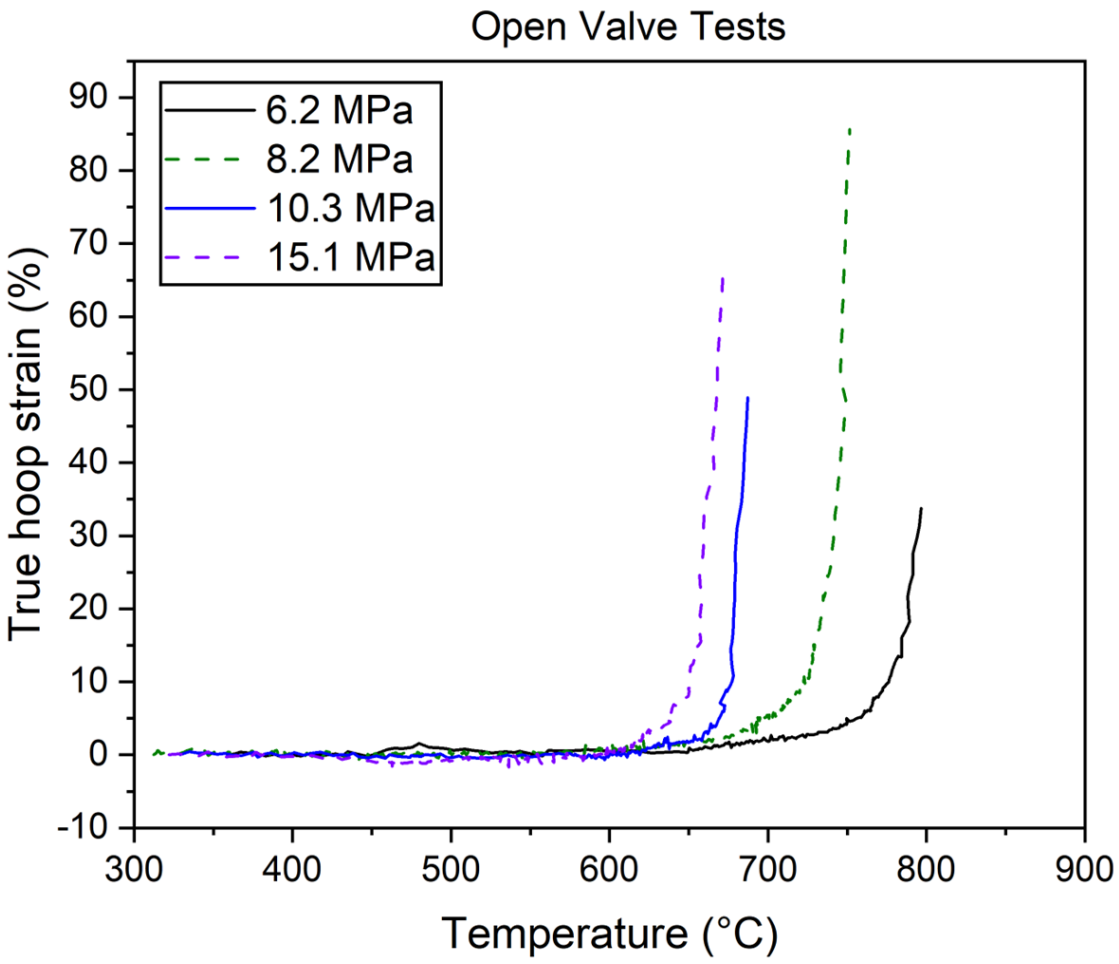

Figure 75. Hoop strain – temperature curves for the open valve tests to demonstrate the difference between the time and temperature domains.

between strain rate and temperature during a transient is necessary for LOCA modeling, as it forms the basis of the steady-state creep assumption. Strain-rate and temperature dependence are discussed in a later section.

7.3.2: Comparison of BISON modeling to 2D DIC results

BISON modeling was performed by Capps et al. [133] for some of the testing presented in this work using the pressure and temperature histories. Strain-temperature plots comparing BISON predictions and DIC experimental results for this testing for the 6.2 MPa and 15.9 MPa open valve tests are shown in Figure 76. Hoop strain comparisons to BISON predictions for 6.2 MPa and 15.9 MPa are shown in Figure 76(a) and Figure 76(c), respectively. Axial strain comparisons to BISON prediction for 6.2 MPa and 15.9 MPa are shown in Figure 76(b) and Figure 76(d), respectively.

BISON models consistently overestimated hoop strain and underestimated axial strain compared to the samples from this testing with the same heating rate. However, the fidelity of the 6.2 MPa curve was greater, showing a closer profile form. This indicates that the parameters/model input into BISON better reflects the behavior of lower pressure, higher temperature accident behavior.

It should be noted that systematic error exists in the tests due to the combination of the laser-engraved patterns and optical heat waves. This, along with the DIC software settings needed for analysis, accounts for the rise to nearly 1.5% axial strain at less than 500 °C for the 15.9 MPa test, which eventually settles down to near zero until the final stages of ballooning. The rise to ~0.5% axial strain for the 6.2 MPa open valve test could be due to the loose constraint of the bottom end of the cladding train.

Capps et al. [133] also compared BISON models with DIC data produced from Choi et al. [181] at heating rates of 1 and 28 °C/s. The result of these are reproduced in Figure 77 by Capps et al. [133]. The BISON prediction curve for the 1 °C/s test shows remarkable fidelity to the experimental data until the end of life, where the final predicted strain was ~80% and the final experimental strain was ~62%. Looking at the comparison at 28 °C/s, the BISON model overpredicts hoop strain starting at ~600 °C, then changes to underpredicting hoop strain after ~800 °C. These results highlight the disparity in BISON model predictive capabilities for varying

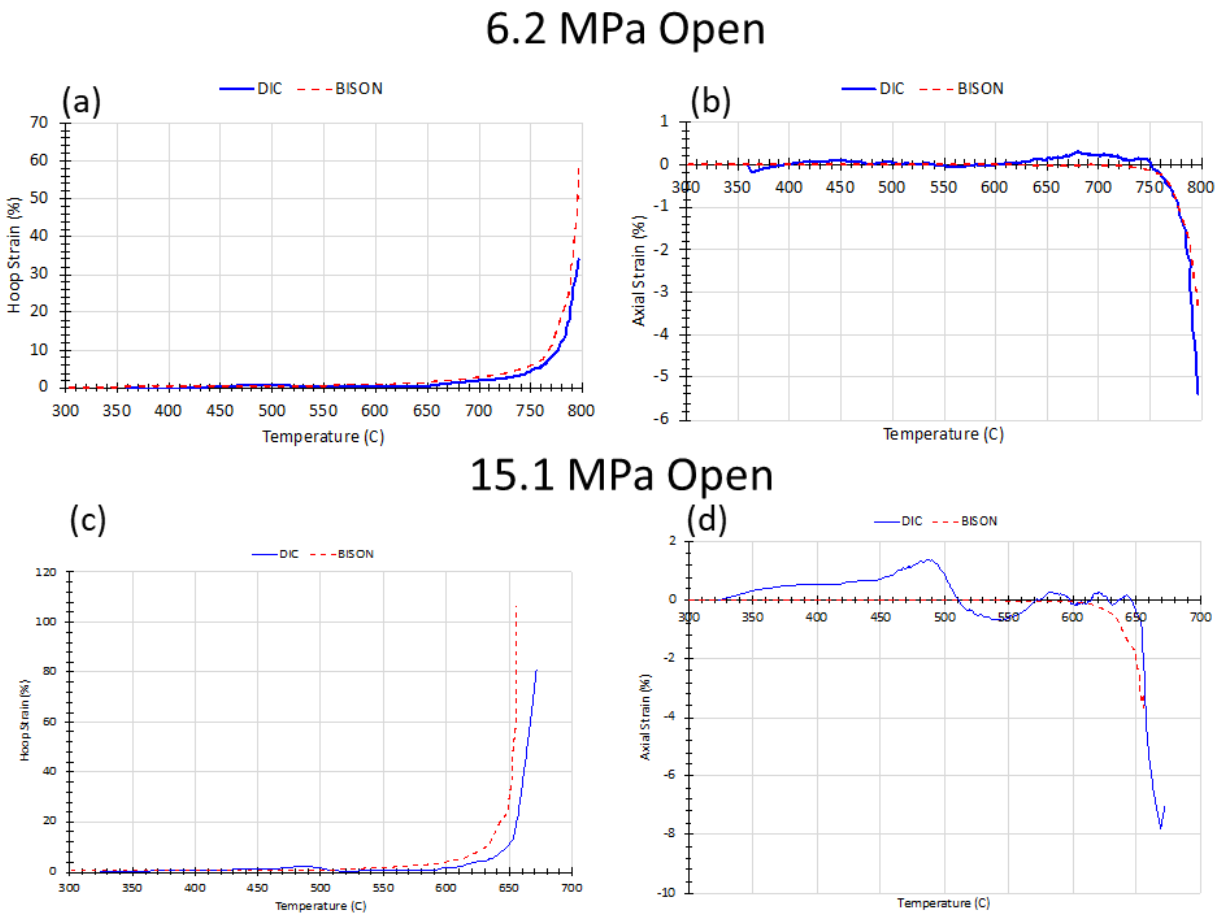

Figure 76. (a) and (c) show BISON predicted hoop strain compared to DIC measurements for the 6.2 MPa and 15 MPa open valve tests, respectively. (b) and (d) show similar plots for axial strain measurements.

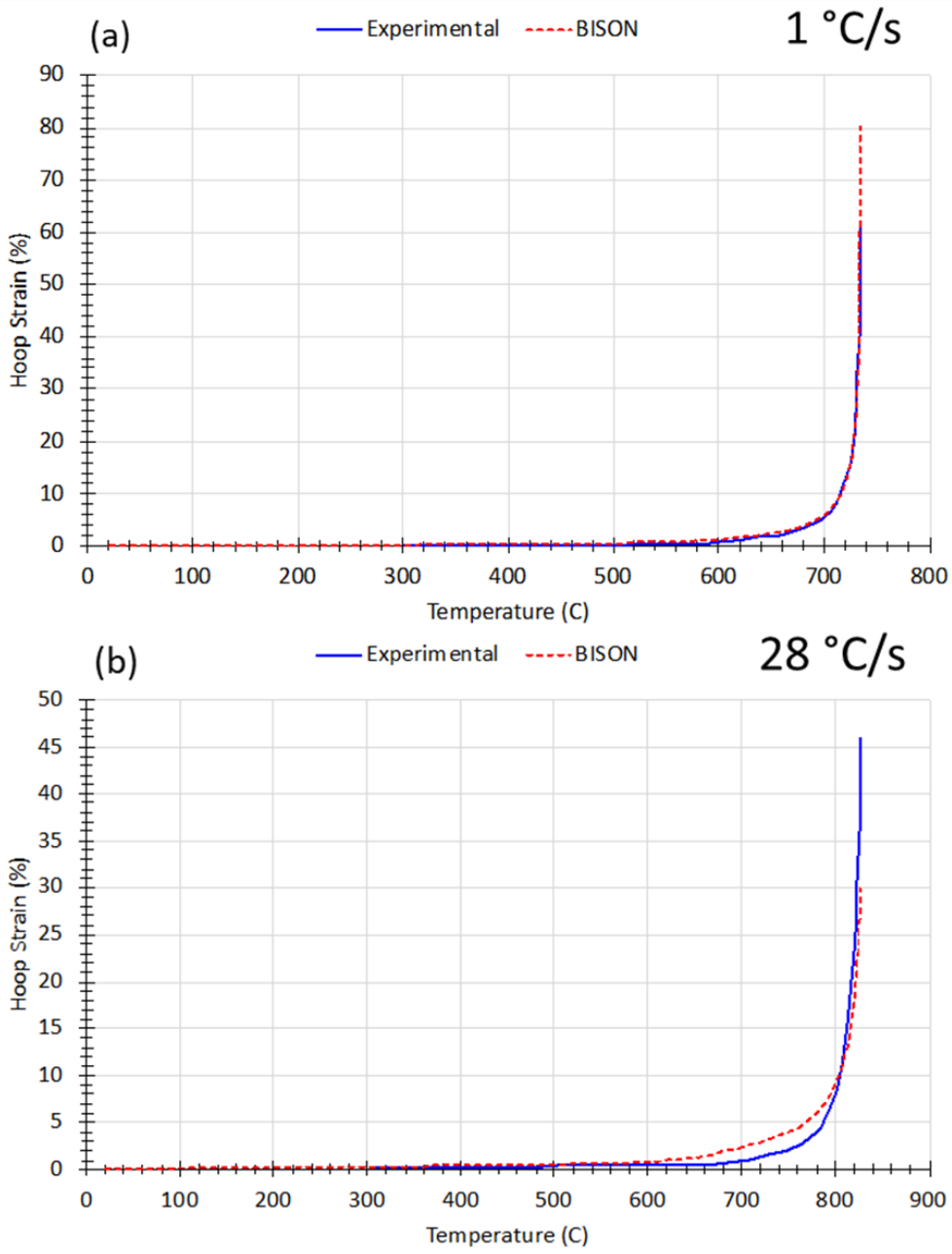

Figure 77. BISON comparisons to DIC data generated from KAERI experiments at 8 MPa internal pressure. (a) shows results for a heating rate of 1 °C/s and (b) shows results for a heating rate of 28 °C/s.

heating rates due in part to lack of inclusion of detailed material parameters such as grain size and texture/anisotropy in the input parameters.

Combining the observed discrepancies between differences in pressure with the same heating rate, Figure 76, and differences in heating rates for the same pressure [133], Figure 77, it appears that BISON model accuracy is greater for lower pressures and heating rates. However, the final strain predictions for all the selected tests were considerably off. The ability to predict final strains of the claddings is necessary, as the amount of strain has implications for fuel relocation as well as coolant flow blockage. As such, these results highlight the need for improving model capabilities to better define criteria for safe and economic operations of LWRs, particularly in high burnup scenarios.

7.3.3: IR thermography and Limitations

IRT was applied during all tests, yielding axial temperature profiles immediately prior to burst, as depicted in Figure 78. Though IRT usage was discontinued in later tests due to technical challenges, some notable findings emerge from the data. Typically, the profiles displayed higher temperatures in proximity to the thermocouple, with decreasing temperatures further along the profile. This is expected given that the cladding train was directly exposed to laboratory air via the 38 mm viewport.

In certain tests, a spike in the IR readings was noticed towards the center of the line profile. This spike generally coincided with the base of the ballooning region. However, this temperature spike might be an artefact since the emission surface was not planar at the ends of the balloon region. There was not an evident uniform correlation across the tests upon initial observation, as some exhibit a rise in temperature midway down the axial length, while others display a continued decrease. These discrepancies could be attributed to a number of factors including low resolution of the IR camera, deformation-induced uneven heating near the SiC shell, and minor setup variations affecting the visible cladding length.

The emissivity value required to match the thermocouple at burst fell within the 0.8-0.9 range. This corresponds to literature values associated with oxide formation. Burgoyne et al. [197] reported that emissivity values for Zircaloys transition from ~0.27 in the as-received condition to near 0.85 with just a few microns of oxide formation. A SEM micrograph from the region opposite

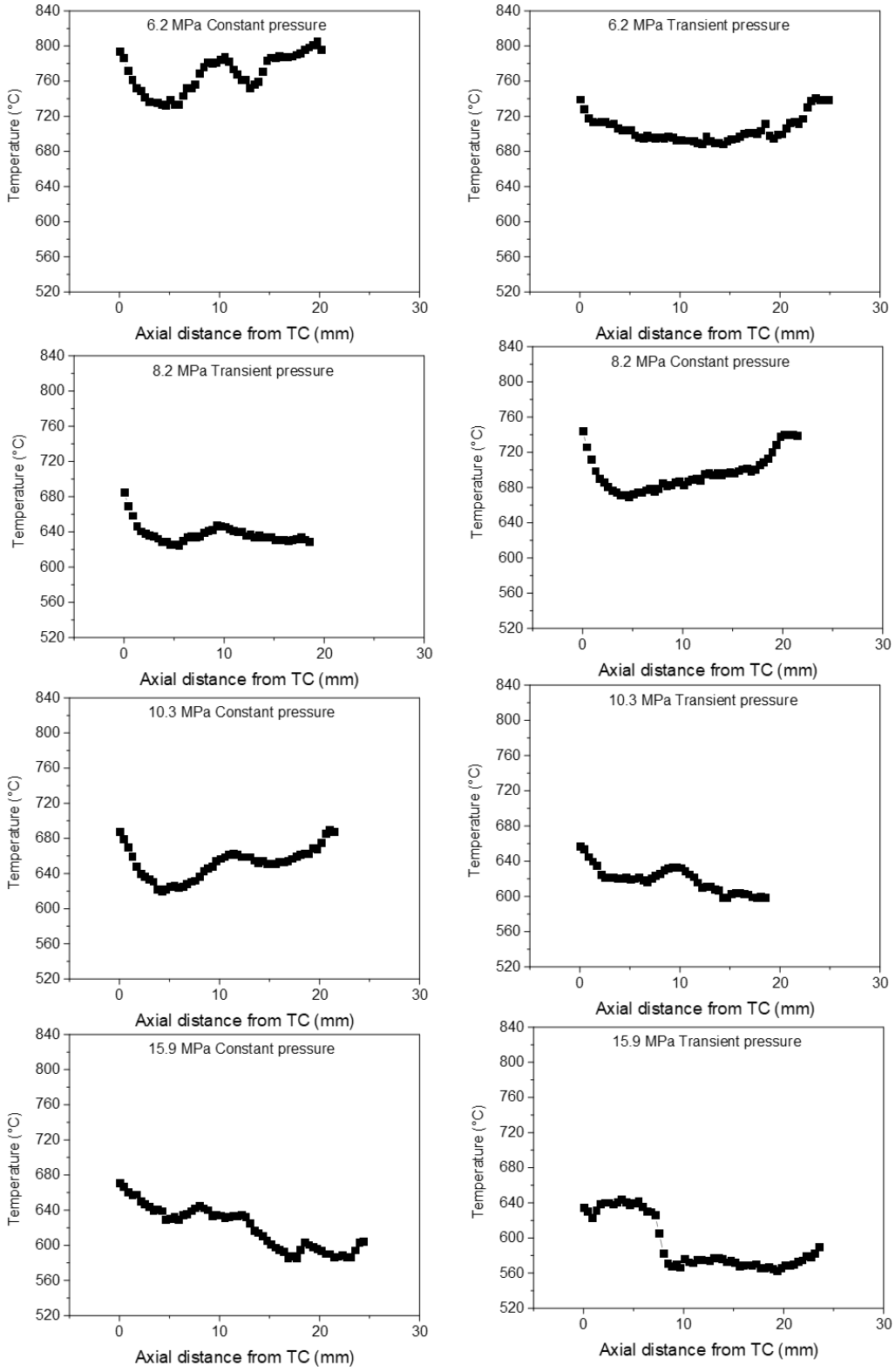

Figure 78. Axial temperature profiles generated from IR images right before burst for all tests in the 2D DIC data set.

the burst zone for the ~15.9 MPa closed test is presented in Figure 79, showing the formation of an oxide scale ~1-2 μm in thickness. The zirconia oxide presented is representative of the scales for most of the tests, and the changing emissivity value between the start of the test and burst was consistent for all tests. This suggests the changing emissivity seen during this air testing was the result of a 1-2 μm oxide formation. Consequently, it is reasonable to consider the IRT measurements generally reliable. Yet, the non-constant emissivity poses a challenge for recording high fidelity temperature readings. If IRT is utilized in future tests, applying a high emissivity paint could ensure a consistent emissivity value throughout the testing process.

This inference was strengthened when comparing different points in the ramp, as a changing emissivity indicates increasing opacity. Figure 80(b) displays axial profile measurements at 475 °C and the final frame before burst from a preliminary test not included in the matrix, with the axial profiles color-coded as blue and red, respectively. The corresponding IR images are shown in Figure 80(a), adhering to the color scheme of the arrows. At 475 °C, an emissivity of 0.72 was required to match the TC in view, while at burst an emissivity of 0.9 was needed.

However, Figure 80(b) demonstrates that the IR profile shape is not consistent throughout the entire test. For most of the test, the axial readings resembled the 475 °C profile, with a ~20-40 °C temperature difference from the thermocouple halfway along the profile and an upwards temperature trend towards the end. This mid-profile temperature drop is primarily due to the ~38 mm viewport in the front of the furnace being exposed to lab air. In contrast, the profile at burst showed a continual decreasing temperature trend, with a maximum ΔT of ~80 °C from T_{Sample}. Several factors could be driving the relative temperature drop for the lower half of the cladding during balloon and burst events, including expansion of the Ar gas, deformation of the cladding bringing the ballooning region closer to the SiC shell, and geometric effects on emission/reflection.

The goal when establishing this framework was to eventually incorporate steam testing, as this has the most fidelity to accident conditions. Air testing was pursued at first to simplify baseline issues with implementing *in-situ* techniques. Beyond trying to remain material-agnostic, oxidation and oxygen concentration are not expected to impact the balloon behavior of the α-Zr phase [102,198] but could have a significant effect on strain behavior in the β-Zr phase. To introduce steam into the test, as is common with SATS testing, a quartz reaction tube is used to contain the environment. The first tests associated with this project attempted to utilize the IR camera with a

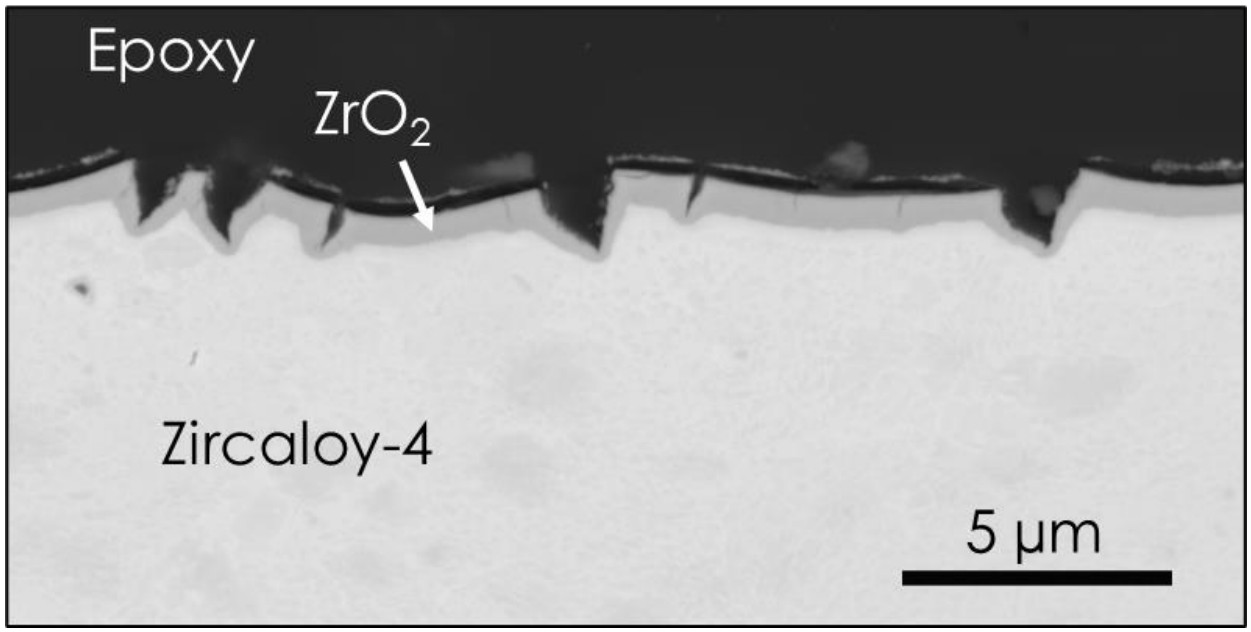

Figure 79. SEM micrograph of the oxide scale formed after testing in air.

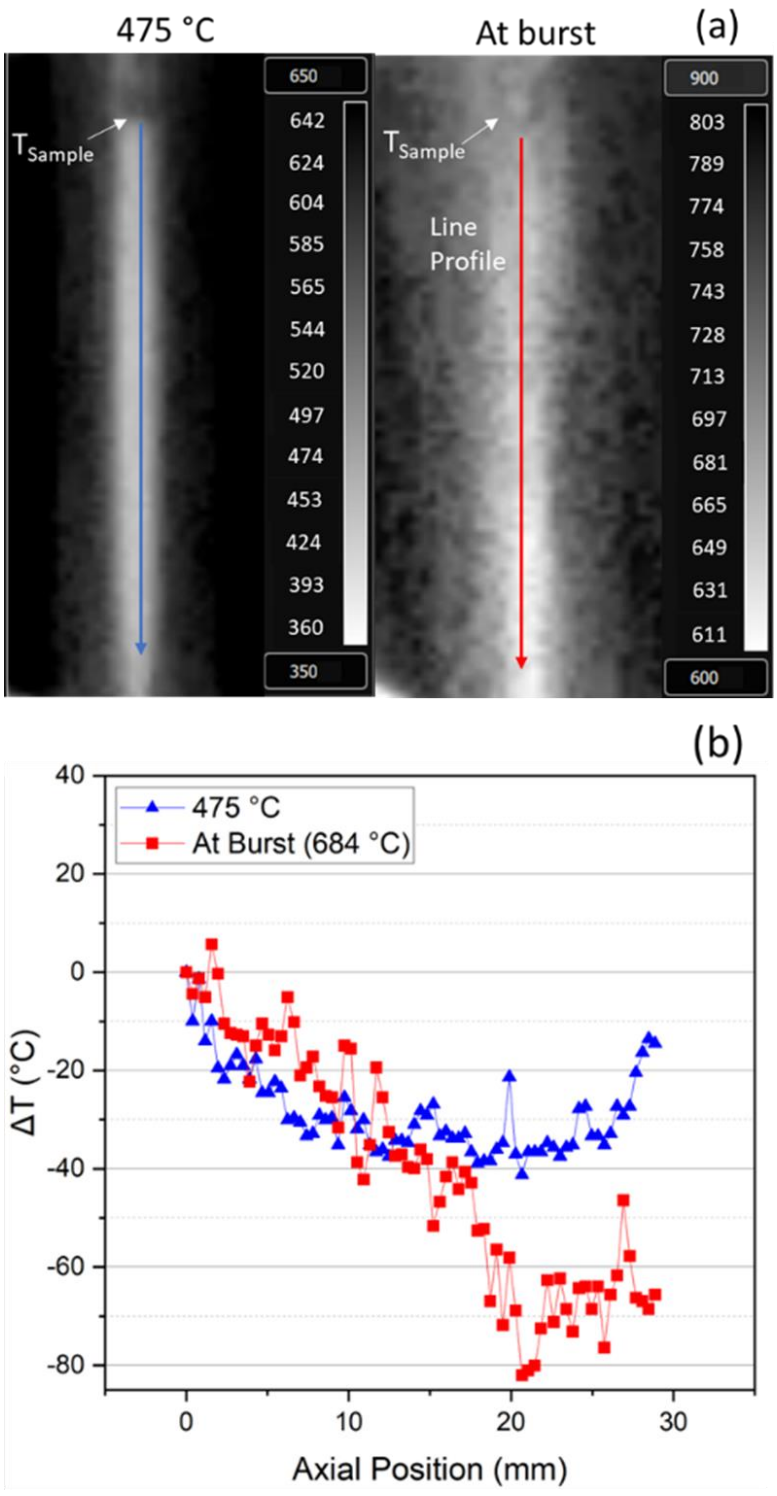

Figure 80. (a) IR images at 475 °C and right before burst. (b) Axial profiles (indicated by arrows in (a)) from the two IR images.

quartz reaction tube and flowing steam. However, it was found that during testing the quartz reaction tube itself emitted IR leading to washing out of the IR signal. As the current iteration incorporates a steam environment, IR thermography will not be included until either washing out by the quartz tube can be mitigated or the experimental setup altered.

7.3.4: Strain Rates at Failure

Models of cladding performance usually involve some form of failure criterion to terminate the simulation. A commonly applied "plastic instability" threshold in TRANSURANUS[199] and BISON [125] fuel performance codes indicates failure occurs once an effective strain rate of 2.78 %/s is reached. To compare this criterion with in-situ data, the final measured effective and hoop strain rates are plotted against burst pressure in Figure 81(a). The effective, or equivalent, plastic strain was calculated using an isotropic assumption as given by ,

$$\varepsilon_{eff} = \sqrt{\frac{2}{3}(\varepsilon_{hoop}^2 + \varepsilon_{axial}^2 + \varepsilon_{radial}^2)}, \quad (18)$$

where ε_{hoop}, ε_{axial}, and ε_{radial} are the strains in the hoop, axial, and radial directions, respectively. Resultant strain curves were smoothed and numerically differentiated. Tests where the burst occurred in view of the camera are not included in the discussion due to the non-uniform deformation inherent to the burst location.

Final strain rates are also plotted against the front thermocouple reading (T_{Sample}) in Figure 81(b). The final effective and hoop strain rates are depicted in squares and triangles, respectively, along with linear fits of both quantities. As DIC is inherently a surface measurement, radial strain was determined assuming constancy of volume during plastic deformation.

It should be noted the α-Zr phase for which testing encompassed is inherently anisotropic due to the hcp crystal structure. A simple isotropic assumption is relevant for a first comparison as Hill parameters are not available for these samples. Similarly, evolution of the relevant parameters during a temperature ramp remains uncertain. However, future work should include anisotropy effects.

Most of the measured strain rates at fracture shown in Figure 81 significantly exceed the plastic instability criterion (2.78%/s). The final effective strain rate was higher than the final hoop strain rate, with the difference between the two varying between tests. The largest difference, 0.9

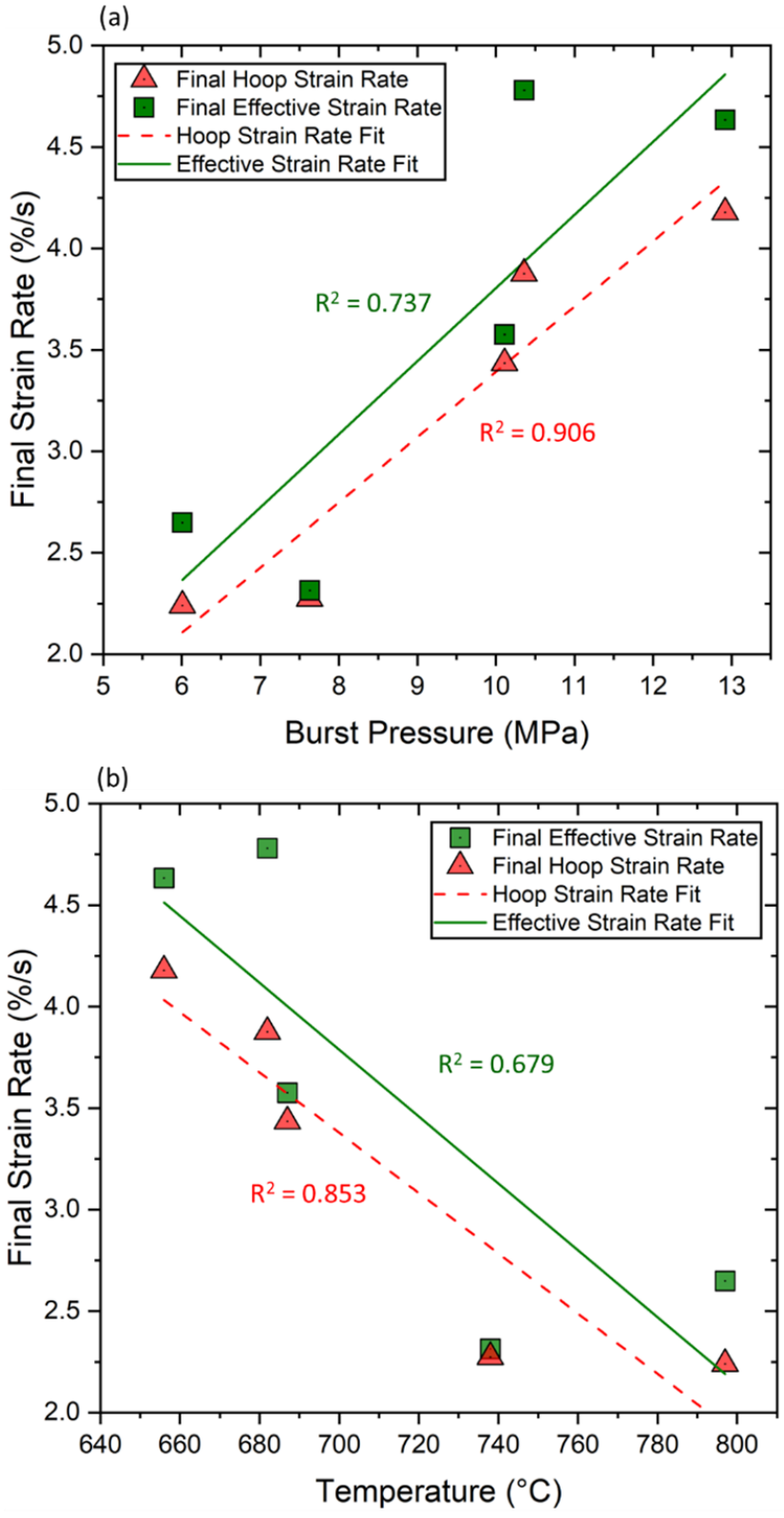

Figure 81. Final hoop and effective strain rates against (a) burst pressure and (b) T_{Sample} reading at burst for tests that burst out-of-view of the camera.

%/s, was observed in the 8.2 MPa closed valve test, while the smallest difference, 0.04 %/s, was found in the 6.2 MPa closed valve test. Both final hoop and effective strain rates increased with burst pressure, but the former displayed a tighter trend. A decreasing trend was observed between final strain rates and burst temperature, as shown in Figure 81(b). This inverse relationship is expected, as higher pressures typically lead to lower burst temperatures. The slopes of the burst pressure trendlines for the final hoop and effective strain rates were in relative agreement, with values of 0.322 and 0.360 %/(MPa·s), respectively. A similar relationship was found for temperature with slopes of -0.0149 and -0.0165 %/(°C·s) for the hoop and final strain rate trendlines, respectively.

At lower burst pressures and higher temperatures, the final effective strain rates are closest to the described plastic instability criterion of 2.78 %/s. The 6.2 MPa open and closed valve tests recorded final effective strain rate values of 2.65 and 2.314 %/s, respectively. The remaining tests exhibited failure at strain rates exceeding the critical value. The 8.2 MPa closed, 10.3 MPa open, and 10.3 MPa closed valve samples reached effective strain rates ≥ 2.78%/s at 2, 4, and 4 seconds before burst, respectively. This corresponds to a discrepancy of 7 %, 15 %, and 15 % effective strain at failure compared to that point, respectively.

7.3.5: Ex-situ Strain Comparison

Burst pressure is presented against burst temperature in Figure 82 as well as reported in Table 14. Open and closed valve tests are shown in squares and triangles, respectively. For comparison of this augmented testing against historical data, the empirical Chapman correlation for Zircaloys based on a 1 °C/s heating rate [28,30,27] is included in the black line. Data used to develop the Chapman correlation spanned heating rates from 1 - 28 °C/s with limited data past ~9 MPa for low heating rates. As such, a dashed line is included to reflect the extrapolation for this lower heating rate correlation. Generally, the burst data aligns with the historical Chapman correlation particularly at lower pressures. For pressures > ~10MPa, a deviation from the correlation is observed. This discrepancy could be associated with the aforementioned extrapolation (indicated by the dashed line), or possibly due to constraints of the balloon region near the compression fittings, which will be discussed next.

The balloon region formed near the top fitting due to the influence of the SiC shell and the direct exposure of the top compression fitting to the IR lamps. Images of some of the tests are

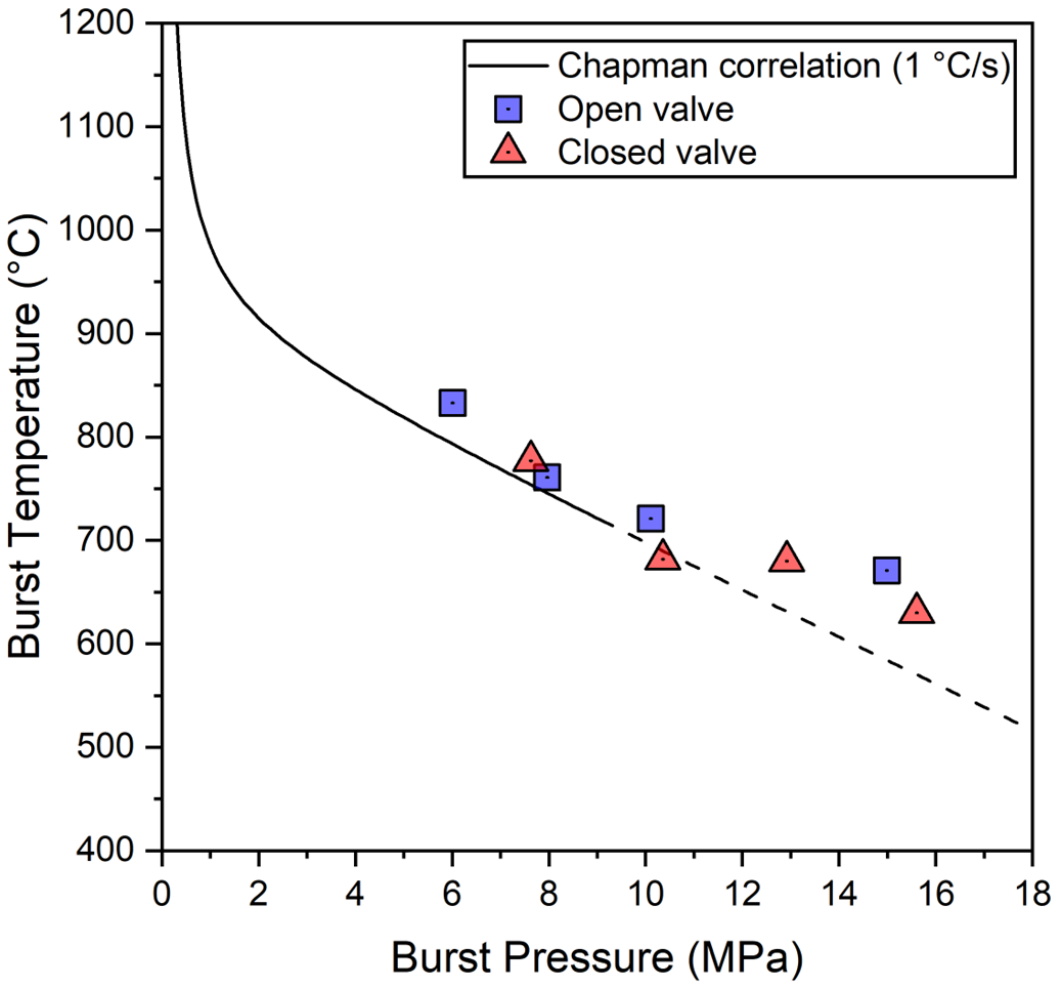

Figure 82. Burst temperature versus pressure data for all tests. The solid line represents the empirical Chapman [28] correlation, with the dashed portion indicating the extrapolated portion of the curve compared to data input into the correlation. The data reported here represents the thermocouple reading closest to the rupture. The average temperature difference between the two TCs was 35 ± 15 °C.

presented in Figure 83(a) to illustrate the profile form after testing. To quantitatively characterize the balloon, post-test diametric strain profiles were measured and are presented in Figure 83(b).

All measurements were conducted with the burst opening perpendicular to the image plane as shown in Figure 83(a). Open and closed valve tests are represented with hollow and solid symbols, respectively. The symbols are divided by nominal fill pressure at RT with the 6.2 MPa, 8.2 MPa, 10.3 MPa, and 15.1 MPa tests being shown as squares, triangles, circles, and diamonds, respectively.

Given the overlap of the initial portion of the strain-time curves of the 6.2 MPa closed valve and 8.2 MPa open valve tests, the post-test strain profiles exhibited similar form and magnitude. It should be noted, however, that the 8.2 MPa open valve test burst in view of the camera, leading to larger DIC strain measurements later in the test. This relationship of loading profile with strain is not consistent for all ex-situ comparisons. For instance, the 8.2 MPa closed and open valve tests also displayed similar balloon profiles despite a ~2.39 MPa difference in burst pressure. Notably, the 15.1 MPa nominal pressure samples, Figure 83(b), showed significantly lower post-test diametric strains compared to the other tests. It is currently unclear as to why these particular tests burst more towards the center.

Figure 83 clearly shows that the axial balloon geometry is asymmetric for all tests. The section of the balloon region opposite the top compression fitting (closer to 1) displays a gradual decrease in the strain gradient further away from the balloon peak. However, symmetry is evident on both sides of the balloon region, particularly near the peak of the balloon. To illustrate this quantitatively, the derivatives with respect to the axial profile of the 6.2 MPa open and closed valve tests are presented in Figure 84, alongside the strain profiles. For both tests, the derivative profiles displayed a linear downtrend from ~0.05 to 0.35 normalized axial distance. The lower end of the profile (closer to 0) shows an increase in the strain gradient before transitioning to this linear segment. This is most likely due to the impingement of the cladding near the compression fitting. Regardless, the linear derivative implies a constant second derivative and a parabolic form to the balloon region. As such symmetry of the balloon profile is observed for a portion of the normalized axial distance, corresponding to the peak of ballooning. This observation of symmetry is relevant, as DIC analysis was performed in the center of ballooning and indicates possibly limited effect of the constraint on *in-situ* observations.

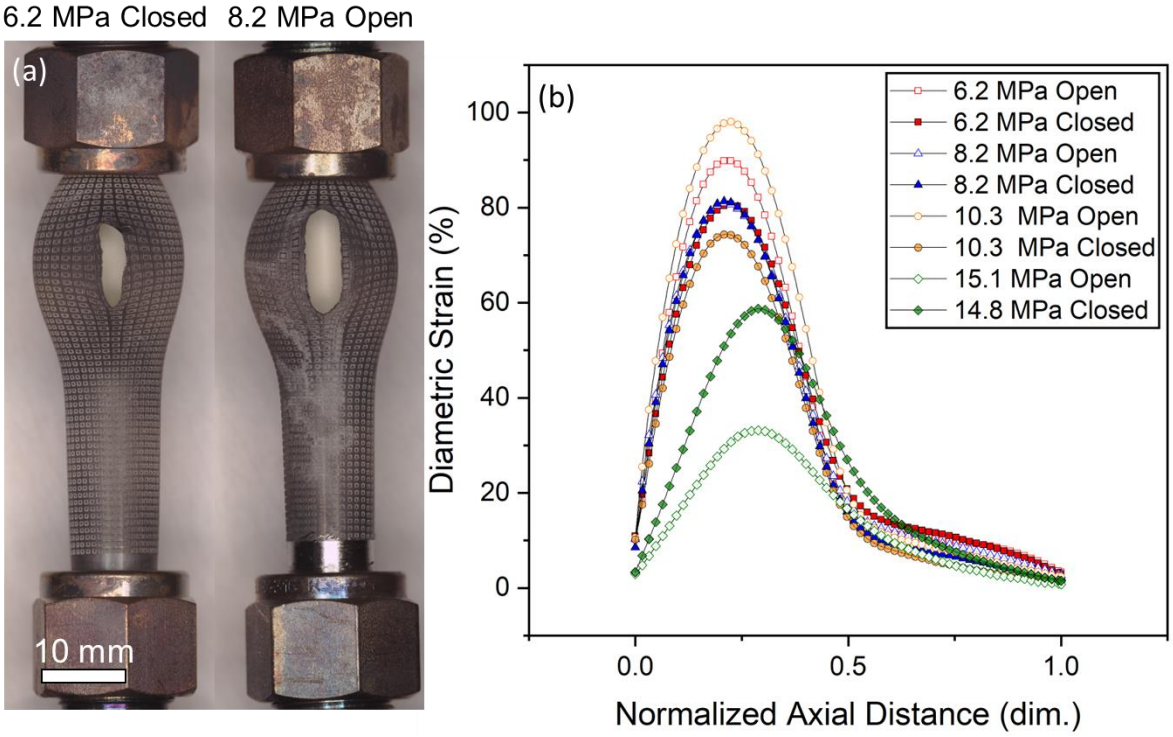

Figure 83. (a) Optical images of the 6.2 MPa closed and 8.2 MPa open valve tests. (b) Diametric engineering strain versus normalized distance along the axial direction for all tests. Zero is defined at the top compression fitting. The edge of the cladding profiles used to determine strain was determined using pixels boundaries resolvable up to ± 2 pix. All data was gathered at the same digital scale of 42.2 pix/mm, leading to an uncertainty in the diametric strain curves of ± 1%.

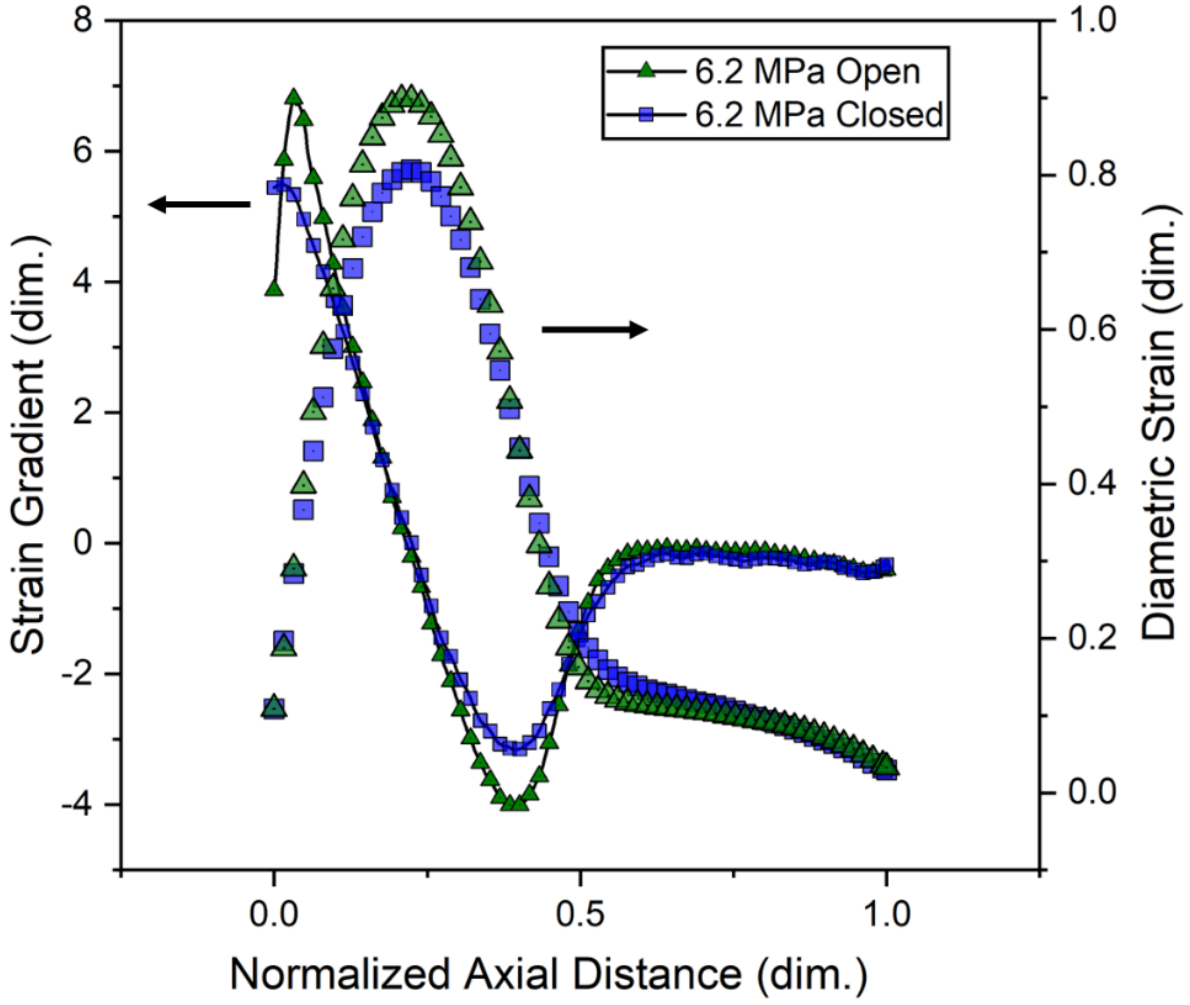

Figure 84. Diametric strain profiles along the axial direction alongside numerical derivatives of those profiles to demonstrate symmetry of the peaks.

However, it is important to remember that while this symmetry suggests a limited effect of the constraint on in-situ observations, there may still be other factors not accounted for in this analysis that could affect the observations. Results should be interpreted with caution, and more research is likely needed to confirm these findings and to fully understand the behavior of the material under these conditions.

7.3.6: Strain Rate and Arrhenius Temperature Dependence

LOCA modeling of Zircaloy claddings often assumes that ballooning is primarily governed by steady-state creep following a power law with an Arrhenius temperature dependence, Eq. 17. For a system with an Arrhenius temperature dependence, the inverse temperature and the natural logarithm of the quantity of interest should produce linear relations. In terms of steady-state creep rates this dependence is best shown by reworking Eq. 17,

$$ln(\dot{\varepsilon}) = \ln(A) + n * \ln(\sigma) - \frac{Q}{RT}, \tag{19}$$

where the slope of the line is proportional to the activation energy, Q.

To examine the validity of the steady-state assumption, Figure 85 and Figure 86 present the inverse temperature and the natural logarithm of the strain rate in the hoop direction. It is important to note that whether the burst region was in view of the cameras had a significant impact on the measured temperature dependence. Therefore, samples that burst in view of the camera, where the analysis region was near or on the burst location, are discussed separately.

Figure 85 includes the tests where burst occurred out of view of the camera, namely the 6.2 MPa open valve, 6.2 MPa closed valve, 8.2 MPa closed valve, and 10.3 MPa closed valve tests, denoted by hexagons, triangles, diamonds, and circles, respectively. As the 10.3 MPa open valve test burst between the front and back thermocouples, it was not included but briefly discussed below. In most of the tests, the strain rates were affected by noise caused by heat waves from the furnace. These heat waves introduced spatially dependent errors into the images, resulting in disturbances in the strain rate measurements. However, towards the end of the test, when the strain became sufficiently large, the effect of heat waves on the measurements was significantly reduced. The temperature dependence analysis was performed on data after reaching a true hoop strain of 0.02 to mitigate the influence of noise. Similar analysis for axial strain is not presented as the noise

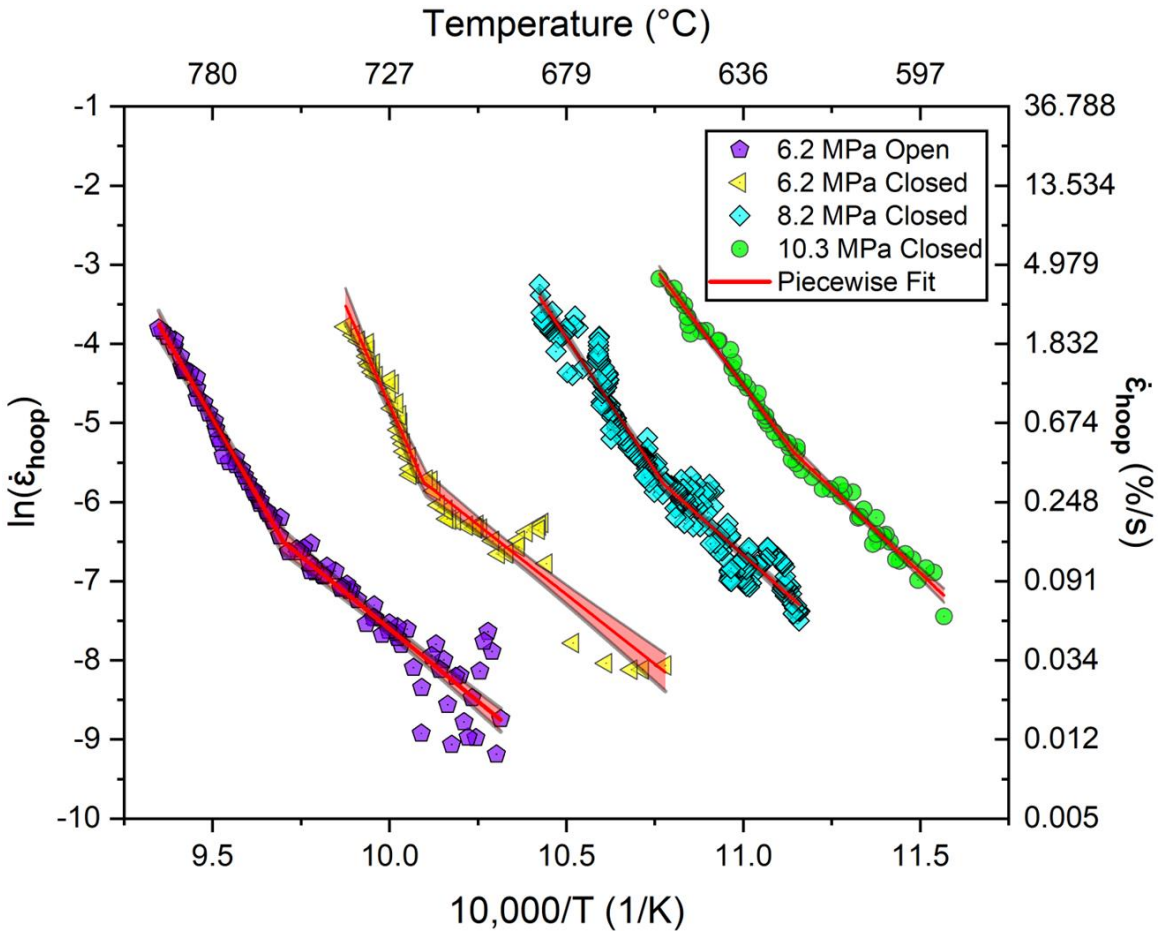

Figure 85. Natural logarithm of strain rate against inverse temperature for the tests that burst out-of-view of the DIC camera. Shaded regions represent 95% confidence interval associated with the bilinear regression.

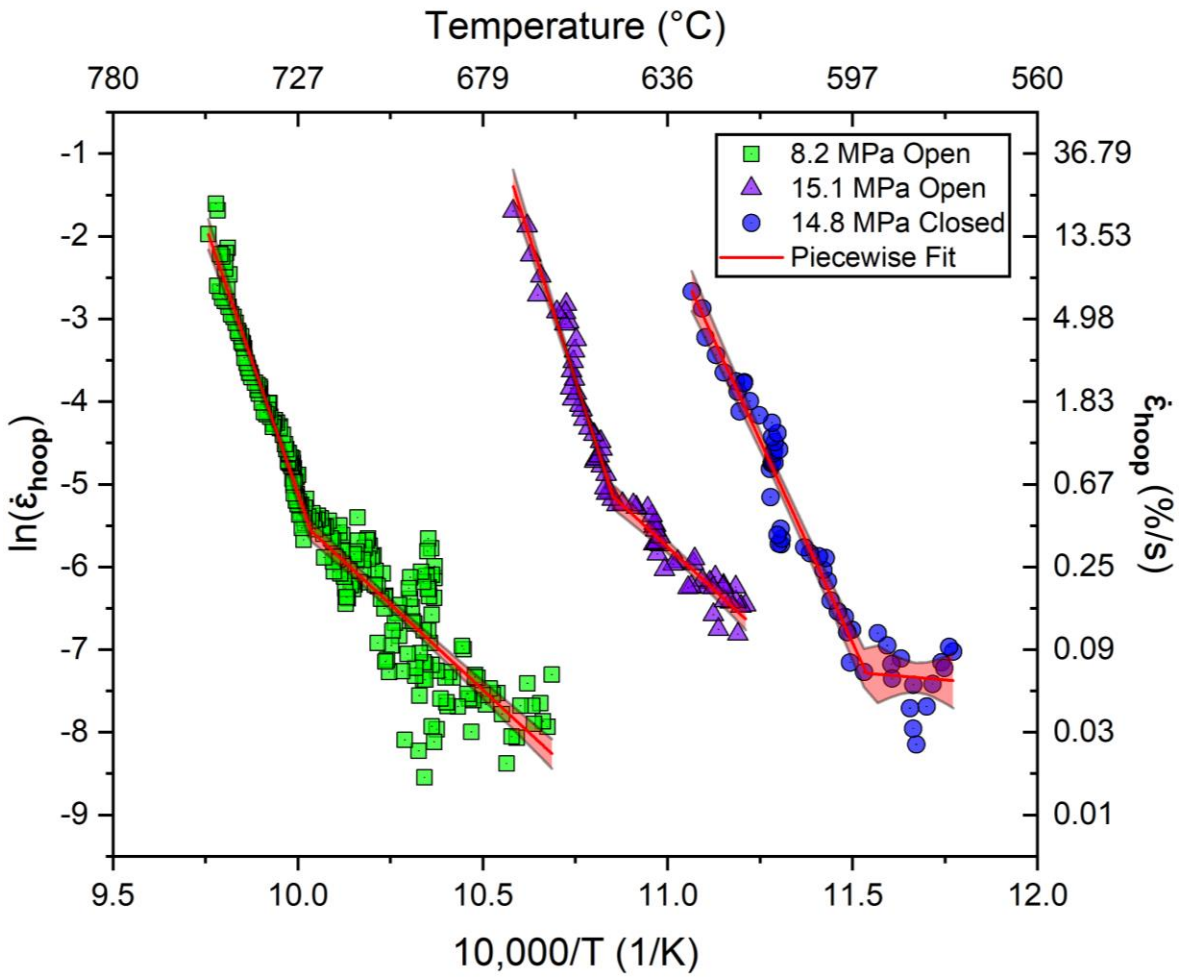

Figure 86. Arrhenius style plots for the tests that burst in-view of the camera. Shaded regions represent 95% confidence interval associated with the bilinear regression.

was too significant. Regardless, hoop strain measurements alone were able to provide insight into temperature dependence.

Figure 85 shows distinct linear trends in the strain rate-temperature plots. Two linear regions were observed, suggesting a possible transition in deformation mechanisms. Piecewise linear fits with two segments were applied to the curves in Figure 85 to determine the temperature dependence. The transition point between the two segments was determined using a Levenberg-Marquardt method. The resulting data from the temperature dependence analysis is presented in Table 15, including the error values representing the standard error of the regression.

The lower temperature segments in Figure 85 exhibited slopes, or "activation energies" ranging from 293 to 355 kJ/mol. The average activation energy for the low temperature segment in the tests shown in Figure 85 was 320 ± 28 kJ/mol. On the other hand, the higher temperature linear segments had activation energies ranging from 493 to 840 kJ/mol, with an average value of 635 ± 150 kJ/mol. These findings indicate higher activation energies and greater variation in temperature dependence near the end of life.

Figure 86 shows the temperature dependence for samples where burst occured in-view of the DIC camera, i.e., the strain measurement occurred near or at the rupture location. The 8.2 MPa open valve, 15.1 MPa open valve, and 14.8 MPa closed valve tests are presented in squares, triangles, and circles, respectively. The 0.02 strain threshold for analysis was applied to the samples in Figure 86 for consistency.

Similar to Figure 85, two distinct linear segments were observed for the 8.2 MPa and 15.1 MPa open valve tests. The lower temperature segments yielded activation energies of 344 ± 18 kJ/mol and 344 ± 29 kJ/mol for the 8.2 MPa and 15.1 MPa open valve tests, respectively. The higher temperature segments of these two tests resulted in activation energies of 1076 ± 45 kJ/mol and 1156 ± 45 kJ/mol, respectively.

Regarding the 14.8 MPa closed valve test, it is possible that a transition occurred shortly after the qualitative 0.02 strain threshold. However, by examining Figure 86, a transition around 600 °C is plausible. A piecewise fit was still applied to the data, with the higher temperature segment providing a more appropriate fit. Due to the scatter and limited data range in the lower temperature regime, the fit for this segment yielded an implausible activation energy of 31.4 ± 117

Table 15. Activation energies and transition parameters for two segment linear fits.

Sample Name	Low Temperature Q (kJ/mol)	High Temperature Q (kJ/mol)	Strain (%)	Temperature (°C)	Pressure (MPa)	Strain Rate (%/s)
6.2 MPa Open	304 ± 17	647 ± 36	5.27	758	6.04	0.150
6.2 MPa Closed	293 ± 21	840 ± 73	7.09	717	7.98	0.321
8.2 MPa Open	344 ± 18	1076 ± 45	9.91	723	8.00	0.385
8.2 MPa Closed	330 ± 15	560 ± 19	7.18	655	10.8	0.310
10.3 MPa Open	N/A	886 ± 32	N/A	N/A	N/A	NA
10.3 MPa Closed	355 ± 15	493 ± 16	8.12	624	13.76	0.466
15.1 MPa Open	344 ± 29	1156 ± 45	7.77	648	15	0.584
14.8 MPa Closed	31.4 ± 117	813 ± 38	3.05	594	16.1	0.069

kJ/mol. An activation energy of 813 ± 38 kJ/mol was determined for the high temperature segment. The average activation energy of the high temperature segments for the samples that burst in view of the camera was found to be 1015 ± 179 kJ/mol.

Lastly, the 10.3 MPa open valve test burst between the front and back of the furnace. Above 2% strain, the test exhibited linear behavior without an apparent transition. Therefore, a single linear segment was fit to the data, but not presented, resulting in an activation energy of 886 ± 32 kJ/mol.

Combining the values from the lower temperature regimes in Figure 85 and Figure 86, excluding the 14.8 MPa closed valve test, yielded an average activation energy of 328 ± 25 kJ/mol. This value is consistent with the activation energy of approximately 320 kJ/mol commonly used in LOCA models based on conventional creep testing.

While the low temperature segments displayed activation energies in agreement with creep and historic models, the high temperature segments were unusually high. These values are denoted "activation energies" due to the method of analyses in this work, but it is likely these values are not emblematic of creep activation energy. As will be discussed in the next section, the high temperature segments could be representative of plastic instability. The high temperature "activation energies" should be treated as apparent values.

The parameters obtained from these fits were further analyzed to determine potential criteria for the observed transition in behavior. The common point of the two segments provided information on the temperature, pressure, strain, and strain rate at the time of the transition, as shown in Table 15 . A clear trend is observed: higher pressures correspond to lower temperatures at the transition point. This suggests that if there is indeed a transition to another deformation mechanism, it is both temperature and stress dependent. Considering Ashby deformation maps, mechanism boundaries depend on temperature, stress, and strain rate, so this behavior would be consistent with a shift in creep mechanism. Additional explanations include possible dynamic crystallization or simple generation of network dislocation structures that could promote accelerated creep. However, as will be investigated in the next section, the stress states at the transition in behavior are well beyond yield. All tests exhibiting the transition occurred at true hoop strains below 10%. The average true strain at the transition was found to be 6.9 ± 2.1%, while

the average strain rate was 0.33 ± 0.17%/s. These findings provide important insights into the conditions at which the transition in behavior occurs.

7.3.7: Comparison of transition points against plasticity models

The observed transitions in the temperature dependence of Zircaloy-4, given the connection between temperature and pressure, suggests a connection to yielding behavior. To investigate this, a comparison was made with the plasticity model developed by Geelhood et al. at Pacific Northwest National Laboratory (PNNL). However, it should be noted that the PNNL model's correlation was based on data analysis up to a certain temperature range, and caution was advised when extrapolating to higher temperatures.

The PNNL correlation has two sets of governing equations for stress and strain. Linear elasticity describes the materials before yield according to Hooke's Law. After yield, the flow curve is determined by the following equation:

$$\sigma = K\varepsilon^{n}\left(\frac{\dot{\varepsilon}}{10^{-3}}\right)^{m}, \tag{20}$$

where σ is the stress, $\dot{\varepsilon}$ is the strain rate, K is the strength coefficient, n is the strain hardening exponent, and m is the strain rate exponent. The yield stress is defined as the intersection of Hooke's law and the above equation, given by:

$$\sigma_{yield} = \left[\frac{K}{E^{n}}\left(\frac{\dot{\varepsilon}}{10^{-3}}\right)^{m}\right]^{\left(\frac{1}{1-n}\right)}, \tag{21}$$

where E is the elastic modulus. Various factors such as cold work and fluence, which are defined in discrete temperature intervals, are considered in the equations. Factors like cold work and fluence are taken into account in discrete temperature intervals.

Typical stress relief treatments for metals reduce the dislocation density to something equivalent to ~10% CW. For this qualitative investigation, a 0% cold work assumption was made to provide predictive bounds. However, it should be acknowledged that residual effects of cold work might still be present, albeit mitigated by the stress-relief process and the transient nature of the test. To complete the description, a YS curve was generated at 50% CW for an upper bound comparison. Since burst testing is a biaxial stress state, the effective stress was considered. Irradiation effects are neglected in the model due to the as-received material condition.

Comparisons were made between the stress state at the points of transition in temperature dependence, Table 15, and the high temperature extended PNNL model. Figure 87 displays the hoop stress (blue) and isotropic effective stress (red) at the transition point plotted against temperature. The yield stress predictions from the PNNL model with 0% and 50% cold work assumptions are presented in green and red curves, respectively. The hoop stress at the transition was notably higher than the predictions of the 0% cold work curve, ranging from approximately 1.5 to 3 times higher. On the other hand, the 50% cold work curve exhibited closer agreement with the hoop stress, with values approximately 1.25 to 2 times higher. The comparison of effective stress, as expected, was generally lower than the hoop stress and reasonably aligned with the 50% cold work predictions. It should be noted that the exact cold work condition of the cladding remains uncertain. Nevertheless, the effective stress at the transition point was significantly higher than the yield stress predicted by the models, indicating that the claddings had surpassed the yield point. Given the significantly greater experimental values, is is possible that the stress state is well beyond yield and much of ballooning could be related to plastic instability. This is consistent with the strain levels summarized in Table 15 and being well above (>10X) the ~0.2% plastic deformation level associated with yielding.

7.3.8: SEM and Oxide Analysis

Figure 88(a) shows a SEM micrograph of the region opposite the burst for the 14.8 MPa closed valve sample after testing. In Figure 88(b), a higher magnification micrograph focused on a laser-engraving is presented. It can be observed that the engraving structure takes a semi-circular form that is distorted in the hoop direction due to ballooning. Post-test analysis revealed that the depth of the laser engravings was approximately 20 μm, equivalent to around 4% of the cladding thickness after testing.

Since the testing was conducted in an air environment, ZrO_2 formation was found on the outer diameter of all Zircaloy specimens, as shown in Figure 88(b). The initial surface roughness, combined with the presence of laser engravings, led to variations in oxide formation. Generally, the thickness of the oxide layer was around 1 μm. On either end of the laser engravings, the material was raised compared to the surrounding cladding. This debris oxidized more extensively compared to the material between the engravings.

To investigate the composition of the oxide scale, EDS was performed on selected points

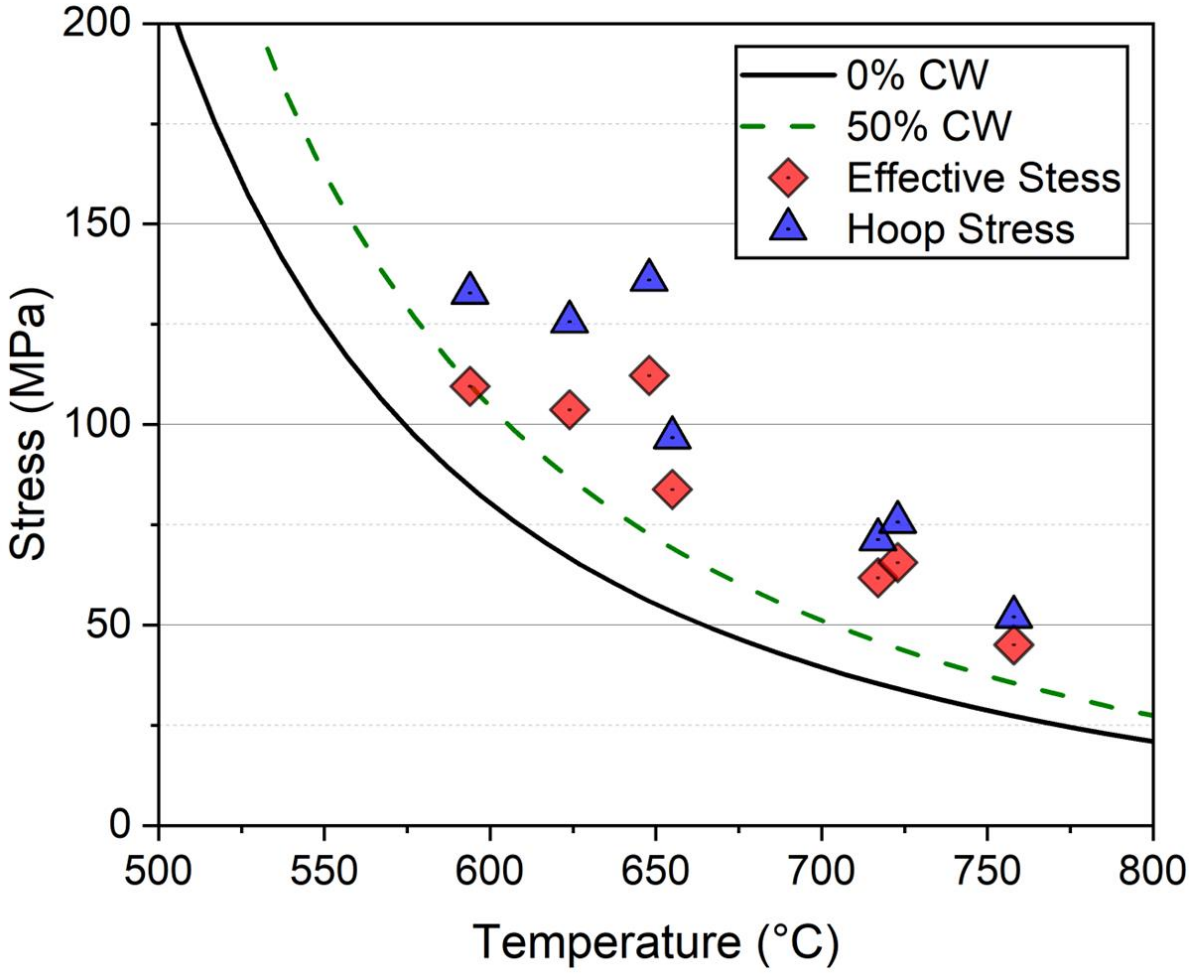

Figure 87. Comparison of PNNL YS models with 0% and 50% CW compared to hoop effective stress at the transition point. Inherent uncertainties for the hoop and effective stress encompass ~0.8 MPa due to uncertainty in the pressure transducer. Uncertainty also arises from the noise floor of the strain-time curves for which the data is explicitly collected. Conservative limits of this noise floor is ± 0.01 for this data set, which results in an uncertainty of ~3 MPa when hoop stress is adjusted using strain.

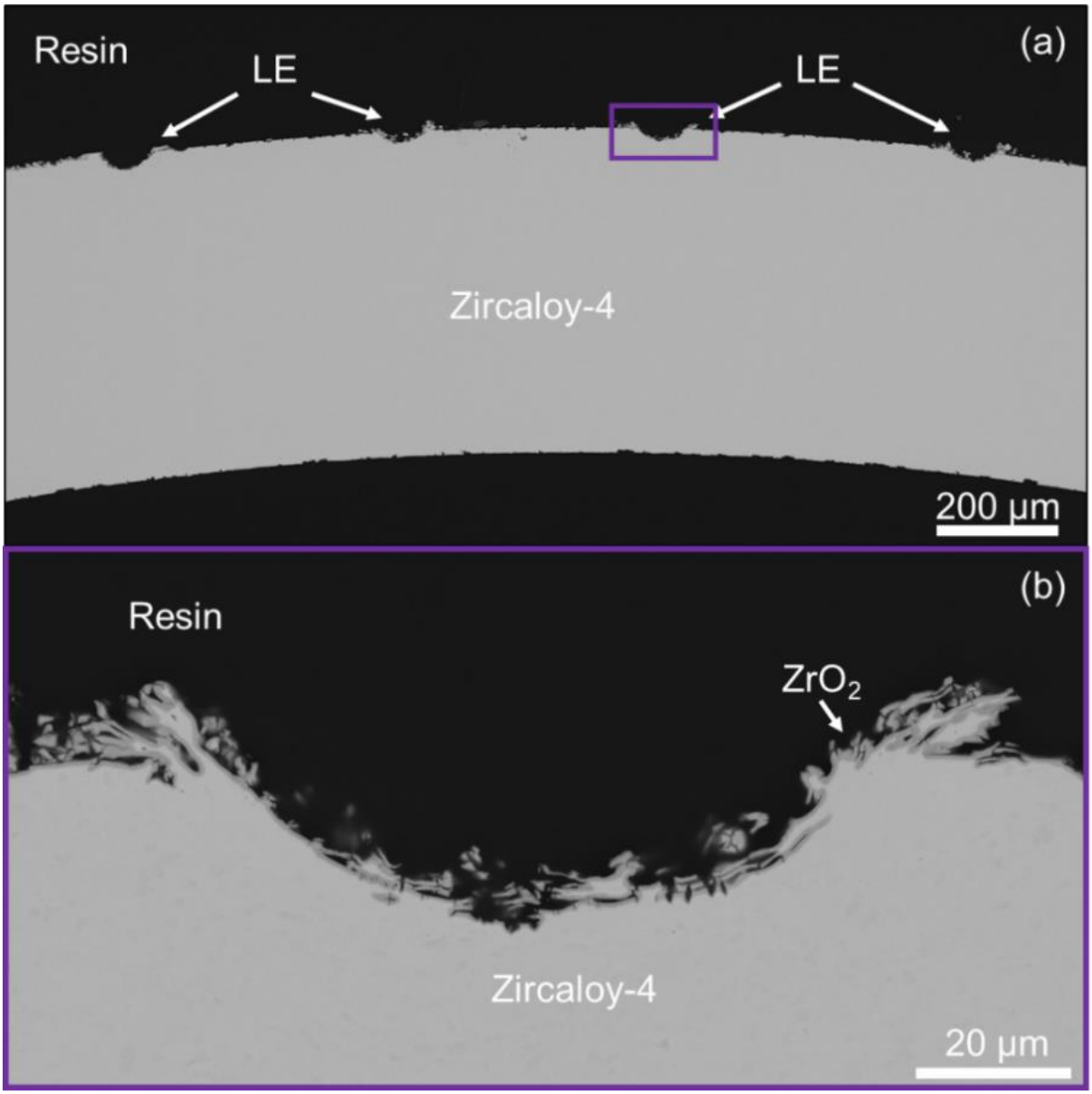

Figure 88. (a) SEM micrograph of the backside of a cladding after testing. (b) Higher magnification micrograph showing the structure of a side of a laser engraving.

of the oxide layer. The EDS analysis revealed that the scale consisted mainly of oxygen and zirconium, with negligible amounts of nitrogen present. This suggests that nitride formation in the scale was minimal.

Section 7.4: DISCUSSION

7.4.1: Arrhenius Temperature dependence and steady state creep assumption

An exponential Arrhenius temperature dependence was observed for strain rate in the hoop direction in all of the tests analyzed in Figure 85 and Figure 86. The temperature dependence was distinct in the last portion of the test (approximately the last 70-100 °C). As the tests generally failed at hoop strains of 20-60 %, these high temperature portions account for most of the deformation during testing.

Six of the eight tests presented demonstrated two distinct strain rate temperature dependencies, regardless of whether the burst region was in-view. Fits of the lower temperature segments resulted in an average activation energy of 328 ± 25 kJ/mol. This value is in agreement with the activation energy of ~320 kJ/mol used in the seminal LOCA model by Erbacher et al. [18] for the α-Zr phase. It is also consistent with the activation energy for self-diffusion [121], suggesting that the lower temperature activation energy reflects creep behavior and aligns with existing models.

However, the higher temperature regimes showed different activation energies depending on whether the cladding burst in-view or out-of-view of the camera. Claddings that burst out-of-view had an average activation energy of 635 ± 150 kJ/mol, while those that burst in-view had an average activation energy of 1015 ± 179 kJ/mol. This highlights the importance of considering the location of analysis in the balloon region when using measurement techniques like DIC. As in, strain rate profiles at azimuthal locations around the cladding could have a range of activation energies in the second high temperature regime. Similarly, it exemplifies the relevance for more nuanced, albeit exceedingly difficult, consideration of the local strain development for modeling efforts. More global in-situ characterizations, such as measuring diametric changes, could miss such behavior. Again, it should be reiterated that the “activation energies” measured for the high temperature segment are likely not reflective of conventional creep activation energies but are denoted so due to the framework of analysis.

The transition in temperature dependence suggests a change in either a creep parameter or deformation mechanism. In the context of steady-state creep, this could indicate a shift to a different stress regime, power law breakdown, transition to plastic deformation or failure mechanisms, or the onset of tertiary creep. The findings presented in this chapter strongly indicate that ballooning in Zircaloy-4 claddings is primarily governed by time-independent failure mechanisms, specifically plastic instability, rather than steady-state creep. The comparison of effective stress, as shown in Figure 87, clearly demonstrates that the transition point between the high and low temperature segments occurs well beyond the predicted yield values, providing strong evidence for the presence of plastic instability. The repeatability of the transition suggests the potential to employ failure criteria derived from conventional mechanical testing to improve the prediction of balloon behavior. These findings highlight the importance of considering plastic instability in understanding and modeling the ballooning phenomenon.

Modeling efforts beyond simple empirical values and thresholds developed in this work are a major goal of this framework. However, plastic instability is significantly more challenging phenomena to model than uniform plastic deformation prior to instability. Any such models would have to account for the evolution of non-uniform strains. In the context of this study, there are two distinct localizations: firstly, the nodal and characteristic curvature that shapes the balloon over a substantial portion of the tube, and secondly, the shorter-scale localized region within the balloon where rupture occurs. These phenomena of "diffuse" and "localized" necking are not exclusive to pressurized thin-walled tubing. Descriptions like these based on strain hardening and strain rate sensitivity have seen extensive use to develop forming limits for the manufacturing of sheet metals [200].

Models such as Swift's [135] or the Marciniak-Kuzinsky [201] could be utilized to better predict the onset of ballooning. However, describing strain post the onset of diffuse necking (or ballooning) morphs into a complex problem because the uniformity of the strain field is compromised, and deformation eventually concentrates in the rupture region. Implementing *in-situ* strain measurements, especially across the entire balloon region, could provide empirical descriptions that are then used to form more fundamental understandings of the ballooning process. Modeling efforts to describe the instability process could follow low temperature investigations such as that of Larsson et al.[143].

Alternatively, the observed variation in activation energies may be attributed to the combined effects of stress and temperature, extending beyond conventional creep regimes. Hayes and Kassner [121] discussed the possibility of continuously varying activation energy and stress exponent with temperature and stress based on their literature review, including the work by Ardell and Sherby [129] on creep testing of pure Zr. Although these findings were for pure Zr and not specifically for alloyed specimens, it is not unreasonable to consider the assumption of varying activation energy, as seen in the Erbacher Zircaloy model [18], albeit ~ 10 kJ/mol over the entire α phase.

It is important to note that the "activation energies" measured from a single transient test are not directly comparable to those obtained from large-scale isothermal creep testing. However, discussing these "activation energies" is relevant given the assumption of an Arrhenius temperature dependence in conventional models and the observed exponential behavior. The in-situ observations support the applicability of an exponential Arrhenius temperature-dependent description of cladding strain rate. Considering the variation in “activation energies” determined from high temperature segments, further testing is needed to definitively conclude this observation and improve material models. In future testing, reducing noise and systematic errors is crucial to investigate possible transitions in behavior occurring near or before the 2% strain threshold. Implementing techniques such as 3D DIC and speckle paint patterns could enhance the accuracy of the measurements. Laser-engraved patterns were chosen in the current experiments to mitigate baseline issues and facilitate testing in a steam environment. It was believed that a speckle paint pattern could interfere with steam effects. Additionally, expanding the range of test conditions and increasing the sample size will help generate statistically significant results and avoid interpolations between data sets.

Thermal gradients during testing may also contribute to the observed behavior. The average temperature difference between the front and back thermocouples was 35 ± 15 °C. Burst typically occurred near the hottest location, with the rupture forming near the highest reading TC for six of the eight tests. Historic burst testing [28] efforts have demonstrated the significant influence of azimuthal thermal gradients on the final diametric strain of α-Zr. While quantities like diametric strain provide more global measurements compared to DIC, thermal gradients still need to be considered.

The effects of the SiC shell and the resulting constraint from the compression fitting profile also possibly influenced ballooning results. The transition to higher activation energies may be attributed to the stress induced at the top of the balloon region. Similarly, the observed transition in the test could indicate that the expected strain behavior occurred until the interaction with the compression fitting was sufficient to induce a large stress. This stress could dominate the deformation behavior and lead to an artificially higher activation energy. Future efforts will focus on reducing temperature gradients and optimizing the configuration of the cladding train to minimize these effects. However, as will be shown in Chapter 9, similar behavior was found for 3D DIC testing.

7.4.2: Strain-time behavior and loading considerations

The final strain rates measured for the samples that burst out-of-view of the camera were generally close to or greater than the plastic instability criterion of 2.78%/s. The lower pressure tests, such as the 6.2 MPa open and closed samples, had final effective strain rates that were closest to the critical value, with values of 2.65%/s and 2.31%/s, respectively. It is evident that the plastic instability criterion provides a conservative threshold for failure, particularly accurate for lower pressures. Given the trend of greater final strain rates with higher burst pressure, Figure 81, it could be possible to improve this failure criterion for applicability beyond low heating rates and higher pressures. This could be critical to model fidelity as the higher-pressure tests deformed 0.07-0.15 in effective strain after surpassing a 2.78 %/s rate. Rigorous and repeat testing of this observation is needed before implementation.

From Figure 74, it can be observed that the isobaric condition approximately reflected a closed valve pressure profile from the onset of ballooning until rapid deformation. The rate of pressure change decreased at around 370 s when ballooning began for the 6.2 MPa closed valve test. Although the pressurization rate was lowered, it remained positive, indicating that the increase in pressure due to temperature rise was greater than the decrease resulting from volume expansion. From 370 s until 433 s, the pressure continued to increase, reaching a maximum value of approximately 8 MPa. During this time window, the hoop strain curves for the 6.2 MPa closed and 8.2 MPa open valve tests showed considerable overlap, with a 7% hoop strain at 433 s. This point corresponds to the transition in temperature dependence for the 6.2 MPa closed valve test. After 433 s, the hoop strain rapidly increased for the closed valve test and deviated from the curve of the

open valve sample. A corresponding decrease in pressure was observed. While the temperature was still increasing, the pressurization rate became negative, indicating that volume expansion became the dominant factor. There may exist a critical parameter, such as volume, strain, or strain rate, at which this switch in the pressurization driving mechanism occurs. The value of this parameter is likely heavily influenced by experimental setup considerations such as heating method, gas volume, and rod internals. Therefore, data from isobaric or "open valve" testing could provide a more reliable baseline across different experimental setups and cladding geometries.

Section 7.5: CONCLUSIONS

Zircaloy-4 cladding segments were subjected to simulated LOCA transients, and 2D-DIC was used to analyze the in-situ behavior of the cladding balloons. The strain rate exhibited an exponential Arrhenius temperature dependence, with two distinct segments indicating a potential change in the deformation mechanism. The “low” temperature regime showed an average activation energy of 328 ± 25 kJ/mol, consistent with existing LOCA models based on creep parameters. However, a transition to an unusually higher activation energy was observed in the “high” temperature segment, and this transition varied depending on whether the rupture occurred in or out of view of the DIC camera. The average activation energies for the high temperature segment were 635 ± 150 kJ/mol for out-of-view ruptures and 1015 ± 179 kJ/mol for in-view ruptures. This “activation energy” for the high temperature segment is not likely reflective of a traditional creep activation energy and should be treated as apparent. The stress-state at these transition points were compared to yield stress models, indicating that the high temperature segment may be beyond yield and possibly representative of plastic instability. This novel observation demonstrates the nuance of cladding behavior that is revealed through techniques like DIC, compared to conventional global measures like diametric strain. The transition in behavior occurred at an average hoop strain of 6.9 ± 2.1%, suggesting a possible threshold for modeling purposes.

Further testing with improved noise reduction and unconstrained cladding assemblies is needed to confirm and expand upon these findings particularly for the “high temperature” regime. Additionally, the measured strain rates showed a linear relationship with rupture pressure, and at lower pressures, they were in relative agreement with a conventional criterion of 2.78%/s. Future work will focus on optimizing furnace configuration to minimize the influence of heat waves,

investigating the impact of compression fittings on ballooning, and utilizing 3D DIC to overcome limitations of a single image plane.

Chapter 8: Accelerated Creep Testing of Zircaloy-4 using *In-situ* Techniques

Chapter Foreword

This chapter presents the results from accelerated creep testing conducted on SRA Zry-4. Given the centrality of accelerated qualification to the framework developed in this dissertation, the testing was conducted to maximize the amount of data from a limited set of samples. A novel approach was employed within this framework to obtain multiple creep data points from a single specimen. The procedures developed for this known alloy system can be extended to ATF concepts, as shown for Cr coated Zr in the subsequent chapter. Conducting tests on uncoated Zr claddings serves to establish a necessary reference point for Cr-coated concepts and verifies the efficacy of this accelerated methodology. Beyond validation of this technique for later use, this chapter served to investigate the unique shift in thermomechanical behavior observed in Chapter 7 that could be attributed to changes in creep parameters/regimes as opposed to the previously discussed time-independent failure mechanisms.

A pressurization methodology involving discrete internal loading steps was employed to determine creep behavior across a broad stress range from a single sample. Testing was performed on Zircaloy-4 at 550 °C, 600 °C, 650 °C and 700 °C, with a total of nine tests conducted yielding 39 stress-strain rate data points. The time at temperature before initial pressurization as well as the duration of the loading steps were varied to investigate effects on strain rate. Higher than expected strain rates were found for the 700 °C test that was held for a shorter duration before pressurization. Strain rates recovered from subsequent loading steps for that shorter hold time 700 °C test eventually came into agreement with model predictions and tests with longer hold times before initial pressurization. Microstructural evolutions are speculated to be the source of these initial discrepancies. Recovered strain rates and creep parameters are evaluated and compared to models detailed in Chapter 5. Isotropic variants of the models were found to bound experimental strain rates at higher temperatures.

Section 8.1: INTRODUCTION

Chapter 7 presented *in-situ* data from transient testing, showing a marked deviation from behaviors traditionally described by steady-state LOCA models. Specifically, a transition was

observed in the strain rate dependency from a lower temperature segment, where activation energy was consistent with steady-state creep-based models, to a high-temperature regime displaying activation energies that were 2-3 times higher. Preliminary stress state comparisons at these transition points with the plasticity models discussed in Chapter 7 suggested that time-independent failure mechanisms—such as plastic instability—might be largely responsible for the balloon deformation, rather than creep. On the other hand, there is a possibility that creep remained dominant implying that a change in other creep parameters, such as the stress exponent, could lead to greater apparent activation energy in the high-temperature segments. This hypothesis of continued creep domination is supported by the sustained Arrhenius behavior observed in the high-temperature segment before failure. Therefore, modified creep testing in an accelerated manner was performed on SRA Zry-4 claddings from 550 to 700 °C using this new *in-situ* framework. Systematically increasing the load at temperature while measuring strain enabled the determination of multiple strain rate and stress data points from a single sample.

The results from this testing were compared against existing high temperature LOCA models, as outlined in Chapter 5. Three high temperature creep models are prominent for Zircaloys: (1) the historic Erbacher model [18], (2) the Kaddour model [119], and (3) the Donaldson model [120]. While the Erbacher and Kaddour models were products of axial tension testing, the Donaldson model originated from biaxial internal pressure testing. The Erbacher and Kaddour models require the application of Hill parameters for comparison against measured hoop strain data. Two sets of anisotropic factors were utilized including the isotropic case and anisotropic Hill parameters used most recently by Massih [19] in a comparative study.

Section 8.2: EXPERIMENTAL METHODS

Segments of SRA Zry-4 cladding were subjected to isothermal creep testing through internal loading and evaluated using the developed SATS *in-situ* measurement framework. The Zry-4 is from the same batch as that described in the previous chapter. While detailed descriptions of the isothermal testing methods, camera configuration, and cladding train setup can be found in Chapter 6, a brief discussion is provided here. The Zry-4 cladding segments were 11.4 cm in length with a nominal wall-thickness and outer diameter of 0.575 mm and 9.5 mm, respectively. An 8 mm diameter alumina rod was present inside the cladding segment to

simulate fuel volume and thermal mass. As opposed to the 2D DIC testing in Chapter 7, the end of the cladding train was not loosely held in place and completely free to expand/contract.

For this work, stereo DIC was utilized with cameras capturing images at a frequency of 1 Hz. Figure 89(a) presents an image of the setup during testing, while Figure 89(b) offers a schematic representation of the furnace and camera orientation. Figure 90(a) displays the cladding train prior to the application of a DIC pattern. A traditional speckle pattern was employed for DIC using high-temperature paint, as shown in Figure 90(b). Two Type S thermocouples were utilized during testing, both placed 12 mm above the cladding centerline. One thermocouple, controlling furnace output, was situated directly in front of the viewport, while the other was located 180° from the control thermocouple. Due to interference with DIC measurements, the thermocouples were not placed at the centerline.

The accelerated creep testing involved internal loading variations during the tests, all of which were conducted in a steam environment. After reaching the target isotherm temperatures of 550, 600, 650, or 700 °C, samples were pressurized with Ar, and the load was increased after specified time intervals. Detailed loading histories for the low (550 and 600 °C) and high (650 and 700 °C) temperature tests are provided in Table 16 and Table 17, respectively. The tables also include average readings from the control (front) and back thermocouples for the duration of the test.

Two tests were conducted at 650 °C with identical pressure steps but different time intervals to assess the influence of the duration spent at a given pressure step on strain. Likewise, an additional test at 650 °C and another at 700 °C were subject to pressurization following a 25-min hold to investigate the impact of time at temperature prior to pressurization. All remaining tests were pressurized within approximately 1-2 minutes of reaching the target temperature. The shorter hold samples were pressurized after the temperature readings from both thermocouples reached stability. DIC strain measurements were synchronized with the pressure and temperature history, enabling the determination of stress dependencies. Linear fits of the strain profiles were employed to calculate the strain rate for each loading step.

Hoop and axial strain measurements were utilized to adjust stress via the thin-walled approximation at the start of a given pressure step,

$$\sigma_\theta = \frac{PR}{h}, \tag{22}$$

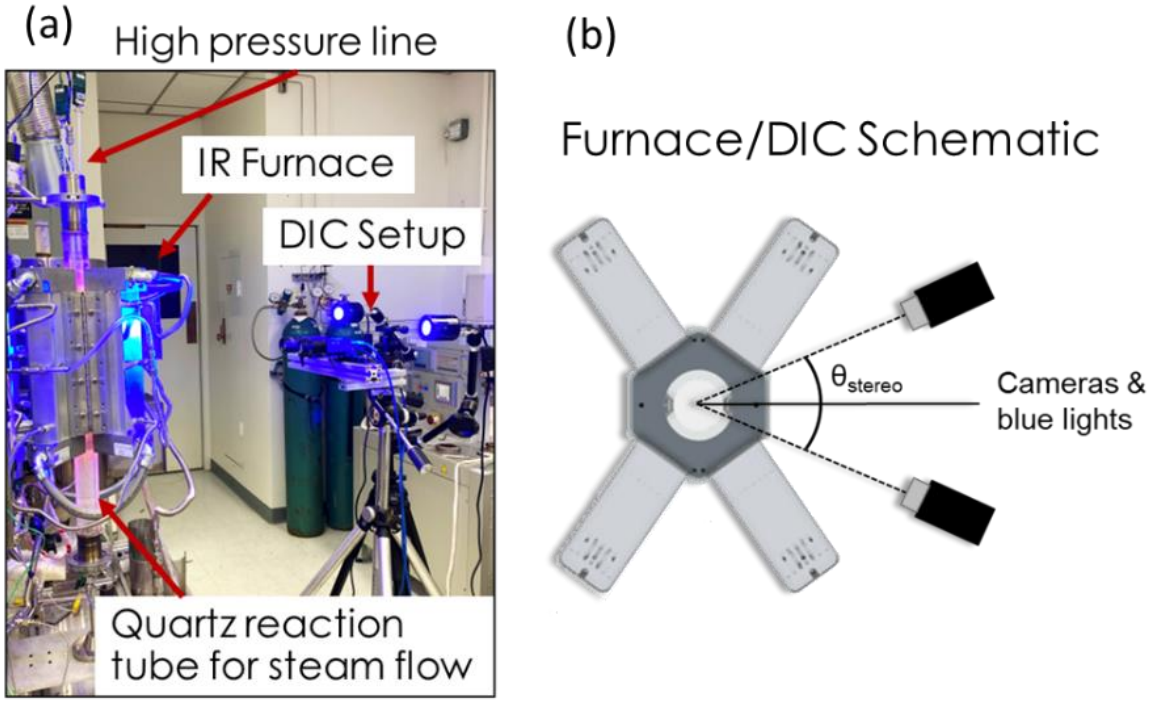

Figure 89. (a) Image of the DIC and furnace during testing and (b) top-down schematic of the furnace and DIC system.

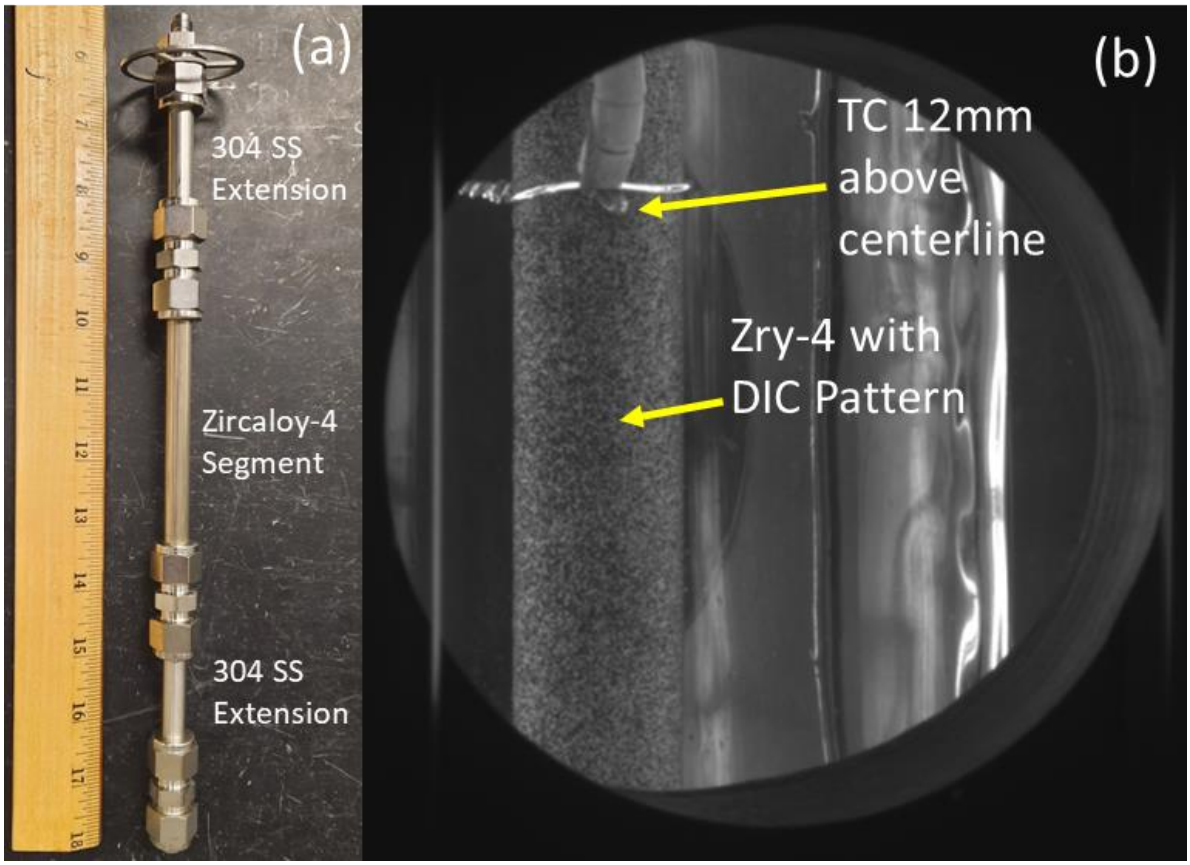

Figure 90. (a) Cladding strain with Zry-4 specimen and 304 SS extension pieces. (b) Image from one of the cameras illustrating thermocouple placement.

Table 16 Low temperature Zry-4 test conditions.

550°C Test 1	550°C Test 2	600°C Test 1	600°C Test 2
8.17 MPa, 1500 s	8.17 MPa, 1000 s	6.16 MPa, 1000 s	6.26 MPa, 1100 s
10.38 MPa, 1000 s	9.70 MPa, 700 s	8.31 MPa, 800 s	8.45 MPa, 650 s
11.58 MPa, 1680 s	10.98 MPa, 500 s	10.46 MPa, 250 s	9.74 MPa, 151 s
N/A	12.33 MPa, 500 s	11.74 MPa, 18 s	N/A
N/A	13.90 MPa, 579 s	N/A	N/A
Control Temperature (°C)	**Control Temperature (°C)**	**Control Temperature (°C)**	**Control Temperature (°C)**
550 ± 1	552 ±1	601 ± 1	601 ± 2
Back Temperature (°C)	**Back Temperature (°C)**	**Back Temperature (°C)**	**Back Temperature (°C)**
560 ± 5	559 ± 5	602 ± 2	616 ± 4

Table 17. High temperature Zry-4 test conditions.

650°C Test 1	650°C Test 2	650 °C Test 3 (25 min)	700°C Test 1	700°C Test 2 (25 min)
4.72 MPa, 1000 s	4.62 MPa, 700 s	4.82 MPa, 700 s	3.34 MPa, 700 s	3.37 MPa, 700 s
5.44 MPa, 500 s	5.52 MPa, 300 s	5.85 MPa, 300 s	4.14 MPa, 300 s	4.05 MPa, 300 s
6.06 MPa, 300 s	6.27 MPa, 200 s	6.87 MPa, 200 s	4.89 MPa, 200 s	4.90 MPa, 200 s
N/A	6.93 MPa, 200 s	7.46 MPa, 200 s	5.52 MPa, 200 s	5.58 MPa, 200 s
N/A	7.69 MPa, 200 s	8.48 MPa, 200 s	6.19 MPa, 60 s	6.23 MPa, 200s
N/A	8.41 MPa, 225 s	9.00 MPa, 42 s	N/A	6.90 MPa, 130s
Control Temperature (°C)	**Control Temperature (°C)**	**Control Temperature (°C)**	**Control Temperature (°C)**	**Control Temperature (°C)**
650 ± 1	651 ± 2	651 ± 2	701 ± 1	700 ± 1
Back Temperature (°C)	**Back Temperature (°C)**	**Back Temperature (°C)**	**Back Temperature (°C)**	**Back Temperature (°C)**
619 ± 3	679 ±4	642 ± 4	687 ± 2	655 ± 3

where σ_θ is the hoop stress (MPa), P is the pressure (MPa), R is the mean radius (mm), and h is the wall-thickness (mm). Wall-thickness was adjusted at the start of each pressure step using strain measurements. Similarly, at the beginning of a pressure step the radius was corrected using the principle of volume conservation and strain measurements.

Section 8.3: RESULTS

8.3.1: Strain-curves from lower temperature testing (550 and 600 °C)

Hoop strain curves for the 550 °C and 600 °C tests are presented in Figure 91.(a) and Figure 91.(b), respectively. Adjacent-averaged strain profiles are also included for all tests to facilitate the visualization of trends. It is important to note that the pressure steps between the test temperatures are not identical. As the 550 and 600 °C tests were among the first in this exploratory experimental campaign, the experimental parameters were still being fine-tuned. The objective was to maximize the number of steps while ensuring sufficient data points per step. This optimization process is evident in the five steps completed for the 550 °C Test – 2, compared to the three steps for the remaining lower temperature tests. Similar to the intentional variation in time steps at 650 °C, the differences in loading and time intervals provide valuable insight into the effects of stress history.

Excellent agreement was observed in the first two pressure steps between the 600 °C samples. There was a discrepancy of approximately ~1.5 MPa in the third steps of the tests, still providing valuable data on strain rate. For the 600 °C – 2 sample, the pressure was loaded to a final value of 11.74 MPa, leading to the failure of the cladding 15 seconds after the increase. The final pressure step is excluded from further analysis given the brief interval. However, this segment was found to align with the general strain rate trends for the test.

8.3.2: Strain rate – stress dependence of the lower temperature regime

Strain-rates were determined by linear fits of the strain curves for each pressure step in Figure 91.. This implicitly assumes steady state creep conditions have been achieved, which may not be true at these lower temperatures. While non-linear strain might have been present, particularly during the initial pressure step, a consistent approach of linear fitting across all steps was adopted. For materials following power law creep, a common method of investigating stress dependence is to take the logarithm of both sides of the steady-state creep

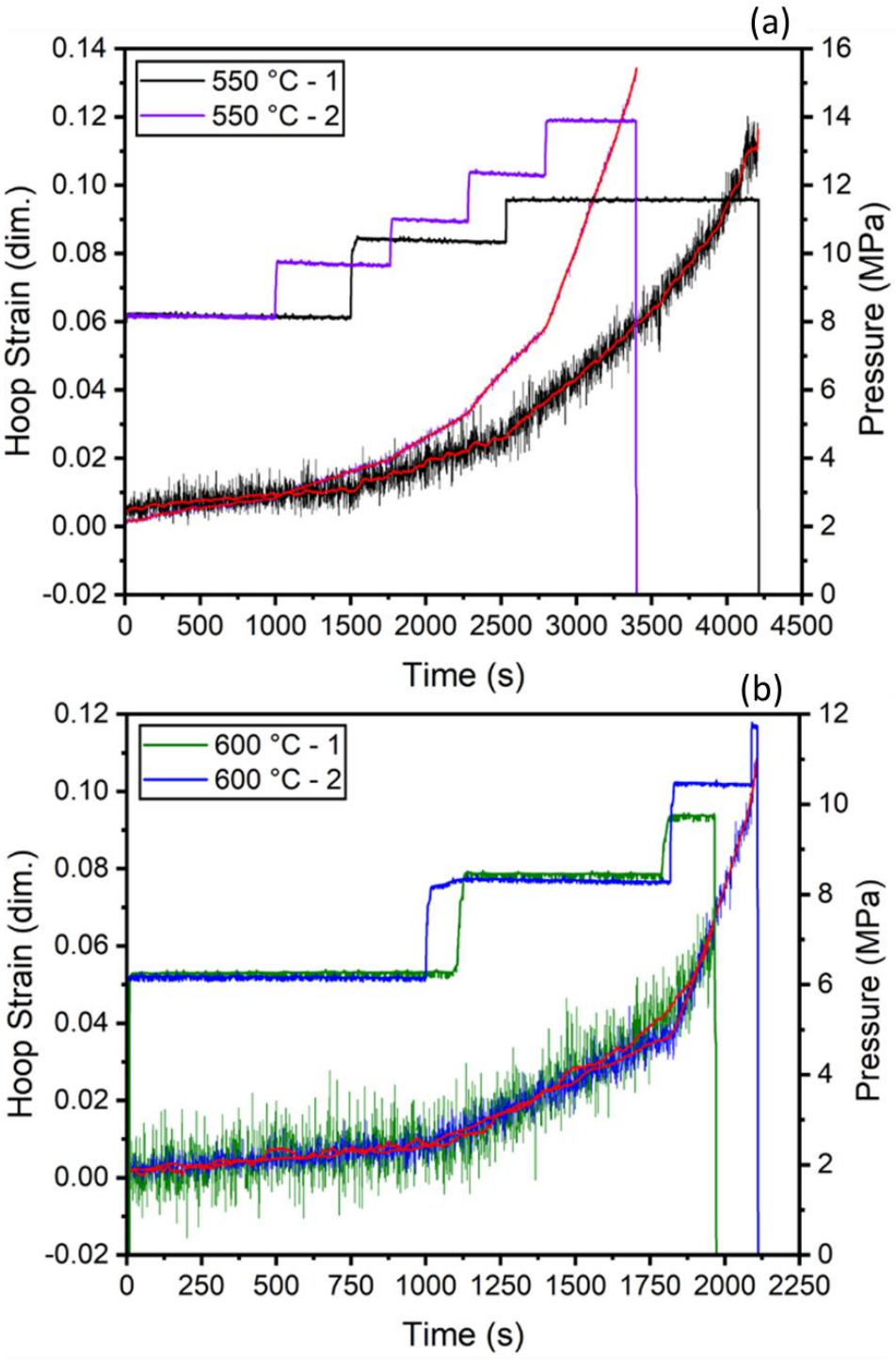

Figure 91. Strain curves and pressure histories for the (a) 550 °C and (b) 600 °C accelerated creep testing.

equation:

$$\ln(\dot{\varepsilon}) = \ln\left(\frac{A}{T}\right) - \frac{Q}{RT} + n\ln(\sigma), \tag{23}$$

indicates linear relationship between $\ln(\dot{\varepsilon})$ and ln(σ) with the slope proportional to n. At a given temperature the remaining factors are assumed to be constant. Strain rate plotted against stress for both test temperatures are presented in log-log form in Figure 92.

Both curves in Figure 92 are composites of the two tests performed at the target temperatures and demonstrated distinct linear trends. Linear fitting of each composite curve was performed, illustrated by the trend lines. Stress exponents were derived from the slopes of these fits, yielding 4.88 ± 0.35 and 5.09 ± 0.26 for the tests conducted at 550 °C and 600 °C, respectively. The error in the stress exponents represent the standard error of the linear fits for the stress-strain rate curves.

While grouping the data by temperature yields stress exponents in accordance with each other and with those found in literature, this grouped behavior is not fully representative of the variation between individual samples, particularly in the case of the 550 °C tests. To underscore this point, the data from Figure 92 was presented with clear demarcation between individual tests. The tests conducted at 550 °C demonstrated some variability in stress dependency. This discrepancy is most pronounced at the first pressure step, where the 550 °C – 1 test (represented in green) exhibits a slightly lower strain rate for the same initial stress. It may be a consequence of sample-to-sample variability, or possibly, furnace conditions were still equilibrating during the first step for 550 °C -2 (purple) even with the control thermocouple reading 550 °C. However, the second and third steps of this test exhibit greater concordance with the group trend. The difference between the first pressure steps could be attributed to factors such as temperature stabilization or microstructural changes, which will be explored further in the context of high-temperature data. Alternatively, it might be the result of primary creep effects with varying loading and time interval histories, or it could stem simply from sample-to-sample variability. Regardless of these discrepancies, the data exhibits good consistency considering the differences in loading histories.

8.3.3: Comparison of low temperature testing to model predictions

Proper comparison of model predictions to measured hoop strain necessitates the assumption of Hill parameters due to the anisotropy of α-Zr. Previously, the activation energy,

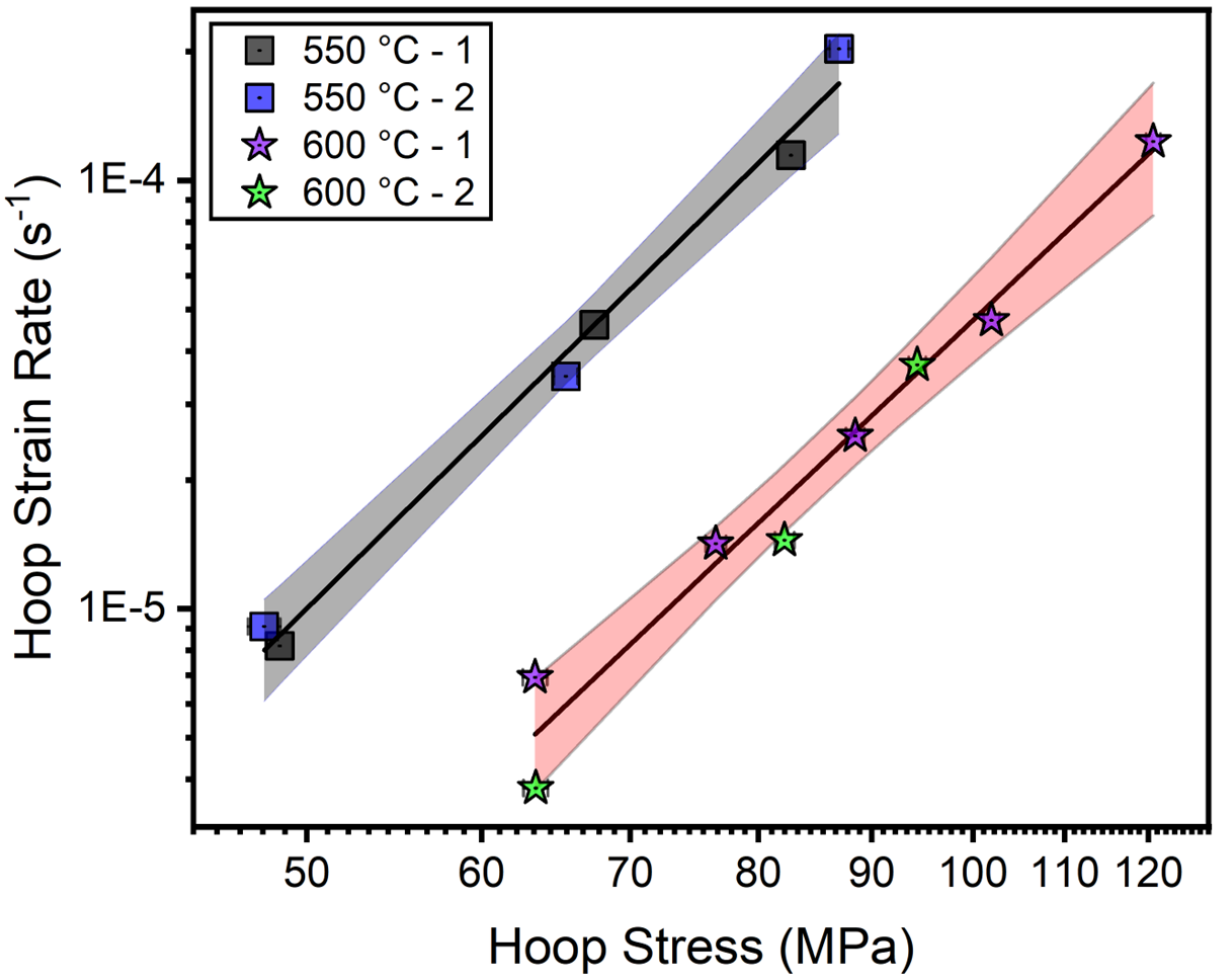

Figure 92. Strain rate and stress trends for the 550 °C and 600 °C testing. Error associated with the pressure transducer and the error associated with the linear fit for each pressure step are within the symbol size. Standard error of the linear fits of strain rates are at most an order of magnitude lower than the measured strain rate. The shaded region represents the 95% confidence interval for the linear fit.

Q, and the stress exponent, n, have been assumed to be independent of direction [123]. Assuming constancy, the structure constant A, can be converted from the effective value to the hoop direction by the relation,

$$A_\theta = \left[\frac{1}{4}(F+G)+H\right]^{\frac{n-1}{2}}\left(H+\frac{1}{2}F\right)(F+G)^{\frac{-(n+1)}{2}}A_z, \quad (24)$$

where A_θ is the hoop direction structure constant, and F, G, and H are the Hill parameters. This assumption is fundamental to creep-based modeling, with implementation in the seminal Erbacher model. Hill parameters for this batch of Zry-4 is unknown. To set bounds for the comparison of the Erbacher and Kaddour models, two sets of Hill parameters were selected. The first set represents the anisotropic case, with parameters initially utilized in the Erbacher model and later employed by Massih [19], i.e., F = 0.956, G = 0.304, and H = 0.240. The second set corresponds to the isotropic case where F = G = H = 0.5.

Figure 93 depicts the strain rate predictions from the models alongside the experimental data at 550°C and 600°C. Input parameters for the specific models (Donaldson, Kaddour, and Erbacher) are detailed in Chapter 5. The creep rate data from the current study are a factor of 5 to 10 higher than the upper bound of the model predictions. The Kaddour, Donaldson, and Erbacher models are represented by blue, black, and green lines, respectively. Solid lines correspond to the isotropic models, while dashed and dotted lines represent anisotropic model predictions using the Hill parameters from Massih. The Donaldson creep data, collected based on the tangential direction, did not require anisotropic coefficients to generate hoop strain rate predictions. While presented here for comparison, this creep model is still only valid for the specific anisotropic (textured) Zr alloy samples tested by Donaldson.

The isotropic models in Figure 93 predict higher strain rates than their anisotropic counterparts. However, this pattern does not apply to all possible sets of anisotropic factors. These factors are coarse, empirical coefficients relating the mechanical behavior across the axes. Certain sets of anisotropic coefficients can yield the opposite effect—i.e., higher strain predictions. For instance, swapping the F and H values from the set used by Massih results in almost a tenfold increase in the anisotropic strain rate predictions. The anisotropic case employed by Massih was chosen given its relevance to both historical and recent descriptions of cladding LOCA behavior.

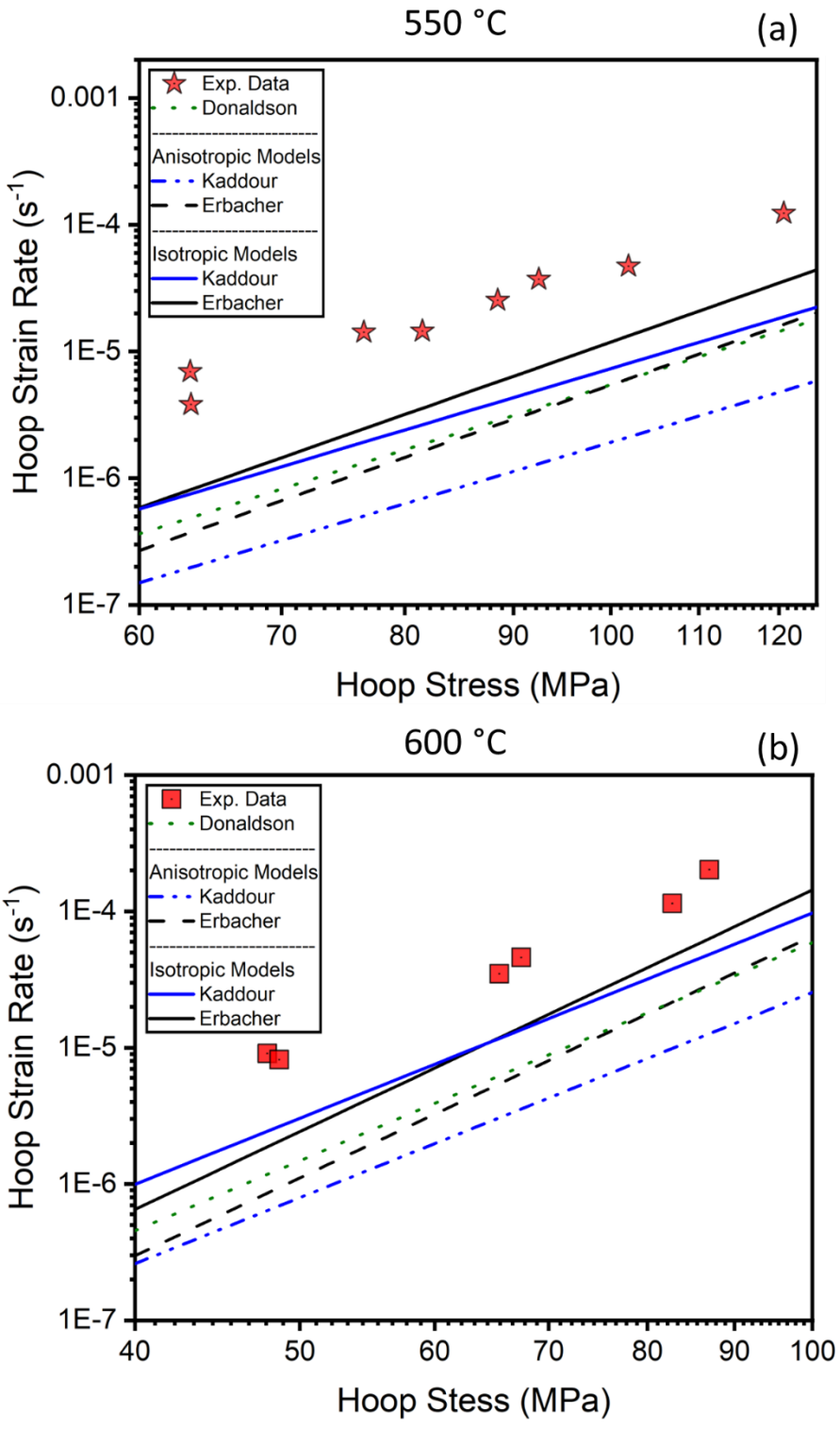

Figure 93. Strain rate data compared to model predictions using anisotropic and isotropic factors.

The difference in magnitude between the lower temperature experimental data and the models may be attributed to several factors beyond the correct selection of anisotropic coefficients. A likely explanation is that the current data set were acquired at insufficient times to achieve steady state creep conditions for these low temperatures. Primary creep invariably corresponds to higher strain rates compared to steady state creep . Additionally, these models were developed based on higher temperatures, which align more closely with conventional LOCA considerations and the α to α + β phase boundary. Lastly, the current testing is not directly comparable to models implemented in BISON due to the interpolation scheme between low and high-temperature regimes discussed in Chapter 5. However, since the experimental values are within the range of 10^{-5} to 10^{-4}, the underpredictions may have negligible impacts on creep-based LOCA modeling results.

At lower temperatures, the experimental data significantly exceeds both the isotropic and anisotropic predictions—almost an order of magnitude higher compared to the latter. However, the stress exponent of ~5 for the experimental data is consistent with the models as well as dislocation-controlled creep behavior. This suggests that the experimental data, although underpredicted, exhibits behavior somewhat consistent with steady-state creep. Further investigation with lower noise levels is necessary to investigate possible influences of primary creep.

No specific deviation in the stress dependence was identified that could suggest an apparent shift in deformation behavior at these lower temperatures. It is worth noting that the stress states for these lower temperature tests presented are near or below the transition points discussed in Chapter 7. This first phase of testing focused on optimizing the process to extract the maximum amount of data from a single sample. Subsequent testing, with enhancements to the experimental setup, may allow for more precise targeting of the transition stresses observed in transient testing.

This lower temperature testing aimed to establish a foundation and investigate potential transitions. However, the later high-temperature testing, which will be detailed subsequently, holds more relevance for direct comparisons with conventional LOCA models.

8.3.4: Higher temperature testing and the effects of hold time before pressurization

The raw hoop strain data and pressure step history for the 650 °C and 700 °C tests are presented in Figure 94(a) and Figure *94*(b), respectively. As mentioned above, the 650 °C Test-2 (red) featured intentionally varied time intervals for each pressure step to study potential time-related effects on strain rate. 650 °C Test-3, subjected to a 25 min hold at temperature before pressurization, is represented in orange, while Test-1, which endured a ~1-2 min hold before pressurization, is illustrated in green. It should be noted that Test-3 was intended to be an exact replication of Test-1 but with a longer hold time before initiating the test. However, due to experimental factors associated with manual pressure increases, each pressure step was consistently higher by about ~1 MPa. Still, comparing 650 °C Test-1 and Test-3 allows for a study of the sensitivity of strain curves to alterations in pressure history.

It is apparent from Figure 94(a) that the 650 °C Test-2 had higher levels of noise, which was significantly reduced in later tests through process optimization. Still, the trend of the strain curves showed considerable agreement for the first pressure step. Note that the longer time interval 650 °C test, Test-2, only lasted to the third step and ~3.5% strain. Ballooning and failure occurred out of view for all tests, away from the analysis region near the compression fitting. This was likely caused by straining of the cladding until it contacted the compression fitting, where after stress concentration led to rapid ballooning. Future testing could utilize a better cladding train configuration to centralize ballooning to the analysis region.

The difference in the 700 °C strain curves is evident during the first pressure step (~3.5 MPa) in Figure 94(b). The sample that was held for 25 min (blue) shows much lower, linear strain. In contrast, the hoop strain for the sample held for 1-2 minutes (black) displays a rapidly increasing strain at the onset of the pressure step, which then stabilizes. This decreasing strain rate might represent primary creep. However, examining the latter portions of the strain curves shows linear strain rates. The reasoning for this observed difference will be further discussed in the subsequent section.

8.3.5: Strain-rate and stress dependency for 650 and 700 °C testing

The strain rate and associated stress data derived from the curves presented in Figure 94 are visualized in Figure 95. The experiments conducted at 650 °C (Tests 1, 2, and 3) are marked

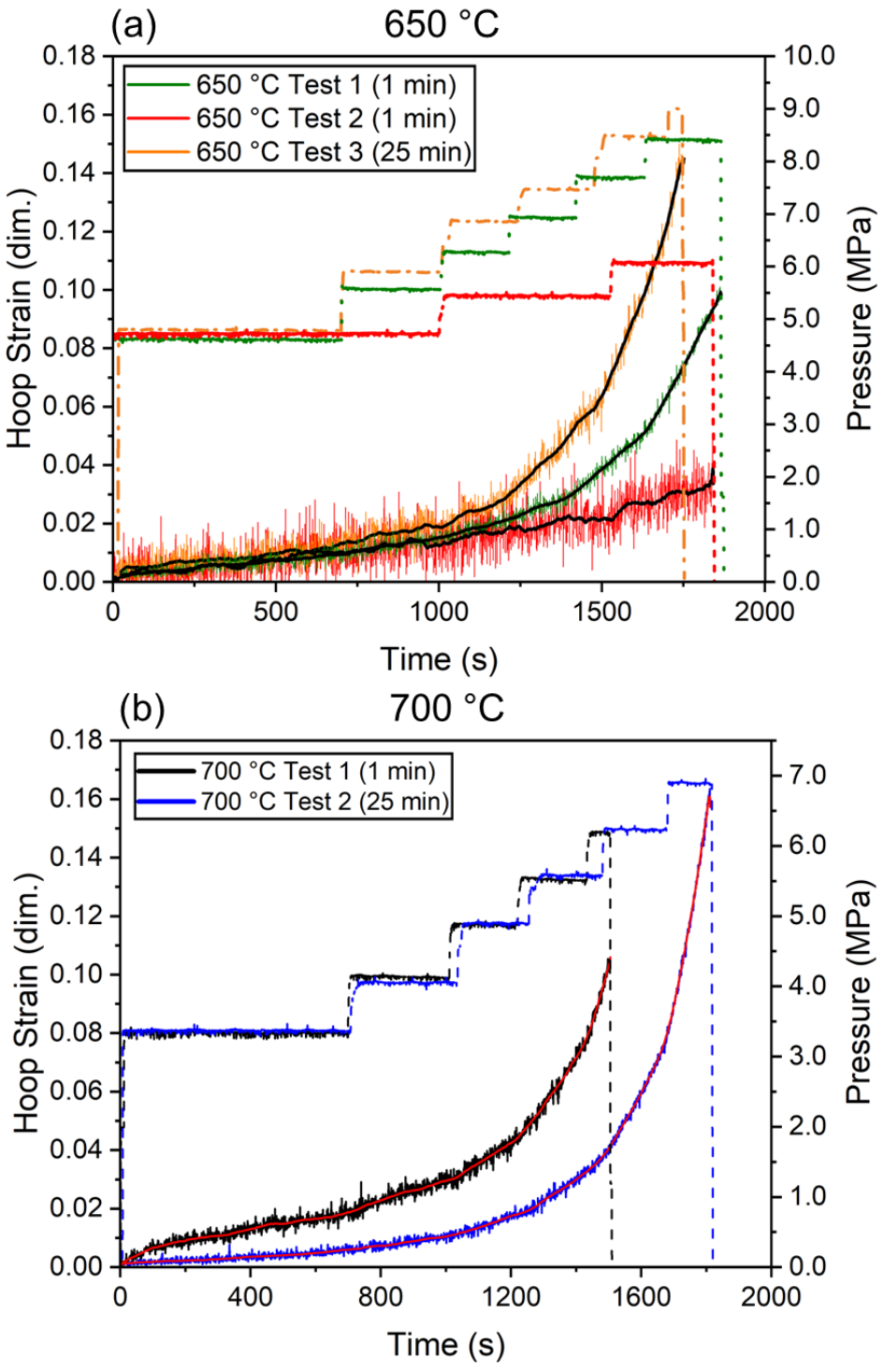

Figure 94. Hoop strain profiles and corresponding pressure steps for (a) 650 °C and (b) 700 °C tests.

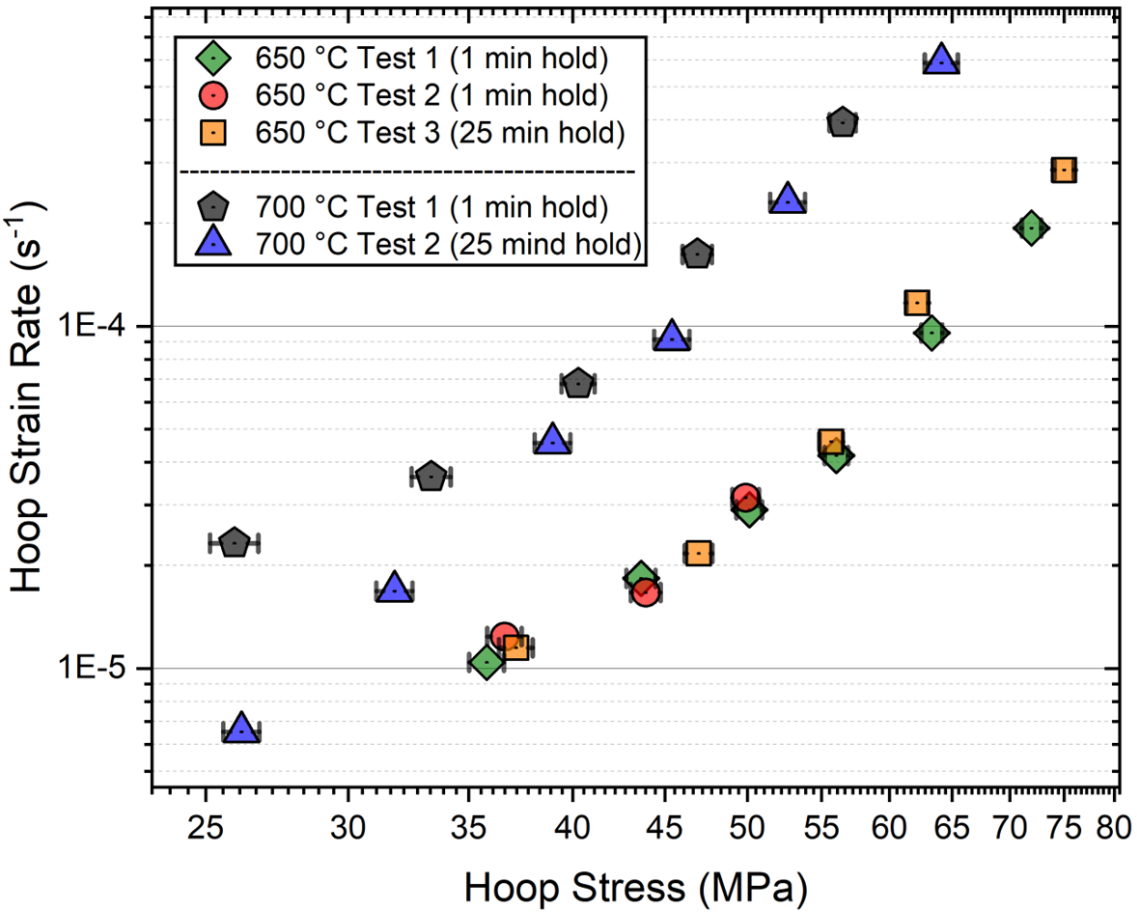

Figure 95. Log-log plot of strain rate and stress for all tests at 650 °C and 700 °C. Error bars in the x-axis result from the 0.103 MPa inherent error associated with the pressure transducer. Error for the strain rate determination (y-axis) is the error associated with the linear fit of each pressure step. The standard error of the linear fit was within the symbols, and at most one order of magnitude lower than the measurement.

with green diamonds, red circles, and orange squares respectively. The 700 °C tests (Tests 1 and 2) are indicated by black hexagons and blue triangles.

A clearly linear strain rate-stress relationship throughout the entire test was only found for the 700 °C Test – 2 sample, which was held for 25 minutes prior to pressurization. Analyzing the slope of this line produced a stress exponent (n) of 5.05 ± 0.10. The error for this stress exponent represents the standard error of the linear fit of log-log strain rate and stress. This finding is broadly in line with existing models, particularly in agreement with the 5.0 used in the Kaddour model. In contrast, the 700 °C Test – 1 sample, which was held for about 2 minutes before pressurization, exhibited higher strain rates for the first two pressure/stress steps. These high values were influenced by the accelerated creep at the beginning of these steps seen in Figure 94. Despite this non-linearity in the first few steps, strain rate was determined using linear fits of the segments for consistency. The strain-rates of the two 700 °C samples started to align after the second step, though the sample preheated for 2 minutes still displayed slightly higher strain rates. This third step corresponded to roughly 20 minutes at 700 °C, suggesting this observation could be associated with the time needed for temperature stabilization.

All data was collected from the region between the thermocouple that controlled furnace output and the cladding centerline. Furnace power output was governed by the control thermocouple reading to ensure it maintained the prescribed heating to temperature. As such, the temperature in the analysis region may not have reached equilibrium until later in the test, causing higher strain rates linked with that temperature. Kaddour et al. [119] found that Zry-4 was not affected by thermal or stress history during creep testing. This indicates that once the analysis region attained the target temperature, the recorded strain rates could be representative. The possible influence of temperature stability is contradicted when considering the 650 °C tests. If temperature in the analysis region was still stabilizing, the expected strain rates should be considerably different. Yet, as shown in Figure 95 for the 650 °C samples, variations in pre-pressurization hold time or load time interval had a negligible impact on the strain rates for a given stress. Similarly, despite 650 °C Test-3 undergoing approximately 1 MPa higher pressure steps, the strain rates still followed the general trend of the 650 °C tests. To fully evaluate this behavior, a more comprehensive understanding of the temperature gradient is necessary.

Baseline temperature experiments were executed to evaluate the temperature stabilization and gradient across the defined analysis region, bounded by the cladding centerline and thermocouples placed 12 mm above. Four temperature profiles were produced in total, with two each for 650 °C and 700 °C. For these experiments, additional thermocouples were affixed at the centerline of the cladding, directly below the thermocouples located 12 mm above, using Pt/Rd wire. Figure 96 presents an image of the thermocouples on the cladding for these profiles. The tests followed the same heating history from 300 °C as the experimental samples, except there was no applied load, after which the samples were then held for 25 min at temperature to evaluate temperature stability. The temperature readings for the tests at 650 °C and 700 °C are shown in Figure 97(a) and Figure *97*(b), respectively. Measurements from the centerline and control thermocouple (12 mm above) are displayed as dashed red and dotted blue lines, respectively. The absolute difference between the two is also presented in green.

During the ramp-up from 300 °C, the difference between the readings from the two thermocouples increased, with the centerline thermocouple indicating a reading around 30 °C higher when the control thermocouple reached the target temperature for all profiles. This variation during the ramp-up can be attributed to the use of IR heating. As power is ramped up, the emission spectrum of the IR lamps changes in intensity and shape, heating the center more directly. This effect is minimized during the hold due to the stable emission profile and the high thermal conductivity of Zr, reflected by the fact that after ~1-2 min the centerline thermocouple stabilized, reaching within 10 °C of the target temperature. After 2 minutes, the difference between the readings from the two thermocouples was within about 5 °C, suggesting that the temperature gradient across the analysis region at pressurization and the initial steps was within 5-10 °C and relatively stable. Hence, the behavior observed for the 700 °C Test 1 sample cannot be attributed to temperature stabilization. Future work is focused on optimizing furnace control to minimize the overshoot at the centerline and speed up stabilization.

The observed discrepancy between the two 700 °C samples may then indicate that the microstructure of the sample achieved a comparable state to the specimen held for 25 min before pressurization. To determine the cause of the observed differences, further analysis of the microstructure post-test is necessary. Examining the microstructure after testing could provide insights into how grain growth and microstructural changes influenced the strain rate-stress relationship. Additionally, a more thorough investigation into temperature stabilization is

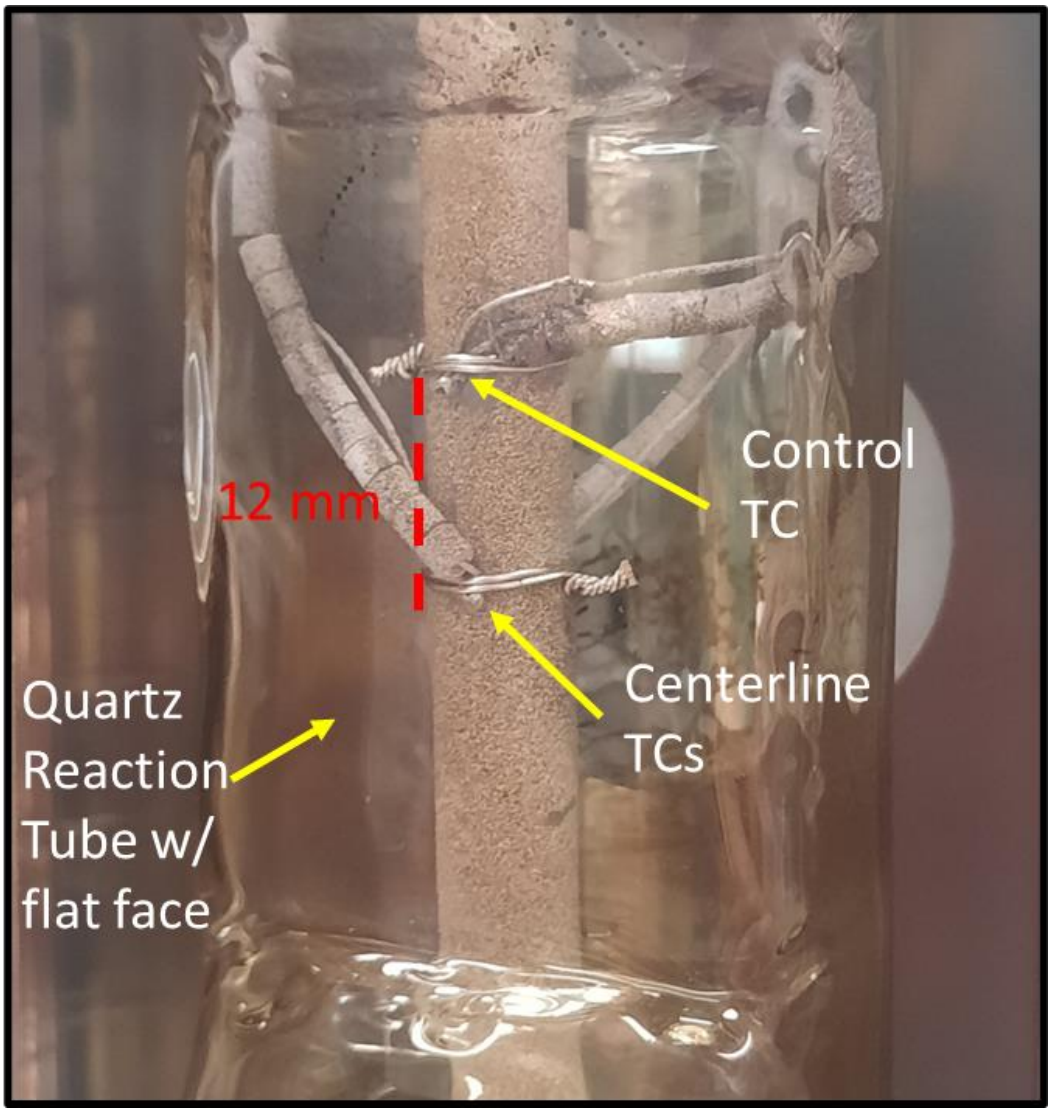

Figure 96. Thermocouple setup for temperature gradient determination.

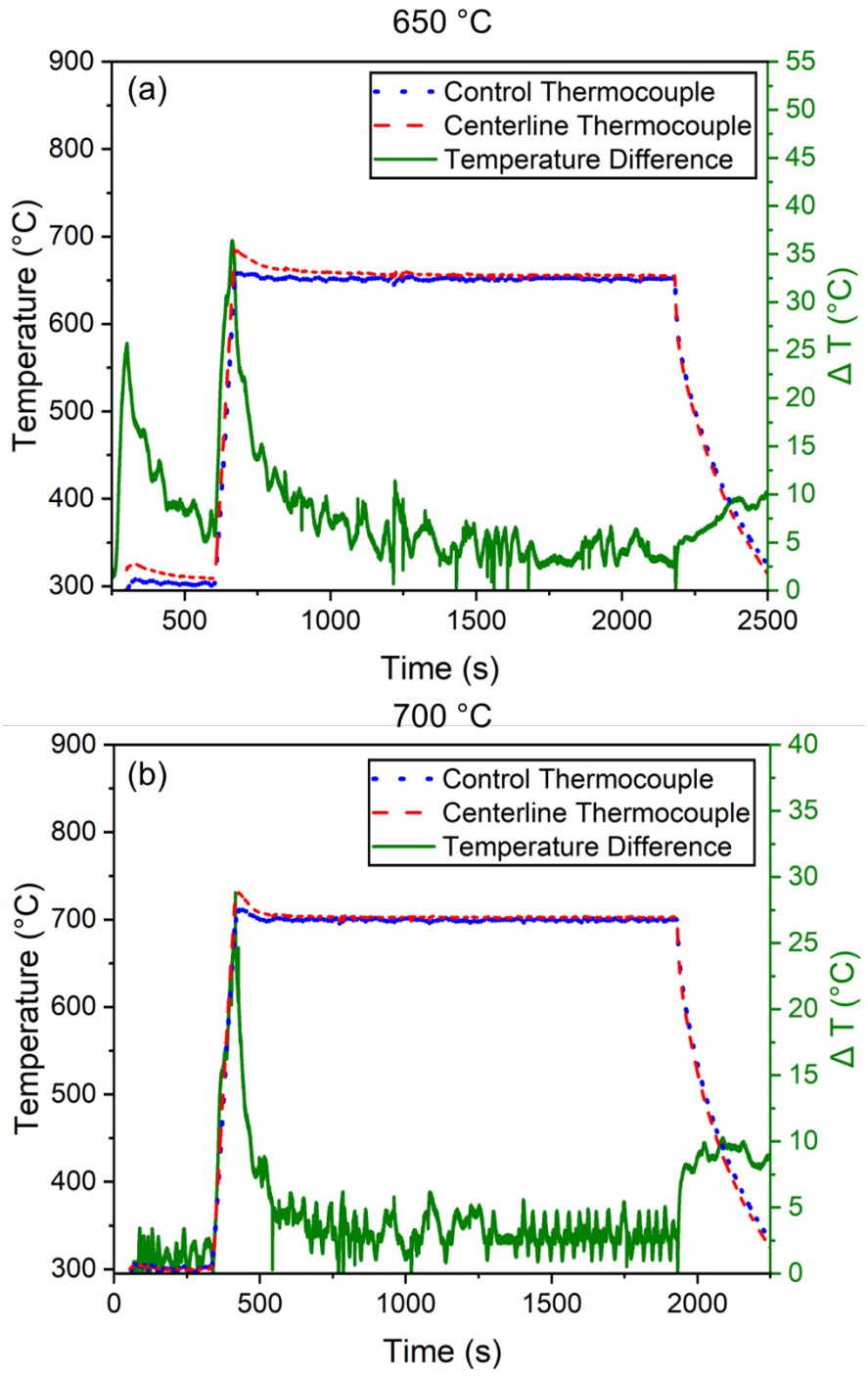

Figure 97. Temperature readings from and absolute difference between the centerline thermocouple and control thermocouple 12 mm above.

needed to better understand its potential impact on the observed strain rates. Through these analyses a comprehensive understanding of the factors affecting the strain rate-stress relationship in Zry-4 cladding samples can be attained, which will assist in refining the experimental process and yielding more precise results for comparison with models.

8.3.6: Preliminary considerations of a shift in creep behavior at low stresses

The strain-rate trends for the tests at 650 °C demonstrated behavior similar to that of the shorter hold time 700 °C Test 1. Two distinct linear regimes appear to be present, with a transition at the fourth step (~57 MPa hoop stress). To explore this behavior, two segmented linear fits were applied to the data, as shown in Figure 98. The segments for the lower stress regime yielded stress exponents of 2.95 ± 0.34 and 1.77 ± 0.36 for the 650 °C and 700 °C data sets, respectively. As for the higher stress portion of the data, a stress exponent of 6.06 ± 0.45 was derived from the 650 °C data, while the 700 °C data provided an exponent of 5.17 ±0.26. These higher stress segments aligned relatively well with model predictions and the mechanisms of dislocation-controlled creep. The disparities in the stress exponents for each segment between the two temperatures could be associated with the scarcity of data near the common point of the linear segments.

The lower creep stress exponents might also be associated with a switch to a different dominant creep mechanism such as grain boundary, sub-grain boundary sliding, or viscous glide (which have stress exponents of 1 to 3). A stress exponent of n=5 is predicted for climb of dislocations (dislocation power law creep).

The lower stress exponent could be associated with microstructural instabilities in the stress relieved alloy. It would be very useful to confirm whether this bilinear behavior also occurs if the sample is initially tested at the highest pressure and pressure is subsequently stepped down (inverse of the sequence used for the data presented). This would confirm whether this behavior is associated with microstructural instabilities causing a change in predominant deformation mode.

This investigation was preliminary and necessitates extensive future testing as well as error mitigation, yet it still provided insights into potential behavior that conventional models may not capture. Testing that covers the potential change in the stress exponent displayed in Figure 98 is required and is more readily achievable with the developed experimental process. However, this

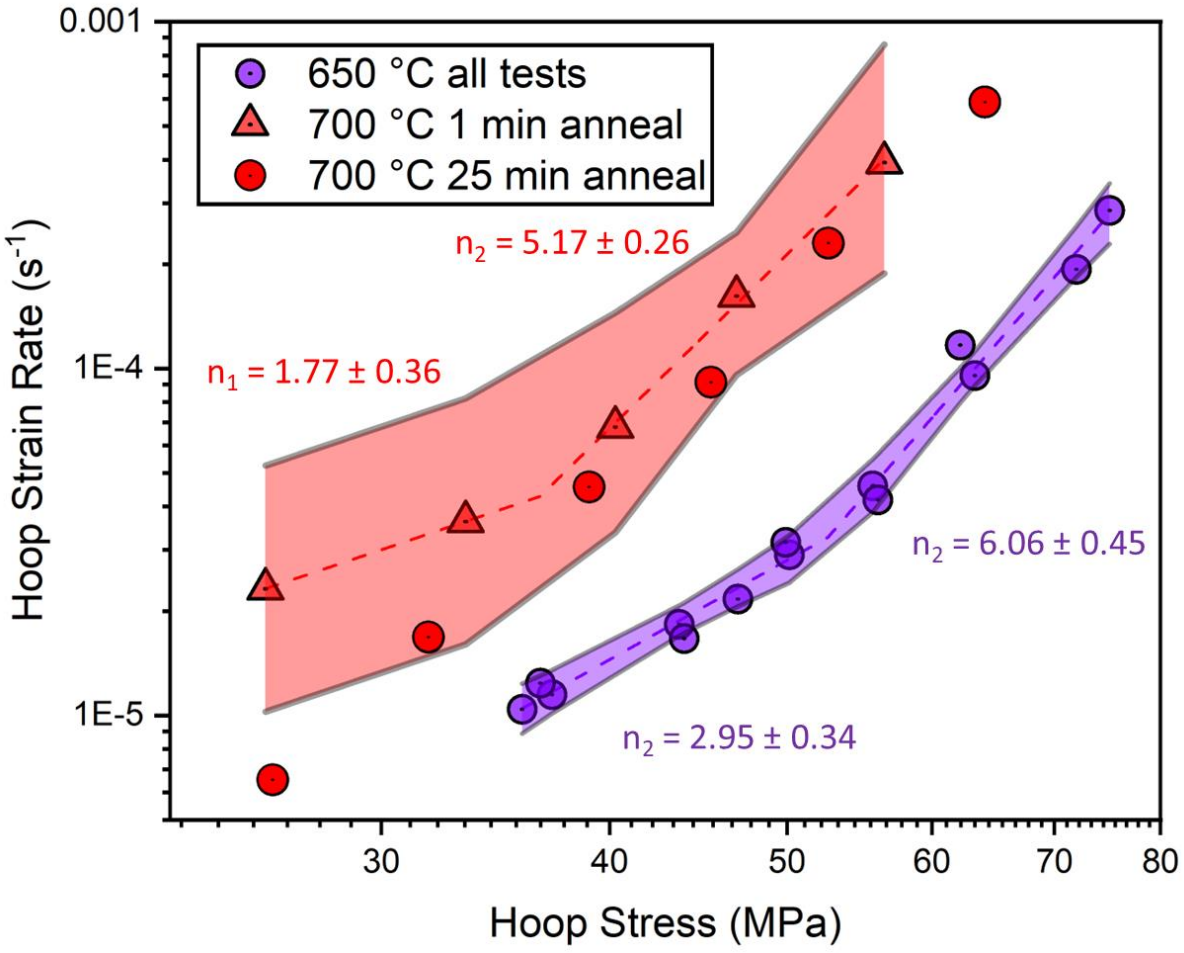

Figure 98. Piece-wise fits of the hoop strain rate and stress data. The error in the stress exponents represents the standard error for each segment of the bilinear fits. The shaded region represents the 95% CI of the fit.

potential change in stress exponent was not near the stress values linked to the shift in temperature dependence found in Chapter 7. Similarly, the stress exponent at higher stresses aligned more closely with those in the existing LOCA models, which is examined in the subsequent section.

8.3.7: Comparison of high temperature testing to literature models

Figure 99 depicts the experimental strain rates from the high temperature testing in comparison with the three models outlined in this work. The 650 °C and 700 °C comparisons are presented in Figure 99(a) and Figure 99(b), respectively. The color schemes for the respective models follow that of the lower temperature analysis. The same set of anisotropic factors were used for this comparison.

Both the 650 °C and 700 °C data showed closer alignment with the isotropic models than the tests at 550 and 600 °C. The first pressure step for all three 650 °C tests and the short hold time 700 °C Test 1 sample are considerably above the Kaddour model. After the first pressure step, the data aligned with the isotropic models, bounded by the Kaddour model on the upper end and the Erbacher model on the lower end. Similar to the lower temperature analysis, the anisotropic models employing Hill parameters from seminal models and Massih [19] were almost an order of magnitude lower than the experimental data.

8.3.8: Model fitting across all tested temperatures

The Kaddour model form of the steady-state creep equation was utilized to fit all the data presented in this chapter, spanning from 550 to 700 °C. Table 18 provides the parameters of these fits, together with their respective standard errors. Figure 100(a) depicts a log-log plot of the compensated strain rate versus hoop stress, representing the entire data set adjusted by the fit parameters. Figure 100(b) presents a comparison of the generated hoop strain model predictions against the data collected in this chapter.

The stress exponent determined from the fit agreed with the general value of ~5 for LOCA models and indicates dislocation glide-controlled deformation. The activation energy of 221 ± 8.5 kJ/mol was lower than the ~300 kJ/mol utilized for LOCA models and the activation energy found for the first segment present in transient testing in Chapter 7. The largest concern arises from the structure constant and the error associated with the fit. With the magnitude of error close to that of

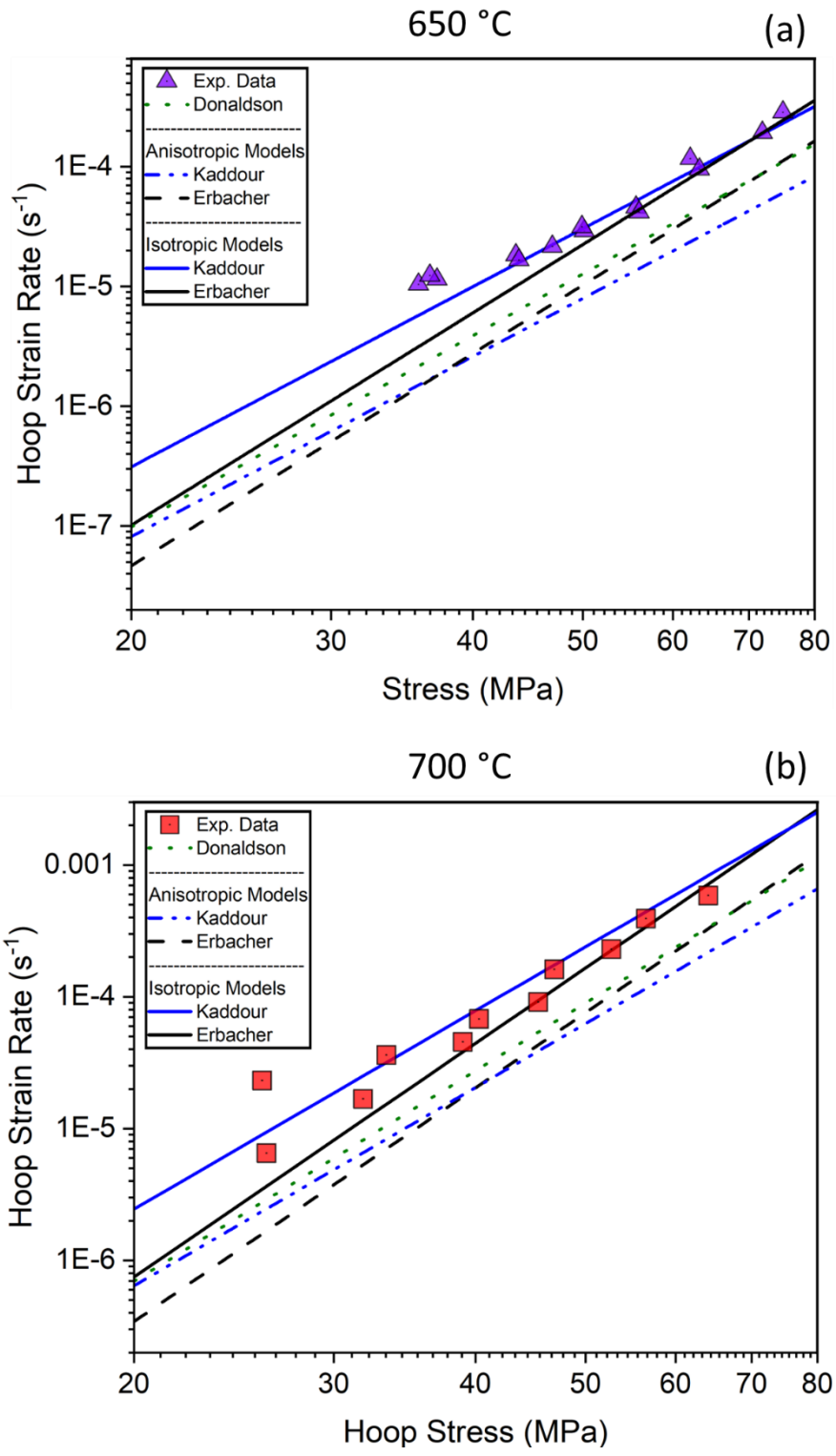

Figure 99. Comparative log-log plot of stress and strain rate between experimental results and Kaddour model. Anisotropic and isotropic cases of the Kaddour model is presented.

Table 18. Parameters of fit from the data in this chapter including all tests at 550, 600, 650, and 700 °C. These parameters are only applicable to the hoop direction for this specific Zry-4 material.

Parameter	Fit Value	Standard Error of the Fit
A (K-MPa^{-n}-s^{-1})	783	607
n	4.82	0.25
Q (kJ/mol)	221	8.5

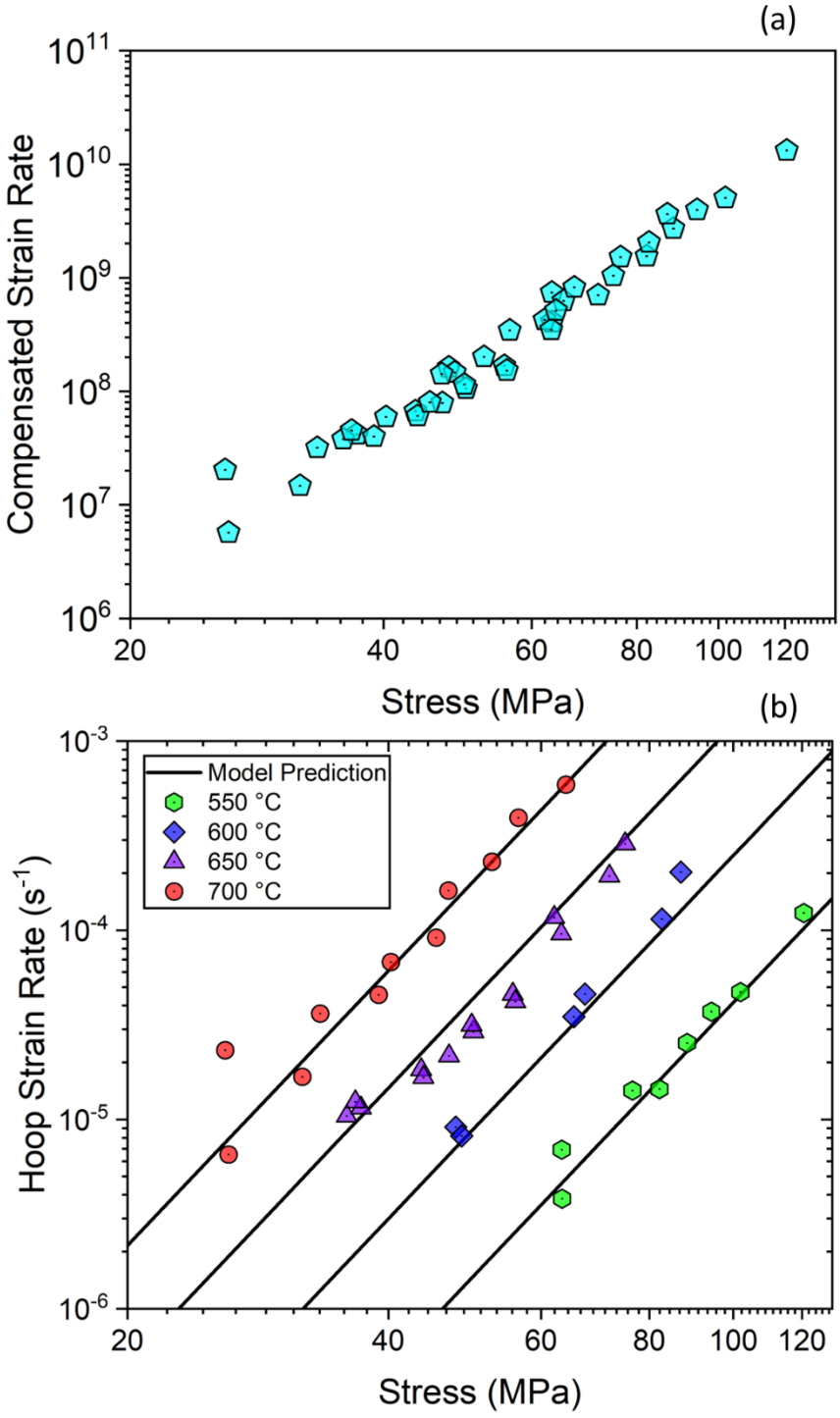

Figure 100. (a) Compensated hoop strain rate versus hoop stress and (b) predictions using model parameters against experimental data.

the fitted value, this may be non-physical and an indication that the fit is not well suited.

This decreased activation energy might be an indication of primary creep influences. If a genuine steady-state is not achieved— a distinct possibility especially for the lower temperature tests— these values could be skewed. To address this, future tests might consider implementing longer pressure steps or monitoring the strain rate in-situ. Nevertheless, current LOCA models based on creep do not consider primary creep. If the impact of primary creep is evident on the scale of the pressure steps used in these tests, it is likely also significant under LOCA conditions. Additionally, a potential significant contributor to the discrepancy between model values and the experimental values from the current study is the parameter range over which the data was collected. Models such as the Donaldson, Erbacher, or Kaddour model were developed for higher temperatures of the α-phase.

8.3.9: Axial Strain Measurements, and future testing

Axial strain has been neglected thus far in this chapter for a few reasons: (1) relevance and magnitude of hoop strain in comparison, (2) noise considerations for small deformation, and (3) an observed change from negative to positive strain rates. In most tests, noise in the axial strain measurements were significantly lower compared to the hoop direction. However, the discernible strain signal in the axial direction was not enough to gather reliable strain rates at lower temperatures or stresses.

The axial strain demonstrated negative strain rates early in the test profile where the signal was robust and the noise relatively low. However, positive non-linear strain rates were found later in the tests for some of the samples. The transition from negative to positive strain was not always near failure, with some tests showing more distinct changes. An example of this behavior is shown in Figure 101, with the 550 °C Test 2 and 700 °C Test 2 in Figure *101*(a) and Figure *101*(b), respectively. Although an internal loading applies a tensile stress in both directions, the axial strain rates were negative. This implies that while a tensile load was applied, the hoop strain dominated the axial strain via conservation of volume until the change in direction, similar to the observations during transient testing in Chapter 7. Despite the change in axial behavior, the hoop strain retained linear form throughout the steps.

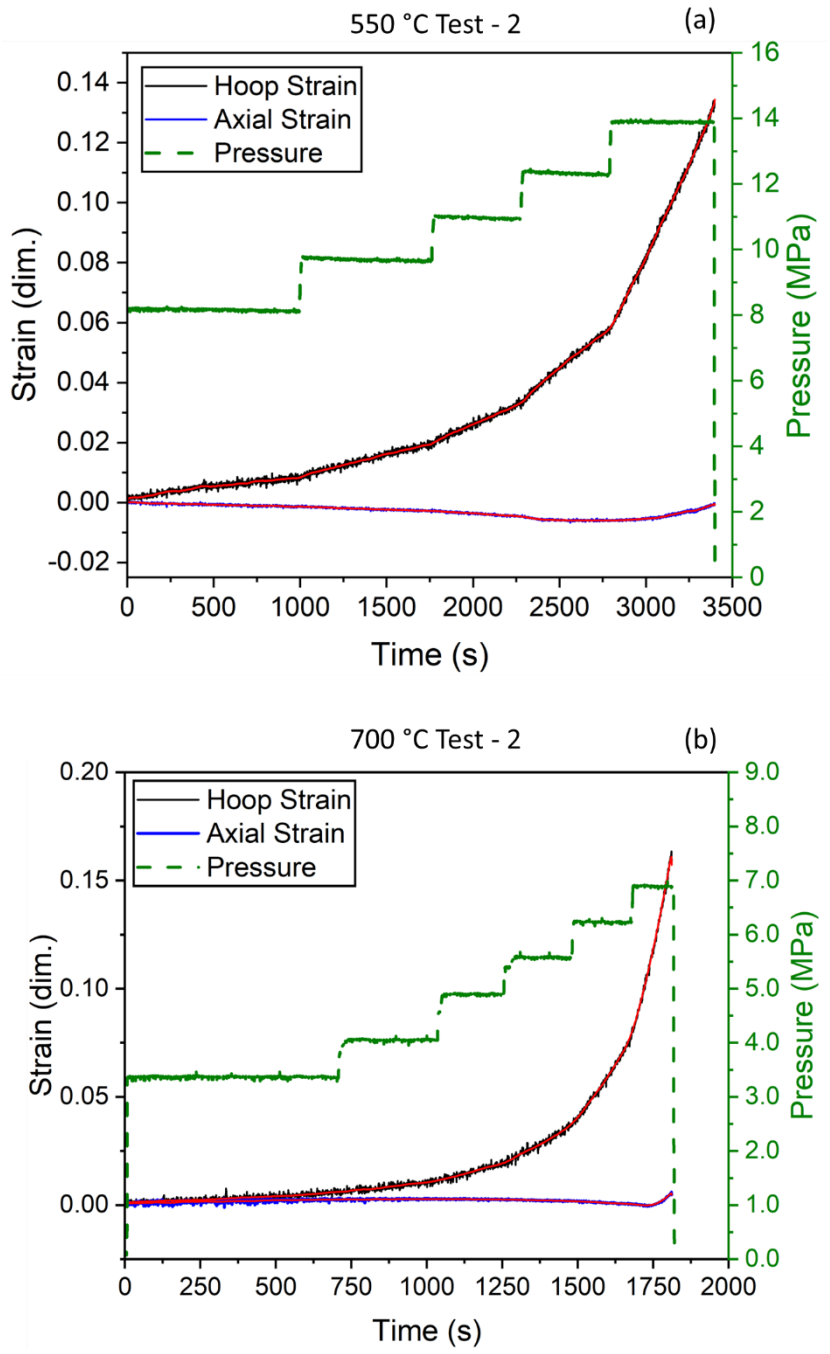

Figure 101. Hoop and axial strain profiles for two of the tests that show a transition from negative axial strain rates to positive values.

Section 8.4: DISCUSSION

8.4.1: Recovered creep parameters and comparisons to literature models

The high-temperature creep testing results showed stress-strain rate relations that largely align with existing literature models employing isotropic coefficients. For the 650 °C and 700 °C tests, the results fell within bounds set by the isotropic versions of the Erbacher and Kaddourmodels. However, the data obtained from the 550 °C and 600 °C tests exceeded all anisotropic and isotropic models. This may be evidence that the test conditions were still in the primary creep regime rather than in the steady state creep regime for the low temperatures. Longer pressure steps and *in-situ* strain rate monitoring could set the bounds for determining the onset of steady state regime.

The strain rate data from 650 °C tests and the shorter hold time 700 °C Test-1 indicate a possible trend shift from a stress exponent of around 2-3 to 5-6. This shift, however, was not observed in the 25-min hold 700 °C Test-2, which maintained strain rate predictions consistent with the isotropic models and a stress exponent of roughly 5. A 25 min hold at 650 °C did not exhibit the same inconsistency. Considering that the baseline temperature profiles indicated relatively stable temperatures were achieved in the analysis region before pressurization, it is likely that these observations are not the result of experimental factors.

There may exist a time and temperature dependent microstructural process such as additional stress relief, recrystallization, and grain growth that could explain the discrepancy at 700 °C. Given that these temperatures are within the range for RXA processes, it is possible that microstructural changes could occur during these extended hold times and test durations, despite the fact that these conventional anneals generally take place over longer time scales.

Based on the recrystallization rates reported by Hunt et al. [202], the sample is fully recrystallized after reaching 700 °C. However, recrystallization temperature depends on the amount of cold work (stored energy) present in the sample. It may be difficult to recrystallize SRA Zry-4 without introducing additional cold work depending on the SRA conditions. The observed discrepancy may be tied to grain growth, the impact of introducing a load, or other evolutions in the microstructure. The kinetics of this microstructure change could be significantly slower at 650 °C compared to 700 °C, leading to negligible effect on the former on the time scale of this testing or introduction of the same hold time. These observations are

preliminary, requiring extensive testing to correlate the effects of time, stress, and temperature with the microstructure and resulting material behavior.

This work was carried out in a steam environment, whereas the models referenced were conducted under vacuum or inert environments. Previous research by Rosinger et al [33] and Chow et al. [85] showed that increased oxygen concentration enhances creep strength, meaning lower strain rates for Zr alloys. However, the results in this work indicate reduced creep resistance, suggesting that the effects of the steam environment on these temperatures were minimal.

8.4.2: Validation of methods and uncertainties in drawing effective comparisons

The stress exponents recovered across all temperatures agreed with that of steady-state creep models, ~5-6, particularly at higher stresses. These results validate, to a degree, the accelerated methodologies employed in this work to determine creep behavior. However, this was the first iteration of the accelerated qualification testing. Enhancements are planned for this methodology, including improved temperature and pressure control, upgrades to optical systems, and augmentations to the furnace. These enhancements will reduce experimental uncertainties and yield higher fidelity material parameters. With reduced noise levels, real-time processing of strain data could be used to identify when a minimum creep rate is reached, as done by Zhou et al. [203] for dry storage conditions. It will ultimately be important to experimentally demonstrate that steady state creep conditions have been achieved as opposed to. primary creep. This could not only further the amount of data gather from one sample, but also ensure that steps occur after a minimum strain rate is achieved. It would also be useful to perform some confirmatory studies where the highest pressure was applied first, followed by step downs in applied pressure, to confirm whether quantitatively similar creep results are obtained with the “step-up” sequential test method.

Uncertainties beyond experimental error could explain the discrepancies between the experimental data and nominal model predictions. Specifically, this stems from (1) the lack of knowledge of Hill parameters and (2) lack of details on material condition of the tested material and that used to develop reference models. The conventional use of any model developed from axial tensile testing must select appropriate anisotropic Hill coefficients to create effective parameters or for use in other directions. An all-encompassing set of coefficients for all

"Zircaloy-4" is unlikely given the variation in heat treatment, chemistry, and proprietary processing routes associated with industrial Zr alloys. Hayes and Kassner [121] compiled multiple datasets from a range of creep testing, with a distinct difference between material conditions. CWSR/SRA Zry-4 demonstrated greater strain rates than RXA counterparts across multiple experimental setups. Thus, the relatively high experimental values might reflect comparing this SRA material to a completely different initial microstructure. This hypothesis is further obscured by the lack of detailed material conditions in previous testing that generated these models. This testing partly served as an initial capability demonstration. Future work aims to investigate the uncertainties related to anisotropy and material conditions, which should lead to a better understanding of structure-property-process relationships.

8.4.3: Effective isotropy due to activation of deformation mechanisms

The observed agreement with isotropic models, even with the aforementioned uncertainties, could indicate more fundamental mechanisms at play. The claddings behaving in an isotropic manner at higher temperatures could be reasonable due to two main factors: (1) the effects of recrystallization/grain growth on texture and (2) the activation of new slip systems.

As discussed in Chapter 1, the slip and deformation mechanisms of Zr alloys are intricate, with dependencies on temperature, strain rate, and stress. It is plausible that at temperatures of 650 and 700 °C, additional slip planes get activated, resulting in a more isotropic behavior. This notion is supported by Rosinger et al. [127] who showed Hill parameters tending towards isotropy during 800 °C creep testing. If the steady-state assumption for Zr LOCA behavior is correct, attempts to utilize anisotropic models for transient phenomenon may misrepresent strain at these LOCA relevant temperatures (> 600 °C).

8.4.4: Implications for LOCA models and future work

The testing carried out in this work aimed, in part, to assess potential changes in the stress exponent that might explain the shift in activation energy discovered in Chapter 7. The fitting of the data set presented in this chapter resulted in a stress exponent of ~5, similar to LOCA models, and an activation energy of ~220 kJ/mol, below those utilized by LOCA models. Additionally, the activation energy derived from this testing was below those observed from both segments during transient testing in the previous chapter. This implies the transition in deformation behavior from a low to high "activation energy" observed in transient testing is not

a result in creep activation energy change. However, primary creep could have resulted in a lower activation energy, particularly at lower temperatures, due to possibly insufficient time to reach a steady-state. In a broader sense, if primary creep is present on the scale of these pressure steps (~200-1000s), then the notion of secondary creep being dominant during a LOCA is not realistic.

A lot of the testing did not extend precisely to the conditions at the transition points observed in the transient testing, as efforts were made to prevent premature failure, thereby optimizing the volume of data gleaned from each sample. Still, the stress exponent was in the range of steady state models. Future work with this refined process could be employed to perform testing near or beyond the transition points. However, further work is also needed for transient testing to generate statistics on the transition points.

Isotropic variants of the Kaddour and Erbacher models were found to better predict high temperature creep in the α phase. These isotropic versions as well as the experimental strain rate data were considerably greater than the variants implemented in BISON. Yet, the BISON results using the Erbacher model overpredicted the creep rate compared against strain data from transient testing in Chapter 7. This conflicting behavior could indicate two possibilities: (1) the anisotropic consideration when developing effective model parameters and subsequent isotropic calculations in BISON greatly affect the predictions and/or (2) mechanisms other than steady-state creep dominate balloon deformation, as suggested in the previous chapter. For (1), this potential issue could be mitigated when anisotropic environments, such as in the work by Recuero et al. [134], is implemented in BISON.

Section 8.5: CONCLUSIONS

The high-temperature creep testing performed in this chapter has provided insights into the stress-strain rate relationships of Zr alloys. The data collected at 650 °C and 700 °C fall within the boundaries of the isotropic versions of the Erbacher and Kaddour models, validating to some extent the methodologies used in this work. The findings of this research suggest that claddings might behave in an isotropic manner at higher temperatures, possibly due to activation of additional slip planes or a dynamic microstructure. This is a preliminary conclusion, and more testing is necessary to definitively validate this hypothesis. However, the data for 550 °C and 600 °C exceeded all anisotropic and isotropic models, which is possibly due to the models being developed based on

higher temperature testing. Alternatively, the test duration may have been insufficient to achieve steady state creep conditions as opposed to primary creep with higher strain rates.

The possible effects of microstructural instabilities on the 700 °C testing with varying hold times before pressurization warrants further investigation. The discrepancy observed might be attributed to grain growth or other microstructural evolutions, which may not be adequately captured in the current LOCA models. As such, future efforts will seek to combine the *in-situ* transient and creep burst testing methodologies with microstructural investigations.

Most notably, the stress exponent observed in this testing was consistent with literature models of ~5. While a possible change from ~2-3 to 5-6 was present for the 650 °C and the shorter hold time 700 °C test, the general trend of the curves was well described by a stress exponent of 5, which is consistent with power law (dislocation glide) creep. This possible change in stress exponent requires further testing, but more importantly the higher stress segments were on the order of ~5-6. No deviation from this trend at higher stresses was found, implying a change in the stress exponent may not be responsible for the transition in deformation behavior observed in the previous chapter on transient testing. Yet, further investigation into the transition from testing also requires significantly more exploration to statistically characterize.

In summary, this initial testing has served as a valuable capability demonstration and a foundation for further work. It has highlighted the need for continued research, especially to reduce the uncertainties related to anisotropy and material conditions, for a better understanding of structure-property-process relationships in Zr alloys. Future work should focus on refining testing methodologies, minimizing possible impacts of primary creep, expanding the range of tested conditions, and improving models to account for observed behaviors.

Chapter 9: Preliminary Application of Framework to ATF claddings

Chapter Foreword

The overarching goal of this dissertation was to develop, validate, and demonstrate a LOCA burst testing framework for accelerated qualification of ATF claddings. This chapter presents the initial testing of Cr-coated Zr and FeCrAl claddings, providing initial insights into the potential applicability of this framework for ATF claddings. A comprehensive matrix for all ATF materials remains incomplete, but these early investigations provide valuable insights for future efforts.

The use of 3D DIC in this research illustrates the continuous enhancement and expanding possibilities for analysis within this testing framework. This framework, it should be noted, is not static but constantly evolving with the goal of increasing the capabilities, precision, and reliability of the data generated. Future work is planned to involve extensive creep and transient burst testing, and this discussion serves as an introductory exploration of the developed framework on ATF claddings.

Section 9.1: INTRODUCTION

Previous chapters of this dissertation have concentrated on examining established Zr cladding systems and authenticating the methodologies used. The major goal of this work was to develop a framework specifically for application to ATF systems. Rapid qualification methodologies have explicit value for ATF efforts.

Traditional burst testing efforts, including transient and creep tests, can prove costly due to the substantial quantity and size of samples required. This issue is particularly challenging given the limited sample availability associated with developing cladding systems. The methodologies developed within this framework aim to accelerate data collection and reduce the quantity of material required for studying burst-related phenomena. As a result, a larger quantity of material is available for investigations into other areas of interest. Therefore, this chapter introduces preliminary work conducted on ATF cladding systems, demonstrating the successful utilization of the framework and revealing early insights into their behavior. It is crucial, however, to note that this work is limited in scope and seeks to elucidate further understanding that could be attained.

The *in-situ* framework continues to evolve, with each iteration revealing additional use cases. Initially, the goal was to synchronize strain, temperature, and load in an attempt to produce a more comprehensive description of the ballooning process, particularly in the reference frames of existing models. The process of implementing these techniques revealed that conventional creep descriptions of Zr might be inadequate and set the foundation for future model development. Traditionally, deformation considerations have primarily focused on characterizing and predicting the maximum balloon diameter, often involving ex-situ or point measurements at the ballooning center. Even the 2D DIC testing in this dissertation focused on strain measurements in the ballooning center due to constraints to a single image plane and suboptimal patterning.

Nonetheless, with the advent of 3D strain surfaces generated from stereo/3D DIC, it is conceivable that analysis could provide more holistic descriptions of the balloon region. Consequently, this section emphasizes how the implementation of stereo DIC expands the scope of analysis and paves the way for further exploration in this area.

Section 9.2: EXPERIMENTAL METHODS

Both transient and isothermal creep testing was performed using the newly developed SATS *in-situ* framework, using the 3D DIC techniques outlined in Chapter 5. Compared to Chapter 7, significant changes were made the experimental setup, including the employment of a conventional paint pattern and a higher heating rate of 5 °C/s for transient testing. Transient testing was performed on C26M2 FeCrAl, as well as Cr coated and bare Zry-4, while isothermal testing was conducted on a single Cr coated specimen at 600 °C for comparison to data from the previous chapter. The Cr coating tested was from the same batch of samples denoted Cr#2 in Chapter 3. Details on material condition is described in Chapter 7 and cladding geometry is reported in Table 19.

The stereo DIC cladding train setup was refined for transient testing by the inclusion of an additional thermocouple to further synchronize temperature measurements in the analysis region with strain data. This thermocouple was strategically placed at the cladding centerline, where burst is most likely to occur, offset from the center to avoid obstructing the pattern. Figure 102. presents an image from one of the preliminary tests, which enabled temperature tracking in the burst/balloon region while continuing to generate reliable strain data.

Table 19. Material condition and geometry of the ATF and reference claddings.

Material Parameter	Zry-4	Cr#2/Zry-4	C26M2 FeCrAl
Length (mm)	114.3	114.3	114.3
Outer Diameter (mm)	9.5	9.5	9.52
Wall Thickness (mm)	0.575	0.575	0.375
Coating Thickness (µm)	N/A	6-7	N/A

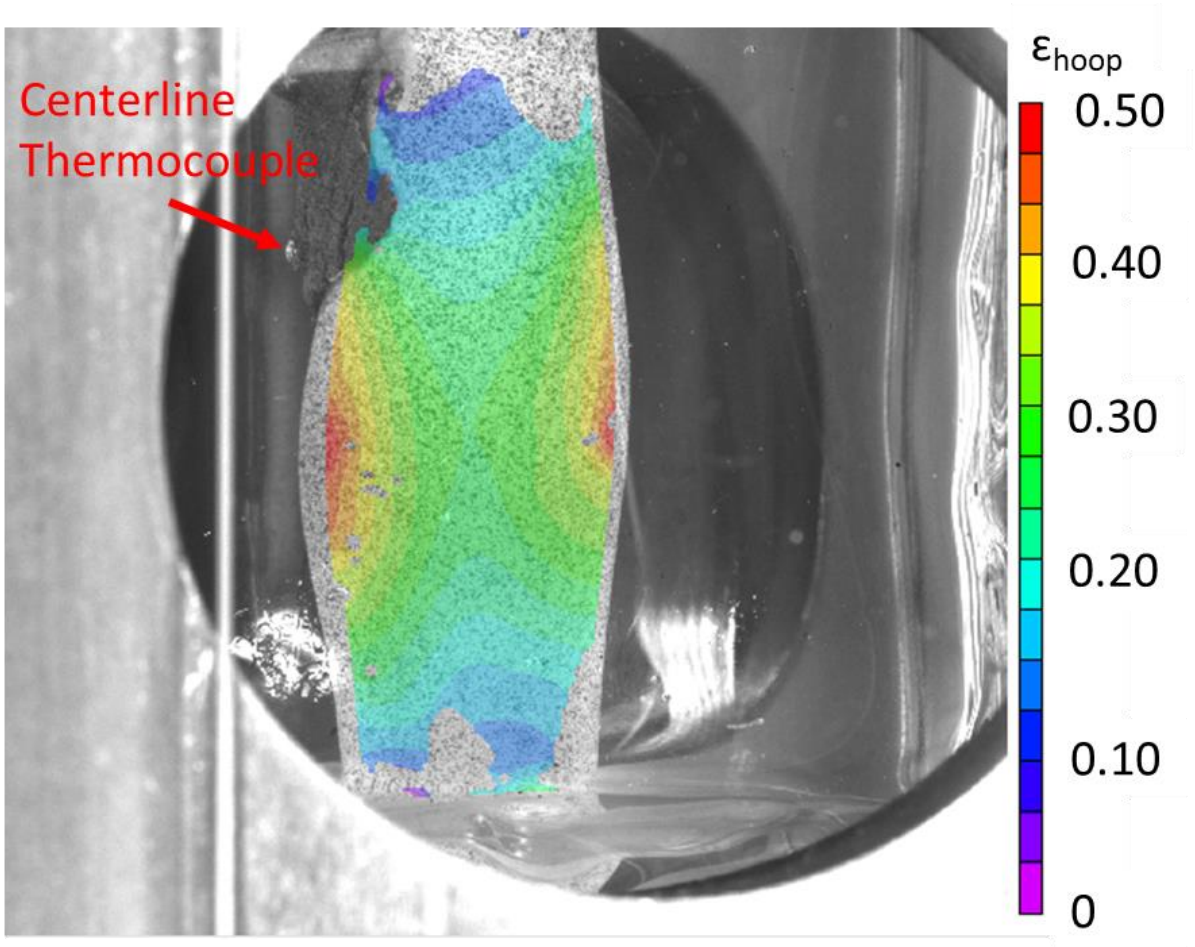

Figure 102. Hoop strain map of a preliminary sample showing the centerline thermocouple placement.

The center thermocouple could not be wrapped to ensure contact during transient testing, as a Pt/Rd wire would constrict ballooning, thereby negating any insights obtained from DIC. Multiple attempts were made to secure the thermocouple at the designated location. Initially, one of the two thermocouple wires was secured with the top thermocouples, allowing for the bead to be bent into position. This technique was successfully utilized for the bare Zry-4 sample subjected to a transient test, where contact was maintained. Ensuring consistent contact throughout proved challenging with this technique, and further options were explored. Subsequent testing utilized a metal-based adhesive commercially available as Quicksteel. This adhesive ensured sufficient adhesion throughout the transient, although investigations into its impact on cladding performance are ongoing.

Section 9.3: RESULTS

9.3.1: Transient testing of bare and Cr coated Zry-4 using 3D DIC

Transient burst testing of both bare and Cr-coated Zry-4 samples was conducted with a heating rate of 5 °C/s. Both samples were subjected to an isobaric loading condition, maintaining an internal pressure of 9.66 MPa. The bare and Cr-coated Zry-4 samples failed at respective temperatures of 739 °C and 828 °C. As it was closer to rupture, burst temperature for this testing utilized the thermocouple reading from the centerline. A temperature gradient was observed between the centerline thermocouple and the two positioned 12 mm above. At the moment of burst, the control thermocouple read 709 °C for the bare sample and 741 °C for the Cr-coated sample.

Nevertheless, the burst temperature and pressure measurements corresponded with previous testing of both bare and Cr-coated Zry-4, as depicted in Figure 103. Data for the bare sample is represented in black, and the Cr-coated data is depicted in blue. This consistency preliminarily indicates that the modifications made, such as the shortened cladding length, thermocouple weld paste (used for the Cr#2 sample), and the paint pattern, did not impact the burst criteria.

Figure 104(a) displays the hoop strain map of the bare Zry-4 cladding taken from the frame after burst, demonstrating the deformation gradient present. To investigate strain variations across the balloon region, a line profile was extracted along the axial direction near the rupture site for both the bare and Cr-coated tests, as depicted in Figure 104(a). Figure 104(b) and Figure *104*(c) presents the hoop strain from these line profiles plotted against the axial position at four different

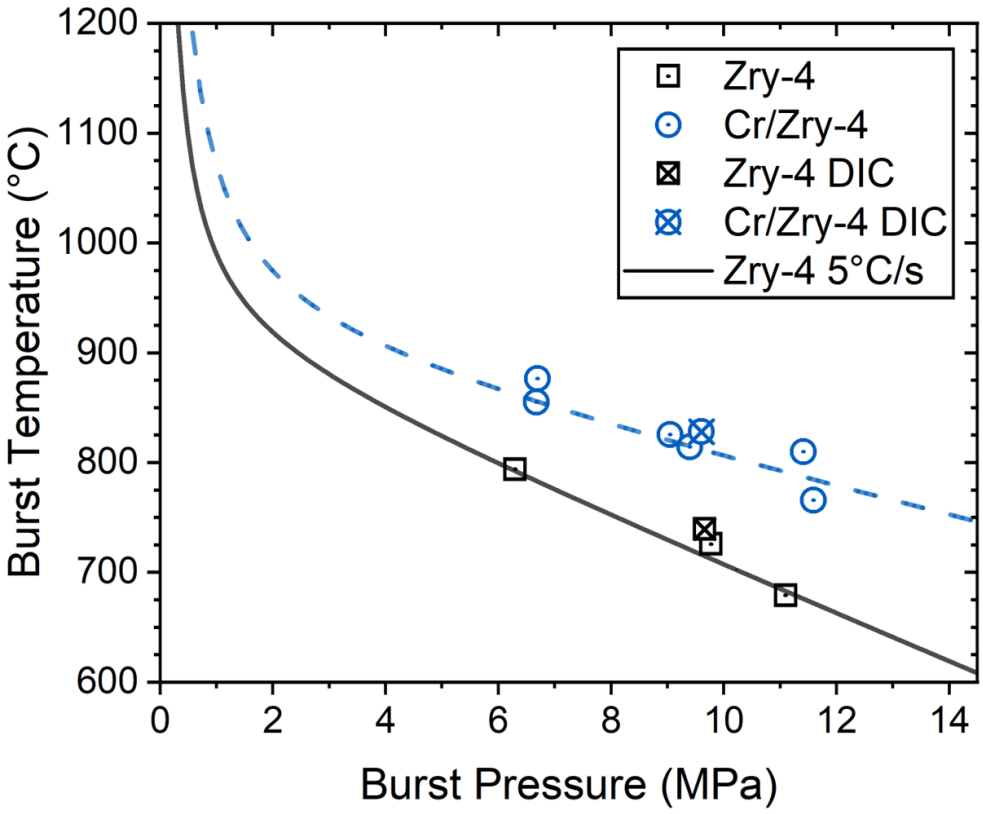

Figure 103. Burst temperature and pressure for the bare and Cr#2 coated DIC tests.

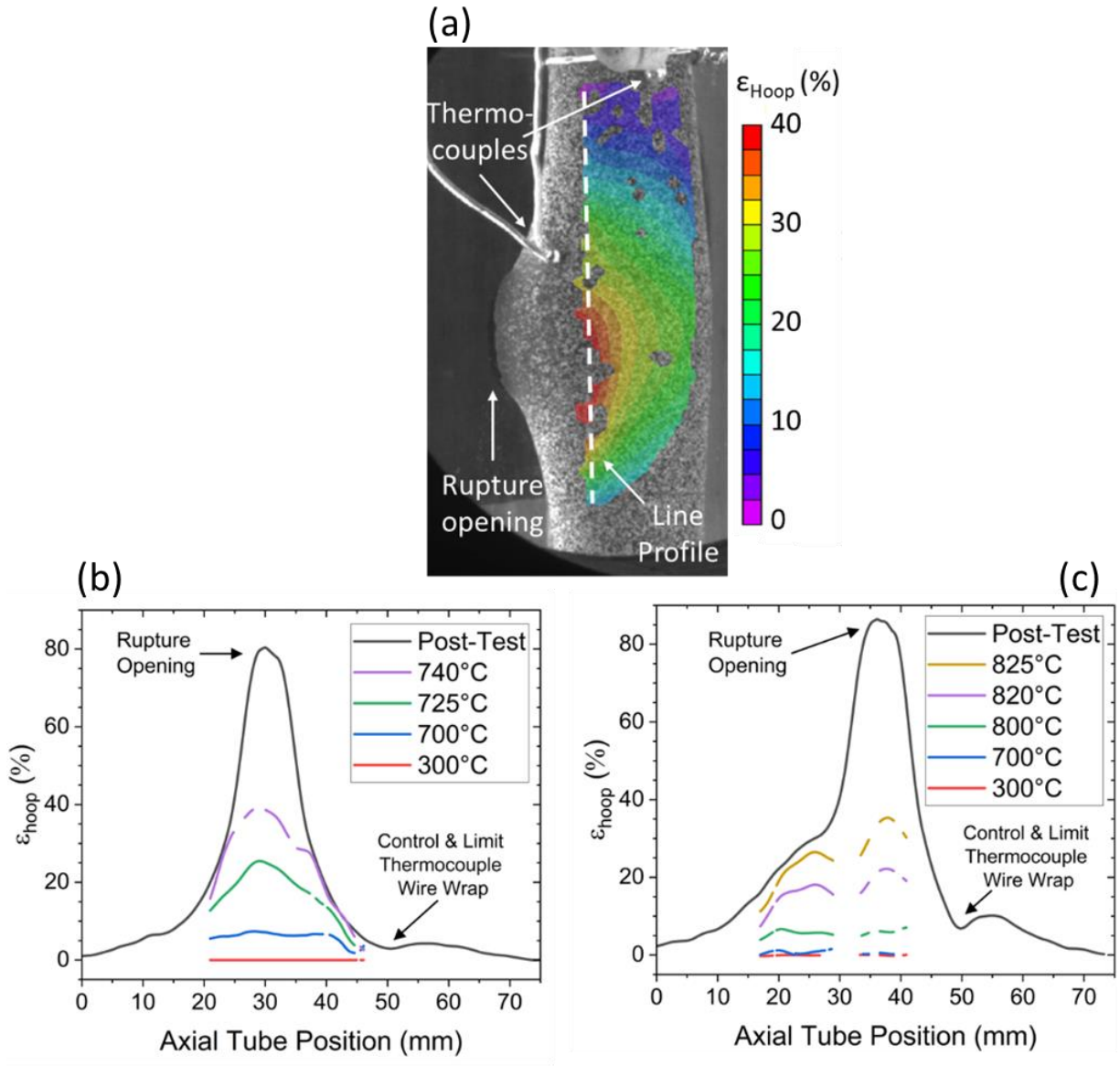

Figure 104. Line profiles of hoop strain collected along the axial direction using the strain map. The strain map (a) illustrates the position of the line profile. The bare Zry-4 and Cr coated strain profiles are presented in (b) and (c), respectively.

temperatures preceding burst. The black curve represents the post-test diametric strain profiles measured using a structured light microscope, as carried out in earlier chapters, for comparison. The post-test profile was collected with the rupture opening oriented 90 °C to microscope.

Relatively uniform hoop strain can be seen across the balloon region until closer to failure for both tests in Figure 104. This uniformity is apparent when comparing the curves at 300 °C with those at 700 °C and 800 °C for the bare and Cr coated samples, respectively. Beyond these temperatures, the anticipated nodal shape begins to form, with the balloon bounded by the post-test curve. The post-test final strain peak is significantly larger than the latter curves for both tests. However, this discrepancy results from the post-test curve incorporating the rupture edges.

These line profiles, and the accompanying analytical tools, represent significant enhancements to the data collected from burst testing. Firstly, these line profiles directly show the inherently local evolution of ballooning, as well as when this process starts. Uniform deformation is present in the analysis region until there is a switch to non-uniform mechanisms. Although preliminary, this data underscores how 3D DIC can enhance our ability to investigate previous observations from in-situ data.

Figure 105(a) and Figure 105(b) present the average strain values and the resulting strain rate of the entire strain map for the Cr coated and bare Zry-4 samples against temperature. From Figure 105, it is evident that the strain curves resemble each other in shape, with the Cr coated sample offset by approximately 80 °C.

Figure 106 presents a log-log plot of strain rate and temperature for the two samples. A 2% strain threshold was again applied to these curves, where measurable deformation began, for consistency with 2D DIC testing. Both the Cr#2 and bare sample demonstrated the transition in temperature dependence observed in Chapter 7 with 2D DIC. Therefore, the transition has been validated across multiple measurement systems, patterning techniques, and cladding train configurations. Hence, we can conclude that the balloon development near compression fittings, as discovered for the laser-engraved samples in Chapter 7, was not responsible for the transition.

These transitions also occurred at temperatures close to when the nodal balloon shape began forming in the line profiles, indicating the transition in temperature dependence is associated with the shift from uniform expansion to nodal ballooning. In mechanical tests like tensile tests,

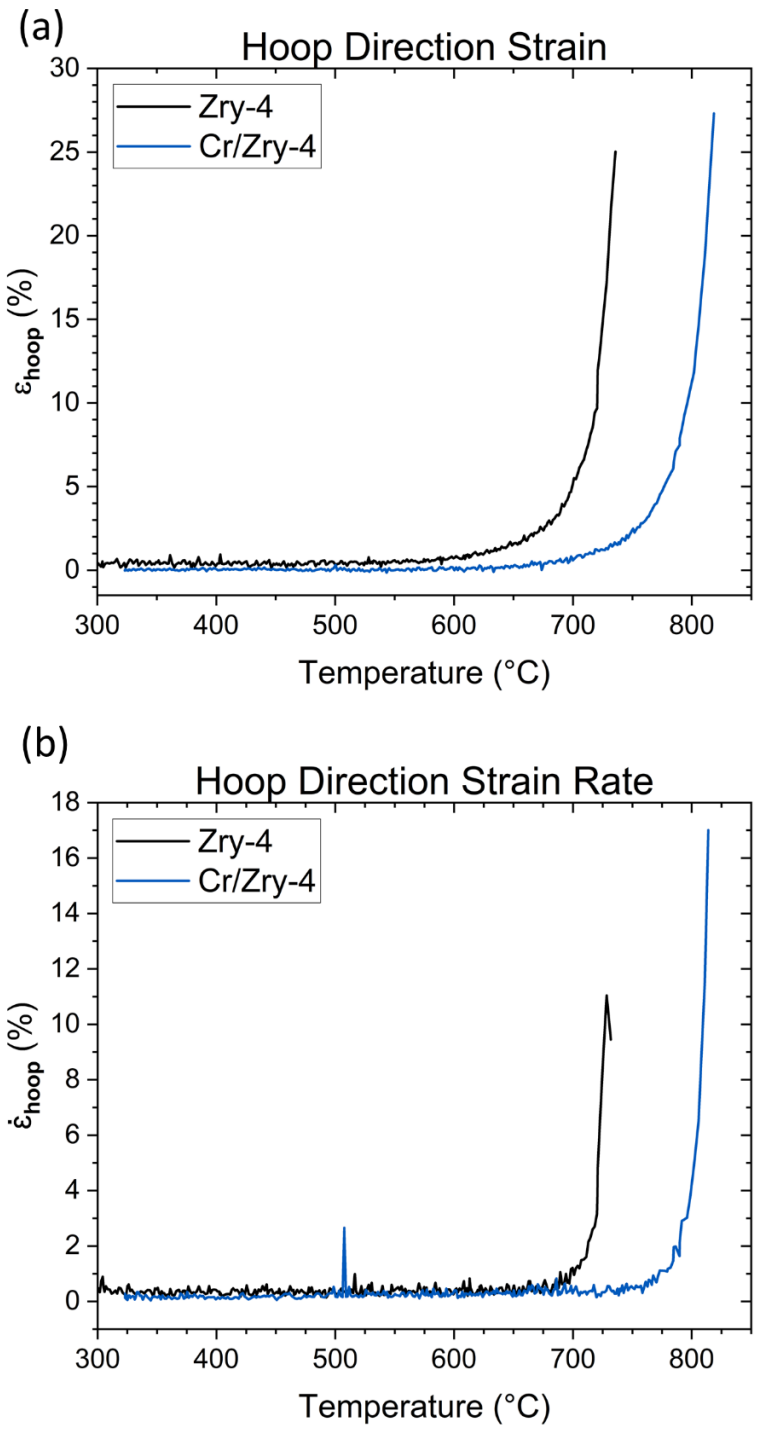

Figure 105. Hoop strain (a) and hoop strain rate (b) data in respect to temperature.

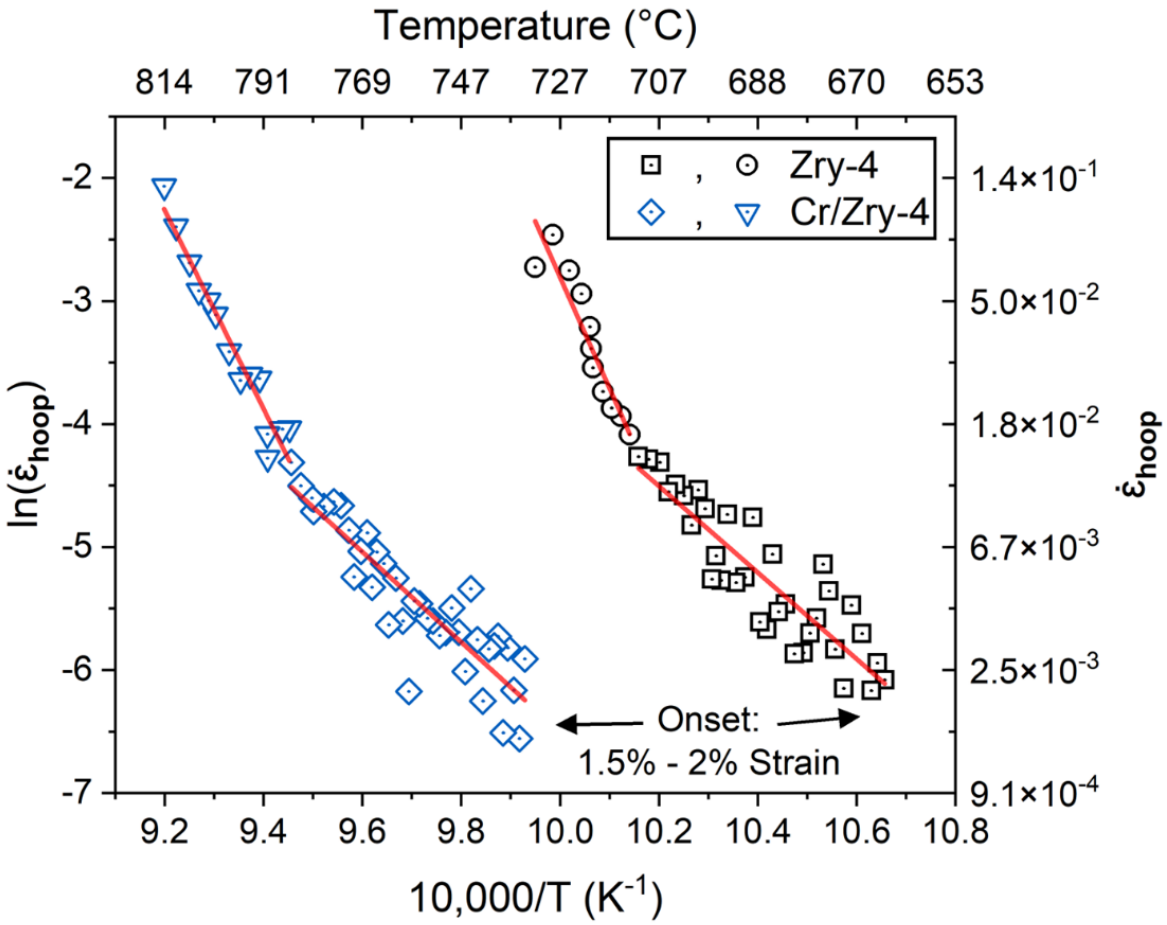

Figure 106. Semi-log plot of hoop strain rate and inverse temperature to highlight Arrhenius temperature dependence.

such a switch from uniform to non-uniform behavior indicates subsequent plastic instability and failure. The correlation between observations strengthens the hypothesis that the higher temperature segment, which accounts for most of the ballooning, represents plastic instability.

Activation energies were determined from the slopes of the two segments for both tests, as displayed in Table 20. The low temperature activation energies were found to be approximately 300 kJ/mol, in agreement with each other, steady-state models, and the previous 2D DIC testing in Chapter 7. The high temperature segments showed greater discrepancy but still in great agreement, with 672 ± 42 kJ/mol and 751 ± 92 kJ/mol for the bare and Cr coated specimens, respectively. These values are also in line with the lower end of the high-temperature segments discovered in Chapter 7.

Both the Cr-coated and bare samples demonstrated similar behavior in regard to the presence of and parameters associated with these transitions. The large difference between the behavior of the two is the temperature at which both the strain signal crossed the 2% threshold to define the first segment as well as the transition point to the higher temperature segment. The difference between the curves is ~80 °C, starkly similar to the difference in burst temperature. To rigorously confirm this observation, further testing and the development of a comprehensive test matrix are necessary.

9.3.2: Step-loaded isothermal testing of Cr coated Zry-4

Step loaded isothermal burst testing was conducted for Cr#2 coated Zry-4 at 600 °C, with loading conditions similar to that of the bare testing presented in the previous chapter. The sample was pressurized again after ~1-2 min at temperature. The resulting data is presented in Figure 107., with Figure *107*.(a) showing the strain curves for the Cr#2 sample against the 600 °C Test-1 data and Figure *107*.(b) presenting the strain rate and stress data on a log-log plot.

The Cr#2 sample showed lower creep strain comparably to the bare sample, with linear strain segments associated with the pressure steps. This is reflected in the strain-rates for a given stress in Figure 107.(b), where the strain rates were generally lower Note that the general trend of the strain rate-stress curves is similar, with a stress exponent of approximately 5 found for both bare and coated systems.

The increased creep strength imparted by the Cr coating aligns with the previous literature

Table 20. Activation energies determined from each segment in the strain-rate temperature dependence curves.

	Zry-4	Cr/Zry-4
Low Temperature, Q	292 ± 26	305 ± 25
High Temperature, Q	751 ± 93	672 ± 47

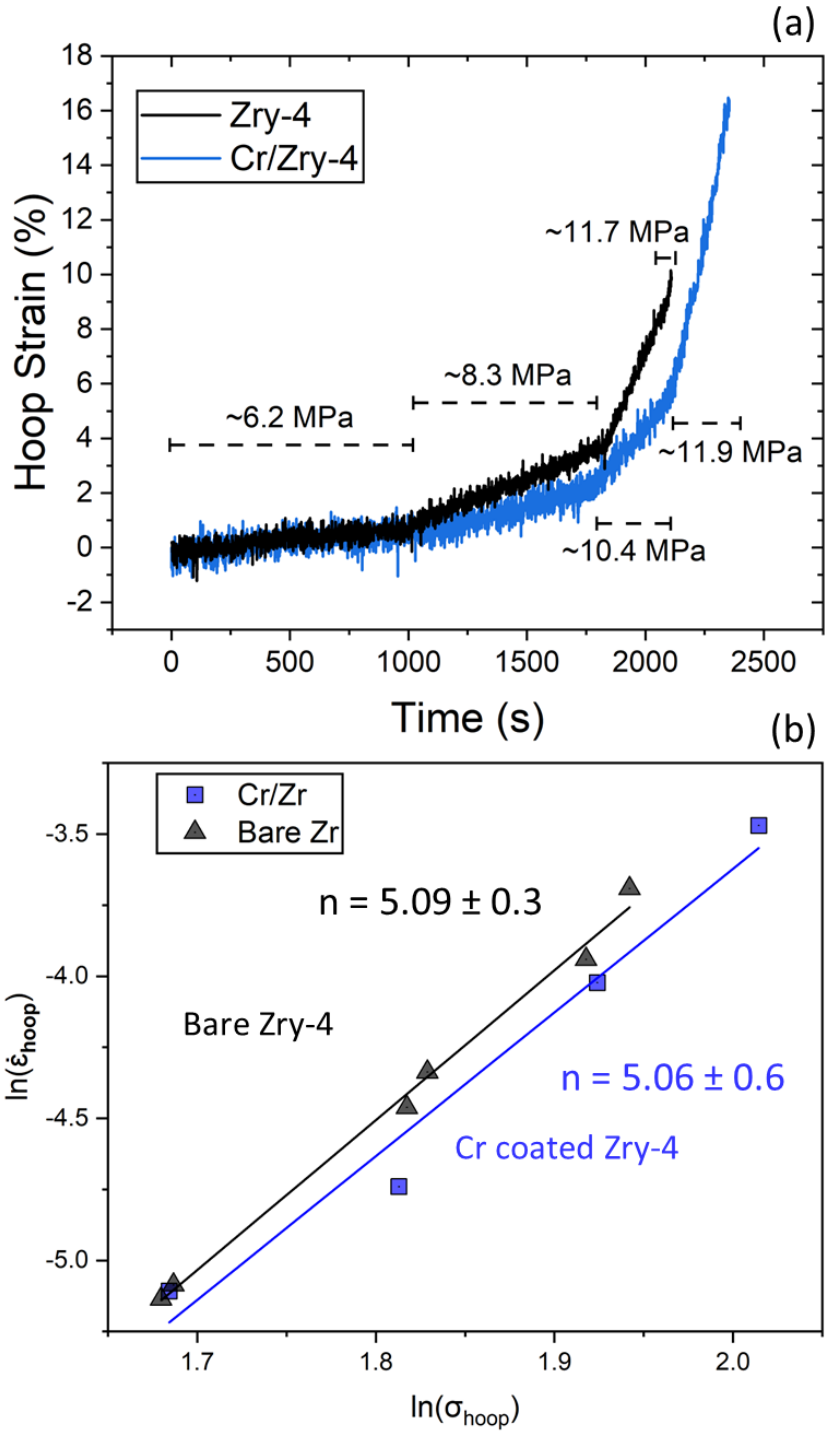

Figure 107. Strain and strain rate data from the accelerated creep test of Cr#2 at 600 °C compared to bare Zry-4. Strain histories are shown in (a) and the strain rate – stress relation in double logarithmic relations in (b).

detailed in Chapter 2. To gather further insights, extensive testing and investigations into microstructure and residual stress effects are required. However, the consistent stress dependence with the coating suggests that the underlying creep mechanism, controlled by dislocation movement, remains unaltered.

9.3.3: Transient testing of C26M FeCrAl

Transient testing of C26M FeCrAl was conducted at a heating rate of 5 °C/s under a constant 6.2 MPa load. Ar was substituted for steam for two main reasons:

(1) FeCrAl has slow reaction kinetics with steam, meaning its behavior in steam and Ar should be similar.
(2) To study the potential effects of fluid type on the optical environment and noise—critical for testing on materials with lower overall ballooning and strain rates.

This test sought to explore the application of this framework to Fe-based materials and to assess the current resolution capabilities as well as noise limitations. The earlier discussions on Cr coated materials underscored the depth of analysis possible with full field strain measurements. To leverage advanced techniques like the VFM method in future research, understanding the present capabilities of the framework is crucial.

Figure *108*.depicts the thermocouple placements and a hoop strain map for the final frame before rupture. Thermocouple readings were taken from two locations, using a control thermocouple 12 mm above the cladding centerline and a centerline thermocouple embedded within adhesive. Temperature readings were 975°C and 888°C for the centerline and control thermocouples, respectively. The readings of the two thermocouples at burst and burst hoop stress for this test are presented against previous ex-situ C26M testing from Chapter 4 in Figure *109*.. The thermocouple reading 12 mm above the cladding centerline gave a burst temperature comparable to the previous ex-situ testing. However, the thermocouple reading at the centerline was considerably higher compared to the trendline. This observation needs further investigation; however, it could indicate that a thermocouple measurement in or near the rupture region is critical. The issue of measuring a “true” burst temperature is long-standing, with implementations such as this possibly leading to more accurate descriptions than thermocouples well away from rupture. However, this reading could be influenced by the adhesive paste, which could serve to change

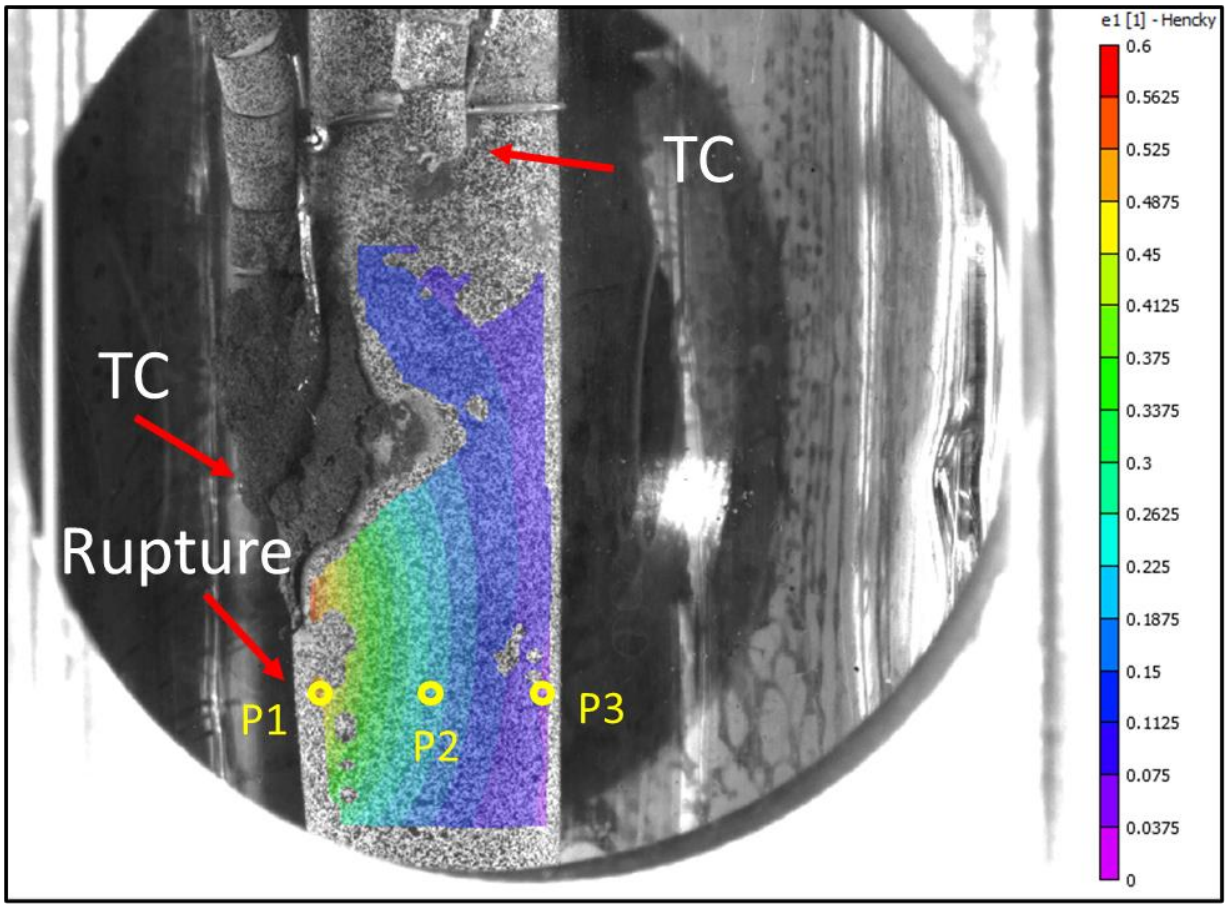

Figure 108. Hoop strain map from frame just before rupture. TC location at cladding centerline and 12 mm above are presented. Points of analysis utilized in subsequent figures (P_1, P_2, P_3) across the hoop direction.

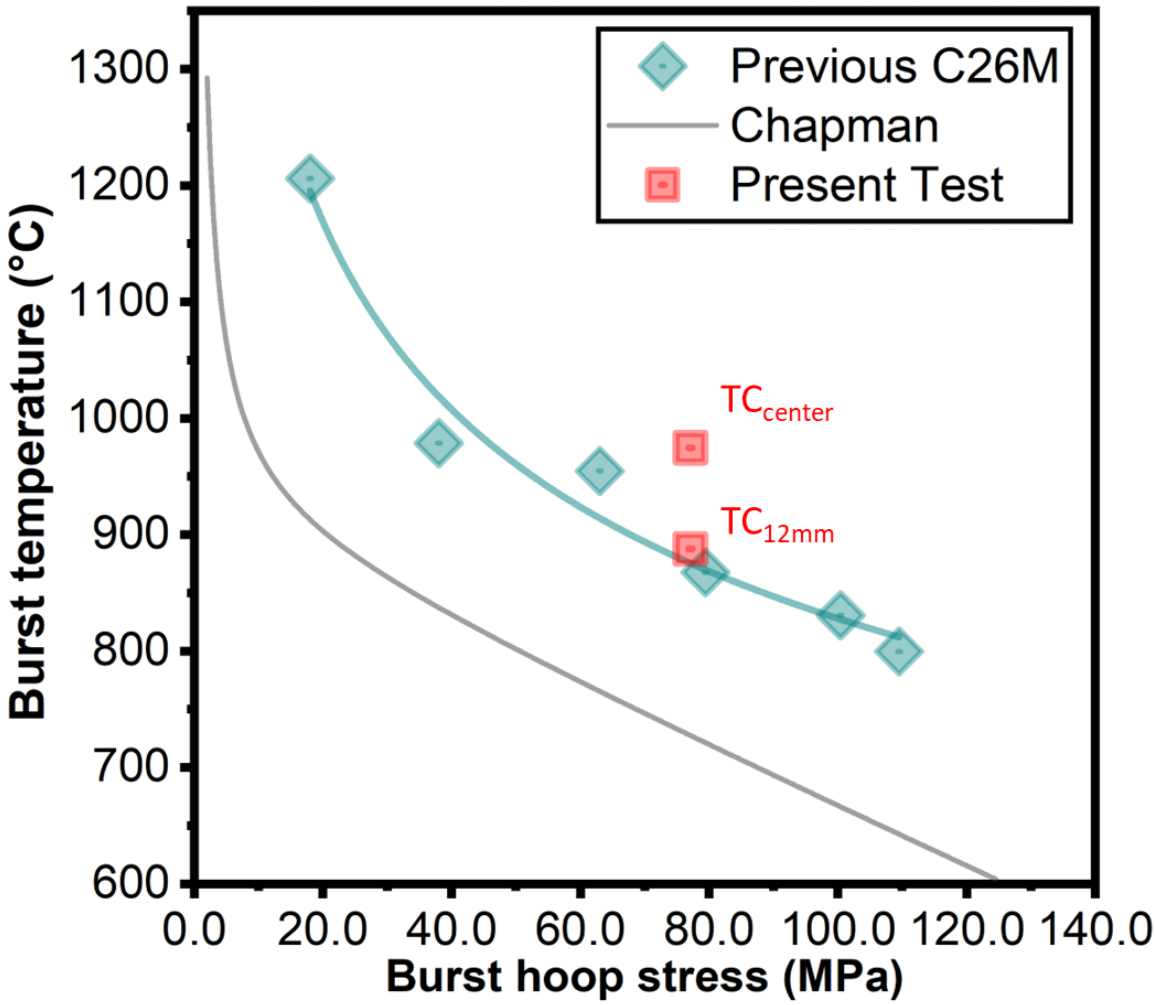

Figure 109. Thermocouple readings at burst and burst hoop stress for centerline and 12 mm above positions compared to previous ex-situ data. Chapman correlation for Zircaloys is included in grey.

incident IR heating.

To investigate the gradient evident from the strain map, strain data was extracted from the points labeled P_1 to P_3 in Figure 108. Figure *110*. presents the hoop strain for P_1 to P_3 and the centerline thermocouple reading. A well-defined strain gradient across the hoop direction is now quantitatively evident, with greater strain naturally near the rupture. Note, strain data recovered from P_2 and P_3 are rather similar for most of the test (up to ~100 s out of the 125 s test duration). The noise level at a data point depends on its position in the strain map, with the mid-point (P_2) showing the least noise. This discrepancy may be attributed to the camera perspectives and cladding geometry. The most similar perspective between the cameras is at the center, and therefore this position is the easiest to correlate between cameras. Positions on either side of the center results in divergent perspectives between the cameras which can make correlation of points less accurate. Additionally, issues like a changing optical environment or manual exposure adjustments, which differs between cameras, in the software can further introduce errors into these perspectives. Due to P_2 exhibiting the least noise, it was chosen for further analysis.

Hoop and axial strain from P_2 are presented in Figure *111*. alongside the centerline thermocouple reading. Contrary to the Zry-4 testing, positive axial strain was observed for the entirety of the test. The positive axial strain in this FeCrAl sample might indicate that tensile stress in the axial direction outweighs the effects of plastic incompressibility in the hoop direction. A noteworthy observation is the correlation between decreasing temperature change and the rapidly increasing strain towards the end of the test. A crack was observed in the adhesive paste and slight motion of the thermocouple witnessed, indicating the thermocouple might have detached from the cladding. With loss of contact, the thermocouple could move into the cooler regions, potentially leading to a lower heating rate. Additionally, the paste might interfere with the incident infrared, causing asymmetrical and more intense heating near it. The effect and reliability of the metallic paste on these temperature profiles remains ambiguous. This is critical for future research since any loss of contact obscures temperature-strain rate correlations. However, such relationships were still explored.

The strain rate versus temperature relationship for the FeCrAl sample was explored similarly to the Zry-4 testing, i.e., in an Arrhenius fashion. Data from P_2—both raw and smoothed strain rate—for the last ~70 °C of the test is presented against inverse temperature in Figure 112.

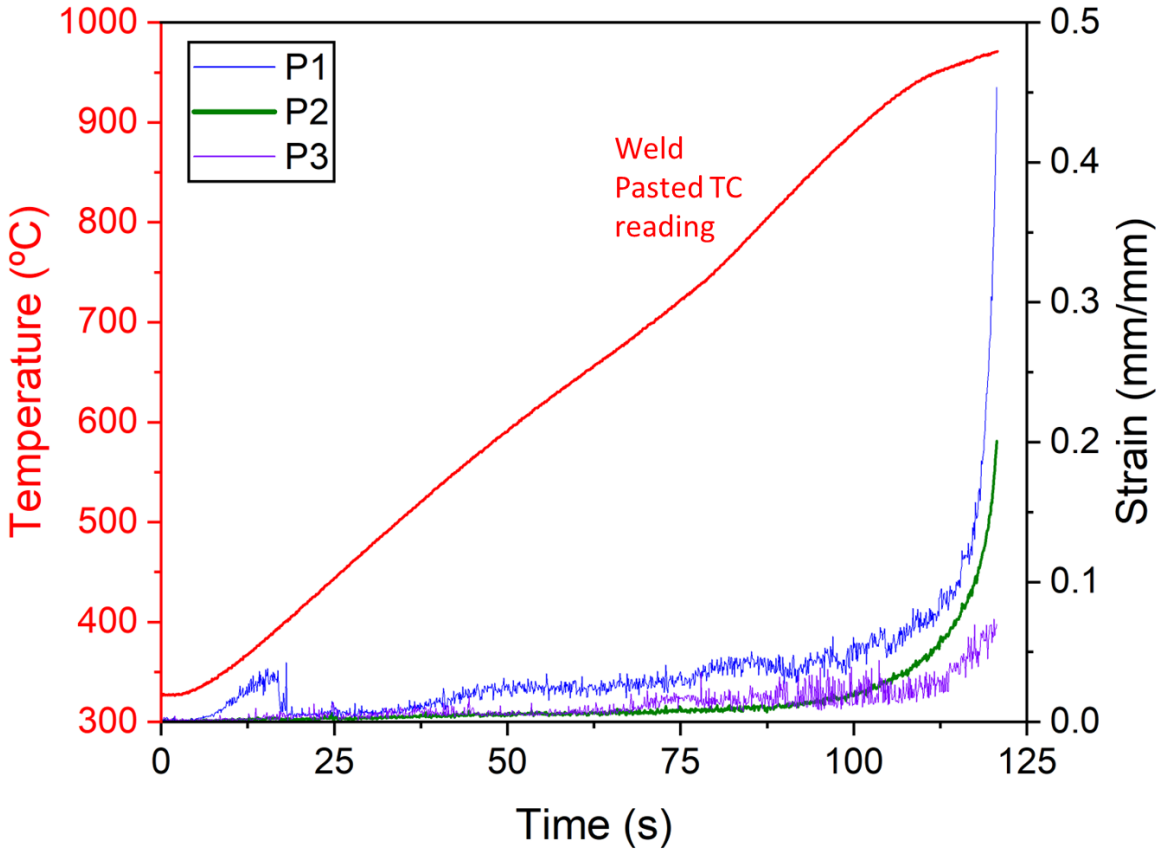

Figure 110. Hoop strain data from the 3 points illustrated in the previous figure and centerline thermocouple reading during the test.

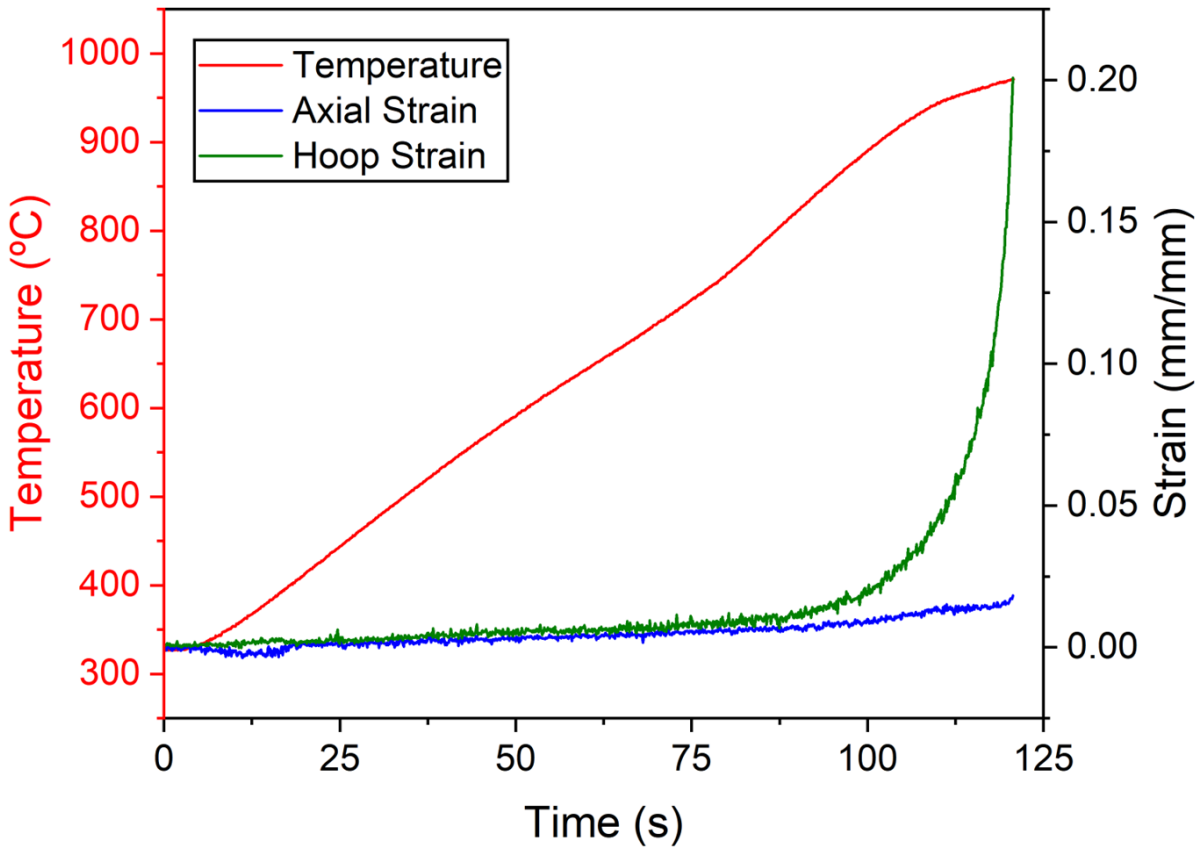

Figure 111. Hoop strain, axial strain, and temperature reading through the test for P_2.

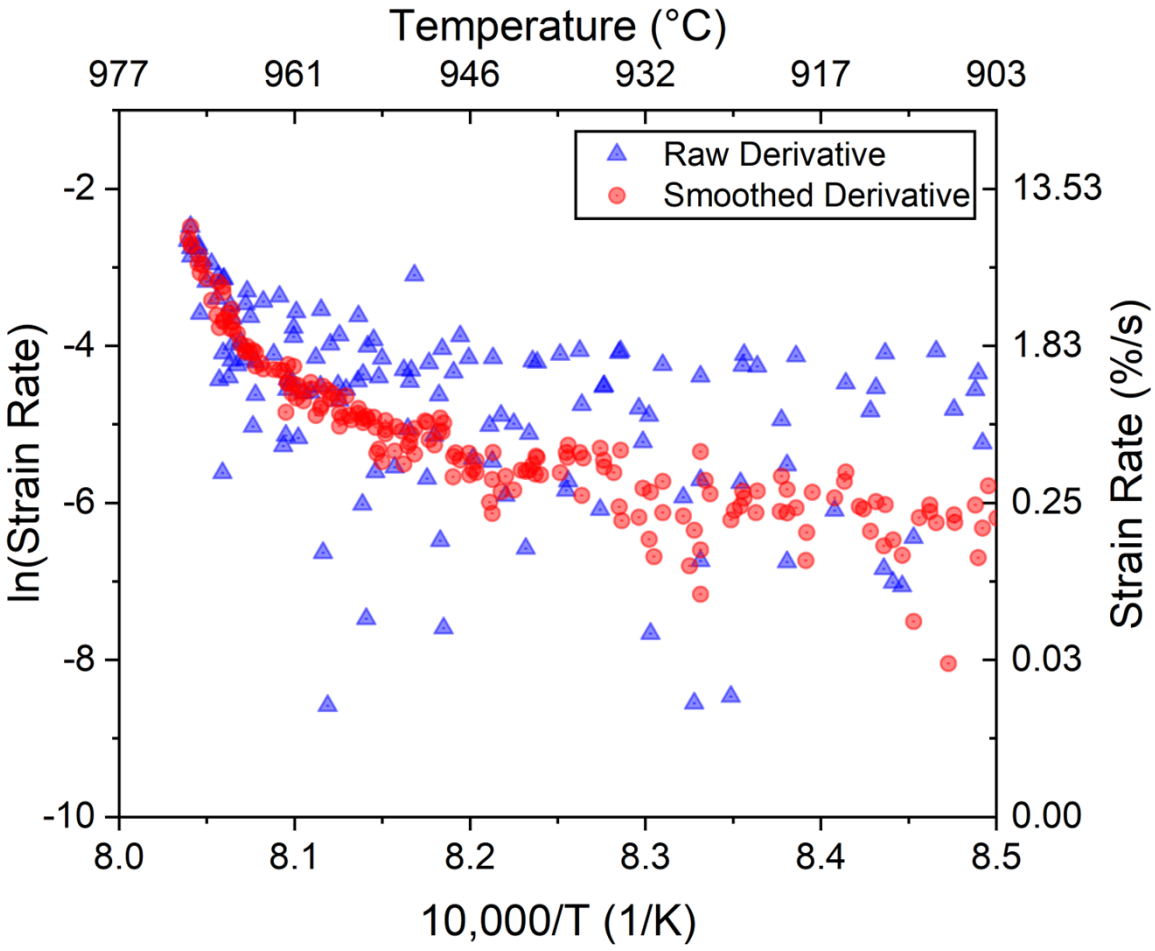

Figure 112. Arrhenius plot of raw and smoothed strain rate data for P_2.

The pronounced level of noise in strain rate, even though P_2 was the lowest strain of the three analyzed locations, is evident in the raw data. A clear signal in the raw data is only apparent in the last 10 °C (~2 s) end of the test. The smoothed curve still showed considerable noise until ~30 °C before burst, where a possible transition in deformation behavior is found at ~12 °C before burst. However, the effects of smoothing are well apparent, and this data set should be interpreted qualitatively as well as with caution. It is possible that the smoothing process (necessary to even distinguish the overall strain rate versus temperature trend) blended and weighted any bilinear behavior. As such, any relevant comparison between the FeCrAl and Zry-4 systems cannot be made at this time, and FeCrAl activation energies were not determined. To really address this question, systematic and experimental error needs to be reduced behavior. Note, the bare and Cr coated comparison above is for average strains of the balloon region, which inherently smooths over any noise, while the present analysis is from a single point of thousands. However, with the lower balloon strain yet high strain gradient, sound point data analysis is crucial to refining understanding.

Noise considerations aside, fundamentally FeCrAl and Zr alloys have drastically different balloon behavior. The ballooning process for FeCrAl is inherently "shallower", a difference detailed in Chapter 4 with ex-situ comparison of T35Y2, C26M, and Zry-2. The straining and failure process may be more localized to near the rupture region. If an instability is driving the deformation process, the effects of it are not as distributed around the FeCrAl cladding circumference as for Zry-4. A thorough understanding of this difference requires significantly more investigation. But similar to the preliminary comparisons of bare and Cr coated behavior leading to insights, comparison between such different materials could give insight into how to approach FeCrAl understanding. Discussion beyond this is speculation, where further testing and minimized noise is necessary.

9.3.4: Consideration of error in stereo-DIC and future strategies to mitigate error

The quantification of error and uncertainty in stereo DIC is a pressing matter, especially within the context of the SATS project. The richness of DIC data brings along the intricate challenge of managing and estimating errors. Key sources of these errors encompass:

(1) Camera noise and calibration inaccuracies.
(2) Sub-pixel registration discrepancies.

(3) Interpolation errors arising during displacement and strain calculations between pixels.
(4) Method-dependent errors during strain calculations from displacement fields.
(5) Quality inconsistencies in the speckle pattern.
(6) Systematic errors, including those resulting from changes in optical environment and illumination.

Although all of these considerations contribute to noise/error, sources 1, 5, and 6 are potentially the most impactful. They are also the most controllable within the SATS testing environment.

For the camera-related errors (1), rigorous camera calibration and positioning can minimize noise, thereby grounding it to baseline random values. The successful noise reduction achieved throughout the Zry-4 creep testing in Chapter 8 showcased the on-going optimization efforts. The FeCrAl testing, on the other hand, illustrates that further improvements are necessary.

Addressing the speckle pattern quality (5) requires the development of methods to consistently produce an optimal speckle size for the given optical setup. The quality of the speckle pattern has a direct impact on the precision of displacement measurements. Consistency in speckle size and distribution is therefore crucial. New methodologies should be sought to produce consistent and suitably random patterns on the cladding surface. A preferred option is to reproduce the same exact pattern for each sample.

As for the systematic errors (6), optimizing the insulation of the SATS furnace and adjusting the flow rate to ensure laminar flow can enhance environmental stability. The flow rate and type of fluid environment, be it steam or argon, can affect the clarity and accuracy of DIC measurements. Establishing a laminar flow and ensuring the furnace environment remains stable are a high priority, as it reduces potential interference in the optical environment. Combining the optimal intensity of blue light with blue light filters may also counteract illumination inconsistencies from the furnace during the ramp.

Section 9.4: DISCUSSION AND CONCLUSIONS

The transient and accelerated creep testing presented in this chapter marked the successful implementation of this framework on ATF claddings, meeting a primary objective of this dissertation. Although preliminary, insights drawn from this chapter underscore the enhanced resolution attained by incorporating *in-situ* techniques into SATS.

The Cr coated claddings displayed a transition in strain rate temperature dependence, as observed earlier for bare Zry-4 in Chapter 7, but offset by approximately 80 °C. Despite the shift in temperature, the activation energies of the Cr coated and bare materials agreed with each other and results from 2D DIC testing. This data supports the hypothesis that the Cr#2 coating delays burst rather than fundamentally altering it, given the temperature shift in the strain rate data corresponds to the increase in burst temperature observed in Chapter 3.

Such behavior could suggest a residual stress in the coating effectively reduces the net stress from the applied load. This residual stress could also explain the increased creep strength of the Cr-coated sample, despite a similar stress dependency of about 5 at 600 °C. The residual stress would effectively lower the stress, which is not accounted for in the dataset, resulting in lower strain rates for the same apparent stress. A definitive assessment of this hypothesis requires further investigation, including coating microstructural characterization and residual stress analysis.

This chapter also showcased the potential of 3D DIC for further characterization possibilities. For both the Cr coated and bare samples, hoop strain line profiles along the axial direction revealed uniformity in the balloon region until approximately 50 °C (10 seconds) before the burst. This point corresponded to the transition in temperature dependence of the strain rate and also when the characteristic form of ballooning began to take shape. Thus, this transition from uniform to non-uniform profiles, associated with the change in temperature dependence, strengthens the hypothesis that plastic instability could be responsible for the majority of ballooning.

Line profiles are just one of the ways full 3D strain and displacement fields can be leveraged to deepen understanding of cladding behavior. For instance, half of the strain data points in the field could be used to generate parameters and tested on the rest of the field. Current efforts are being made to utilize the full map to refine predictive capabilities and characterize the balloon region as a whole.

Preliminary testing of FeCrAl has emphasized the need for ongoing refinement in experimental techniques. Due to the lower strain/strain rate observed in FeCrAl alloys, it is crucial to enhance error mitigation for subsequent testing. Improvements in pattern optimization, environmental fluid flow adjustments, camera configuration, and calibration techniques can notably reduce the noise floor. In essence, while the initial tests with FeCrAl underline the

importance of continual refinement in experimental approaches, the overarching goal is to minimize the noise floor. This will enable the detection of even subtle strain/strain rate variations, leading to a more precise understanding of material behavior.

Chapter 10: Conclusions

While traditional ex-situ LOCA testing offers invaluable baselines for both historical and ATF cladding behavior, the complexity introduced by transient factors complicates the process. Variables like heating rate, thermal gradients, filler rod form, and heating source all introduce elements of uncertainty, and the insights gained are typically restricted to as-received and post-failure states. These constraints make in-depth characterization and subsequent model development for incumbent Zr and new ATF cladding materials more time-consuming, expensive, and significantly more difficult. The first four chapters of this dissertation highlighted these limitations in *ex-situ* testing, identifying the need for *in-situ* thermomechanical data to properly assess the effects of a Cr coating on Zr and to further current FeCrAl modeling efforts.

This dissertation presented a new *in-situ* framework, developed and validated to address the drawbacks of traditional burst testing methods, thereby expediting the characterization process. While the framework was ultimately designed for ATF claddings, the bulk of the experimentation was conducted on incumbent Zry-4 claddings to validate the methodologies and explore current knowledge gaps. The exploration of these gaps underscored the value of this *in-situ* framework, both in terms of data collection speed and the insights it provides into fundamental LOCA behavior.

The thermomechanical data derived from testing Zr alloys enabled a thorough analysis of historical bases, as demonstrated in Chapter 7 with the steady-state creep assumption. These transient heating experiments revealed a novel deviation, where the activation energy transitioned from a value consistent with steady-state creep and LOCA models to an apparent "activation energy" ~2-3 times higher. The second segment of strain rate temperature dependence, observed later in the test and at higher temperatures, accounted for the majority of strain during ballooning. This behavior was consistently found in transient testing, with the transition between the two regimes occurring above a critical temperature and/or applied stress dependent threshold.

Analysis of cladding behavior utilized concepts and nomenclature of "activation energies" due to the historic reference frame of secondary creep mechanisms dominating Zr LOCA behavior and the Arrhenius dependence observed between strain rate and temperature. This transition in behavior was interpreted using simplified creep analysis leading to a discussion of a dramatic

increase in creep activation energy, but it is likely due to the onset of a plastic instability process that accelerated localized deformation/ballooning. Preliminary comparison to plasticity models supported the notion that plastic instability is largely responsible for the observed higher temperature strain rate behavior. The stress states at the transition point between the high and low temperature deformation regimes for all samples had far surpassed the yield point, indicating that the high temperature strain rate behavior was representative of plastic instability/failure. This signature deviation is an important indicator, but likely does not reflect an actual change in creep deformation activation energy/mechanism.

Preliminary tests on Zry-4 using stereo DIC supported this plastic instability hypothesis developed from 2D DIC testing with the ability to analyze more of the balloon development. Line profiles confirmed uniform hoop strain in the balloon region until just before burst, when a nodal balloon shape began to form. This point coincided with the transition in temperature dependence, suggesting that this change represented a shift from uniform to non-uniform deformation mechanisms. The onset of plastic instability, in a conventional mechanical testing framework, represents a similar transition from uniform to non-uniform deformation.

The presence of two distinct activation energy regimes, although possibly spurious for the higher temperature regime due to the reasons discussed above, could represent a measurable transition in temperature dependence indicative of a change in governing deformation mechanism. While limited in sample size, the two 3D DIC samples (Cr coated and bare) heating at a rate of 5 °C/s demonstrated similar apparent activation energies compared to the 1 °C/s 2D DIC testing. This preliminary parity indicates the mechanism may be independent of heating rate, and more dependent on temperature.

However, caution must be used when assuming the mechanism or physical significance. The onset of plastic instability was posited to be associated with the increased apparent activation energy at high temperatures, due considerations discussed above. The instability here could be a result of beyond-conventional-testing definitions of plastic instability arising from a loss of balance between strain hardening and geometric softening. Other influences could be dynamic recrystallization or alterations in the creep mechanisms such as the ratio of primary to secondary creep during the test (which may be intertwined with microstructural instability). These influences are likely temperature dependent, and as a result could encourage a local instability from a

temperature gradient. Much further work beyond SATS testing is needed, such as experiments looking at microstructural evolution of SRA Zr during LOCA transients or the effects of load on any said evolution.

Regardless of the physical meaning, this work shows there are two key deformation phenomena present during Zr alloy LOCA behavior: (1) a transition away from a temperature dependence associated with traditional steady-state creep mechanisms and (2) there is a definable relationship between strain rate and temperature for the ballooning process. The Arrhenius analysis led to the notion of a second "activation energy" at high temperatures and high strains, but this may just suggest a different exponential relationship between strain rate and temperature is present at high temperatures and strains.

The validity of this second, apparent activation energy that encompasses most of ballooning for Zr claddings requires extensive testing and scrutiny. However, it could prove useful as the basis of constitutive equations in future efforts to utilize inverse techniques such as the VFM. Such methods would need not only significantly reduced noise in stereo DIC, but also a greater understanding of the temperature gradient across the balloon region.

Accelerated creep testing was conducted to investigate changes in the stress exponent that could account for an apparent shift in activation energy. Although the stress state did not perfectly align with the transition points from transient testing, a stress exponent of approximately 5 was consistently observed across all tested temperatures. This suggests that a change in the stress exponent might not be the primary driver of the transition in LOCA behavior. However, these tests were exploratory in nature, with an emphasis on optimizing the accelerated technique to yield the maximum amount of data. Consequently, a true steady state may not have been achieved particularly at lower temperatures, resulting in greater than expected strain rates due to primary creep. Yet, if primary creep is present on the time scale of this accelerated testing, this would suggest that primary creep should also be considered rather than just steady-state creep. Future efforts will aim to extend to the transition stress states and ensure steady-state conditions are achieved to definitively assess these observations.

Creep testing at higher temperatures resulted in strain rates that demonstrated adequate agreement with isotropic versions of models found in the literature. This indicates that Zry-4 might exhibit effective isotropy at these temperatures. However, the potential influences of primary creep

and uncertainty in the material conditions used in the literature models render this observation not entirely conclusive. Anisotropy is a critical element in conventional modeling of Zr, particularly when using creep parameters derived from axial testing. Future work aims to forge a better link between microstructure, material condition, and anisotropy.

This hypothesis regarding plastic instability dominating the majority of ballooning, despite necessitating further exploration into plasticity behavior, signifies a substantial shift in the modeling paradigm for Zr LOCA behavior. The high-temperature segments were dependent on the analysis point but remained relatively consistent. Criterion for diffuse necking (ballooning) onset and localized necking (rupture) based on more fundamental mechanical descriptions could be correlated with the instability points in transient testing. *In-situ* data of the ballooning process could provide empirical descriptions of deformation past these instability points to rupture.

Plasticity-based descriptions may yield more accurate results. Distinguishing between "creep" and "plasticity" dominance essentially separates two regimes: time-dependent and independent behaviors. This separation of variables is a valid starting point that greatly simplifies modeling efforts. However, at a microstructural level, the differences between dislocation motion driven by time-dependent creep or time-independent plasticity/yielding are less clear and likely interactive. Likewise, mechanical testing conducted at a fixed temperature does not capture the effects of transients. Thermal effects on the microstructure, such as dislocation annihilation or dynamic recrystallization due to deformation at elevated temperature, are not considered in current models. Long term investigations should seek to establish models that move beyond this separation of time dependence and independent behavior. Currently, collaborations with modeling experts are ongoing to approach LOCA modeling from a microstructural perspective.

DIC was preliminarily applied to Cr coated Zry-4 and C26M FeCrAl, marking the successful development of an accelerated qualification burst testing framework. Most notably, a transition in strain rate temperature dependence was also found for Cr coated Zr during transient testing. The apparent activation energies derived from these two test segments were consistent with those from bare samples and 2D DIC testing, but the strain behavior shifted by approximately 80 °C. This shift aligned with the observed increase in burst temperature between the samples.

This observation, indicative of a similar strain rate behavior shifted to higher temperatures, supports the hypothesis developed in Chapter 3 that the Cr coating may delay burst rather than

fundamentally alter the behavior. This shift may be related to residual stresses in the coating that effectively reduce the stress state for a given load, compared to bare samples. Preliminary accelerated creep tests support this observation, with lower strain rates recorded at 600 °C despite similar stress exponents observed between Cr coated and bare samples. Future work will pursue a more thorough understanding of the relationship between coating residual stress, microstructural characterization, and observations from burst testing. Regardless, these preliminary investigations show the value of the *in-situ* framework for characterizing and qualifying ATF claddings.

This dissertation has laid a solid foundation for future testing of ATF claddings, including extended work on Cr coated Zr claddings and FeCrAl alloys. Yet, the capabilities of the new framework could extend beyond ATF claddings. Cladding systems in next-generation reactor concepts could be evaluated under extreme conditions using SATS. Similarly, accelerated creep testing could be employed for rapid characterization of any material in tube geometry. Syncing DIC strain measurements with upgraded pressure systems could also be utilized to enable strain-controlled testing.

However, all observations made in this dissertation come with a significant caveat – they are based on as-received, un-irradiated material testing. Currently, efforts are underway to integrate a version of the validated framework into the SATS located in an ORNL hot-cell. As such, the insights from this research provide a baseline for comparison against future irradiated cladding testing.

References

[1] R.A. Knief, Nuclear engineering: theory and technology of commercial nuclear power, 2. ed., [ANS reprint], American Nuclear Society, La Grange Park, Ill, 2008.

[2] D.R. Olander, A.T. Motta, B. Wirth, Light water reactor materials. Volume 1: Fundamentals, American Nuclear Society, La Grange Park, Illinois, 2017.

[3] H. Pomerance, Thermal Neutron Capture Cross Sections, Phys. Rev. 88 (1952) 412–413. https://doi.org/10.1103/PhysRev.88.412.

[4] H.G. Rickover, L.D. Geiger, B. Lustman, History of the development of zirconium alloys for use in nuclear reactors, 1975. https://doi.org/10.2172/4240391.

[5] K.A. Terrani, Accident tolerant fuel cladding development: Promise, status, and challenges, J. Nucl. Mater. 501 (2018) 13–30. https://doi.org/10.1016/j.jnucmat.2017.12.043.

[6] P. Billot, P. Belsu, A. Giordano, J. Thomazet, Development of a mechanistic model to assess the external corrosion of the Zircaloy claddings in PWRs, in: Zircon. Nucl. Ind. Eighth Int. Symp. Int. Symp., ASTM International, 1989: p. 165.

[7] B. Cox, Some thoughts on the mechanisms of in-reactor corrosion of zirconium alloys, J. Nucl. Mater. 336 (2005) 331–368. https://doi.org/10.1016/j.jnucmat.2004.09.029.

[8] R.T. Webster, Zirconium and Hafnium, in: ASM Handbook Committee (Ed.), Prop. Sel. Nonferrous Alloys Spec.-Purp. Mater., ASM International, 1990: pp. 661–669. https://doi.org/10.31399/asm.hb.v02.a0001084.

[9] A. Miquet, D. Charquet, C.H. Allibert, Solid state phase equilibria of zircaloy-4 in the temperature range 750–1050°C, J. Nucl. Mater. 105 (1982) 132–141. https://doi.org/10.1016/0022-3115(82)90367-1.

[10] D. Caillard, M. Gaumé, F. Onimus, Glide and cross-slip of a-dislocations in Zr and Ti, Acta Mater. 155 (2018) 23–34. https://doi.org/10.1016/j.actamat.2018.05.038.

[11] A. Akhtar, A. Teghtsoonian, Plastic deformation of zirconium single crystals, Acta Metall. 19 (1971) 655–663. https://doi.org/10.1016/0001-6160(71)90019-8.

[12] I.J. Beyerlein, C.N. Tomé, A dislocation-based constitutive law for pure Zr including temperature effects, Int. J. Plast. 24 (2008) 867–895. https://doi.org/10.1016/j.ijplas.2007.07.017.

[13] L. Capolungo, P.E. Marshall, R.J. McCabe, I.J. Beyerlein, C.N. Tomé, Nucleation and growth of twins in Zr: A statistical study, Acta Mater. 57 (2009) 6047–6056. https://doi.org/10.1016/j.actamat.2009.08.030.

[14] Committee B10, ed., Deformation Mechanisms, Texture, and Anisotropy in Zirconium and Zircaloy, ASTM International, 100 Barr Harbor Drive, PO Box C700, West Conshohocken, PA 19428-2959, 1988. https://doi.org/10.1520/STP966-EB.

[15] H.M. Chung, T.F. Kassner, Deformation Characteristics of Zircaloy Cladding in Vacuum and Steam under Transient-Heating Conditions: Summary Report, Argonne National Laboratory, 1978.

[16] R.A. Holt, Mechanisms of irradiation growth of alpha-zirconium alloys, J. Nucl. Mater. 159 (1988) 310–338. https://doi.org/10.1016/0022-3115(88)90099-2.

[17] R.B. Adamson, C.E. Coleman, M. Griffiths, Irradiation creep and growth of zirconium alloys: A critical review, J. Nucl. Mater. 521 (2019) 167–244. https://doi.org/10.1016/j.jnucmat.2019.04.021.

[18] F. Erbacher, H. Neitzel, H. Rosinger, H. Schmidt, K. Wiehr, Burst Criterion of Zircaloy Fuel Claddings in a Loss-of-Coolant Accident, in: D. Franklin (Ed.), Zircon. Nucl. Ind., ASTM International, 100 Barr Harbor Drive, PO Box C700, West Conshohocken, PA 19428-2959, 1982: pp. 271-271–13. https://doi.org/10.1520/STP37058S.

[19] A.R. Massih, An Evaluation of High-temperature Creep of Zirconium Alloys: Data versus Models, Swed. Radiat. Saf. Auth. (2014).

[20] F. Onimus, S. Doriot, J.-L. Béchade, Radiation Effects in Zirconium Alloys, in: Compr. Nucl. Mater., Elsevier, 2020: pp. 1–56. https://doi.org/10.1016/B978-0-12-803581-8.11759-X.

[21] K.-C. Lan, W. Zhong, P.A. Mouche, H.-M. Tung, H. Lee, B.J. Heuser, J.F. Stubbins, The challenge of acquiring a satisfactory EBSD result of CWSR Zircaloy-4 cladding tube: CHALLENGE OF ACQUIRING A SATISFACTORY EBSD RESULT OF CWSR ZIRCALOY-4 CLADDING TUBE, J. Microsc. 272 (2018) 25–34. https://doi.org/10.1111/jmi.12729.

[22] M. Reocreux, The Blowdown, Refill, and Reflood Phase during a LOCA: Survey of the Main Physical Phenomena, in: French Atomic Energy Commission, Varese, Italy, 1980.

[23] U.S. Nuclear Regulatory Commission, Alternate Risk-Informed Approach for Addressing the Effects of Debris on Post-Accident Long-Term Core Cooling, Federal Register Volume 80 (2015) 21658–21659.

[24] Defence in Depth in Nuclear Safety, International Atomic Energy Agency, Vienna, 1996.

[25] Atomic Energy Commission Reports: Opinions and Decisions of the Atomic Energy Commission with Selected Orders, U.S. Atomic Energy Commission, 1973.

[26] F. Erbacher, S. Leistikow, Zircaloy Fuel Cladding Behavior in a Loss-of-Coolant Accident: A Review, in: R. Adamson, L. Van Swam (Eds.), Zircon. Nucl. Ind., ASTM International, 100 Barr Harbor Drive, PO Box C700, West Conshohocken, PA 19428-2959, 1987: pp. 451-451–38. https://doi.org/10.1520/STP28138S.

[27] R.H. Chapman, Multirod Burst Test Program progress report, July--December 1977. [BWR; PWR], Oak Ridge National Lab., Tenn. (USA), 1978.

[28] R. Chapman, J. Crowley, A. Longest, G. Hofmann, Zirconium Cladding Deformation in a Steam Environment with Transient Heating, in: J. Schemel, T. Papazoglou (Eds.), Zircon. Nucl. Ind., ASTM International, 100 Barr Harbor Drive, PO Box C700, West Conshohocken, PA 19428-2959, 1979: pp. 393-393–16. https://doi.org/10.1520/STP36692S.

[29] D.A. Powers, R.O. Meyer, Evaluation of simulated-LOCA tests that produced large fuel cladding ballooning, U.S. Nuclear Regulatory Commission, 1979.

[30] D.A. Powers, R.O. Meyer, Cladding Swelling and Rupture Models for LOCA Analysis, US Nucl. Regul. Comm. (1980).

[31] B.D. Clay, T. Healey, G.B. Redding, Deformation and rupture of transiently heated Zircaloy tube, in: Spec. Meet. Behav. Water React. Fuel Elem. Accid. Cond., Spaatind, Norway, 1976.

[32] M.E. Markiewicz, F.J. Erbacher, Experiments on Ballooning in Pressurized and Transiently Heated Zircaloy-4 Tubes, Karlsruhe Insititute, 1988.

[33] H.E. Rosinger, A model to predict the failure of zircaloy-4 fuel sheathing during postulated loca conditions, J. Nucl. Mater. 120 (1984) 41–54. https://doi.org/10.1016/0022-3115(84)90169-7.

[34] N. Capps, C. Jensen, F. Cappia, J. Harp, K. Terrani, N. Woolstenhulme, D. Wachs, A Critical Review of High Burnup Fuel Fragmentation, Relocation, and Dispersal under Loss-Of-Coolant Accident Conditions, J. Nucl. Mater. 546 (2021) 152750. https://doi.org/10.1016/j.jnucmat.2020.152750.

[35] M.A. Snead, Y. Yan, M. Howell, J.R. Keiser, K.A. Terrani, Severe Accident Test Station Design Document, 2015. https://doi.org/10.2172/1252142.

[36] C.P. Massey, K.A. Terrani, S.N. Dryepondt, B.A. Pint, Cladding burst behavior of Fe-based alloys under LOCA, J. Nucl. Mater. 470 (2016) 128–138. https://doi.org/10.1016/j.jnucmat.2015.12.018.

[37] R. Sweet, A. Nelson, B. Wirth, Thermo-mechanical analysis of SiC and FeCrAl cladding behavior under a loss-ofcoolant accident, Oak Ridge National Lab, 2018. https://info.ornl.gov/sites/publications/Files/Pub117658.pdf.

[38] S.B. Bell, K.A. Kane, C.P. Massey, L.A. Baldesberger, D. Lutz, B.A. Pint, Strength and rupture geometry of un-irradiated C26M FeCrAl under LOCA burst testing conditions, J. Nucl. Mater. 557 (2021) 153242. https://doi.org/10.1016/j.jnucmat.2021.153242.

[39] J.D. Hales, S.R. Novascone, B.W. Spencer, R.L. Williamson, G. Pastore, D.M. Perez, Verification of the BISON fuel performance code, Ann. Nucl. Energy. 71 (2014) 81–90. https://doi.org/10.1016/j.anucene.2014.03.027.

[40] K. Kane, S. Bell, N. Capps, B. Garrison, K. Shapovalov, G. Jacobsen, C. Deck, T. Graening, T. Koyanagi, C. Massey, The response of accident tolerant fuel cladding to LOCA burst testing: A comparative study of leading concepts, J. Nucl. Mater. 574 (2023) 154152. https://doi.org/10.1016/j.jnucmat.2022.154152.

[41] E. Hollnagel, Y. Fujita, The Fukushima Disaster - Systematic Failures as the Lack of Resilience, Nucl. Eng. Technol. 45 (2013) 13–20. https://doi.org/10.5516/NET.03.2011.078.

[42] M. Aoki, G. Rothwell, A comparative institutional analysis of the Fukushima nuclear disaster: Lessons and policy implications, Energy Policy. 53 (2013) 240–247. https://doi.org/10.1016/j.enpol.2012.10.058.

[43] V.H.M. Visschers, M. Siegrist, How a Nuclear Power Plant Accident Influences Acceptance of Nuclear Power: Results of a Longitudinal Study Before and After the Fukushima Disaster: How a Nuclear Power Plant Accident Influences Acceptance of Nuclear Power, Risk Anal. 33 (2013) 333–347. https://doi.org/10.1111/j.1539-6924.2012.01861.x.

[44] V. Lauber, S. Jacobsson, The politics and economics of constructing, contesting and restricting socio-political space for renewables – The German Renewable Energy Act, Environ. Innov. Soc. Transit. 18 (2016) 147–163. https://doi.org/10.1016/j.eist.2015.06.005.

[45] IAEA Report on Decommissioning and Remediation after A Nuclear Accident, International Atomic Energy Agency, International Experts Meeting, 2013.

[46] Deterministic Safety Analysis for Nuclear Power Plants, International Atomic Energy Agency, 2009.

[47] B.A. Pint, K.A. Terrani, Y. Yamamoto, L.L. Snead, Material Selection for Accident Tolerant Fuel Cladding, Metall. Mater. Trans. E. 2 (2015) 190–196. https://doi.org/10.1007/s40553-015-0056-7.

[48] S.J. Zinkle, K.A. Terrani, J.C. Gehin, L.J. Ott, L.L. Snead, Accident tolerant fuels for LWRs: A perspective, J. Nucl. Mater. 448 (2014) 374–379. https://doi.org/10.1016/j.jnucmat.2013.12.005.

[49] H.-G. Kim, I.-H. Kim, Y.-I. Jung, D.-J. Park, J.-Y. Park, Y.-H. Koo, Adhesion property and high-temperature oxidation behavior of Cr-coated Zircaloy-4 cladding tube prepared by 3D laser coating, J. Nucl. Mater. 465 (2015) 531–539. https://doi.org/10.1016/j.jnucmat.2015.06.030.

[50] J. Bischoff, C. Delafoy, C. Vauglin, P. Barberis, C. Roubeyrie, D. Perche, D. Duthoo, F. Schuster, J.-C. Brachet, E.W. Schweitzer, K. Nimishakavi, AREVA NP's enhanced accident-tolerant fuel developments: Focus on Cr-coated M5 cladding, Nucl. Eng. Technol. 50 (2018) 223–228. https://doi.org/10.1016/j.net.2017.12.004.

[51] J.-C. Brachet, I. Idarraga-Trujillo, M.L. Flem, M.L. Saux, V. Vandenberghe, S. Urvoy, E. Rouesne, T. Guilbert, C. Toffolon-Masclet, M. Tupin, C. Phalippou, F. Lomello, F. Schuster, A. Billard, G. Velisa, C. Ducros, F. Sanchette, Early studies on Cr-Coated Zircaloy-4 as

enhanced accident tolerant nuclear fuel claddings for light water reactors, J. Nucl. Mater. 517 (2019) 268–285. https://doi.org/10.1016/j.jnucmat.2019.02.018.

[52] A.S. Kuprin, V.A. Belous, V.N. Voyevodin, V.V. Bryk, R.L. Vasilenko, V.D. Ovcharenko, E.N. Reshetnyak, G.N. Tolmachova, P.N. V'yugov, Vacuum-arc chromium-based coatings for protection of zirconium alloys from the high-temperature oxidation in air, J. Nucl. Mater. 465 (2015) 400–406. https://doi.org/10.1016/j.jnucmat.2015.06.016.

[53] C. Meng, L. Yang, Y. Wu, J. Tan, W. Dang, X. He, X. Ma, Study of the oxidation behavior of CrN coating on Zr alloy in air, J. Nucl. Mater. 515 (2019) 354–369. https://doi.org/10.1016/j.jnucmat.2019.01.006.

[54] B.R. Maier, B.L. Garcia-Diaz, B. Hauch, L.C. Olson, R.L. Sindelar, K. Sridharan, Cold spray deposition of Ti2AlC coatings for improved nuclear fuel cladding, J. Nucl. Mater. 466 (2015) 712–717. https://doi.org/10.1016/j.jnucmat.2015.06.028.

[55] K. Lambrinou, M. Verwerft, J. Vleugels, A. Weisenburger, C. Lorrette, Y. de Carlan, Innovative accident-tolerant fuel cladding materials: the H2020 IL TROVATORE Perspective, in: Jeju Island, Korea, 2017.

[56] H.-B. Ma, J. Yan, Y.-H. Zhao, T. Liu, Q.-S. Ren, Y.-H. Liao, J.-D. Zuo, G. Liu, M.-Y. Yao, Oxidation behavior of Cr-coated zirconium alloy cladding in high-temperature steam above 1200 °C, Npj Mater. Degrad. 5 (2021) 7. https://doi.org/10.1038/s41529-021-00155-8.

[57] S.J. Zinkle, L.L. Snead, Designing Radiation Resistance in Materials for Fusion Energy, Annu. Rev. Mater. Res. 44 (2014) 241–267. https://doi.org/10.1146/annurev-matsci-070813-113627.

[58] J. Brachet, M. Dumerval, V. Lezaud-Chaillioux, M. Le Saux, E. Rouesne, D. Hamon, S. Urvoy, T. Guilbert, Q. Houmaire, C. Cobac, G. Nony, J. Rousselot, F. Lomello, F. Schuster, H. Palancher, J. Bischoff, E. Pouillier, Behavior of Chromium Coated M5TM Claddings under LOCA Conditions, in: Water React. Fuel Perform. Meet., Jeju Island, Korea, 2017.

[59] W.J. Bryan, D. Jones, Wear resistant coating for fuel cladding, US5268946A, 1993.

[60] D.J. Park, H.G. Kim, Y.I. Jung, J.H. Park, J.H. Yang, Y.H. Koo, Behavior of an improved Zr fuel cladding with oxidation resistant coating under loss-of-coolant accident conditions, J. Nucl. Mater. 482 (2016) 75–82. https://doi.org/10.1016/j.jnucmat.2016.10.021.

[61] I. Younker, M. Fratoni, Neutronic evaluation of coating and cladding materials for accident tolerant fuels, Prog. Nucl. Energy. 88 (2016) 10–18. https://doi.org/10.1016/j.pnucene.2015.11.006.

[62] DE-NE0008221 GE Final Technical and Scientific Report, General Electric Research, 2018.

[63] D.J. Park, H.G. Kim, J.Y. Park, Y.I. Jung, J.H. Park, Y.H. Koo, A study of the oxidation of FeCrAl alloy in pressurized water and high-temperature steam environment, Corros. Sci. 94 (2015) 459–465. https://doi.org/10.1016/j.corsci.2015.02.027.

[64] B.A. Pint, K.A. Terrani, M.P. Brady, T. Cheng, J.R. Keiser, High temperature oxidation of fuel cladding candidate materials in steam–hydrogen environments, J. Nucl. Mater. 440 (2013) 420–427. https://doi.org/10.1016/j.jnucmat.2013.05.047.

[65] B.A. Pint, Performance of FeCrAl for accident-tolerant fuel cladding in high-temperature steam, Corros. Rev. 35 (2017) 167–175. https://doi.org/10.1515/corrrev-2016-0067.

[66] Z. Yang, J. Pan, Z. Wang, Y. Wu, G. Jia, J. Li, X. Xiao, New insights into the mechanism of yttrium changing high-temperature oxide growth of Fe-13Cr–6Al–2Mo–0.5Nb alloy for fuel cladding, Corros. Sci. 172 (2020) 108728. https://doi.org/10.1016/j.corsci.2020.108728.

[67] Y. Yamamoto, B.A. Pint, K.A. Terrani, K.G. Field, Y. Yang, L.L. Snead, Development and property evaluation of nuclear grade wrought FeCrAl fuel cladding for light water reactors, J. Nucl. Mater. 467 (2015) 703–716. https://doi.org/10.1016/j.jnucmat.2015.10.019.

[68] Y. Yamamoto, M.N. Gussev, B. Kim, T.S. Byun, Optimized properties on base metal and thin-walled tube of generation II ATF FeCrAl, 2015. https://doi.org/10.2172/1214036.

[69] K.A. Kane, S.K. Lee, S.B. Bell, N.R. Brown, B.A. Pint, Burst behavior of nuclear grade FeCrAl and Zircaloy-2 fuel cladding under simulated cyclic dryout conditions, J. Nucl. Mater. 539 (2020) 152256. https://doi.org/10.1016/j.jnucmat.2020.152256.

[70] N.M. George, K. Terrani, J. Powers, A. Worrall, I. Maldonado, Neutronic analysis of candidate accident-tolerant cladding concepts in pressurized water reactors, Ann. Nucl. Energy. 75 (2015) 703–712. https://doi.org/10.1016/j.anucene.2014.09.005.

[71] X. Wu, T. Kozlowski, J.D. Hales, Neutronics and fuel performance evaluation of accident tolerant FeCrAl cladding under normal operation conditions, Ann. Nucl. Energy. 85 (2015) 763–775. https://doi.org/10.1016/j.anucene.2015.06.032.

[72] K. Hironaka, T. Nozawa, T. Hinoki, N. Igawa, Y. Katoh, L.L. Snead, A. Kohyama, High-temperature tensile strength of near-stoichiometric SiC/SiC composites, J. Nucl. Mater. 307–311 (2002) 1093–1097. https://doi.org/10.1016/S0022-3115(02)01049-8.

[73] K. Shimoda, T. Hinoki, H. Kishimoto, A. Kohyama, Enchanced high-temperature performances of SiC/SiC composites by high densification and crystalline structure, Compos. Sci. Technol. 71 (2011) 326–332. https://doi.org/10.1016/j.compscitech.2010.11.026.

[74] P. Joshi, B. Kombaiah, M.N. Cinbiz, K.L. Murty, Characterization of stress-rupture behavior of nuclear-grade C26M2 FeCrAl alloy for accident-tolerant fuel cladding via burst testing, Mater. Sci. Eng. A. 791 (2020) 139753. https://doi.org/10.1016/j.msea.2020.139753.

[75] K. Kane, S. Lee, S. Bell, N. Brown, B.A. Pint, Burst behavior of nuclear grade FeCrAl and Zircaloy-2 fuel cladding under simulated cyclic dryout conditions, J. Nucl. Mater. forthcoming (2020).

[76] A. Chalupová, J. Krejčí, L. Cvrček, M. Ševeček, V. Rozkošný, A. Přibyl, P. Halodová, P. Gávelová, COATED CLADDING BEHAVIOR DURING HIGH-TEMPERATURE

TRANSIENTS, Acta Polytech. CTU Proc. 24 (2019). https://doi.org/10.14311/APP.2019.24.0009.

[77] M. Ridley, S. Bell, B. Garrison, T. Graening, N. Capps, Y.-F. Su, P. Mouche, B. Johnston, K. Kane, Effects of Cr/Zircaloy-4 coating qualities for enhanced accident tolerant fuel cladding, Ann. Nucl. Energy. 188 (2023) 109799. https://doi.org/10.1016/j.anucene.2023.109799.

[78] J. Jiang, H. Zhai, P. Gong, W. Zhang, X. He, X. Ma, B. Wang, In-situ study on the tensile behavior of Cr-coated zircaloy for accident tolerant fuel claddings, Surf. Coat. Technol. 394 (2020) 125747. https://doi.org/10.1016/j.surfcoat.2020.125747.

[79] J. Ribis, A. Wu, J.-C. Brachet, F. Barcelo, B. Arnal, Atomic-scale interface structure of a Cr-coated Zircaloy-4 material, J. Mater. Sci. 53 (2018) 9879–9895. https://doi.org/10.1007/s10853-018-2333-1.

[80] S.B. Bell, T. Graening, A. Evans, P. Kelly, B.A. Pint, K.A. Kane, Burst and oxidation behavior of Cr-coated Zirlo during simulated LOCA testing, J. Nucl. Mater. 564 (2022) 153679. https://doi.org/10.1016/j.jnucmat.2022.153679.

[81] P.I.M. Stack, Size of Oxidation Feature from Image Analysis, Oak Ridge National Laboratory, 2021. https://github.com/TriplePointCat/SOFIA-CV.

[82] N.B. Pilling, R.E. Bedworth, The Oxidation of Metals at High Temperatures, Annu. Gen. Meet. Annu. Gen. Meet. XXIX (1923) 529–591.

[83] M. Dumerval, Q. Houmaire, J.C. Brachet, H. Palancher, J. Bischoff, E. Poullier, BEHAVIOR OF CHROMIUM COATED M5 CLADDINGS UPON THERMAL RAMP TESTS UNDER INTERNAL PRESSURE (LOSS-OF-COOLANT ACCIDENT CONDITIONS), in: Prague, Czech Republic, 2018.

[84] J. Yang, M. Steinbrück, C. Tang, M. Große, J. Liu, J. Zhang, D. Yun, S. Wang, Review on chromium coated zirconium alloy accident tolerant fuel cladding, J. Alloys Compd. 895 (2022) 162450. https://doi.org/10.1016/j.jallcom.2021.162450.

[85] C.K. Chow, P.C. Bera, H.E. Rosinger, Creep behavior of oxidized Zircaloy-4 fuel sheathing, in: ASM Canadian Council and Canadian Nuclear Society, Metals Park, Ohio, 1982: pp. 112–116.

[86] X. Hu, C. Dong, Q. Wang, B. Chen, H. Yang, T. Wei, R. Zhang, W. Gu, D. Chen, High-temperature oxidation of thick Cr coating prepared by arc deposition for accident tolerant fuel claddings, J. Nucl. Mater. 519 (2019) 145–156. https://doi.org/10.1016/j.jnucmat.2019.01.039.

[87] J.-C. Brachet, E. Rouesne, J. Ribis, T. Guilbert, S. Urvoy, G. Nony, C. Toffolon-Masclet, M. Le Saux, N. Chaabane, H. Palancher, A. David, J. Bischoff, J. Augereau, E. Pouillier, High temperature steam oxidation of chromium-coated zirconium-based alloys: Kinetics and process, Corros. Sci. 167 (2020) 108537. https://doi.org/10.1016/j.corsci.2020.108537.

[88] X. Han, C. Chen, Y. Tan, W. Feng, S. Peng, H. Zhang, A systematic study of the oxidation behavior of Cr coatings on Zry4 substrates in high temperature steam environment, Corros. Sci. 174 (2020) 108826. https://doi.org/10.1016/j.corsci.2020.108826.

[89] E.B. Kashkarov, D.V. Sidelev, M.S. Syrtanov, C. Tang, M. Steinbrück, Oxidation kinetics of Cr-coated zirconium alloy: Effect of coating thickness and microstructure, Corros. Sci. 175 (2020) 108883. https://doi.org/10.1016/j.corsci.2020.108883.

[90] D. Arias, J.P. Abriata, The Cr–Zr (Chromium-Zirconium) system, Bull. Alloy Phase Diagr. 7 (1986) 237–244. https://doi.org/10.1007/BF02868997.

[91] C.M. Cotell, G.J. Yurek, R.J. Hussey, D.F. Mitchell, M.J. Graham, The influence of grain-boundary segregation of Y in Cr2O3 on the oxidation of Cr metal, Oxid. Met. 34 (1990) 173–200. https://doi.org/10.1007/BF00665014.

[92] Y. Yamamoto, K. Kane, B.A. Pint, A. Trofimov, H. Wang, Report on Exploration of New FeCrAl Heat Variants with Improved Properties, Oak Ridge National Lab, 2019. https://info.ornl.gov/sites/publications/Files/Pub130413.pdf.

[93] K.G. Field, X. Hu, K.C. Littrell, Y. Yamamoto, L.L. Snead, Radiation tolerance of neutron-irradiated model Fe–Cr–Al alloys, J. Nucl. Mater. 465 (2015) 746–755. https://doi.org/10.1016/j.jnucmat.2015.06.023.

[94] Y. Yan, J.R. Keiser, K.A. Terrani, G.L. Bell, L.L. Snead, Post-quench ductility evaluation of Zircaloy-4 and select iron alloys under design basis and extended LOCA conditions, J. Nucl. Mater. 448 (2014) 436–440. https://doi.org/10.1016/j.jnucmat.2013.05.071.

[95] K.A. Terrani, B.A. Pint, Y.-J. Kim, K.A. Unocic, Y. Yang, C.M. Silva, H.M. Meyer, R.B. Rebak, Uniform corrosion of FeCrAl alloys in LWR coolant environments, J. Nucl. Mater. 479 (2016) 36–47. https://doi.org/10.1016/j.jnucmat.2016.06.047.

[96] K.A. Terrani, S.J. Zinkle, L.L. Snead, Advanced oxidation-resistant iron-based alloys for LWR fuel cladding, J. Nucl. Mater. 448 (2014) 420–435. https://doi.org/10.1016/j.jnucmat.2013.06.041.

[97] Project Plan to Prepare the U.S. Nuclear Regulatory Commission for Efficient and Effective Liscensing of Accident Toleran Fuels, U.S. Nuclear Regulatory Commission, 2019.

[98] B.A. Pint, L. Baldesberger, K. Kane, Steam Oxidation, Burst and Critical Heat Flux Testing of FeCrAl Cladding in the Severe Accident Test Station, in: Boston, Massachusetts, United States of America, 2019.

[99] J.G. Gigax, J.S. Weaver, N. Li, Microstructural Characterization of FeCrAl C26M Tubes, Los Alamos National Laboratory, 2018.

[100] S.N. Dryepondt, C. Massey, M.N. Gussev, K. Linton, K. Terrani, Tensile Strength and Steam Oxidation Resistance of ODS FeCrAl Sheet and Tubes, 2018. https://doi.org/10.2172/1507875.

[101] D.T. Hoelzer, C.P. Massey, S.J. Zinkle, D.C. Crawford, K.A. Terrani, Modern nanostructured ferritic alloys: A compelling and viable choice for sodium fast reactor fuel cladding applications, J. Nucl. Mater. 529 (2020) 151928. https://doi.org/10.1016/j.jnucmat.2019.151928.

[102] T. Manngård, A.R. Massih, Modelling and Simulation of Reactor Fuel Cladding under Loss-of-Coolant Accident Conditions, J. Nucl. Sci. Technol. 48 (2011) 39–49. https://doi.org/10.1080/18811248.2011.9711677.

[103] G.E. Dieter, Mechanical metallurgy, 3rd ed, McGraw-Hill, New York, 1986.

[104] G. Booth, The welding engineer's guide to fracture and fatigue, 1st edition, Elsevier, Boston, MA, 2015.

[105] B.A. Pint, K.A. Terrani, Y. Yamamoto, L.L. Snead, Material Selection for Accident Tolerant Fuel Cladding, Metall. Mater. Trans. E. 2 (2015) 190–196. https://doi.org/10.1007/s40553-015-0056-7.

[106] G.T. Hahn, M. Sarrate, A.R. Rosenfield, Criteria for crack extension in cylindrical pressure vessels, Int. J. Fract. Mech. 5 (1969). https://doi.org/10.1007/BF00184612.

[107] W. Maxey, J. Kiefner, R. Eiber, A. Duffy, Ductile Fracture Initiation, Propagation, and Arrest in Cylindrical Vessels, in: H. Corten (Ed.), Fract. Toughness Part II, ASTM International, 100 Barr Harbor Drive, PO Box C700, West Conshohocken, PA 19428-2959, 1972: pp. 70-70–12. https://doi.org/10.1520/STP38819S.

[108] E.S. Folias, An axial crack in a pressurized cylindrical shell, Int. J. Fract. Mech. 1–1 (1965). https://doi.org/10.1007/BF00186748.

[109] L. Freund, D. Parks, J. Rice, Running Ductile Fracture in a Pressurized Line Pipe, in: J. Rice, P. Paris (Eds.), Mech. Crack Growth, ASTM International, 100 Barr Harbor Drive, PO Box C700, West Conshohocken, PA 19428-2959, 1976: pp. 243-243–20. https://doi.org/10.1520/STP33950S.

[110] G.T. Hahn, M. Sarrate, M.F. Kanninen, A.R. Rosenfield, A model for unstable shear crack propagation in pipes containing gas pressure, Int. J. Fract. 9 (1973) 209–222. https://doi.org/10.1007/BF00041863.

[111] K.D. Ives, A.K. Shoemaker, R.F. McCartney, Pipe Deformation During a Running Shear Fracture in Line Pipe, J. Eng. Mater. Technol. 96 (1974) 309–317. https://doi.org/10.1115/1.3443246.

[112] S. Dryepondt, K.A. Unocic, D.T. Hoelzer, C.P. Massey, B.A. Pint, Development of low-Cr ODS FeCrAl alloys for accident-tolerant fuel cladding, J. Nucl. Mater. 501 (2018) 59–71. https://doi.org/10.1016/j.jnucmat.2017.12.035.

[113] K.G. Field, M.A. Snead, Y. Yamamoto, K.A. Terrani, Handbook on the Material Properties of FeCrAl Alloys for Nuclear Power Production Applications (FY18 Version: Revision 1), 2018. https://doi.org/10.2172/1474581.

[114] R. Sweet, C.P. Massey, S.B. Bell, K.A. Kane, Wrought FeCrAl alloy (C26M) cladding behavior during burst experiments and performance under LOCA conditions, in: American Nuclear Society, 2022.

[115] N. Capps, Y. Yan, A. Raftery, Z. Burns, T. Smith, K. Terrani, K. Yueh, M. Bales, K. Linton, Integral LOCA fragmentation test on high-burnup fuel, Nucl. Eng. Des. 367 (2020) 110811. https://doi.org/10.1016/j.nucengdes.2020.110811.

[116] M. Bales, A. Chung, J. Corson, L. Kyriazidis, Interpretation of Research on Fuel Fragmentation, Relocation, and Dispersal at High Burnup, 2021.

[117] H.J. Neitzel, H.E. Rosinger, The Development of a Burst Criterion for Zircaloy Fuel Cladding under LOCA Conditions, Karlsruhe Institure, 1980.

[118] Assessment of BISON: A Nuclear Fuel Performance Analysis Code, Idaho National Laboratory, Idaho Falls, Idaho 83415, 2017.

[119] D. Kaddour, S. Frechinet, A.F. Gourgues, J.C. Brachet, L. Portier, A. Pineau, Experimental determination of creep properties of Zirconium alloys together with phase transformation, Scr. Mater. 51 (2004) 515–519. https://doi.org/10.1016/j.scriptamat.2004.05.046.

[120] A.T. Donaldson, T. Healey, R.A.L. Horwood, Biaxial creep deformation of Zircaloy-4 PWR fuel cladding in the α , (α +β), and β phase temperature range, in: British Nuclear Energy Society, European Nuclear SocietyBehav, Stratford-upon-Avon, United Kingdom, 1985: pp. 83–89.

[121] T.A. Hayes, M.E. Kassner, Creep of zirconium and zirconium alloys, Metall. Mater. Trans. A. 37 (2006) 2389–2396. https://doi.org/10.1007/BF02586213.

[122] M. Limbäck, T. Andersson, A Model for Analysis of the Effect of Final Annealing on the In- and Out-of-Reactor Creep Behavior of Zircaloy Cladding, in: E. Bradley, G. Sabol (Eds.), Zircon. Nucl. Ind. Elev. Int. Symp., ASTM International, 100 Barr Harbor Drive, PO Box C700, West Conshohocken, PA 19428-2959, 1996: pp. 448-448–21. https://doi.org/10.1520/STP16185S.

[123] H.E. Rosinger, P.C. Bera, W.R. Clendening, Steady-state creep of zircaloy-4 fuel cladding from 940 to 1873 K, J. Nucl. Mater. 82 (1979) 286–297. https://doi.org/10.1016/0022-3115(79)90011-4.

[124] G.-H. Choi, C.-H. Shin, J.Y. Kim, B.J. Kim, Circumferential steady-state creep test and analysis of Zircaloy-4 fuel cladding, Nucl. Eng. Technol. 53 (2021) 2312–2322. https://doi.org/10.1016/j.net.2021.01.010.

[125] J.D. Hales, R.L. Williamson, S.R. Novascone, G. Pastore, B.W. Spencer, D.S. Stafford, K.A. Gamble, D.M. Perez, R.J. Gardner, W. Liu, J. Galloway, C. Matthews, C. Unal, N. Carson, BISON Theory Manual The Equations Behind Nuclear Fuel Analysis, Idaho National Laboratory, n.d.

[126] S. Suman, Burst criterion for Indian PHWR fuel cladding under simulated loss-of-coolant accident, Nucl. Eng. Technol. 51 (2019) 1525–1531. https://doi.org/10.1016/j.net.2019.04.004.

[127] H.E. Rosinger, J. Bowden, R.S.W. Shewfelt, The anisotropic creep behaviour of zircaloy-4 fuel cladding at 1073 K, 1982.

[128] D. Kamerman, M. Nelson, Multiaxial Plastic Deformation of Zircaloy-4 Nuclear Fuel Cladding Tubes, Nucl. Technol. 209 (2023) 872–886. https://doi.org/10.1080/00295450.2022.2160174.

[129] A.J. Ardell, O.D. Sherby, The Steady-State Creep of Polycrystalline Alpha Zirconium at Elevated Temperatures, in: Trans. Metal. Soc. AIME, 1967.

[130] E.R. Gilbert, S.A. Duran, A.L. Bement, Creep of Zirconium from 50 to 850 °C, in: Appl.-Relat. Phenom. Zircon. Its Alloys, ASTM, Philadelphia, PA, 1968: pp. 210–225.

[131] P.M. Sargent, M.F. Ashby, Deformation maps for titanium and zirconium, Scr. Metall. 16 (1982) 1415–1422. https://doi.org/10.1016/0036-9748(82)90439-2.

[132] K.J. Geelhood, W.G. Luscher, PNNL Stress/Strain Correlation for Zircaloy, Pacific Northwestern National Laboratory, 2008.

[133] N. Capps, M. Ridley, Y. Yan, S.B. Bell, K. Kane, BISON Validation to In-situ Cladding Burst Test and High Burnup LOCA Experiments, Curr. Rev. (2022).

[134] A. Recuero, D. Schwen, S. Biswas, M3 Milestone: Anisotropic Inelastic Deformation 2021, Idaho National Laboratory, Idaho Falls, Idaho 83415, 2021.

[135] H.W. Swift, Plastic instability under plane stress, J. Mech. Phys. Solids. 1 (1952) 1–18. https://doi.org/10.1016/0022-5096(52)90002-1.

[136] M. Considère, Memoire sur l'emploi du fer et de l'acier dans les constructions," in Annales des Ponts et Chausées, Annales des Ponts et Chausées. 9 (1885) 574–605.

[137] R. Hill, On discontinuous plastic states, with special reference to localized necking in thin sheets, J. Mech. Phys. Solids. 1 (1952) 19–30. https://doi.org/10.1016/0022-5096(52)90003-3.

[138] W. Bleck, Z. Deng, K. Papamantellos, C.O. Gusek, A comparative study of the forming-limit diagram models for sheet steels, J. Mater. Process. Technol. 83 (1998) 223–230. https://doi.org/10.1016/S0924-0136(98)00066-1.

[139] Y.-M. Hwang, Y.-K. Lin, H.-C. Chuang, Forming limit diagrams of tubular materials by bulge tests, J. Mater. Process. Technol. 209 (2009) 5024–5034. https://doi.org/10.1016/j.jmatprotec.2009.01.026.

[140] M.C. Butuc, J.J. Gracio, A. Barata da Rocha, A theoretical study on forming limit diagrams prediction, J. Mater. Process. Technol. 142 (2003) 714–724. https://doi.org/10.1016/S0924-0136(03)00813-6.

[141] M. Kim, F. Rickhey, H. Lee, N. Kim, Analytical determination of forming limit curve for zirlo and its experimental validation, J. Manuf. Process. 23 (2016) 122–129. https://doi.org/10.1016/j.jmapro.2016.06.006.

[142] Z. Marciniak, K. Kuczyński, Limit strains in the processes of stretch-forming sheet metal, Int. J. Mech. Sci. 9 (1967) 609–620. https://doi.org/10.1016/0020-7403(67)90066-5.

[143] M. Larsson, A. Needleman, V. Tvergaard, B. Storåkers, Instability and failure of internally pressurized ductile metal cylinders, J. Mech. Phys. Solids. 30 (1982) 121–154. https://doi.org/10.1016/0022-5096(82)90020-5.

[144] V. Tvergaard, A. Needleman, K.K. Lo, Flow localization in the plane strain tensile test, J. Mech. Phys. Solids. 29 (1981) 115–142. https://doi.org/10.1016/0022-5096(81)90019-3.

[145] P. Bridgman, The stress distribution at the neck of a tension specimen, Harvard University Press, 1964. https://doi.org/10.4159/harvard.9780674287839.

[146] P.W. Bridgman, Studies in Large Plastic Flow and Fracture: With Special Emphasis on the Effects of Hydrostatic Pressure, Harvard University Press, 1964. https://doi.org/10.4159/harvard.9780674731349.

[147] S. Coppieters, T. Kuwabara, Identification of Post-Necking Hardening Phenomena in Ductile Sheet Metal, Exp. Mech. 54 (2014) 1355–1371. https://doi.org/10.1007/s11340-014-9900-4.

[148] G.R. Johnson, W.H. Cook, Fracture characteristics of three metals subjected to various strains, strain rates, temperatures and pressures, Eng. Fract. Mech. 21 (1985) 31–48. https://doi.org/10.1016/0013-7944(85)90052-9.

[149] Y. Bai, T. Wierzbicki, A new model of metal plasticity and fracture with pressure and Lode dependence, Int. J. Plast. 24 (2008) 1071–1096. https://doi.org/10.1016/j.ijplas.2007.09.004.

[150] X. Wang, J. Shi, Validation of Johnson-Cook plasticity and damage model using impact experiment, Int. J. Impact Eng. 60 (2013) 67–75. https://doi.org/10.1016/j.ijimpeng.2013.04.010.

[151] J.W. Hancock, A.C. Mackenzie, On the mechanisms of ductile failure in high-strength steels subjected to multi-axial stress-states, J. Mech. Phys. Solids. 24 (1976) 147–160. https://doi.org/10.1016/0022-5096(76)90024-7.

[152] M. Jutras, IMPROVEMENT OF THE CHARACTERISATION METHOD OF THE JOHNSON-COOK MODEL, Laval University, 2008.

[153] A.L. Gurson, Continuum Theory of Ductile Rupture by Void Nucleation and Growth: Part I—Yield Criteria and Flow Rules for Porous Ductile Media, J. Eng. Mater. Technol. 99 (1977) 2–15. https://doi.org/10.1115/1.3443401.

[154] V. Tvergaard, Influence of voids on shear band instabilities under plane strain conditions, Int. J. Fract. 17 (1981) 389–407. https://doi.org/10.1007/BF00036191.

[155] V. Tvergaard, A. Needleman, Analysis of the cup-cone fracture in a round tensile bar, Acta Metall. 32 (1984) 157–169. https://doi.org/10.1016/0001-6160(84)90213-X.

[156] M. Balourdet, C. Bernaudat, V. Basini, N. Hourdequin, The Prometra Programme: Assesment of Mechanical Properties of Zircaloy 4 Fuel Cladding During an RIA, in: Trans. 15th Int. Conf. Struct. Mech. React. Technol., International Association for Structural Mechanics in Reactor Technology, Seoul, South Korea, 1999.

[157] D. Mohr, M. Dunand, K.-H. Kim, Evaluation of associated and non-associated quadratic plasticity models for advanced high strength steel sheets under multi-axial loading, Int. J. Plast. 26 (2010) 939–956. https://doi.org/10.1016/j.ijplas.2009.11.006.

[158] J.H. Sung, J.H. Kim, R.H. Wagoner, A plastic constitutive equation incorporating strain, strain-rate, and temperature, Int. J. Plast. 26 (2010) 1746–1771. https://doi.org/10.1016/j.ijplas.2010.02.005.

[159] G.B. Broggiato, F. Campana, L. Cortese, Identification of Material Damage Model Parameters: an Inverse Approach Using Digital Image Processing, Meccanica. 42 (2007) 9–17. https://doi.org/10.1007/s11012-006-9019-5.

[160] H. Zhang, S. Coppieters, C. Jiménez-Peña, D. Debruyne, Inverse identification of the post-necking work hardening behaviour of thick HSS through full-field strain measurements during diffuse necking, Mech. Mater. 129 (2019) 361–374. https://doi.org/10.1016/j.mechmat.2018.12.014.

[161] N. Tardif, S. Kyriakides, Determination of anisotropy and material hardening for aluminum sheet metal, Int. J. Solids Struct. 49 (2012) 3496–3506. https://doi.org/10.1016/j.ijsolstr.2012.01.011.

[162] M. Dunand, D. Mohr, Hybrid experimental–numerical analysis of basic ductile fracture experiments for sheet metals, Int. J. Solids Struct. 47 (2010) 1130–1143. https://doi.org/10.1016/j.ijsolstr.2009.12.011.

[163] A. Deb, J.H. Prevost, B. Loret, Adaptive meshing for dynamic strain localization, Comput. Methods Appl. Mech. Eng. 137 (1996) 285–306. https://doi.org/10.1016/S0045-7825(96)01068-7.

[164] W.B. Castelló, F.G. Flores, A triangular finite element with local remeshing for the large strain analysis of axisymmetric solids, Comput. Methods Appl. Mech. Eng. 198 (2008) 332–343. https://doi.org/10.1016/j.cma.2008.08.009.

[165] J. Kajberg, G. Lindkvist, Characterisation of materials subjected to large strains by inverse modelling based on in-plane displacement fields, Int. J. Solids Struct. 41 (2004) 3439–3459. https://doi.org/10.1016/j.ijsolstr.2004.02.021.

[166] T.D. Nguyen, B.L. Boyce, An inverse finite element method for determining the anisotropic properties of the cornea, Biomech. Model. Mechanobiol. 10 (2011) 323–337. https://doi.org/10.1007/s10237-010-0237-3.

[167] C. Schwarzbach, E. Haber, Finite element based inversion for time-harmonic electromagnetic problems, Geophys. J. Int. 193 (2013) 615–634. https://doi.org/10.1093/gji/ggt006.

[168] S. Coppieters, S. Cooreman, H. Sol, P. Van Houtte, D. Debruyne, Identification of the post-necking hardening behaviour of sheet metal by comparison of the internal and external work in the necking zone, J. Mater. Process. Technol. 211 (2011) 545–552. https://doi.org/10.1016/j.jmatprotec.2010.11.015.

[169] M. Grédiac, F. Pierron, S. Avril, E. Toussaint, The Virtual Fields Method for Extracting Constitutive Parameters From Full-Field Measurements: a Review, Strain. 42 (2008) 233–253. https://doi.org/10.1111/j.1475-1305.2006.tb01504.x.

[170] F. Pierron, M. Grédiac, The virtual fields method: extracting constitutive mechanical parameters from full-field deformation measurements, Springer, New York London, 2012.

[171] S. Kramer, W. Scherzinger, Implementation and Evaluation of the Virtual Fields Method: Determining Constitutive Model Parameters From Full-Field Deformation Data., 2014. https://doi.org/10.2172/1158669.

[172] J. Zhao, Y. Sang, F. Duan, The state of the art of two-dimensional digital image correlation computational method, Eng. Rep. 1 (2019). https://doi.org/10.1002/eng2.12038.

[173] M.A. Sutton, J.H. Yan, V. Tiwari, H.W. Schreier, J.J. Orteu, The effect of out-of-plane motion on 2D and 3D digital image correlation measurements, Opt. Lasers Eng. 46 (2008) 746–757. https://doi.org/10.1016/j.optlaseng.2008.05.005.

[174] K. Denys, S. Coppieters, M. Seefeldt, D. Debruyne, Multi-DIC setup for the identification of a 3D anisotropic yield surface of thick high strength steel using a double perforated specimen, Mech. Mater. 100 (2016) 96–108. https://doi.org/10.1016/j.mechmat.2016.06.011.

[175] D. Solav, K.M. Moerman, A.M. Jaeger, K. Genovese, H.M. Herr, MultiDIC: An Open-Source Toolbox for Multi-View 3D Digital Image Correlation, IEEE Access. 6 (2018) 30520–30535. https://doi.org/10.1109/ACCESS.2018.2843725.

[176] D. Campello, N. Tardif, A. Maynadier, M. Baietto, M. Coret, J. Desquines, A new experimentalt setup for high temperature creep test on Zircaloy-4 fuel rods internally pressurized, in: n.d.

[177] D. Campello, N. Tardif, J. Desquines, M.-C. Baietto, M. Coret, A. Maynadier, P. Chaudet, Validation of a multimodal set-up for the study of zirconium alloys claddings' behaviour under simulated LOCA conditions, Strain. 54 (2018) e12279. https://doi.org/10.1111/str.12279.

[178] K. Kane, N. Capps, B. Garrison, B. Johnston, S. Bell, K. Linton, Development and Implementation of Digital Image Correlation for Out-of-Cell Burst Testing, 2021. https://doi.org/10.2172/1828255.

[179] K. Kane, B. Garrison, S. Bell, B. Johnston, N. Capps, K. Linton, Report Summarizing Progress in Digital Image Correlation Analysis of Burst Phenomenon, Oak Ridge National Laboratory, 2022.

[180] K. Kane, S. Bell, B. Garrison, M. Ridley, M. Gussev, K. Linton, N. Capps, Quantifying deformation during Zry-4 burst testing: a comparison of BISON and a combined in-situ digital image correlation and infrared thermography method, J. Nucl. Mater. 572 (2022) 154063. https://doi.org/10.1016/j.jnucmat.2022.154063.

[181] D.-H. Kim, G.-H. Choi, H. Kim, C. Lee, S.-U. Lee, J.-D. Hong, H.-S. Kim, Measurement of Zircaloy-4 cladding tube deformation using a three-dimensional digital image correlation system with internal transient heating and pressurization, Nucl. Eng. Des. 363 (2020) 110662. https://doi.org/10.1016/j.nucengdes.2020.110662.

[182] M.N. Gussev, M. Howell, K.A. Terrani, A. Nelson, Execution of Targeted Experiments to Inform BISON for ATF Materials: An Advanced Approach to Tube Burst Testing, Oak Ridge National Lab., Tenn. (USA), n.d.

[183] E.V. Murphy, F. Havelock, Emissivity of zirconium alloys in air in the temperature range 100–400°c, J. Nucl. Mater. 60 (1976) 167–176. https://doi.org/10.1016/0022-3115(76)90163-X.

[184] P. Mathew, I. George, Total emissivity of Zircaloy-4 at high temperatures, in: 1996.

[185] B. Bouvry, G. Cheymol, L. Ramiandrisoa, B. Javaudin, C. Gallou, H. Maskrot, N. Horny, T. Duvaut, C. Destouches, L. Ferry, C. Gonnier, Multispectral pyrometry for surface temperature measurement of oxidized Zircaloy claddings, Infrared Phys. Technol. 83 (2017) 78–87. https://doi.org/10.1016/j.infrared.2017.04.013.

[186] T. Burgoyne, A. Garlick, The Effect of Oxidation and Crud Deposits on the Emissivity of Zircaloy-2 Cladding, n.d.

[187] M.A. Sutton, Image Correlation for Shape, Motion and Deformation Measurements: Basic Concepts, Theory and Applications, 2010.

[188] M. Postlethwait, K. Sikka, M. Modest, J. Hellmann, High-Temperature, Normal Spectral Emittance of Silicon Carbide Based Materials, J. Thermophys. Heat Transf. 8 (1994).

[189] S. Leistikow, G. Schanz, Oxidation kinetics and related phenomena of zircaloy-4 fuel cladding exposed to high temperature steam and hydrogen-steam mixtures under PWR accident conditions, Nucl. Eng. Des. 103 (1987) 65–84. https://doi.org/10.1016/0029-5493(87)90286-X.

[190] T. Manngård, A.R. Massih, Modelling and Simulation of Reactor Fuel Cladding under Loss-of-Coolant Accident Conditions, J. Nucl. Sci. Technol. 48 (2011) 39–49. https://doi.org/10.1080/18811248.2011.9711677.

[191] R. Sweet, N. George, K. Terrani, B. Wirth, BISON Fuel Performance Analysis of FeCrAl cladding with updated properties, Oak Ridge National Laboratory, Oak Ridge, TN, 2016.

[192] C.P. Massey, K.A. Terrani, S.N. Dryepondt, B.A. Pint, Cladding burst behavior of Fe-based alloys under LOCA, J. Nucl. Mater. 470 (2016) 128–138. https://doi.org/10.1016/j.jnucmat.2015.12.018.

[193] K.A. Gamble, T. Barani, D. Pizzocri, J.D. Hales, K.A. Terrani, G. Pastore, An investigation of FeCrAl cladding behavior under normal operating and loss of coolant conditions, J. Nucl. Mater. 491 (2017) 55–66. https://doi.org/10.1016/j.jnucmat.2017.04.039.

[194] J. Kim, J.W. Yoon, H. Kim, S.-U. Lee, Prediction of ballooning and burst for nuclear fuel cladding with anisotropic creep modeling during Loss of Coolant Accident (LOCA), Nucl. Eng. Technol. 53 (2021) 3379–3397. https://doi.org/10.1016/j.net.2021.04.020.

[195] Report on Fuel Fragmentation, Relocation, Dispersal (FFRD), Nuclear Energy Agency, 2020.

[196] A.R. Massih, Transformation kinetics of zirconium alloys under non-isothermal conditions, J. Nucl. Mater. 384 (2009) 330–335. https://doi.org/10.1016/j.jnucmat.2008.11.033.

[197] T. Burgoyne, A. Garlick, The Effect of Oxidation and Crud Deposits on the Emissivity of Zircaloy-2 Cladding, in: Spaatind, Norway, 1976.

[198] J. Ferner, H.E. Rosinger, The effect of circumferential temperature variation on fuel-cladding failure, J. Nucl. Mater. 132 (1985) 167–172. https://doi.org/10.1016/0022-3115(85)90411-8.

[199] V. Di Marcello, A. Schubert, J. van de Laar, P. Van Uffelen, The TRANSURANUS mechanical model for large strain analysis, Nucl. Eng. Des. 276 (2014) 19–29. https://doi.org/10.1016/j.nucengdes.2014.04.041.

[200] F. Abed-Meraim, T. Balan, G. Altmeyer, Investigation and comparative analysis of plastic instability criteria: application to forming limit diagrams, Int. J. Adv. Manuf. Technol. 71 (2014) 1247–1262. https://doi.org/10.1007/s00170-013-5530-8.

[201] Z. Marciniak, K. Kuczyński, T. Pokora, Influence of the plastic properties of a material on the forming limit diagram for sheet metal in tension, Int. J. Mech. Sci. 15 (1973) 789–800. https://doi.org/10.1016/0020-7403(73)90068-4.

[202] C.E.L. Hunt, E.M. Schulson, Recrystallization of zircaloy-4 during transient heating, J. Nucl. Mater. 92 (1980) 184–190. https://doi.org/10.1016/0022-3115(80)90101-4.

[203] Y. Zhou, B. Devarajan, K.L. Murty, Short-term rupture studies of Zircaloy-4 and Nb-modified Zircaloy-4 tubing using closed-end internal pressurization, Nucl. Eng. Des. 228 (2004) 3–13. https://doi.org/10.1016/j.nucengdes.2003.06.013.

Vita

Samuel Bell was born in Pomona , California to Graham and Julie Bell. After graduating from Damien High School in 2014, he attended the University of California, Santa Barbara (UCSB) where he received a bachelor's degree with a double major in Physics and Earth Science in 2019. During the summer of 2016, he gained his first experience in world of science by completing an internship at the Jet Propulsion Laboratory.

After graduating from UCSB, he joined Dr. Steven Zinkle's research group at the University of Tennessee, Knoxville to pursue a doctorate in Materials Science and Engineering. He studied the behavior of nuclear fuel cladding during accident scenarios, earning a Doctor of Philosophy degree in August of 2023. He is excited to continue his career exploring material performance by joining the research staff at Oak Ridge National Laboratory.